

Approved : \_\_\_\_\_

Timothy A. Shedd, Assistant Professor

Date : \_\_\_\_\_

**CHARACTERIZATION OF BUBBLE  
ENTRAINMENT, INTERFACIAL ROUGHNESS  
AND THE SLIDING BUBBLE MECHANISM IN  
HORIZONTAL ANNULAR FLOW**

by

Daniel J. Rodríguez

A dissertation submitted in partial fulfillment of  
the requirements for the degree of

Doctor of Philosophy  
(Mechanical Engineering)

at the  
UNIVERSITY OF WISCONSIN-MADISON  
2004

# CHARACTERIZATION OF BUBBLE ENTRAINMENT, INTERFACIAL ROUGHNESS AND THE SLIDING BUBBLE MECHANISM IN HORIZONTAL ANNULAR FLOW

Daniel J. Rodríguez

Under the supervision of Assistant Professor Timothy A. Shedd

Department of Mechanical Engineering

At the University of Wisconsin-Madison

Flow boiling inside pipes is a widely implemented means of heat transfer in many branches of industry and energy generation. However, the nature and relative importance of the underlying mechanisms linked to this type of process are still a matter of controversy. This study addresses three particular aspects of the mechanistic approach for the explanation of flow boiling heat transfer. The flow mechanics observed in horizontal two-phase adiabatic air/water flow are studied in an effort to explain flow boiling. Specifically, entrained bubble behavior related to the sliding bubble heat transfer mechanism and pressure drop in the annular flow regime are studied using three optical techniques. Backlit bubble contour imaging is used to obtain estimates of the size distribution and entrained bubble concentration within the thin liquid film in annular flow. Planar Laser Induced Fluorescence (PLIF) is used for qualitatively documenting the bubble entrainment mechanism associated with disturbance waves in annular flow. The PLIF technique also proves useful in directly measuring the film thickness and interfacial roughness of the flow. A more integral view of the pressure drop mechanisms that exist in annular flow is obtained as a result of an automated analysis of the roughness data. A CFD simulation of the sliding bubble mechanism is used to predict the effect of bubble diameter and outer flow conditions on the modulation of turbulence. The results from the simulation are used in constructing an understanding of the cooling effect

of individual sliding bubbles associated with enhanced turbulent mixing. Finally, a cross-cut micro-scale particle image velocimetry (PIV) system with micron scale spatial resolution is proposed for studying the dynamic behavior of entrained bubbles and the liquid flow around them. The estimation of the cumulative effect of a given concentration, size distribution and radial location of entrained bubbles, coupled to the knowledge of the flow parameters that produce those entrainment characteristics, can help elucidate the physics represented by empirical quantities in current saturated flow boiling heat transfer models.

# CHARACTERIZATION OF BUBBLE ENTRAINMENT, INTERFACIAL ROUGHNESS AND THE SLIDING BUBBLE MECHANISM IN HORIZONTAL ANNULAR FLOW

Daniel J. Rodríguez  
Department of Mechanical Engineering  
University of Wisconsin-Madison, 2004  
Professor Timothy A. Shedd, Advisor

Flow boiling inside pipes is a widely implemented means of heat transfer in many branches of industry and energy generation. However, the nature and relative importance of the underlying mechanisms linked to this type of process are still a matter of controversy. This study addresses three particular aspects of the mechanistic approach for the explanation of flow boiling heat transfer. The flow mechanics observed in horizontal two-phase adiabatic air/water flow are studied in an effort to explain flow boiling. Specifically, entrained bubble behavior related to the sliding bubble heat transfer mechanism and pressure drop in the annular flow regime are studied using three optical techniques. Backlit bubble contour imaging is used to obtain estimates of the size distribution and entrained bubble concentration within the thin liquid film in annular flow. Planar Laser Induced Fluorescence (PLIF) is used for qualitatively documenting the bubble entrainment mechanism associated with disturbance waves in annular flow. The PLIF technique also proves useful in directly measuring the film thickness and interfacial roughness of the flow. A more integral view of the pressure drop mechanisms that exist in annular flow is obtained as a result of an automated analysis of the roughness data. A CFD simulation of the sliding bubble mechanism is used to predict the effect of bubble diameter and outer flow conditions on the modulation of turbulence. The results from the simulation are used in constructing an understanding of the cooling effect of individual sliding bubbles associated with enhanced turbulent mixing. Finally, a cross-cut micro-scale particle image velocimetry (PIV) system with micron scale spatial resolution is

proposed for studying the dynamic behavior of entrained bubbles and the liquid flow around them. The estimation of the cumulative effect of a given concentration, size distribution and radial location of entrained bubbles, coupled to the knowledge of the flow parameters that produce those entrainment characteristics, can help elucidate the physics represented by empirical quantities in current saturated flow boiling heat transfer models.

# Acknowledgments

I want to thank my advisor, Professor Timothy A. Shedd, who was enormously generous and supportive since the very first day. I will always be grateful not only for his guidance, but also for the free rein I had to test my own ideas. I hope to carry on his example of enthusiasm, creativity and solid work ethics. I am very lucky for having found in him not only a mentor, but a friend.

My wife, Paola, provided unfailing motivation through the hard times. Her love and patience were unwavering despite our forced separation of more than two years and 5200 kilometers. She always found enough strength to keep hope alive until the end of this small odyssey. I will always treasure her soul and her spirit as the greatest gift from Providence.

My parents, Leonel and Patricia, have always been my first example of love and dedication. They have given me much more than I could ever express in a few lines. I want to thank them for all their love, support and years of sacrifice.

I am very grateful to all of my family. I am especially indebted to my aunt Clara Isabel and my grandparents Jesús and Olga for caring so much about my troubles and rejoicing in my triumphs.

I want to thank Professor Sanford A. Klein for the many hours he spent reviewing my work and for many valuable suggestions. I am also grateful for what I learned during his inspiring lectures.

I am also indebted to Professor Alvaro E. Pinilla for his encouragement in my endeavors and his mentoring during my undergraduate and Master's degrees. I want to thank him for teaching me the real value of Academia.

I want to thank Diego A. Arias for his friendship, our many moments of Colombian conspiracy and for our seamless collaboration in many projects both inside and outside of

engineering.

Patty, Sebastian, Greg, Charlie, Frank, Holly, Mohammed, Alex, Adam, Helge, Rob, Audrey, Katie and Thomas were great office mates and excellent colleagues. I learned many things from them and we shared many good laughs. I am grateful for their friendship and their help. I also want to thank Nicole Weimer and Toyin Oshinowo for their collaboration in acquiring and processing some of the data, and Dan Hoch for his advise in machining some parts.

The author appreciates the financial support for this project provided by the University of Wisconsin-Madison, the National Science Foundation under award number CTS-0134510 and the ASHRAE Grant-in-Aid program.

The present document summarizes my research endeavors at the University of Wisconsin-Madison. It does not fully capture, however, the wealth of extracurricular experiences provided by many outstanding and brilliant people I had the privilege of meeting on its campus.

# Table of Contents

Abstract	i
Acknowledgments	iii
Table of Contents	v
List of Tables	viii
List of Figures	ix
Nomenclature	xii
Greek Nomenclature	xvi
Subscript Nomenclature	xvii
<b>1 Introduction</b>	<b>1</b>
1.1 General Description of the Flow Boiling Process . . . . .	2
1.2 Survey of Flow Boiling Modeling . . . . .	4
1.2.1 General Formulation of Non Flow-Regime-Based Models . . . . .	4
Physical Interpretation of $F_{mic}$ . . . . .	8
Characteristics of the Empirical Databases . . . . .	9
1.2.2 Flow Regime Based Models . . . . .	10
The Kattan, Thome, Favrat Heat Transfer Model . . . . .	11
1.3 Implementation of Representative Correlations . . . . .	15
1.4 Model Predictions and Comparison Against Experimental Data . . . . .	16
1.5 Discussion . . . . .	20
1.6 Sliding Bubble Mechanism . . . . .	24
1.7 Scope and Outline of Current Research . . . . .	27
<b>2 Bubble Entrainment Statistics</b>	<b>31</b>
2.1 Backlit Imaging Experimental Setup . . . . .	32
2.1.1 Backlit Flow Loop . . . . .	32
2.1.2 Backlit Image Acquisition . . . . .	34
2.1.3 Experimental Procedure . . . . .	35
2.1.4 Image Processing . . . . .	36
2.1.5 Bubble Size Uncertainty . . . . .	40
2.2 Backlit Imaging Results . . . . .	41
2.2.1 Bubble Size Distribution . . . . .	41

2.2.2	Mean Bubble Diameter . . . . .	45
2.2.3	Bubble Number Concentration . . . . .	45
2.3	Discussion . . . . .	47
2.3.1	Entrainment Mechanisms . . . . .	47
2.3.2	Bubble Breakup . . . . .	51
2.3.3	Exponential Size Distribution . . . . .	54
<b>3</b>	<b>Cross-cut Imaging of the Base Film and Interfacial Waves</b>	<b>55</b>
3.1	Background . . . . .	57
3.2	PLIF Experimental Setup . . . . .	59
3.2.1	PLIF Flow Loop . . . . .	59
3.2.2	PLIF Image acquisition . . . . .	61
3.3	PLIF Results . . . . .	64
3.3.1	Qualitative PLIF Results . . . . .	64
3.3.2	Quantitative PLIF Results . . . . .	68
	Mean Film Thickness and RMS Value . . . . .	73
	Interfacial Wave Detection . . . . .	77
3.4	Discussion . . . . .	86
<b>4</b>	<b>Interfacial Roughness and Pressure Drop Modeling</b>	<b>91</b>
4.1	Background . . . . .	91
4.2	Implementation of the Owen-Hewitt Model . . . . .	92
4.2.1	Liquid Film Model . . . . .	92
4.2.2	Core Model . . . . .	93
4.2.3	Empirical Correlations . . . . .	97
4.2.4	Modifications to the Original Owen-Hewitt Model . . . . .	99
4.3	Results . . . . .	102
4.4	Discussion . . . . .	106
<b>5</b>	<b>CFD Simulation of the Sliding Bubble Mechanism</b>	<b>109</b>
5.1	Motivation . . . . .	109
5.2	Simulation Setup . . . . .	110
5.2.1	Simulation Geometry and Mesh . . . . .	110
5.2.2	Boundary Conditions . . . . .	112
5.2.3	Turbulence Models . . . . .	112
5.2.4	Solver . . . . .	113
5.3	Simulation Results . . . . .	114
5.3.1	X-Velocity Profiles . . . . .	114
5.3.2	Turbulent Viscosity Ratio . . . . .	115
5.4	Discussion . . . . .	117
5.4.1	Discussion of Simulation Results . . . . .	117
5.4.2	Expected Localized Heat Transfer Enhancement per Entrained Bubble	122

<b>6</b>	<b>Setup and Considerations for Cross-cut micro-PIV Measurements</b>	<b>126</b>
6.1	Test Section and Imaging System Setup . . . . .	126
6.2	Flow Seeding, Depth of Field and Spatial Resolution . . . . .	131
6.2.1	Diffraction Limited Resolution . . . . .	132
6.2.2	Depth of Field . . . . .	133
6.2.3	Super-resolution Using The Sub-correlation PTV Method . . . . .	133
6.2.4	Brownian Motion Error . . . . .	135
6.2.5	Seeding . . . . .	136
6.2.6	Calculations for the Micro-PIV Imaging System . . . . .	137
6.3	Sample Images . . . . .	137
<b>7</b>	<b>Conclusions</b>	<b>144</b>
7.1	Conclusions from Chapter 2 . . . . .	144
7.2	Conclusions from Chapter 3 . . . . .	145
7.3	Conclusions from Chapter 4 . . . . .	146
7.4	Conclusions from Chapter 5 . . . . .	147
7.5	Conclusions from Chapter 6 . . . . .	148
<b>A</b>	<b>EES Implementation of Flow Boiling Correlations</b>	<b>149</b>
<b>B</b>	<b>EES Implementation of the Owen-Hewitt Model</b>	<b>171</b>
<b>C</b>	<b>PLIF Images of Interfacial Waves</b>	<b>182</b>
	<b>Bibliography</b>	<b>198</b>
	<b>Vita</b>	<b>210</b>

# List of Tables

3.1	Length proportions for the idealized interface based on $k_c = 1.5$ . . . . .	86
4.1	Input and output variables for each run modes of the Owen-Hewitt model. .	107
6.1	Pulse width and delay for IEC mode. . . . .	130
6.2	Results of calculation for micro-PIV imaging system. . . . .	138

# List of Figures

1.1	Schematic representation of the vertical flow boiling process. . . . .	3
1.2	Schematic representation of the horizontal flow boiling process. . . . .	3
1.3	Idealized variation of the heat transfer ratio with respect to the heat flux ratio for fixed $x$ and $G$ . . . . .	5
1.4	Boiling of R 134a in a copper tube for upflow, downflow and horizontal flow.	11
1.5	Flow pattern map sample. . . . .	12
1.6	Determination of constants $C$ and $m$ . . . . .	14
1.7	Flow boiling heat transfer model inputs . . . . .	16
1.8	Comparison of model predictions against R134a data from Kattan <i>et al.</i> [1] at $T_{sat} = 4.4^{\circ}\text{C}$ , $D = 10.92$ mm, $G = 299$ kg/m <sup>2</sup> -s and $q = 5\text{-}10$ kW/m <sup>2</sup> . . . .	17
1.9	Comparison of model predictions against R123 data from Kattan <i>et al.</i> [1] at $T_{sat} = 4.4^{\circ}\text{C}$ , $D = 10.92$ mm, $G = 299$ kg/m <sup>2</sup> -s and $q = 5\text{-}10$ kW/m <sup>2</sup> . . . .	17
1.10	Comparison of model predictions against R123 data from Kattan <i>et al.</i> [1] at $T_{sat} = 30.7^{\circ}\text{C}$ , $D = 12$ mm, $G = 101.1$ kg/m <sup>2</sup> -s and $q = 5\text{-}15$ kW/m <sup>2</sup> . . . .	18
1.11	Comparison of model predictions against R717 data from Zürrcher <i>et al.</i> [2] at $T_{sat} = 4^{\circ}\text{C}$ , $D = 14$ mm, $G = 20$ kg/m <sup>2</sup> -s and $q = 5.4$ kW/m <sup>2</sup> . . . . .	18
1.12	Comparison of model predictions against R717 data from Zürrcher <i>et al.</i> [2] at $T_{sat} = 4^{\circ}\text{C}$ , $D = 14$ mm, $G = 80$ kg/m <sup>2</sup> -s and $q = 13.0$ kW/m <sup>2</sup> . . . . .	19
1.13	Comparison of model predictions against R718 data from Sun and Hewitt [3] at $T_{sat} = 93.45^{\circ}\text{C}$ , $D = 9.5$ mm, $G = 240$ kg/m <sup>2</sup> -s and $q = 75$ kW/m <sup>2</sup> . . . .	19
1.14	Thermochromic liquid crystal (TLC) imaging of temperature depression associated to a cap shaped sliding bubble taken from [4]. . . . .	26
1.15	Difference in heat transfer coefficient vs. wall superheat for upflow and downflow conditions as measured by Thorncroft [5]. . . . .	27
2.1	Air/water flow loop schematic. . . . .	33
2.2	Setup for backlit images. . . . .	35
2.3	Image processing steps for base film ROI. . . . .	38
2.4	Image processing steps for disturbance wave ROI. . . . .	39
2.5	Exponential fits to bubble size distributions. . . . .	42
2.6	Power-law exponent. . . . .	44
2.7	Mean diameter normalized using mean base film thickness. . . . .	46
2.8	Bubble number concentration. . . . .	48
2.9	PLIF images of disturbance waves and backlit images of base film for increasing $U_{sg}$ . . . . .	49
2.10	Base film thickness along the side of the tube measured by Schubring and Shedd [6] using optical method developed by Shedd and Newell [7]. . . . .	52
2.11	Critical Weber number. . . . .	53

3.1	Sample image from Hewitt <i>et al.</i> [8]. . . . .	59
3.2	Flow loop schematic for PLIF measurements. . . . .	60
3.3	Setup for PLIF images. . . . .	62
3.4	Reduction of near-wall dark band and distortion. . . . .	63
3.5	PLIF image of stratified flow. . . . .	65
3.6	Typical cross-cut images obtained with the PLIF technique for the wavy-annular and fully annular flow regimes. . . . .	65
3.7	Three stages of the folding action mechanism. . . . .	66
3.8	Schematic of setup orientation and image arrangements for top, side, and bottom PLIF cross-cuts. . . . .	68
3.9	PLIF Imaging of Interfacial Waves. . . . .	69
3.10	PLIF Imaging of the base film. . . . .	70
3.11	Samples of image processing for film thickness measurements. . . . .	73
3.12	Mean film thickness along the top, side and bottom of the pipe. . . . .	75
3.13	RMS values. . . . .	76
3.14	Flowchart representing the iterative scheme used in the quantitative processing of the PLIF images. . . . .	79
3.15	Idealized geometry for interfacial waves and the base liquid film. . . . .	81
3.16	Average wave intermittence. . . . .	81
3.17	Comparison of base film thickness measured by the PLIF method for varying $k_c$ values against film thickness measurements using the TIR method. . . . .	82
3.18	Mean base film thickness along the side and bottom of the pipe for $k_c = 1.5$ . . . . .	84
3.19	Base film standard deviation along the side and bottom of the pipe for $k_c = 1.5$ . . . . .	85
3.20	Mean wave height along the side and bottom of the pipe for $k_c = 1.5$ . . . . .	87
3.21	Comparison of mean wave height along the bottom of the pipe against conductance probe data. . . . .	88
3.22	Mean wave height vs. RMS along the bottom of the pipe. . . . .	88
4.1	Correlation for $\kappa_{tp}$ . . . . .	98
4.2	$A_r$ function by Nikuradse. . . . .	99
4.3	Low $\delta^*$ and high $\delta^*$ roughness height correlations. . . . .	100
4.4	Ratio of the core acceleration term to the experimental $\frac{\partial P}{\partial z}$ value. . . . .	103
4.5	Ratio of the predicted roughness height to the experimental roughness height. . . . .	104
4.6	Comparison between the non-dimensional roughness height correlation from Figure 4.3 and experimental PLIF data. . . . .	104
4.7	Ratio of experimental pressure gradient to predicted interfacial roughness pressure gradient from RM2. . . . .	105
4.8	Interfacial friction factor from RM2. . . . .	105
4.9	Power-law coefficient from RM2. . . . .	106
5.1	Mesh details. . . . .	111
5.2	Universal velocity profile. . . . .	114

5.3	Comparison of the x-velocity profiles. . . . .	116
5.4	$k - \epsilon$ turbulent viscosity ratio. . . . .	118
5.5	RSM turbulent viscosity ratio. . . . .	119
5.6	Turbulent viscosity ratio along the vertical and horizontal planes for the obstacle at the middle of the channel. . . . .	120
5.7	Effect of bubble on the energy cascade. . . . .	121
5.8	Required localized turbulent heat transfer enhancement based on $Q_h = 0.2$ . . . . .	125
6.1	Dimensions of the square channel test section. Axial view. . . . .	129
6.2	Square channel test section. Side View. . . . .	130
6.3	Schematic of setup for cross-cut images inside square channel. . . . .	131
6.4	Entrained bubbles and hollow glass microballoons. . . . .	140
6.5	First sample pair of IEC images. . . . .	141
6.6	Second sample pair of IEC images. . . . .	142
6.7	Second sample pair of IEC images. . . . .	143
C.1	PLIF Images of interfacial waves. $U_{sg} = 28 \text{ m s}^{-1}$ and $U_{sl} = 4.6 \text{ cm s}^{-1}$ . . . . .	183
C.2	PLIF Images of interfacial waves. $U_{sg} = 28 \text{ m s}^{-1}$ and $U_{sl} = 9.3 \text{ cm s}^{-1}$ . . . . .	184
C.3	PLIF Images of interfacial waves. $U_{sg} = 28 \text{ m s}^{-1}$ and $U_{sl} = 14.0 \text{ cm s}^{-1}$ . . . . .	185
C.4	PLIF Images of interfacial waves. $U_{sg} = 37 \text{ m s}^{-1}$ and $U_{sl} = 4.6 \text{ cm s}^{-1}$ . . . . .	186
C.5	PLIF Images of interfacial waves. $U_{sg} = 37 \text{ m s}^{-1}$ and $U_{sl} = 9.3 \text{ cm s}^{-1}$ . . . . .	187
C.6	PLIF Images of interfacial waves. $U_{sg} = 37 \text{ m s}^{-1}$ and $U_{sl} = 14.0 \text{ cm s}^{-1}$ . . . . .	188
C.7	PLIF Images of interfacial waves. $U_{sg} = 47 \text{ m s}^{-1}$ and $U_{sl} = 4.6 \text{ cm s}^{-1}$ . . . . .	189
C.8	PLIF Images of interfacial waves. $U_{sg} = 47 \text{ m s}^{-1}$ and $U_{sl} = 9.3 \text{ cm s}^{-1}$ . . . . .	190
C.9	PLIF Images of interfacial waves. $U_{sg} = 47 \text{ m s}^{-1}$ and $U_{sl} = 14.0 \text{ cm s}^{-1}$ . . . . .	191
C.10	PLIF Images of interfacial waves. $U_{sg} = 56 \text{ m s}^{-1}$ and $U_{sl} = 4.6 \text{ cm s}^{-1}$ . . . . .	192
C.11	PLIF Images of interfacial waves. $U_{sg} = 56 \text{ m s}^{-1}$ and $U_{sl} = 9.3 \text{ cm s}^{-1}$ . . . . .	193
C.12	PLIF Images of interfacial waves. $U_{sg} = 56 \text{ m s}^{-1}$ and $U_{sl} = 14.0 \text{ cm s}^{-1}$ . . . . .	194
C.13	PLIF Images of interfacial waves. $U_{sg} = 65 \text{ m s}^{-1}$ and $U_{sl} = 4.6 \text{ cm s}^{-1}$ . . . . .	195
C.14	PLIF Images of interfacial waves. $U_{sg} = 65 \text{ m s}^{-1}$ and $U_{sl} = 9.3 \text{ cm s}^{-1}$ . . . . .	196
C.15	PLIF Images of interfacial waves. $U_{sg} = 65 \text{ m s}^{-1}$ and $U_{sl} = 14.0 \text{ cm s}^{-1}$ . . . . .	197

# Nomenclature

Symbol	Description	Units
$A_{cs}$	= tube cross-section area	[ $\text{cm}^2$ ]
$A_{frame}$	= area represented by a single frame	[ $\text{cm}^2$ ]
$A_{lam}$	= area unaffected by bubble wakes	[ $\text{cm}^2$ ]
$A_{tot}$	= total observed area	[ $\text{m}^2$ ]
$A_r$	= Nikuradse's transition roughness function	
$A_{ref}$	= reference area	[ $\text{cm}^2$ ]
$A_w$	= area affected by bubble wakes	[ $\text{cm}^2$ ]
$A(r)$	= Airy function	[ $\text{m}^{-2}$ ]
$b$	= power-law exponent	
$Bo$	= boiling number	
$C$	= convective boiling leading constant in Ref. [9]	
$C$	= particle seeding density	[ particles $\text{cm}^{-3}$ ]
$Co$	= convection number	
$D$	= pipe inner diameter	[ mm ]
$D_b$	= bubble diameter	[ $\mu\text{m}$ ]
$D_E$	= effective particle image diameter	[ $\mu\text{m}$ ]
$D_I$	= interrogation spot size	[ $\mu\text{m}$ ]
$D_{max}$	= maximum bubble diameter	[ $\mu\text{m}$ ]
$D_p$	= particle geometric diameter	[ nm ]
$D_{pf}$	= Diffusivity of the particle in the fluid	[ $\text{m}^{-2} \text{s}^{-1}$ ]
$D_{sp}$	= point spread function diameter	[ $\mu\text{m}$ ]
$e$	= interfacial roughness height	[ $\mu\text{m}$ ]
$e$	= smallest distance resolved by detector	[ $\mu\text{m}$ ]
$e_E$	= effective interfacial roughness height	[ $\mu\text{m}$ ]
$e^*$	= non-dimensional roughness height	
$E$	= entrainment parameter	
$f$	= probability density distribution function; friction factor	
$f_i$	= interfacial friction factor	
$F_{dn}$	= downstream nucleation site multiplier	
$F_{fl}$	= fluid specific constant in the Kandlikar model, Ref. [10]	
$F_{mac}$	= two-phase convective enhancement factor	

$F_{mic}$	=	two-phase nucleate flow boiling factor	
$F_{nbf}$	=	nucleate flow boiling correction in Ref. [11]	
$F_{res}$	=	residual flow boiling correction factor in Ref. [11]	
$F_{sup}$	=	suppression factor	
$F_{ww}$	=	wake width bubble diameter multiplier	
$F_{wl}$	=	wake length bubble diameter multiplier	
$Fr$	=	Froude number	
$g$	=	gravitational acceleration	[ $\text{m s}^{-2}$ ]
$G$	=	mass flux	[ $\text{kg m}^{-2} \text{s}^{-1}$ ]
$G_{LF}$	=	liquid film mass flux	[ $\text{kg m}^{-2} \text{s}^{-1}$ ]
$h$	=	local flow boiling heat transfer coefficient	[ $\text{W m}^{-2} \text{K}^{-1}$ ]
$\bar{h}$	=	overall mean heat transfer coefficient for $A_{ref}$	[ $\text{W m}^{-2} \text{K}^{-1}$ ]
$\bar{h}_b$	=	mean $h$ for a single bubble wake area	[ $\text{W m}^{-2} \text{K}^{-1}$ ]
$h_c$	=	critical film height	[ $\mu\text{m}$ ]
$h_{fg}$	=	latent heat of vaporization	[ $\text{J kg}^{-1}$ ]
$h_{lam}$	=	laminar $h$ for area unaffected by bubble wakes	[ $\text{W m}^{-2} \text{K}^{-1}$ ]
$h_{mic}$	=	microscopic flow boiling heat transfer component	[ $\text{W m}^{-2} \text{K}^{-1}$ ]
$h_{mac}$	=	macroscopic flow boiling heat transfer component	[ $\text{W m}^{-2} \text{K}^{-1}$ ]
$h_{nb,o}$	=	normalized nucl. pool boiling $h$ in Ref. [11]	[ $\text{W m}^{-2} \text{K}^{-1}$ ]
$h_v$	=	vapor heat transfer coefficient	[ $\text{W m}^{-2} \text{K}^{-1}$ ]
$\bar{h}_w$	=	mean interfacial wave height	[ $\mu\text{m}$ ]
$h_{wet}$	=	heat transfer coeff. for wetted perimeter in Ref. [9]	[ $\text{W m}^{-2} \text{K}^{-1}$ ]
$I$	=	interfacial wave intermittence	
$J_0(r)$	=	zero-order Bessel function of the first kind	
$k_c$	=	critical standard deviation multiplier	
$k$	=	thermal conductivity	[ $\text{W m}^{-1} \text{K}^{-1}$ ]
$k$	=	turbulent kinetic energy	[ $\text{m}^2 \text{s}^{-2}$ ]
$\dot{m}_{DW}$	=	disturbance wave liquid mass flow rate	[ $\text{kg s}^{-1}$ ]
$\dot{m}_g$	=	gas mass flow rate	[ $\text{kg s}^{-1}$ ]
$\dot{m}_l$	=	liquid mass flow rate	[ $\text{kg s}^{-1}$ ]
$\dot{m}_{LE}$	=	entrained liquid mass flow rate	[ $\text{kg s}^{-1}$ ]
$\dot{m}_{LF}$	=	liquid film mass flow rate	[ $\text{kg s}^{-1}$ ]
$\dot{m}_{LF}^+$	=	non-dimensional liquid film mass flow rate	
$\dot{m}_v$	=	vapor mass flow rate	[ $\text{kg s}^{-1}$ ]
$l_m$	=	mixing length	[ $\mu\text{m}$ ]

$L$	=	pipe length	[ m ]
$m$	=	Reynolds number exponent for convective boiling in Ref. [9]	
$M$	=	molecular weight	[ kg kmol <sup>-1</sup> ]
$M$	=	Magnification	
$N$	=	size of particle ensemble	
$N_p$	=	tracers per realization	
$N_r$	=	number of realizations	
$n$	=	asymptotic exponent; index of refraction; velocity power-law exponent	
$n_{ent}$	=	entrained bubble number concentration	[ cm <sup>-2</sup> ]
$n_{nbf}$	=	nucleated bubble number concentration	[ cm <sup>-2</sup> ]
$n_i$	=	incident index of refraction	
$n_t$	=	transmitted index of refraction	
$n_{sat}$	=	nucleation site density for saturated flow boiling	[ cm <sup>-2</sup> ]
$n_{sup}$	=	unsuppressed nucleation site density	[ cm <sup>-2</sup> ]
$n_{tot}$	=	total bubble number concentration	[ cm <sup>-2</sup> ]
$nf$	=	nucleate flow boiling exponent in Ref. [11]	
$N_I$	=	image density	
$NA$	=	numerical aperture	
$P$	=	pressure	[ kPa ]
$P_{abs}$	=	absolute pressure	[ kPa ]
$P_r$	=	reduced pressure	
$Pr$	=	Prandtl number	
$q$	=	heat flux	[ W m <sup>-2</sup> ]
$Q_{GH}$	=	gas/homogeneous kinetic energy ratio	
$Q_h$	=	ratio of the heat transferred through $A_w$ to the total heat transfer	
$r$	=	radial coordinate	[ m ]
$Re$	=	Reynolds number	
$Re^*$	=	roughness Reynolds number	
$Re_D$	=	Reynolds number based on diameter	
$Re_g$	=	gas Reynolds number	
$Re_{LF}$	=	liquid film Reynolds number	
$Re_y$	=	wall distance based turbulent Reynolds number	
$R_a$	=	wall roughness by ISO 4287/1 standard	[ μm ]
$R_i$	=	interfacial radius	[ mm ]
$R_o$	=	pipe inner radius	[ mm ]

$RMS_b$	=	base film RMS value	[ $\mu\text{m}$ ]
$s$	=	RMS displacement	[ nm ]
$t_{exp}$	=	fluorescence decay time	[ ns ]
$\Delta t$	=	shutter exposure time	[ $\mu\text{s}$ ]
$T$	=	temperature	[ K ]
$T_g$	=	gas temperature	[ K ]
$T_l$	=	liquid temperature	[ K ]
$T_{sat}$	=	saturation temperature	[ K ]
$u$	=	axial velocity	[ $\text{m s}^{-1}$ ]
$\overline{u_H}$	=	core mean homogeneous velocity	[ $\text{m s}^{-1}$ ]
$\overline{u_i}$	=	interfacial velocity	[ $\text{m s}^{-1}$ ]
$\overline{u_i^*}$	=	interfacial friction velocity	[ $\text{m s}^{-1}$ ]
$\overline{u_{max}}$	=	maximum core axial velocity	[ $\text{m s}^{-1}$ ]
$u^*$	=	friction velocity	[ $\text{m s}^{-1}$ ]
$U_{dw}$	=	disturbance wave velocity	[ $\text{m s}^{-1}$ ]
$U_{sg}$	=	superficial gas velocity	[ $\text{m s}^{-1}$ ]
$U_{sl}$	=	superficial liquid velocity	[ $\text{cm s}^{-1}$ ]
$v$	=	radial velocity	[ $\text{m s}^{-1}$ ]
$\dot{V}_g$	=	volumetric gas flow rate	[ $\text{m}^3 \text{s}^{-1}$ ]
$\dot{V}_l$	=	volumetric liquid flow rate	[ $\text{cm}^3 \text{s}^{-1}$ ]
$w$	=	circumferential velocity	[ $\text{m s}^{-1}$ ]
$We$	=	Weber number	
$We_c$	=	critical Weber number	
$x$	=	mass quality	
$x$	=	axial length coordinate for CFD simulation	[ mm ]
$\delta_x$	=	in-plane spatial uncertainty	[ nm ]
$\Delta x$	=	in-plane axial displacement	[ $\mu\text{m}$ ]
$X_{LE}$	=	liquid entrainment fraction	
$X_{tt}$	=	Lockhart-Martinelli Parameter	
$y$	=	radial distance from the pipe wall	[ $\mu\text{m}$ ]
$y^+$	=	radial distance from the pipe in wall units	
$z$	=	axial coord.; circumferential coord. for CFD	[ m ]

# Greek Nomenclature

Symbol	Description	Units
$\alpha$	= void fraction	
$\delta^+$	= base film thickness in wall units	
$\delta^*$	= non-dimensional base film thickness	
$\bar{\delta}$	= mean film thickness	[ $\mu\text{m}$ ]
$\bar{\delta}_b$	= mean base film thickness	[ $\mu\text{m}$ ]
$\bar{\delta}_{Batch}$	= overall batch film thickness	[ $\mu\text{m}$ ]
$\bar{\delta}_{NW}$	= mean non-wave film thickness	[ $\mu\text{m}$ ]
$\bar{\delta}_{SW}$	= mean skip-wave film thickness	[ $\mu\text{m}$ ]
$\delta_z$	= depth of field	[ $\mu\text{m}$ ]
$\varepsilon_B$	= relative Brownian error	
$\theta_{dry}$	= dry angle	[ radians ]
$\lambda$	= wavelength	[ nm ]
$\kappa_B$	= Boltzmann's constant	[ $\text{J K}^{-1}$ ]
$\kappa$	= Von Kármán constant	
$\kappa_{tp}$	= two-phase Von Kármán constant	
$\theta_{strat}$	= stratified dry angle	[ radians ]
$\mu$	= dynamic viscosity	[ $\text{N s m}^{-2}$ ]
$\mu_g$	= gas dynamic viscosity	[ $\text{N s m}^{-2}$ ]
$\mu_H$	= core homogeneous dynamic viscosity	[ $\text{N s m}^{-2}$ ]
$\mu_l$	= liquid dynamic viscosity	[ $\text{N s m}^{-2}$ ]
$\rho$	= density	[ $\text{kg m}^{-3}$ ]
$\rho_H$	= core homogeneous density	[ $\text{kg m}^{-3}$ ]
$\rho_l$	= liquid density	[ $\text{kg m}^{-3}$ ]
$\sigma_{Batch}$	= batch surface tension	[ $\text{N m}^{-1}$ ]
$\sigma$	= surface tension	[ $\text{N m}^{-1}$ ]
$\sigma_{NW}$	= non-wave standard deviation	[ $\mu\text{m}$ ]
$\tau_{avg}$	= average shear stress	[ Pa ]
$\tau_i$	= interfacial shear stress	[ Pa ]
$\tau_0$	= wall shear stress	[ Pa ]

# Subscript Nomenclature

Symbol		Description
<i>abs</i>	=	absolute
<i>avg</i>	=	average
<i>b</i>	=	base film; bubble
<i>B</i>	=	Boltzmann
<i>Batch</i>	=	overall value for all data points in a batch of 100 images
<i>c</i>	=	convective
<i>cs</i>	=	cross-section
<i>dn</i>	=	downstream nucleation
<i>D</i>	=	diameter
<i>ent</i>	=	entrained
<i>exp</i>	=	exposure
<i>E</i>	=	effective
<i>fl</i>	=	fluid
<i>LF</i>	=	liquid film
<i>g</i>	=	gas
<i>GH</i>	=	gas-homogeneous
<i>H</i>	=	homogeneous
<i>i</i>	=	incident; interfacial
<i>I</i>	=	interrogation spot
<i>l</i>	=	liquid
<i>lam</i>	=	laminar
<i>LE</i>	=	liquid entrainment
<i>m</i>	=	mixing
<i>mac</i>	=	macroscopic
<i>max</i>	=	maximum
<i>mic</i>	=	microscopic
<i>nb</i>	=	at nucleate pool boiling in Ref. [11]
<i>nbf</i>	=	at nucleate flow boiling in Ref. [11]
<i>NW</i>	=	non-wave hypothesis PLIF processing
<i>o</i>	=	at normalized conditions in Ref. [11]; inner pipe wall
<i>of</i>	=	at normalized conditions, flow boiling in Ref. [11]

<i>OH</i>	=	Owen-Hewitt
<i>p</i>	=	particle
<i>pf</i>	=	particle-fluid
<i>pool</i>	=	pool boiling
<i>r</i>	=	reduced; realization
<i>ref</i>	=	reference
<i>s</i>	=	superficial
<i>sat</i>	=	saturation
<i>strat</i>	=	stratified
<i>sp</i>	=	point spread function
<i>sup</i>	=	suppression
<i>SW</i>	=	skip-wave hypothesis PLIF processing
<i>t</i>	=	transmitted
<i>tot</i>	=	total
<i>tp</i>	=	two-phase
<i>tt</i>	=	turbulent-turbulent (flow regimes of liquid and vapor phases in $X_{tt}$ )
<i>v</i>	=	vapor
<i>w</i>	=	wake
<i>ww</i>	=	wake width
<i>wl</i>	=	wake length

# Chapter 1

## Introduction

Saturated flow boiling inside tubes is a widely implemented means of heat transfer in many branches of industry that use devices such as steam generators in power plants, thermosiphon reboilers in distillation applications and direct expansion evaporators in refrigeration equipment. However, the nature and relative importance of the underlying mechanisms linked to this type of process are still a matter of controversy. Even though vapor generation inside tubular arrays has been a common practice since the beginning of the industrial revolution, application of specific empirical correlations and expensive prototype testing is still the design approach used by heat transfer engineers.

Empirical methods can be traced back to Rohsenow [12], who hypothesized that the flow boiling heat transfer coefficient was the result of two independent and additive components: bulk convective (macroconvective) transport and nucleate boiling (microconvective). Dengler and Addoms [13] proposed that the nucleate microconvective component of heat transfer is dominant only at conditions of low liquid velocity and that it is progressively suppressed as quality increases, with macroconvective heat transfer becoming dominant for most of the tube length. Chen [14] proposed specific forms for the macroconvective and microconvective components. This has been the most widely used approach. Other, more recent models try to incorporate the flow regime behavior by differentiating the heat transfer that takes place on wet and dry areas around the perimeter of the tube. The limitations of the correlations are made evident when compared to reliable empirical data. The error reported as mean deviation is usually on the order of 20 percent for the more recent correlations, though for

some common conditions the error can be 100's of percent. Such uncertainty in the prediction of heat transfer usually results in over-designed devices and costly testing of equipment. A mechanistic understanding of the physics represented by empirical components of current saturated flow boiling heat transfer models is required for reducing prediction uncertainties. Also, such an understanding will be a valuable tool in enhancing equipment performance or redesigning devices for operation with alternative fluids as required by refrigerant phase-out schedules worldwide.

The following sections include a survey of some of the most widely used models for flow boiling heat transfer, The models were implemented in a common software environment and their predictions were compared against selected sets of experimental data. A discussion on the results of this comparison and on the general capabilities of the models is also provided.

## 1.1 General Description of the Flow Boiling Process

Upstream from the location where the bulk liquid reaches the saturation temperature, the onset of nucleate boiling (ONB) is determined by the nucleation of the first bubbles from sites at the tube wall. At this point bubbles exhibit only limited growth and most of them recondense. Further downstream, not all bubbles condense after their nucleation and the net vapor generation point is reached (NVG). The void fraction is substantial only after NVG, when bubbles exhibit significant net growth. However, a true thermodynamic equilibrium may not exist immediately after NVG is reached. Saturated flow boiling (and two-phase flow) is considered to start only until a bulk saturation condition based on local enthalpy is reached. Prior to this equilibrium point, flow boiling is labeled as subcooled. The scope of this investigation is limited to saturated flow boiling, although some of the correlations can be extended to cover the subcooled regime.

Saturated flow boiling inside tubes involves variations in the flow patterns schematically

represented in 1.1 and Figure 1.2 for vertical and horizontal orientations respectively.

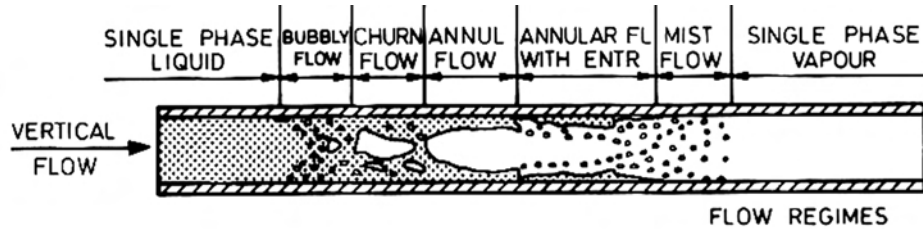


Figure 1.1: Schematic representation of the vertical flow boiling process by Steiner and Taborek [11].

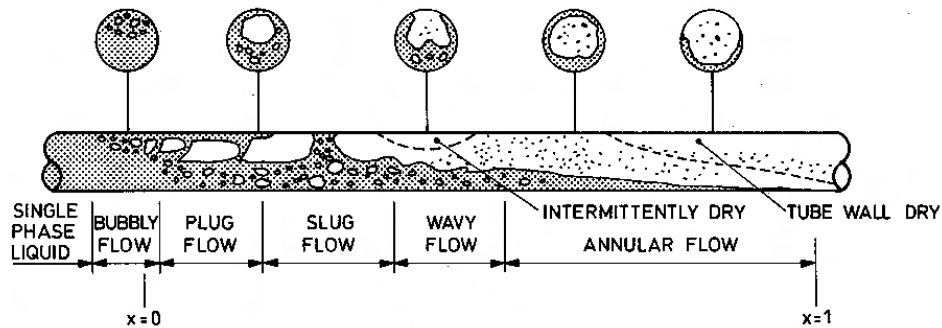


Figure 1.2: Schematic representation of the horizontal flow boiling process by Collier and Thome [15].

For orientations other than the vertical, the radial component of gravity produces an asymmetry of the flow pattern. At low mass quality, different in general from the thermodynamic quality and defined as

$$x = \frac{\dot{m}_v}{\dot{m}_l + \dot{m}_v} , \quad (1.1)$$

only a few bubbles compose the local void fraction. As evaporation progresses, bubbles coalesce forming slugs or plugs. For the horizontal orientation, stratified regimes may appear as mass quality increases. The large difference in density between the vapor and liquid phases requires from mass conservation that a velocity slip exists between the two phases. If the mass flux is high enough, eventually the liquid will be driven by the high vapor kinetic energy in an annular flow pattern. For the latter regime, a continuous thin film of liquid travels

along the wall of the tube with a vapor core traveling along the center. High heat transfer coefficients are achieved for this regime. Subsequently, the heat transfer coefficient peaks at the onset of dryout, and decays monotonously reaching the single phase vapor flow value at the  $x = 1$  limit.

For low mass flux conditions and a horizontal orientation, the flow may remain stratified throughout the entire change of phase process without ever reaching the annular flow regime. Lower heat transfer coefficients result from this situation.

## 1.2 Survey of Flow Boiling Modeling

The following survey is not comprehensive. Its scope is limited to the description of the most widely used correlations as reported by the reviews performed by Webb and Gupte [16], Steiner and Taborek [11], Darabi *et al.* [17], Thome [18] and Kandlikar [19].

### 1.2.1 General Formulation of Non Flow-Regime-Based Models

Ever since Chen [14] proposed his additive model, the same general structure has been followed by the majority of the subsequent models and may be represented by an equation of the general form:

$$h = [(F_{mic}h_{mic})^n + (F_{mac}h_{mac})^n]^{1/n} , \quad (1.2)$$

where  $h$  is the local flow boiling heat transfer coefficient, expressed in terms of the microscopic component multiplied by a nucleate flow boiling factor ( $F_{mic}h_{mic}$ ) and the macroscopic component multiplied by a two-phase enhancement factor ( $F_{mac}h_{mac}$ ). The asymptotic exponent  $n$  may vary from  $n = 1$  to  $n = \infty$ , where the former case corresponds to the basic additive case as appears in the Chen and Gungor-Winterton (1986) [20] correlations. More general asymptotic models usually find the finite value for the exponent that best fits the

empirical data following Kutateladze's [21] power-type addition model. Churchill [22] used 13,000 datapoints to correlate the transition from nucleate boiling dominant behavior to forced convection dominant behavior and obtained an optimum fit with  $n = 3$  (e.g., Steiner and Taborek where  $n=3$ ). The power-type addition results in further suppression of nucleate boiling with increasing mass quality and it produces a smooth transition between forced convection and nucleate boiling dominant behavior with increasing heat flux  $q$ . Figure 1.3 is a schematic representation of the heat transfer ratio ( $h_{tp}/h_c$ ) variation with respect to the heat flux ratio for different values of the asymptotic exponent at constant mass flux  $G$ , mass quality  $x$  and reduced pressure  $P_r$ . Finally, the case of using infinity for the exponent corresponds to choosing the larger of the two terms, as initially proposed by Chawla [23] and later implemented in the Shah [24] and Kandlikar [10] correlations.

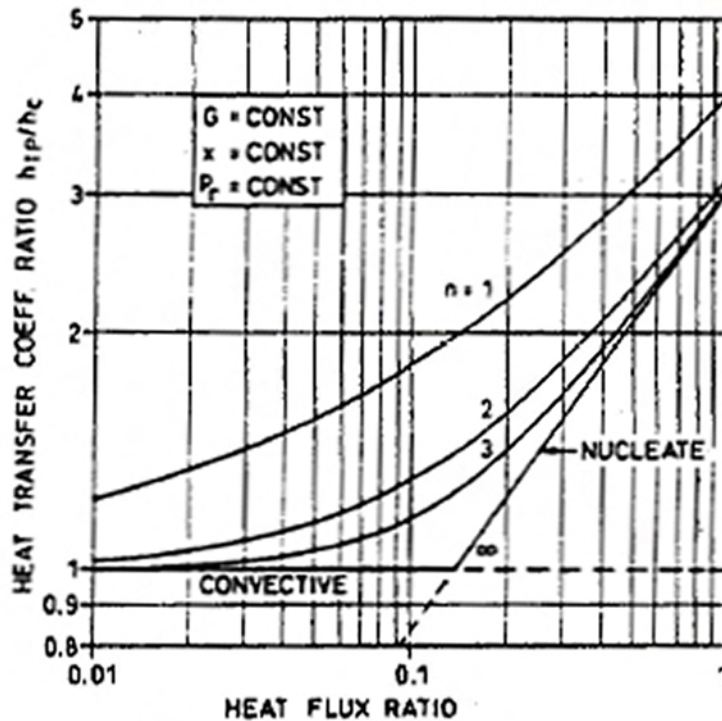


Figure 1.3: Idealized variation of the heat transfer ratio with respect to the heat flux ratio for fixed  $x$  and  $G$  by Steiner and Taborek [11].

The microconvective term ( $F_{mic}h_{mic}$ ) has often been represented by nucleate pool boiling

correlations modified by some nucleate flow boiling factor. Chen used the Forster-Zuber [25] pool boiling correlation while Gungor-Winterton and most subsequent authors have used the Cooper [26] correlation, Eqn. (1.3), due to its good performance and ease of evaluation.

$$h_{pool} = 55P_r^{0.12}(-\log_{10}P_r)^{0.55}M^{-0.5}q^{0.67} \quad (1.3)$$

The nucleate flow boiling factor is physically explained by Chen as representing the reduction in the effective superheat experienced by growing nuclei due to a reduction in the thermal boundary layer thickness related to convective mixing. Thus,  $F_{mic}$  is often correlated with a two-phase Reynolds number.

The macroconvective term ( $F_{mac}h_{mac}$ ) has been conceived as an enhanced single phase convective mechanism. The Dittus-Boelter [27] equation used by Chen is not accurate for  $Re < 10000$  and has been replaced by the Gnielinski [28] correlation for  $2300 < Re < 10000$  and the Petukhov and Popov [29] correlation for  $10000 < Re < 5 \times 10^6$ , with ongoing controversy regarding the appropriate form of Reynolds number that should be used in the evaluation of these correlations. The expressions for mass flux and characteristic length in the definition of  $Re$  vary according to the physical understanding of the macroconvective component that each researcher advocates. The local liquid mass flux ( $G*(1-x)$ ), as well as the total mass flux  $G$ , have been used for mass flux, while the tube diameter,  $D$ , and the mean liquid film thickness,  $\bar{\delta}$ , have been used as characteristic dimensions.

It should be pointed out that in the annular flow regime, the use of correlations for flow inside round tubes may not be appropriate. A flat plate model may not be exactly right either. The annular flow liquid film is different from the one observed on a flat plate and laminar behavior would take place up to  $Re_l \approx 4 \times 10^5$  for the latter. Nearly all experiments would fall in a laminar region if the disruption of the film by bubbles is not considered. Also, the flat plate  $Re$  indicates the characteristic length for growth of the boundary layer. Since

in annular flow the velocity profile can't develop past the interface, it is likely that a parallel plate model is more appropriate, with one plate moving at the vapor velocity. Given the turbulence of the vapor, it is likely that the vapor flow is nearly fully developed at all times. If the resulting parallel plate flow is laminar then some other mechanism should compensate for the increased thermal resistance.

The convective enhancement factor  $F_{mac}$  is considered by Chen as the ratio  $(Re_{tp}/Re_l)^{0.8}$  between the two-phase Reynolds number,  $Re_{tp}$ , and the liquid Reynolds number,  $Re_l$ , which has been often correlated in terms of the Lockhart-Martinelli [35] parameter  $X_{tt}$ . This parameter represents the ratio of the relative viscous pressure drop of the liquid phase to that of the vapor phase. On occasion,  $F_{mac}$  is given in terms of the boiling number  $Bo$  as well. The boiling number was introduced by Davidson (1943) to characterize the effects of heat flux and mass flux in the flow boiling process; it is a ratio of the vapor mass flux generated at the tube wall to the total mass flux flowing in the tube. Thus,

$$F_{mac} = f(X_{tt}, Bo) \quad , \quad (1.4)$$

where,

$$X_{tt} = \left(\frac{1-x}{x}\right)^{0.9} \left(\frac{\rho_v}{\rho_l}\right)^{0.5} \left(\frac{\mu_l}{\mu_v}\right)^{0.1} \quad , \quad (1.5)$$

and

$$Bo = \frac{q}{h_{fg}} \quad . \quad (1.6)$$

Many methods use  $X_{tt}$  in correlating  $F_{mac}$ . Forced convection enhancement in horizontal flow depends strongly on the flow pattern because the slip ratio between phases will determine the liquid flow velocity. Since the flow pattern can not be determined from  $X_{tt}$  alone, it may be more convenient to use the local void fraction and slip ratio in correlating  $F_{mac}$  to better characterize the liquid film velocity.

The physical justification for the use of the boiling number is the characterization of the dominance of nucleate boiling effects at low vapor qualities and/or relatively high superheats. On the other hand, the convection number,  $Co$ , was introduced by Shah to represent the relative importance of convective heat transfer and has also been used by Kandlikar in his correlation.  $Co$  essentially replaces  $X_{tt}$  when viscosity ratio effects are neglected. The convection number is given by

$$Co = \left( \frac{1-x}{x} \right)^{0.8} \left( \frac{\rho_v}{\rho_l} \right)^{0.5} . \quad (1.7)$$

While the Chen correlation is limited to vertical flows, many other non-flow regime-based correlations have included the liquid Froude number  $Fr_l$  in correlating both nucleate flow boiling and convective enhancement factors to include the effects of gravity acting in the radial direction, where  $Fr_l$  is defined as

$$Fr_l = \frac{G^2}{\rho_l^2 g D} . \quad (1.8)$$

### Physical Interpretation of $F_{mic}$

The Steiner and Taborek correlation is perhaps the most physically discerning methodology within the realm of non-flow regime-based models, albeit limited to saturated boiling in vertical upflow. While the definition for  $F_{mac}$  is similar to the one used by other asymptotic models (i.e., defined in terms of mass quality,  $x$ , and the density ratio  $\rho_l/\rho_g$ ), the nucleate boiling (microconvective) term is treated quite differently. The nucleate pool boiling heat transfer coefficients are normalized based on reference values for heat flux, reduced pressure, and surface roughness according to the Gorenflo [30] method, but using high heat flux flow boiling data instead of pool boiling data. This results in normalized values of  $h_{nb,o}$  that are smaller than their comparable nucleate pool boiling values, resulting in what could be

interpreted as suppression. Thus,

$$\text{microconvective term} = h_{nb,o} F_{nbf} \quad , \quad (1.9)$$

with the correction factor  $F_{nbf}$  (Steiner and Taborek's notation for  $F_{mic}$ ) given by

$$F_{nbf} = f(G, x) F_{pf} \left( \frac{q}{q_{of}} \right)^{nf(P_r)} \left( \frac{D}{D_o} \right)^{-0.4} \left( \frac{R_a}{R_{a,o}} \right)^{0.133} F_{res}(M) \quad . \quad (1.10)$$

Equation (1.10) shows that  $F_{nbf}$  includes separate corrections for reduced pressure  $F_{pf}$ , applied heat flux, tube diameter, tube wall roughness,  $R_a$ , and the molecular weight of the fluid  $F_{res}(M)$ . The factor  $f(G, x)$  could play an analogous role to that of  $X_{tt}$  or  $Co$  in other correlations. For vertical flow, Steiner and Taborek found that  $f(G, x) = 1$ , but this may not be true for flows with a component of gravity acting in the radial direction. The more general horizontal and inclined tube orientations are directly addressed by the flow regime-based approach as presented in §1.2.2.

### **Characteristics of the Empirical Databases**

In performing the regression analysis for the determination of constants that appear in the expressions for the enhancement or nucleate flow boiling factors, a large number of reliable experimental heat transfer data are required. Predictions of the heat transfer coefficient are desirable for a broad range of fluids, operating pressures, mass qualities, mass fluxes, wall superheats, tube materials, tube orientations and flow directions (upward or downward for orientations other than horizontal). Subcooled and saturated flow boiling should be covered as well. The choice of a diverse and reliable databank is critical to achieve such versatility for correlations with a strong empirical component. As an indication of the increasing efforts to gather experimental data for regression analysis, the Chen correlation was developed

based on 665 data points for water and some hydrocarbons in vertical tubes, the Kandlikar correlation used over 5000 data points in vertical and horizontal tubes for water, refrigerants and cryogenic fluids, and the Steiner and Taborek correlation was based on 13000 data points for organic and inorganic fluids in vertical upflow.

### 1.2.2 Flow Regime Based Models

Horizontal flow boiling exhibits particular features resulting from stratification that have not been represented by many correlations. Thome [18] describes them as follows: monotonic decrease in  $h$  vs.  $x$  for stratified regimes, a maximum in  $h$  vs.  $x$  and rapid falloff in  $h$  at high vapor qualities, local maximum in  $h$  vs.  $x$  at low qualities and other observed variations of  $h$  with respect to heat flux and mass flux. These trends are better represented with a flow regime based model instead of using the liquid Froude number,  $Fr_l$ , to account for stratification at low mass velocities. A considerable length of the tube can operate with a partially dry wall, especially in horizontal flow. The low quality stratified condition, and the post annular dryout starting at the top of the tube circumference, should be properly characterized, not by a simple Froude number based threshold, but by a comprehensive criterion that provides an estimate of the dry portion of the perimeter. A separate correlation should be employed for the dry angle of the tube to represent single-phase vapor convection instead of flow boiling. Tube orientation affects flow patterns and heat transfer coefficients significantly; upward, downward and horizontal flow can not be assumed to be identical processes, as shown in Figure 1.4. Orientation is especially influential at low mass flux and low heat flux conditions.

At high mass flux, high mass quality flow conditions, the flow pattern changes to mist flow, which is characterized by vapor-phase convection close to the tube wall and evaporation of liquid droplets traveling along the wall and in the vapor core. The majority correlations

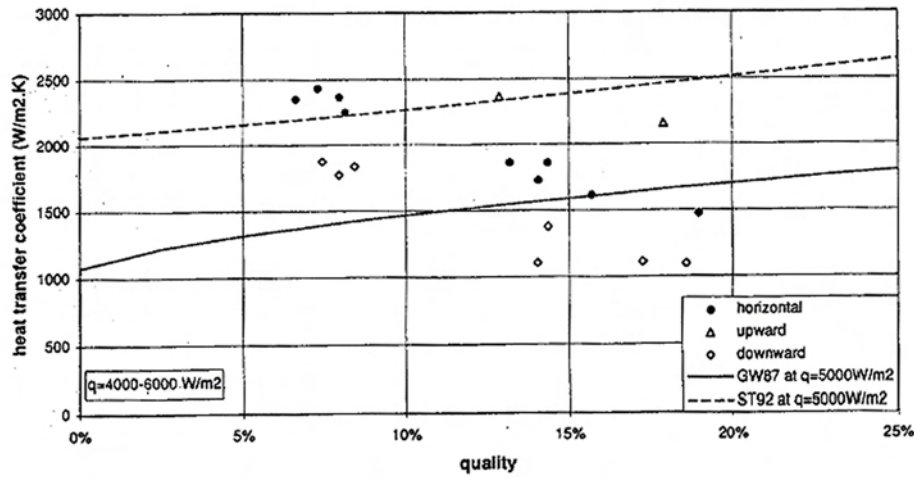


Figure 1.4: Boiling of R 134a in a copper tube for upflow, downflow and horizontal flow [31].

do not make a distinction for a separate treatment of this flow regime and extend the use of a wet wall heat transfer correlation up to this point. Some correlations have been proposed for this regime by Groeneveld and Delorme [32] and Chen *et al.* [33].

### The Kattan, Thome, Favrat Heat Transfer Model

The model proposed by Kattan *et al.* [9], in addition to taking the local flow pattern into account for heat transfer prediction, introduces two other features that distinguish it from previous work: *i*) macroscopic convection for the wetted perimeter is based on the liquid film velocity associated with the Reynolds number derived from a local void fraction correlation and *ii*) vapor-phase convection is used for the dry portion of the tube perimeter. On the other hand, it retains some features from previous models, such as the asymptotic matching ( $n = 3$ ) from Steiner and Taborek and the use of the Cooper pool boiling correlation for the microscopic component of heat transfer.

The determination of the flow regime is accomplished using a flow pattern map developed by the same authors [34] and later improved by Zürcher *et al.* [35]. The map defines regions for each flow regime on a  $G$  vs.  $x$  coordinate system for a specific fluid, saturation tempera-

ture, tube diameter, applied heat flux and inclination angle of the tube from horizontal. An example of a typical flow map depicting the stratified (S), stratified wavy (SW), intermittent (I), annular (A) and mist flow (MF) regimes is shown in Figure 1.5.

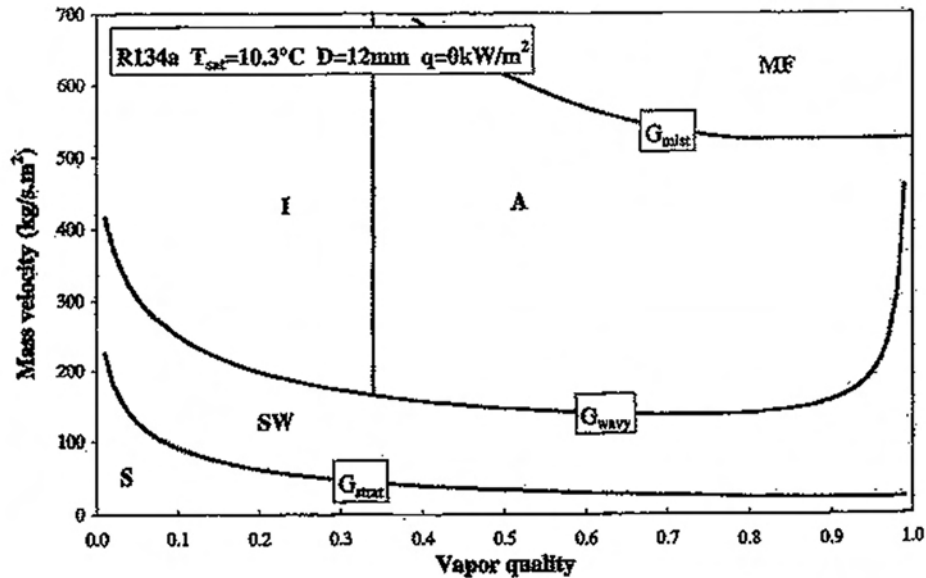


Figure 1.5: Flow pattern map sample [34].

The model's solution for finding heat transfer coefficients in stratified regimes depends on determining the local dry angle,  $\theta_{dry}$ , which is useful in characterizing stratified wavy flow and annular flow with partial dryout. The calculation of  $\theta_{dry}$  uses the Rouhani-Axelsson [36] void fraction correlation, mass quality, mass flux, fluid properties, and tube diameter as inputs; the detailed equations are out of the scope of this section but they can be found in Appendix A or in the original paper [9]. The overall performance of flow regime map and the calculation of  $\theta_{dry}$  are highly dependent on the accuracy of the void fraction correlation that is used. Obtaining reliable void fraction data is quite challenging and further research on this issue is warranted. Even slight changes in the void fraction prediction can cause significant changes in the flow regime map, especially for fluids with large  $(\rho_l/\rho_v)$ .

The heat transfer coefficient is given by

$$h = \frac{\theta_{dry}h_v + (2\pi - \theta_{dry})h_{wet}}{2\pi} , \quad (1.11)$$

where  $h_v$  is the vapor heat transfer coefficient given by the Dittus-Boelter correlation and  $h_{wet}$  is given by the asymptotic expression

$$h_{wet} = (h_{mic}^3 + h_{mac}^3)^{1/3} . \quad (1.12)$$

The microscopic component in (1.12) is given by the Cooper correlation while the macroscopic component is given by

$$h_{mac} = CRe_l^m Pr_l^{0.4} \frac{k_l}{\bar{\delta}} , \quad (1.13)$$

where experimental data for five refrigerants yielded  $C = 0.0133$  and  $m = 0.69$ . From analogy to turbulent film condensation, and for consistency with the use of the Dittus-Boelter correlation for annular flow, the liquid Reynolds number in (1.13) is defined using the average film thickness as the characteristic length and a liquid flow area based on the Rouhani-Axelsson void fraction correlation:

$$Re_l = \frac{4G(1-x)\bar{\delta}}{(1-\alpha)\mu_l} . \quad (1.14)$$

This new representation of the macroscopic contribution avoids the use of the enhancement factor  $F_{mac}$ . However, there is still a strong reliance on experiments for the determination of  $C$  and  $m$ , and further investigation of their physical justification is granted if the applicability of (1.13) is to be extended beyond the set experiments used for the development of these constants. The considerable scatter in the data used for the regression supports the previous

suggestion, as shown in Figure 1.6 where

$$Y_1 = \frac{\left[ \left( \frac{2\pi h_{tp} - \theta_{dry} h_v}{2\pi - \theta_{dry}} \right)^3 - h_{nb}^3 \right]^{1/3}}{Pr_l^{0.4} \frac{k_l}{\delta}} = C Re_l^m . \quad (1.15)$$

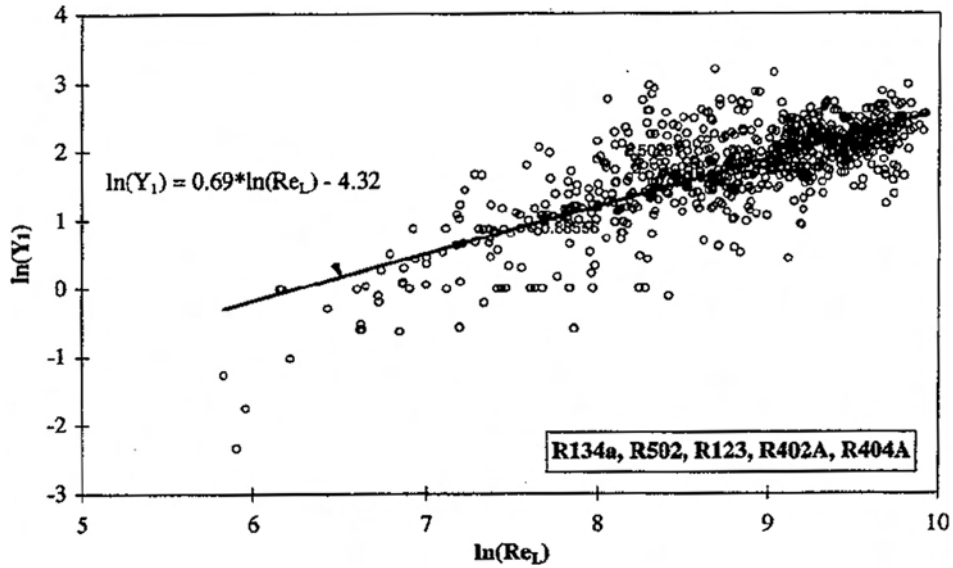


Figure 1.6: Determination of constants  $C$  and  $m$  in [9].

Stratified flow heat transfer is calculated using (1.11), but  $\theta_{dry}$  is replaced by  $\theta_{strat}$ , which is given by geometry assuming a flat liquid-vapor interface. For the annular and intermittent flow regimes, the same equation applies but with  $\theta_{dry} = 0$  for both. The model does not include heat transfer predictions for the bubbly or mist flow regimes, limiting the applicability of the model for mass qualities below 0.15 and at extremely high or low mass flux. However, the mass quality limitation does not represent a big obstacle for direct-expansion evaporators since the inlet mass quality usually ranges from 0.15 to 0.3 after throttling in the expansion valve.

The transition from annular to stratified wavy flow at high qualities marks the onset of partial dryout (starting at the top of the tube for the horizontal orientation) and it coincides with a peak in the local heat transfer coefficient followed by a rapid decrease towards the

vapor-phase convection value at  $x = 1$ . One of the virtues of the Kattan *et al.* model is its capability to correctly predict the location and magnitude of this peak.

### 1.3 Implementation of Representative Correlations

Several flow boiling heat transfer models were implemented using fluid properties and iteration routines from the EES [37] software package. The Chen [14], Shah [24], Gungor-Winterton (1986) [20], Liu-Winterton [38], Kandlikar [10] and Kattan *et al.* [9] correlations were chosen as being representative of various stages of development of flow boiling heat transfer modeling. The implementation of the Kattan *et al.* model is noticeably more complex, since it requires the simultaneous implementation of a flow regime map. The original Kattan *et al.* model uses the flow pattern map described in [34], but the improved version by Zürcher *et al.* [35] was implemented here.

The input parameters for a run of the models are shown in Figure 1.7, which shows a snapshot of an EES input window. Some range limitations exist for the applicable input parameters for each model. Some have restrictions on tube orientation; for instance, the Chen correlation should be limited to vertical flow (i.e., the orientation parameter has no effect on its calculation). The Shah, Gungor-Winterton (1986), Liu-Winterton and Kandlikar correlations include vertical and horizontal orientations. The Kattan *et al.* correlation accepts a continuous range of inclination angles from vertical to horizontal. Many, if not all the correlations have fluid restrictions due to the limited data sets correlated by their empirical constants; for example, the Kandlikar correlation requires a fluid-specific constant that is still unavailable for many substances. Most correlations are inherently limited to saturated flow boiling, although the results for some of them can be extrapolated to subcooled boiling. Foreseeable prediction accuracy limitations exist for out of range values of  $G$ ,  $T_{sat}$ , and  $D$ , although no inherent limitations exist on the calculation algorithms. The approximate range

for these parameters can be inferred from the originating dataset of each correlation.

## FBHT Calculator

<b>Refrigerant:</b>	R134a ▾
<b>Mass Flux (Mass Velocity)</b>	G=100 [kg/m <sup>2</sup> -s]
<b>Tube Diameter</b>	D=0.012 [m]
<b>Tube Orientation</b>	Horizontal ▾
<b>Tube Material</b>	Copper ▾
<b>Wall Heat Flux</b>	$\bar{q}$ =5000 [W/m <sup>2</sup> ]
<b>Saturation Temperature</b>	T <sub>mix</sub> =277.2 [K]

Figure 1.7: Flow boiling heat transfer model inputs.

Mass quality is also a required input, but it was included in a parametric table in order to present the model output in the usual  $h$  vs.  $x$  format. Samples of the model output compared with experimental data for several combinations of input parameters can be seen in §1.4.

## 1.4 Model Predictions and Comparison Against Experimental Data

Samples of predictions obtained from the six models compared against experimental data for several combinations of input parameters can be seen from Figure 1.8 through Figure 1.13.

Figure 1.8 shows horizontal flow boiling data for R134a from Kattan *et al.* [1]. The Kattan *et al.* model is the only one to capture the slope at high qualities, the peak heat transfer coefficient and the subsequent decay after the onset of dryout. However, at mass qualities below 50 percent the other five models performed better. Figure 1.9 shows horizontal flow boiling data for R123 from the same reference at mass qualities below 40 percent. For this

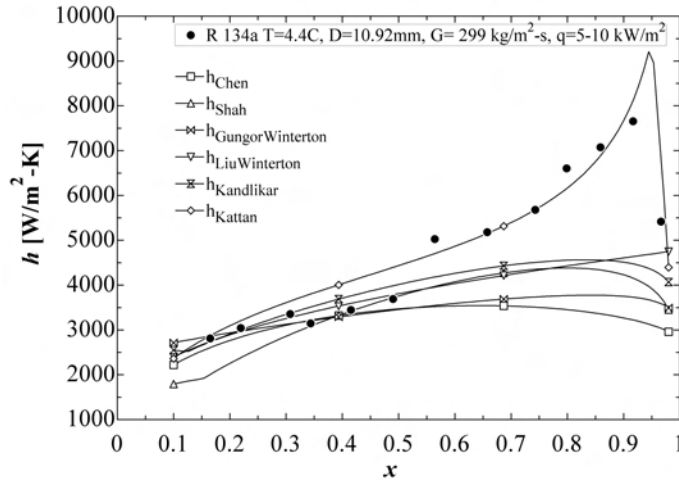


Figure 1.8: Comparison of model predictions against R134a data from Kattan *et al.* [1] at  $T_{sat} = 4.4^{\circ}\text{C}$ ,  $D = 10.92 \text{ mm}$ ,  $G = 299 \text{ kg/m}^2\text{-s}$  and  $q = 5\text{-}10 \text{ kW/m}^2$ .

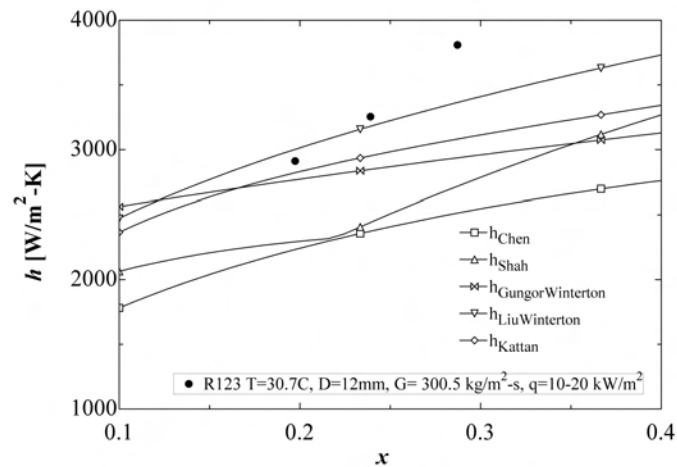


Figure 1.9: Comparison of model predictions against R123 data from Kattan *et al.* [1] at  $T_{sat} = 30.7^{\circ}\text{C}$ ,  $D = 12 \text{ mm}$ ,  $G = 300.5 \text{ kg/m}^2\text{-s}$  and  $q = 10\text{-}20 \text{ kW/m}^2$ .

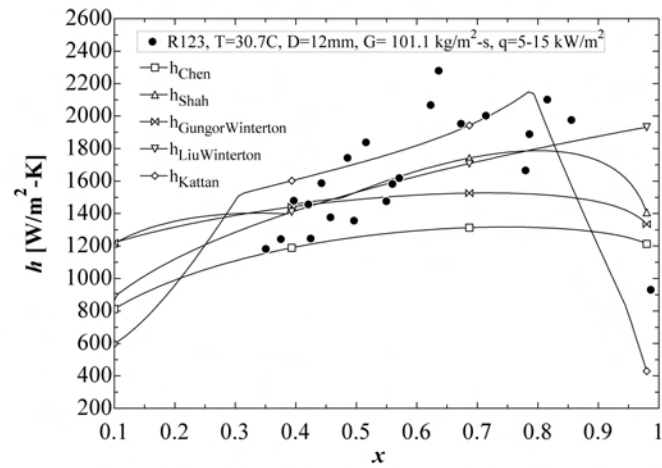


Figure 1.10: Comparison of model predictions against R123 data from Kattan *et al.* [1] at  $T_{sat} = 30.7^{\circ}\text{C}$ ,  $D = 12 \text{ mm}$ ,  $G = 101.1 \text{ kg/m}^2\text{-s}$  and  $q = 5\text{-}15 \text{ kW/m}^2$ .

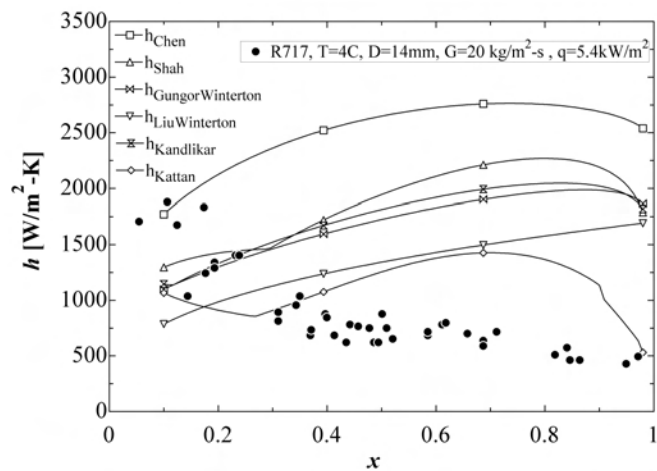


Figure 1.11: Comparison of model predictions against R717 data from Zürcher *et al.* [2] at  $T_{sat} = 4^{\circ}\text{C}$ ,  $D = 14 \text{ mm}$ ,  $G = 20 \text{ kg/m}^2\text{-s}$  and  $q = 5.4 \text{ kW/m}^2$ .

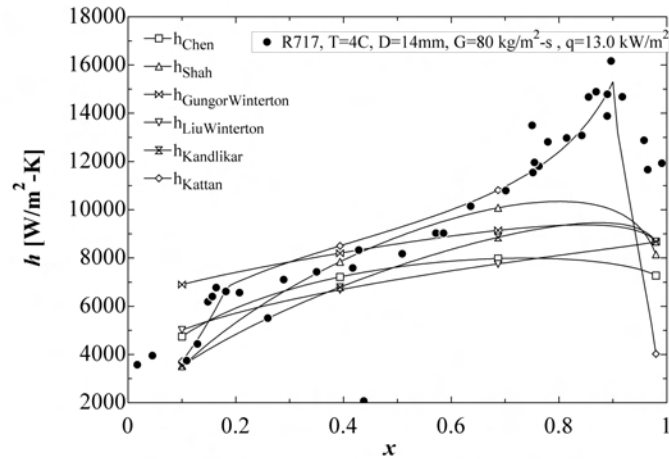


Figure 1.12: Comparison of model predictions against R717 data from Zürcher *et al.* [2] at  $T_{sat} = 4^\circ\text{C}$ ,  $D = 14 \text{ mm}$ ,  $G = 80 \text{ kg/m}^2\text{-s}$  and  $q = 13.0 \text{ kW/m}^2$ .

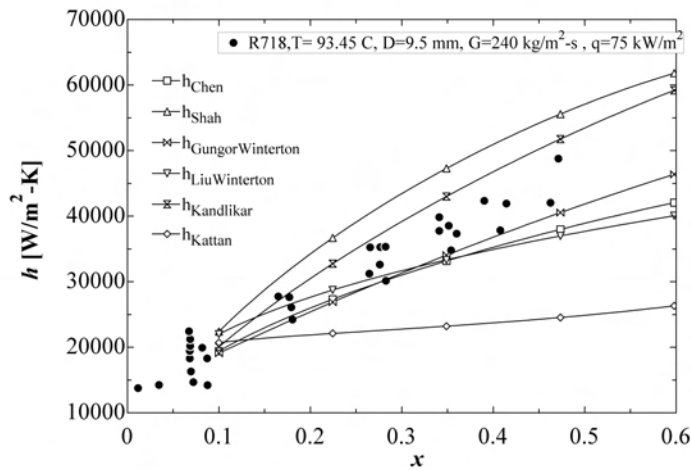


Figure 1.13: Comparison of model predictions against R718 data from Sun and Hewitt [3] at  $T_{sat} = 93.45^\circ\text{C}$ ,  $D = 9.5 \text{ mm}$ ,  $G = 240 \text{ kg/m}^2\text{-s}$  and  $q = 75 \text{ kW/m}^2$ .

relatively high mass flux condition, none of the models appears to capture the correct slope for this data set although the few data points available may weaken this conclusion. Note that a prediction from the Kandlikar model is not available for this substance since the fluid specific constant  $F_{fl}$  has not been tabulated for R123. Lower mass flux data from the same reference shown in Figure 1.10 are best predicted by the Kattan *et al.* model. The scatter in the data from Figure 1.10 appears to be too large to judge the magnitude of the errors. Data for ammonia by Zürcher *et al.* [2] at a low mass flux condition are shown in Figure 1.11. For the resulting stratified flow, all of the models significantly overpredict the heat transfer coefficient over most of the mass quality range. The negative slope trend is partially captured by the Kattan *et al.* model, especially at low qualities. Figure 1.12 shows higher mass flux ammonia data from the same reference. The results for the Kattan model are good, capturing the trends correctly both at high and low mass qualities. This good agreement is possible due to the implementation of the improved flow map developed by Zürcher *et al.* in [35]. Finally, Figure 1.13 shows steam-water data for vertical flow by Sun and Hewitt [3]. These data illustrate how the Kattan *et al.* model is outperformed by other models for these conditions. The data also show that older models perform well or even outperform more recent models when they are applied to the fluids and conditions for which they were originally intended. The degraded performance of the Kattan *et al.* model for vertical steam-water flow is not surprising since this model was developed from data for five refrigerants and the underlying flow regime map is intended for use in horizontal flows where stratified regimes are important.

## 1.5 Discussion

The Chen correlation does not perform well outside the conditions of the limited data that were available at the time. The general applicability of an empirically predicted nucleate

boiling suppression factor is questionable, as shown by the experimental work of Aounallah and Kenning [39], even if it has a valid mechanistic origin (i.e., reduction of the wall superheat due to forced convection). The reduction of the effective superheat (suppression) is not exclusively a convection effect. According to Thome [18], nucleate pool boiling expressions should also be corrected for several flow effects including stratification, premature bubble departure, sliding bubbles, flow effects on the boiling nucleation process and changes in the necessary heat flux for the onset of nucleate boiling (ONB). A correction of nucleate pool boiling expressions for the flow boiling effects is certainly necessary, but it must include the effects of heat flux and mass flux, among other parameters. The Forster-Zuber correlation used by Chen in his microconvective term has limited accuracy for fluids other than water. Other more accurate correlations, such as Cooper's or Stephan and Abdelsalam's [40], are now available for the nucleate pool boiling heat transfer coefficient. The nucleate pool boiling expression to be used for flow boiling heat transfer prediction also depends on the orientation of the surface. For a horizontal tube, the equivalent pool boiling process varies from an upward facing surface at the bottom of the circumference, to a vertical plate at the sides and a downward facing plate at the top of the circumference. In addition, the Chen correlation is appropriate for low pressure water data, but it exhibits large errors for refrigerants.

The Gungor and Winterton (1986) method uses the original form of the Chen correlation, including the unverified concept of a suppression factor. However,  $F_{mac}$  is a function of  $Bo$  and  $X_{tt}$ , and  $F_{mic}$  is a function of  $F_{mac}$  and  $Re_l$ . This definition of the correcting factors does not proceed from a mechanistic approach, but rather from regression analysis. The microscopic component depends on the macroscopic component, and this results in non-physical behavior, as was later recognized by Liu and Winterton [41]. The Liu and Winterton correlation uses the power additive model, which improves the transition behavior of the model, but the correction factors are still only justified from regression analysis and

the suppression factor  $F_{mic}$  remains a function of  $F_{mac}$ . Webb and Gupte [16] showed that, although Liu and Winterton predict their own data set well, the correlation is fundamentally flawed because of an error in their calculation of  $F_{mac}$ .

The model proposed by Shah oversimplifies the problem of correctly defining the microconvective term. The method relies completely on the boiling number,  $Bo$ , to represent the nucleate boiling effects using a single phase convection heat transfer coefficient (instead of a pool boiling correlation) as a basis. Thus, the macroconvective and microconvective components lose their independence with no clear physical justification for this approach. Also, the experimental  $h$  vs.  $x$  trends for the nucleate boiling dominated region are not correctly represented by the model. The inherent deficiencies of this approach are also present in the Gungor and Winterton (1987) [42] method and in Kandlikar's correlation. The latter is usually considered to be an extension of the Shah correlation.

The Kandlikar method exhibits some physical inconsistencies described by Steiner and Taborek [11]. For example, in the absence of nucleate boiling, the heat transfer coefficient does not approach the single phase convection value as  $x$  approaches zero. When boiling is dominant, the  $h$  vs.  $x$  and  $h$  vs.  $G$  trends are misrepresented for the vertical orientation. The effect of pressure on nucleate boiling follows the right trends, but the resulting correction is insufficient at low pressures. The Kandlikar method is also not applicable for high qualities ( $x > 0.8$ ) where partial wall dryout is a possibility.

Some methods do not respect some evident physical constraints. For instance, they do not tend towards single-phase vapor heat transfer at  $x = 1$ . Also,  $F_{mac}$  should tend towards zero as the fluid flow rate goes to zero but many models do not respect this limitation, with  $F_{mac}$  approaching one in the limit.

In general, methods that rely heavily on regression analysis corrections will be seriously affected by the selection of a particular data bank. Under-represented conditions or fluids within the data will produce poor performance when extrapolating the method beyond its

original data range. Fluid dependant parameters such as  $F_{fl}$  in the Kandlikar correlation and  $C$  in the Klimenko [43] correlation have a vague physical meaning. They may, for example, indirectly address a contact angle effect in the bubble nucleation process (i.e. the likelihood for vapor or gas entrapment inside nucleation sites) or a surface tension effect in the dryout behavior of the tubes at high qualities or very low mass flux situations. This approach severely restricts the versatility of the correlations, requiring further experiments to determine these parameters whenever predictions are to be made for a fluid and tube material not covered by the tables provided by the authors. On the other hand, mechanistic approaches rely on experiments mainly for verification of the physical assumptions that support each underlying heat transfer mechanism.

It has been a common practice to use the percentage mean deviation to perform comparisons among correlations [17]. However the value of this, or any other statistical figure, will depend on the experiment data bank that is selected for the evaluation. To date, there is no agreement upon a common data set for testing correlations. Objective comparisons would ideally evaluate performance for different fluid types, geometries and orientations, covering a broad range of equally represented operating parameters. A greater number of data exist representing easier to measure conditions, so the statistics may hide the poor performance of a method at other common, but complex, conditions. Regression analysis methods may perform well within the domain of their original data bank. However, mechanistic approaches, if correctly evaluated, are more likely to provide consistently accurate predictions and follow the physical trends throughout a broad and carefully selected data bank.

In general, the two objectives traced by Steiner and Taborek for the development of their method are still valid for any further development in the field and for addressing the deficiencies of current models:

1. “The nucleate and convective boiling components must be based on meth-

ods that respect the effects of pressure, heat flux, mass velocity and vapor fraction according to established principles.”

2. “The method must respond correctly to all extreme values of the operational parameters, where many other methods fail.”

## 1.6 Sliding Bubble Mechanism

The foregoing assessment shows that the dependence on regression from empirical data limits the generality of the models. Although the reasoning behind splitting the total heat transfer into macroconvective and microconvective components is physically sound, the underlying mechanisms are not well understood. The sliding bubble mechanism is a hypothesis that may produce an explanation at a more fundamental level. The following paragraphs introduce the body of research that shaped this concept and some experimental evidence of its viability.

Mesler [44] challenged the traditional Dengler and Addoms concept of dominant forced convection at high quality. Mesler argued that the use of a thin film enhanced nucleate boiling component (the secondary nucleation hypothesis) still produces agreement with the data where suppression was traditionally assumed. In another work, Mesler [45] tried to describe the role played in flow boiling heat transfer by small entrained bubbles. He related his secondary nucleation heat transfer hypothesis to the latent heat associated with net bubble growth from evaporation at the interface. By this hypothesis, secondary nucleation bubble growth has only a limited effect on condensation heat transfer (since nuclei completely condense from a finite initial radius) while it can have a significant influence on evaporation heat transfer (bubbles grow). Sun and Hewitt [3] have rejected Mesler’s secondary nucleation hypothesis by comparing forced convective evaporation and forced convective condensation under identical conditions. Since they didn’t find significant differences between evaporation and condensation, the effect of bubble growth can be considered negligible. However, the

turbulent mixing enhancement of heat transfer produced by entrained bubbles can not be neglected based on their observations. Thome [46] has also acknowledged the existence of entrained bubbles but, like Mesler, he limited their potential heat transfer contribution to the evaporation that occurs at their interfaces. Thus, a further investigation of turbulent mixing heat transfer enhancement produced by entrained bubbles in flow boiling and condensation situations is warranted.

The existence of sliding bubbles was initially documented by Gunther [46] in 1951, but only recently has the heat transfer enhancement associated to them been studied. The relative importance of evaporation at the bubble interface, as compared to turbulent mixing enhancement of heat transfer in the wake of large sliding bubbles, has been studied by Houston and Cornwell [47], Addlesee and Cornwell [48], Kenning *et al.* [49], Qiu and Dhir [50], Addlesee and Kew [51] and Bayazit *et al.* [4], among others. These studies were often associated with boiling on the outside surface of tube bundles or bubbles sliding under inclined plates. Bayazit *et al.* include a comprehensive review of the sliding bubble mechanism and provide thermochromic liquid crystal (TLC) images of the temperature profile resulting from cap-shaped sliding bubbles driven by buoyancy under an inclined plate. Figure 1.14 shows how the largest temperature depression occurs in the wake and not at the trailing edge of the bubble. This behavior suggests that wake turbulent mixing is a substantial (or even dominant) component of sliding bubble heat transfer enhancement.

The natural question that arises from the observation of large cap shaped sliding bubbles is the following: can the same wake turbulent mixing effect be present for the case of smaller entrained bubbles traveling close to the tube wall in annular flow? Thorncroft's [5] work in subcooled vertical upflow and downflow forced convection boiling provides a possibility for a positive answer. Thorncroft observed and measured the vapor bubble dynamics and noticed that bubbles generated at wall nucleation sites (100 to 300  $\mu m$  in diameter for his experiments) slide in the direction of the flow and do not lift off the wall for upflow. This

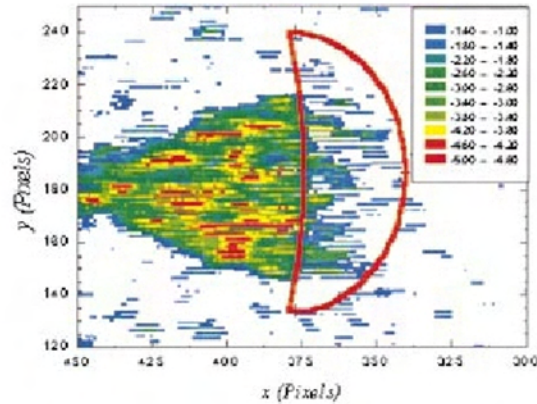


Figure 1.14: Thermochromic liquid crystal (TLC) imaging of temperature depression associated to a cap shaped sliding bubble taken from [4].

behavior is due to the fact that the shear lift force pushes bubbles that lead the local flow (due to buoyancy) towards the wall. For downflow, bubbles lag the local flow, causing the shear lift force to be reversed, and bubbles are pushed away from the surface of the tube. Heat transfer measurements obtained during the same study showed that the heat transfer coefficient is significantly higher in upflow than in downflow, as shown in Figure 1.15. Sliding bubbles traveling in close proximity to the tube wall appear to be a reasonable explanation for this difference in the heat transfer coefficient. Figure 1.4 showed that similar differences between upflow and downflow heat transfer also exist for saturated flow boiling at low qualities.

For vertical annular flow, Thorncroft measured similar heat transfer coefficients for the upflow and downflow conditions. This does not mean that the mechanism is not important for annular flow, but instead that the mechanism may behave differently for this flow regime since the thin liquid film (usually tens to hundreds of microns thick) restricts the radial displacement (lift-off) of bubbles, forcing them to remain close to the tube wall. For a specific upflow experimental condition, Thorncroft determined that 42 percent of the heat removed by bubbles created at the wall was attributable to their sliding after departure

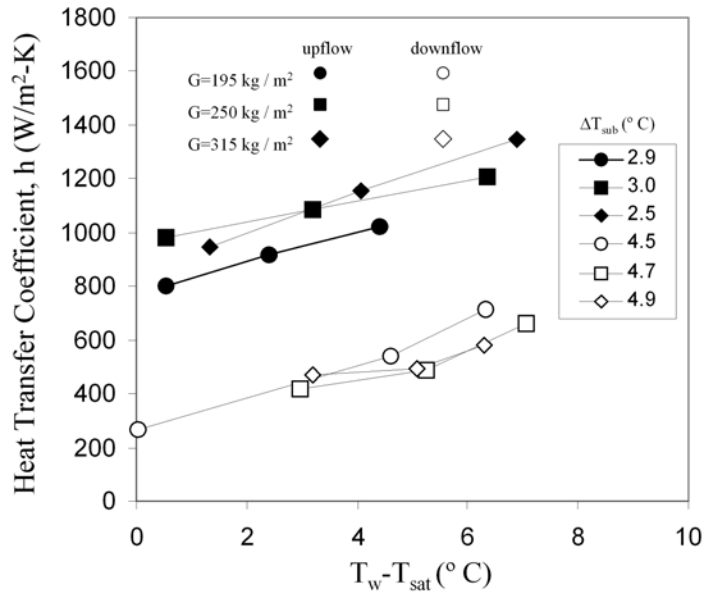


Figure 1.15: Difference in heat transfer coefficient vs. wall superheat for upflow and downflow conditions as measured by Thorncroft [5].

from the nucleation site. Moreover, his experiments with air bubble injection suggest that enhanced turbulent mixing, rather than latent heat transport, accounts for the major part of sliding bubble heat transfer, in agreement with the observations for larger bubbles sliding under inclined plates made by other authors.

Sliding bubbles may quantify or describe the differences between pool and flow boiling behavior providing a better physical understanding of the empirical factors such as  $F_{mic}$ ,  $F_{mac}$ ,  $C$  and  $m$  in the existing correlations.

## 1.7 Scope and Outline of Current Research

This study addresses a particular aspect of the mechanistic approach for the explanation of flow boiling heat transfer. The flow mechanics observed in horizontal two-phase adiabatic air/water flow are studied in an effort to explain flow boiling. Specifically, entrained bubble

behavior in the annular flow regime is studied in connection with the sliding bubble heat transfer mechanism (described above) using three optical techniques. Since a significant portion of the heat removed by bubbles created at the wall is attributable to their sliding after departure from the nucleation site, it is very likely that the effect of bubbles generated by mechanical vapor entrainment is also significant, or even predominant, if the amount of entrained bubbles is larger than those created from wall nucleation. In order to explore this possibility, an estimate of the size distribution and concentration of entrained bubbles should be found.

On Chapter 2, a backlit digital imaging technique applied to obtain images of bubbles within the liquid film of adiabatic air-water horizontal annular flow is described. A digital image processing algorithm was used to isolate bubble contours from other flow features. The resulting bubble entrainment statistics show that the bubble size distribution within the liquid film is exponential, and the parameters of the distribution are dependent on air flow rate and essentially independent of liquid flow rate. The bubble data, together with fluorescent imaging of waves on the liquid film, indicated that gas entrainment in the film is primarily controlled by air flow rate and wave behavior. This behavior was confirmed by the existence of a consistent Weber number based on the maximum observed bubble diameter and disturbance wave velocity.

Chapter 3 describes how the planar laser induced fluorescence (PLIF) technique is applied to horizontal air/water two-phase annular flow in order to clearly image crosscuts of the base liquid film and the interfacial waves at the top, side and bottom of a pipe. Images of the liquid film were captured using a digital video at a resolution of about  $8.2 \mu\text{m pixel}^{-1}$ . Cross-sectional data at 68 annular flow conditions were obtained. An iterative critical standard deviation multiplier scheme was developed to process batches of 100 images corresponding to a subset of those flow conditions. The base film thickness, interfacial roughness and interfacial wave statistics were obtained as a result. The structure of waves changed sig-

nificantly from wavy-annular, where peaked or cresting waves dominate, to fully annular, where the waves were much more turbulent and unstructured. The wave height decreased with increased gas flow and was relatively insensitive to increased liquid flow in the annular regime. The entrainment of gas in the liquid by the waves was very apparent from these images; episodes of liquid entrainment into the gas core were also visible. Although the precise gas entrainment mechanisms were not entirely clear, a viable folding action mechanism is proposed.

Chapter 4 takes advantage of the mean base film thickness and RMS data obtained with the PLIF technique to explore the pressure gradient associated with the interfacial roughness. An annular flow model by Owen and Hewitt [52] is implemented, and a comparison between the experimental pressure gradient and the roughness originated pressure gradient is performed. In general, it is found that interfacial roughness only accounts for part of the total pressure drop that occurs in annular flow. Other alternative mechanisms are proposed that could explain the underprediction of pressure drop that results from attributing all the pressure drop to interfacial friction. The implemented model can also be used to test traditional empirical relations that link the film thickness to the interfacial roughness.

A CFD simulation of the sliding bubble mechanism is presented in Chapter 5. The focus of the simulation is to predict the modulation of turbulence by a bubble entrained in a Couette-like flow. The boundary conditions for the simulation are provided by the interfacial velocity and the base film mass flow rate predicted by the Owen-Hewitt model. The chapter includes a detailed discussion of the special turbulent modelling and grid considerations that arise from the viscosity-dominated nature of the thin liquid film. A calculation that provides an estimate of the localized heat transfer enhancement attributable to sliding bubbles is also performed. The calculation is based on an estimate of the bubble wake dimensions, the entrained bubble number concentration and the flow boiling nucleation site density among other parameters.

Since any present or future numerical simulation of the flow requires experimental validation, adequate measurement techniques are required to study the mean and turbulent flow variables of the liquid film. The high shear rates and the microscopic dimensions associated with the liquid film pose specific difficulties for the measurement of the aforementioned quantities. The successful use of the PLIF technique for obtaining cross-cut images of the film, suggests that a similar setup can be used for performing cross cut micro-PIV measurements. Chapter 6 provides the details about seeding, imaging and timing that should be taken into account for this very particular flow situation. In general, the calculations are aimed at the design of a system that can produce images suitable for a cross-correlation analysis that benefits from the enhanced spatial resolution provided by a sub-correlation particle tracking velocimetry (PTV) method. A special test section was built and a new technique was implemented that inverts the contrast situation of traditional micro-PIV studies. Instead of using fluorescent particles, a fluorescent dye is added to the liquid and opaque tracers are used. Sample images with a sparse tracer concentration are presented that demonstrate the viability of the technique, but no actual PIV measurements are performed.

A final chapter restates the main conclusions of every chapter of this research with the exception of the introductory chapter. The appendices contain the equations from the code used for implementing the flow boiling heat transfer correlations, the equations from the code that implements the Owen-Hewitt annular flow model and a extended set of images obtained with the PLIF technique.

## Chapter 2

# Bubble Entrainment Statistics

In the study of two-phase flow in pipes, discussions regarding entrainment often refer to liquid droplets traveling in the gas or vapor core of annular two-phase flow. The opposite case, that is, bubbles traveling in the liquid film, appears to be just as frequent and suitable for detailed characterization. Bubble entrainment has been qualitatively documented in the existing literature. Jacowitz and Brodkey (1964) [53] documented entrainment in cross cut images of the liquid film for air/water horizontal annular flow. Cooper *et al.* [54] used a two-color piped-light illumination technique that also detected entrained bubbles and clearly distinguished them from droplets. Arnold and Hewitt [55] reported the presence of considerable amounts of entrained bubbles in backlit images of the liquid film for air/water vertical annular flow. More recently, Hewitt *et al.* [8] presented images of liquid in annular flow illuminated in a manner that clearly displayed entrained bubbles. Through the use of high-speed ciné film, they also documented what appeared to be a gas entrainment event at the leading edge of a wave. Other researchers, Thorncroft and Klausner [56] for example, have documented the presence of bubbles in adiabatic annular flows of pure fluids. Mesler [44, 57] constructed a theory for convective flow boiling heat transfer based on bubbles in the liquid film that originate from mechanical rather than thermal sources. In this work, he noted the potential for the generation of so-called secondary nucleation sites through the entrainment of vapor bubbles with droplet impacts and the trapping of a small amount of vapor during the collapse of a large bubble at the liquid surface. That this theory has been accepted as a possibility by some [18] and challenged by others [3] suggests that the role of entrained vapor in convective

boiling warrants additional investigation.

Although previous work has qualitatively documented the presence of entrained bubbles, their size distribution has not been quantified. Size distribution and concentration variations with respect to liquid and gas flow rate, as well as with the circumferential position around the tube, are explored in the present study as a first step towards an assessment of the potential role of bubble entrainment in the heat and mass transfer behavior of horizontal annular flow. The experiments focus on the flow mechanics and bubble statistics of a horizontal, adiabatic air/water system using seventy different annular flow conditions. In addition, the role played by disturbance waves and vapor shear in the entrainment and breakup of bubbles is discussed with the aid of cross-sectional images of the film obtained through fluorescence imaging.

## 2.1 Backlit Imaging Experimental Setup

### 2.1.1 Backlit Flow Loop

The setup shown in Figure 2.1 was used for all the statistical measurements. Compressed air and filtered water, both at 20°C, were combined in a mixing tee. Water entered the air current through multiple 3 mm holes drilled in a regular pattern over the extent of the tube surface enclosed by the tee. The water, initially room temperature, reached a steady state temperature of 284K due to evaporative cooling after several minutes of flow through the loop. Images were captured once this stable temperature was reached. The flow was allowed  $384 L/D$  ( $L = 5.8$  m) of straight tube length (15.1 mm I.D.) to develop before reaching the visualization region. The effects of flow within the mixing tee are minimized by allowing this distance before visualizing the flow. The possible effect of the mixing tee geometry on entrainment was studied by inverting the air and water inlets at the tee. No substantial changes in the flow were observed from this alternative mixing setup.

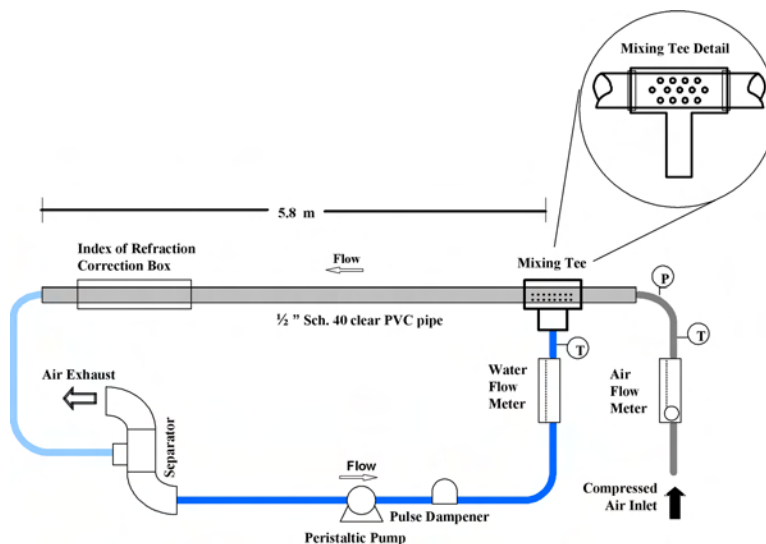


Figure 2.1: Air/water flow loop schematic.

A square cross section, clear acrylic box was fitted over the PVC tube at the viewing section, and the gap was filled with an oil that has an index of refraction almost identical to that of clear PVC. This setup minimizes distortions caused by the curvature of the tube wall. The air/water flow exiting the test section passed into a flow separator, and the water was recirculated from a holding tank using a variable speed drive peristaltic pump fitted with a pulse dampener.

The tubing carrying water from the separator to the mixing tee was also clear and it was frequently and carefully inspected for bubbles. Only a small number of randomly occurring bubbles were detected after the separator or the pulse dampener while in steady state operation. When the level in the liquid reservoir or pulse dampener was low, a significant number of bubbles appeared before the mixing tee, and testing was stopped until maintenance on the apparatus was completed. Thus, these extraneous sources of air bubbles can be considered negligible.

The current setup allows measurable water flow rates ranging from 0.2 to 1.5  $\text{l min}^{-1}$  and air flow rates ranging from 200 to 700  $\text{l min}^{-1}$ . Variable area flowmeters were employed

for measuring the water and air flow rates; only flow rates corresponding to graduations marked by the manufacturer on the meters (i.e., 200  $\text{l min}^{-1}$ , 300  $\text{l min}^{-1}$ , etc.) were used to ensure the highest accuracy and repeatability. These flowmeters have manufacturer-specified accuracies of 3 percent of full scale (0.045  $\text{l min}^{-1}$ ) and 2 percent of full scale (28  $\text{l min}^{-1}$ ) for the liquid and air models, respectively. The air flowmeter was verified to within 5 percent of the indicated flow over its entire range using an insertion thermal flow meter with a NIST-traceable calibration.

### 2.1.2 Backlit Image Acquisition

A Nikon D100 Digital SLR camera with a 6.1 megapixel resolution was used for gathering the data presented below. The required magnification was achieved using a Nikon MicroNikkor 60 mm f/2.8D macro lens and a Tamron 2X teleconverter. The shutter speed was set at 1/200 s and the aperture at f/11. It should be noted that the use of a 2X teleconverter makes the macro lens two f-stops slower and doubles the focal length. Thus, when estimating the depth of field of this optical system, a 120 mm focal length and an f/22 aperture should be used. For the CCD sensor used in the D100, the circle of confusion diameter is 20  $\mu\text{m}$ . With an object distance of 17 cm (as measured from the detector location), the depth of field is thus calculated to be 0.5 mm. This depth of field was also directly measured by moving the camera on a translation stage while observing the range over which small marks on the tube surface remained in focus.

The illumination may be described in general as a diffuse transmitted light system, a schematic of which is presented in Figure 2.2. The hot shoe flash signal from the camera was used to trigger a xenon strobe light, diametrically opposed to the surface of the tube viewed by the camera. The strobe light produced light pulses of approximately 0.03 ms. This short time, not the shutter speed, was what determined the exposure time, making it short enough

to avoid significant image blur at the observed flow velocities. The success of the subsequent image processing relies on providing an even backlighting. A diffuser was installed between the strobe light and the tube for this purpose. Several materials were tested as diffusers, including ground glass, opaque polymers and glossy paper sheets. The best results were obtained using two sheets of glossy paper (44 lb. bond coated on one side) with the glossy side facing the tube.

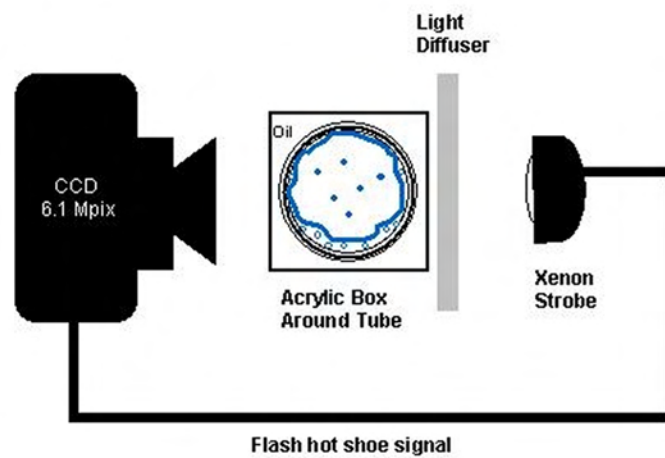


Figure 2.2: Setup for backlit images.

### 2.1.3 Experimental Procedure

The experimental matrix consisted of 5 air flow rates and 14 liquid flow rates (reported below as superficial velocities for each phase:  $U_{superficial}$  = volumetric flow rate for the phase / tube cross sectional area based on I.D.). One hundred images were captured for each flow setting. The Region of Interest (ROI) that was actually processed from each raw image frame was restricted in height in order to avoid curvature distortion of the vertical scale and to maintain an evenly illuminated background. The ROI depicts an area of 12.5 x 3.9 mm at a resolution of  $4.2 \mu\text{m pixel}^{-1}$ .

In general, the greatest difficulty in capturing images was obtaining a good focus on the

contours of bubbles traveling within the liquid film. A good focus should provide enough sharpness for the automated detection of the bubble contours. Even with the use of a rather small aperture ( $f/22$ ), a very narrow depth of field (approximately 0.5 mm) results since the focal length is large and the object is very close to the lens. Therefore, no parts of the liquid film traveling along the opposite side of the tube, or any entrained liquid droplets in the vapor core, were visible in the images. Moreover, the liquid on the opposite side of the tube enhances the desirable light diffusion. The dimensions of the waves create lenses with very short focal lengths, thus actually improving the diffusion of the light. The out-of-focus waves, droplets and bubbles are small and tend to act as scatterers (which cause additional diffusion).

A translation stage fitted with a micrometric screw was used to couple the camera body to a tripod. Very finely trimmed radial translation control was achieved with this setup, and it yielded optimal focus control.

#### 2.1.4 Image Processing

Each set of 100 images was batch processed using a script implemented with National Instruments IMAQ<sup>TM</sup> Vision Builder V.6.0 software. Details on the standard image processing operations used can be found in Gonzalez and Woods [58]. The complete script consists of 19 steps. The raw images were cropped, converted to 8-bit grayscale, and the histogram was stretched to enhance contrast.

The first step in the processing is an image threshold that produces a binary image in which the darker regions of the frame are separated from the light background. Dark regions include both the circular edges produced by bubbles (bubble contours) and the higher crests of the air-water interface. A contour is defined here as the finite width boundary of a closed curve. The width of this dark edge around the bubble image is finite because of optical

dispersion phenomena at the bubble interface. Some of the smaller bubble contours were thin and not completely closed. A contour closing procedure (a dilation followed by an erosion) was used to increase the number of closed bubble outlines by automatically filling in the gaps in nearly continuous boundaries that would otherwise go undetected by the subsequent image processing operations.

Next, the Heywood circularity factor is used as a criterion for finding nearly circular contours. This factor is the ratio of a contour perimeter to the perimeter of a circle with the identical area. Thus, a circle has a Heywood circularity factor of one. Contours with a Heywood circularity factor ranging from 1 to 1.20 were accepted. Those contours consisting of less than 20 pixels were discarded since they were judged too small to resolve accurately. If this finite boundary were 1 pixel thick, the diameter corresponding to a 20 pixel contour would be approximately 6 pixels. However, the actual thickness of the boundary was usually more than 1 pixel, which results in three or fewer pixels left to resolve the diameter; this was considered an insufficient amount.

The image that resulted from the foregoing processing was stored in a memory buffer. The steps described above were applied again in an identical cycle on the raw image, but using a different threshold value optimized for the detection of additional small bubbles located along the brighter horizontal centerline of the ROI; a significant number of these were ignored by the first threshold due to the large difference in contrast. After eliminating duplicate bubbles, the results of this second processing cycle were added to the contours stored in the buffer containing the results of the first cycle.

Figure 2.3 shows the main steps for the image processing of a base film image (i.e., an image of the base liquid film between waves). The first image in the figure shows the raw grayscale image. The second image was obtained after thresholding. Note that the darker areas of the frame are still included. After the Heywood circularity criterion was applied and the smaller pixel clusters were filtered out, only the significant circular contours remain.

A final step in the processing counted and sized the circles, as shown in the third image. Since the liquid films in the annular regime were so thin, bubble overlap was infrequent and was neglected in the image processing. An output file in spreadsheet format was generated containing all the information that resulted from the batch processing of the 100 images at each flow condition in the experimental matrix.

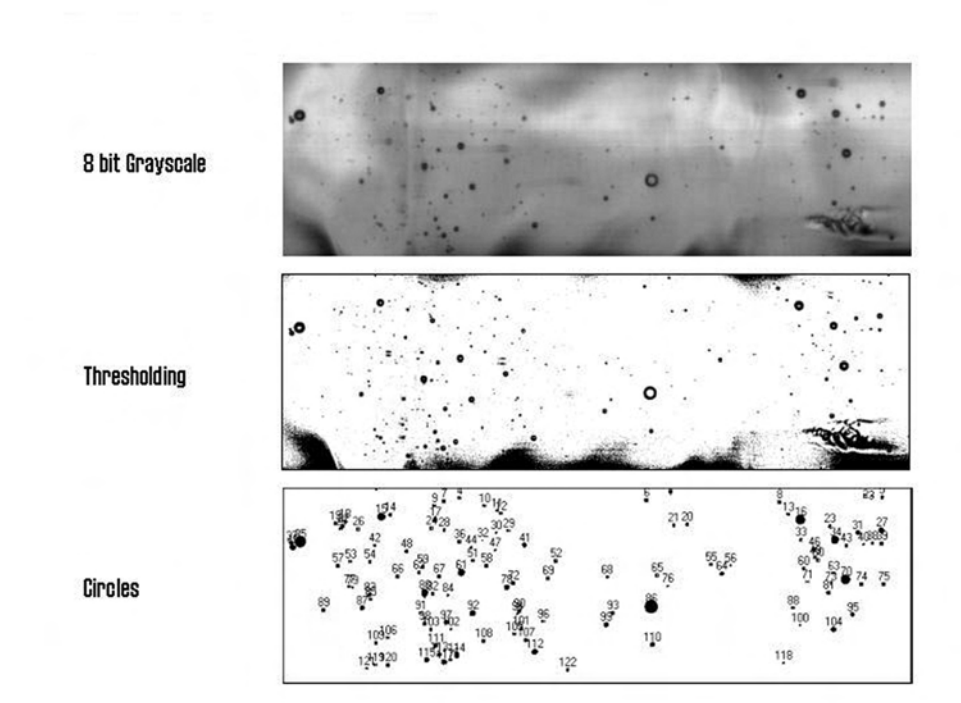


Figure 2.3: Image processing steps for base film ROI.

The base film is predominantly smooth and provides good contrast for bubble contour detection. However, when a disturbance wave appears in the ROI, the increased film thickness and interfacial roughness scatter most of the light and contrast is poor. The increased thickness also allows for substantial bubble overlap. Recently entrained bubbles within disturbance waves were also larger and appeared deformed by shear, which made them unfit for detection using the Heywood criterion. Most of the bubbles that were present in disturbance wave frames were not detected, as shown by the evolution of the image processing in Figure

2.4. Even though multiple relatively large bubbles are visible in the grayscale image, the image processing detects a single bubble. Consequently, the concentration data reported below underestimate the total number of bubbles since the image processing script did not have the capability of differentiating between disturbance wave images and base film images.

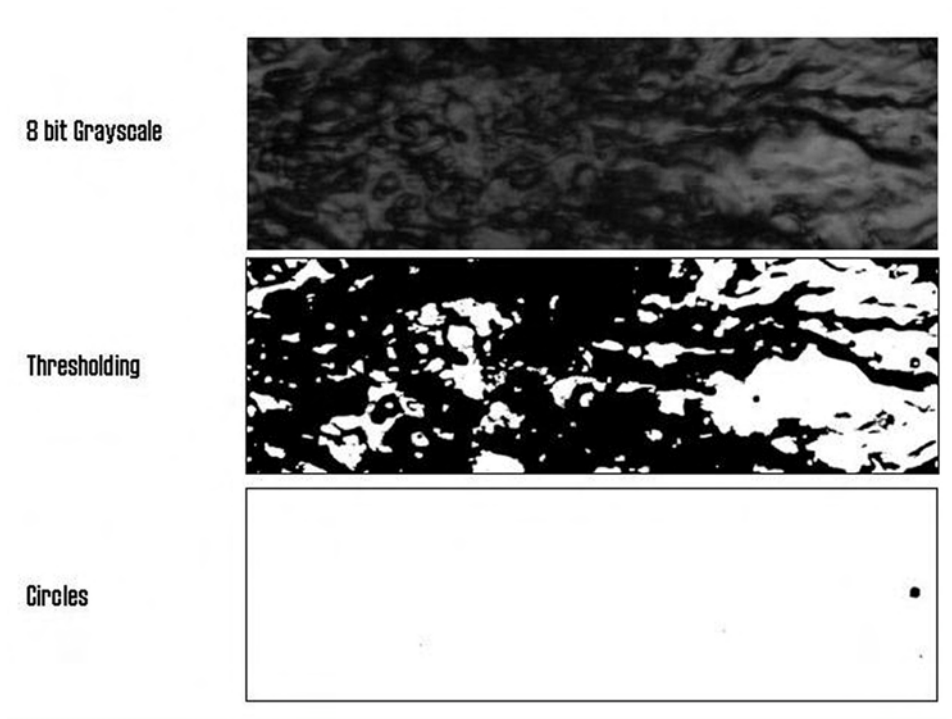


Figure 2.4: Image processing steps for disturbance wave ROI.

However, disturbance waves represent only a small portion of the total images of a given data set. Assuming that frames with less than 30 percent of the average bubble concentration were disturbance wave frames, it was determined from several sets of 100 images along the side of the tube that less than 5 percent of the images contained disturbance waves. Moreover, using wave spacing data obtained by Schubring and Shedd [6], and using a conservative estimate for the length of tube affected by a single interfacial wave (1 cm), it was found that the area affected by interfacial waves, represents between 4 percent and 6 percent of the total area. Furthermore, the rather large bubbles observed within disturbance waves quickly

break up into smaller bubbles. Thus, the statistical data presented below represent the size distribution of entrained bubbles within the base film that exists between the passage of disturbance waves.

### 2.1.5 Bubble Size Uncertainty

Several sources of uncertainty exist when extracting quantitative data from images. In this application, the uncertainty falls primarily into two categories: size distortion due to the imaging optics and illumination system, and alterations to the original image due to the image processing. The uncertainty in the diameter measurement due to the illumination system is believed to be smaller than a pixel. This is based on the fact that for particles of this size illuminated by diffuse, visible light, diffraction of light around bubble edges will produce only small variations in intensity. In addition, parallax and tube curvature distortions are minimized by restricting data analysis to about the center third of the image. Finally, manual comparison between images obtained using the backlit method and images obtained by reflection of light from the bubble surfaces resulted in consistent bubble measurement statistics.

The camera was focused on the inside wall surface prior to each set of runs using backlit droplets at rest on the wall. Since the liquid film in the present study is never more than 0.5 mm thick, which is about the depth of field of the lens system, the bubbles are assumed to be in focus at all times. However, the bubbles flow with a velocity of about 0.5 to 0.9 m s<sup>-1</sup> [59] and the flash lamp pulse width is approximately 30  $\mu$ s, so a bubble in the liquid film may travel about 27  $\mu$ m, or nearly 7 pixels, during the image exposure. The light intensity distribution is approximately Gaussian in time, so the resulting image contains a rapidly decreasing blur to the front and rear (upstream and downstream) of the bubble of about 2 to 3 pixels. This blur was consistently eliminated during the thresholding processes described

above.

Essentially, only the thresholding steps in the image processing algorithm have the potential to introduce additional uncertainty. These processes generally followed the recommendations of Kim and Kim [60] and Lee *et al.* [61] to determine the threshold values that would generate the best value of contrast (VC). In doing so, the motion blur was generally eliminated. According to Koh *et al.* [62], the resulting processed images should give bubble diameters with an uncertainty of between 5 percent and 10 percent of the measured diameter. The optical dispersion effects tend to widen the bubble contour inward. Thus, the outer edge of the contour still corresponds to the outer edge of the bubble from dispersion considerations alone. However, the outer edge is also slightly widened outward by diffraction. Varying amounts of the contour width appear in the final binary image depending on the values used for the threshold that produces it. The measurement of the contour diameter was taken based on the best fit circle to the binary image of the outer edge of the contour. Consequently, the uncertainty is likely to be biased so that the bubble size is overestimated.

## 2.2 Backlit Imaging Results

### 2.2.1 Bubble Size Distribution

Figure 2.5 shows typical examples of bubble size distributions observed along the side of the tube. Notice that the bubble diameters were normalized using the mean base film thickness,  $\bar{\delta}_b$ . The probability density distribution function,  $f$ , was defined so that the ordinate of each datapoint in Figure 2.5 corresponds to the number of observed bubbles per bin divided by the total number of observed bubbles. The total area,  $A_{tot}$ , used for normalizing the bubble counts was the area represented by a single observation frame,  $A_{frame}$ , multiplied by 100 (i.e.,  $A_{tot} = 100A_{frame}$ ). The initial bubble count was performed using equally sized

bins with units of pixels. However, the reported bin size ( $D_b/\bar{\delta}_b$ ) is not the same for all the distributions since the mean base film thickness observed for each flow setting (obtained from Schubring and Shedd [6]) was used to normalize the bubble diameter,  $D_b$ , in the abscissa as  $D_b/\bar{\delta}_b$ . The magnification factor of  $4.2 \mu\text{m pixel}^{-1}$  was used to convert the bubble diameters in pixels to actual length units.

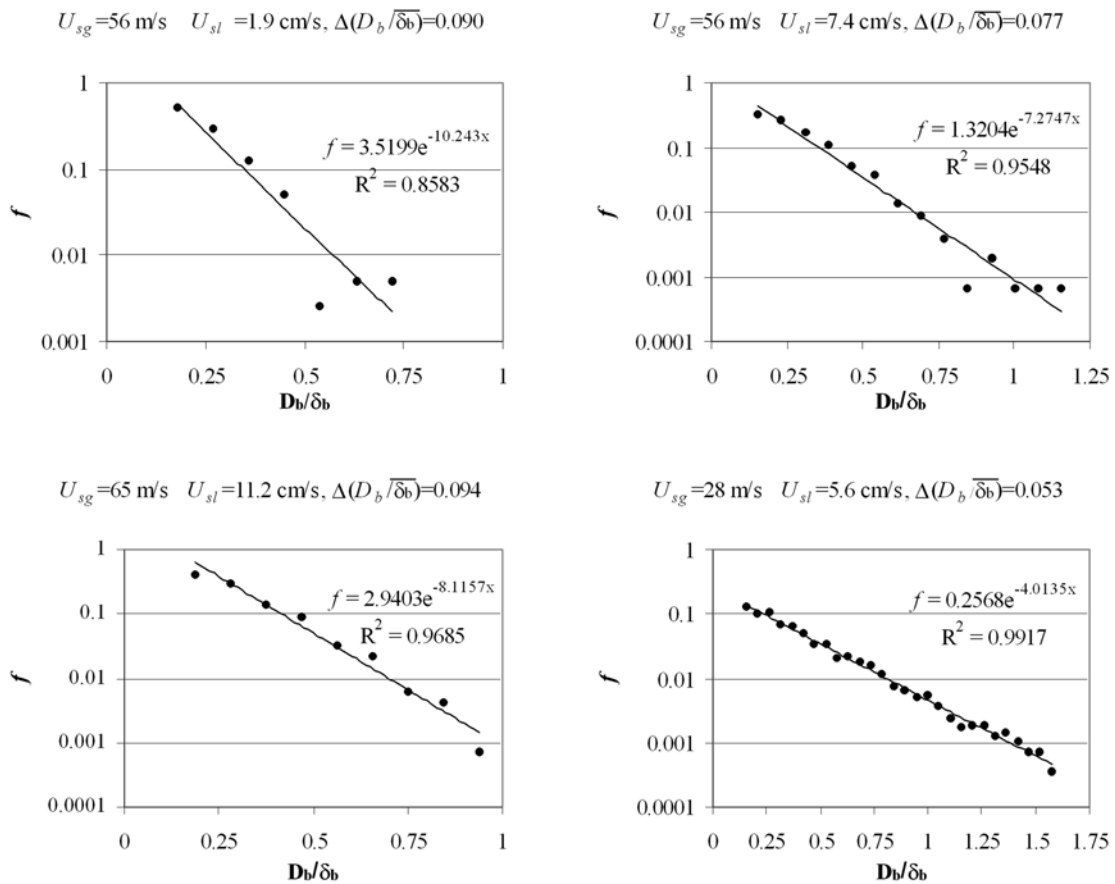


Figure 2.5: Exponential fits to bubble size distributions.

An exponential fit characterizes the probability density function via two parameters:

$$f = Ee^{-b(D_b/\bar{\delta}_b)} . \quad (2.1)$$

Thus,  $E$  is a dimensionless entrainment parameter that is proportional to the total bubble count and  $b$  is the power-law exponent for the distribution. The value of the power law exponent is always positive; increasing exponent values indicate increasing breakup, since this shifts the size distribution toward smaller radii. The behavior of the power-law exponent along the top, side and bottom of the tube for the entire experimental matrix is presented in Figure 2.6.

At the lowest liquid flow rates, as dryout was approached,  $b$  exhibited its highest values and very high sensitivity to increasing liquid flow rates. The behavior of  $b$  was very similar for the top, side and bottom locations, exhibiting noticeable dependence upon air flow rate and seemingly no dependence on water flow rate except near dryout. The general trend indicates that increasing the air flow rate yields an increasing power-law exponent. The physical meaning of this change in the exponent is that the size distribution shifts toward smaller diameters as air flow increases.

Preliminary measurements performed using a lower resolution camera suggested the existence of a peak in the size distribution precisely at the second bin of the histogram. Using the higher resolution setup described above, it was evident that no such peak existed for that particular size since the observation of even smaller bubble diameters (made possible by the increased resolution) yielded even larger amounts of bubbles per bin for smaller diameters. The operation of the image processing filter that discards contours consisting of less than 20 pixels generated a false peak in the size distribution. For this reason, the first bin for every data set was discarded before fitting the distribution to an exponential. The higher resolution results showed that the size distribution is monotonic and exponential, with the largest number of bubbles to be found in the smallest diameter bin of the histogram.

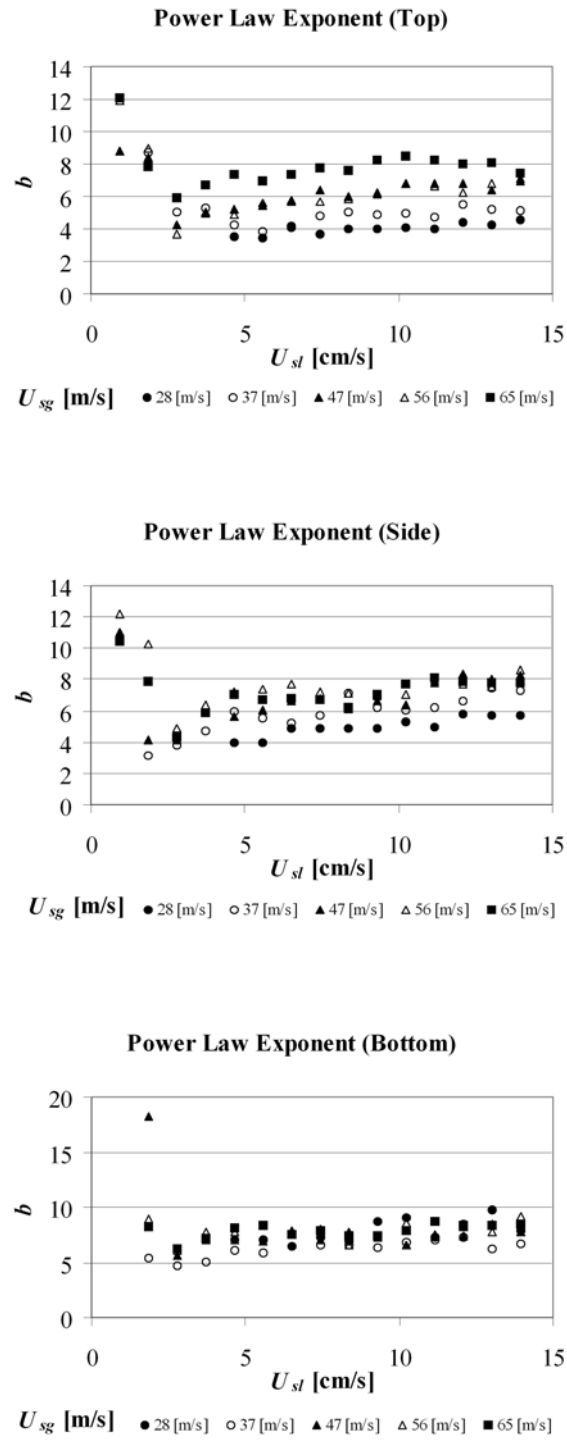


Figure 2.6: Power-law exponent.

### 2.2.2 Mean Bubble Diameter

The arithmetic mean bubble diameter,  $\overline{D}_b$ , ranges between 12 and 26  $\mu m$ . When normalized using the film thickness,  $\overline{D}_b/\delta_b$ , the mean bubble diameter ranges between 15 percent and 45 percent of the film thickness as shown by Figure 2.7. Away from dryout, no strong dependence on water flow rate is observed. Air flow rate dependence is evident along the bottom of the tube. The air flow rate dependence appears to be weaker along the top of the tube with most of bubble diameters ranging between 30 percent and 35 percent of the film thickness.

### 2.2.3 Bubble Number Concentration

The bubble number concentration, presented in Figure 2.8, does not exhibit a clear trend for air flow rate dependence, although a range of variation of an order of magnitude is observed among the data. The total detected number of bubbles divided by the total area studied for each distribution is not necessarily a perfect indicator of bubble concentration in the base film due to the presence of disturbance wave frames, as discussed earlier. Also, the image processing algorithm is not perfect, so some bubbles were missed. Thus, the bubble count underestimates the actual bubble concentration. There is a large reduction in the number of bubbles in the last panel of Figure 2.8 for  $U_{sg} = 47 \text{ m s}^{-1}$  and large liquid velocities. No changes in flow conditions, imaging or other reasonable explanations were found for this change in behavior for this particular set of data.

Experimental studies using steam/water [63] and R113 [64] have shown that nucleation site density during saturated flow boiling is typically in the order of 10 to 100 sites per  $\text{cm}^2$ . Consequently any potential heat transfer mechanism associated to entrained bubbles (e.g., the sliding bubble mechanism described in §1.6) should be comparable to the effect of bubbles originated at wall nucleation sites. This is especially true given the negligible

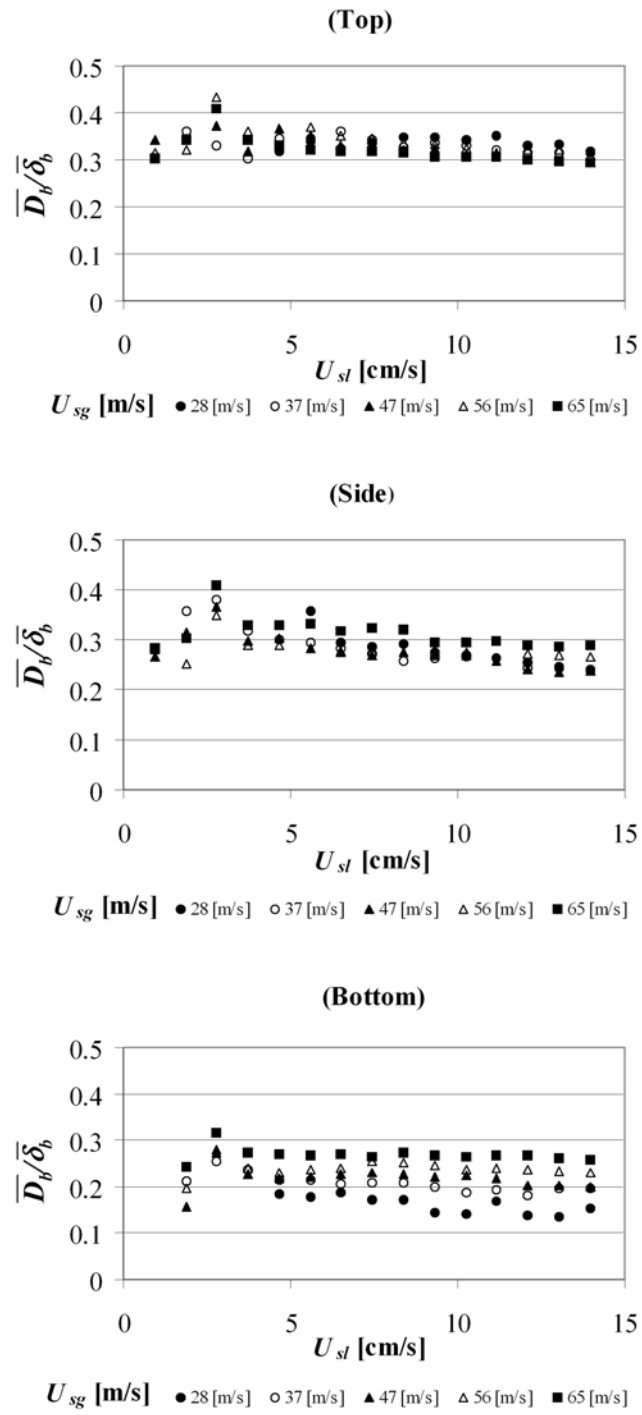


Figure 2.7: Mean diameter normalized using mean base film thickness.

contribution of latent heat transfer during bubble growth at nucleation sites.

## 2.3 Discussion

### 2.3.1 Entrainment Mechanisms

The behavior of the power law exponent, i.e., decreasing with increasing air flow, suggests that the bubble size distribution strongly depends on the flow mechanics. From the observations made in the present study, it is proposed that the dominant mechanism is a continuous folding action within the disturbance waves that entrains relatively large bubbles that break up quickly. The folding action mechanism remains a speculation until more cross cut images are studied in detail. However, the author believes that entrainment caused by disturbance waves may be a scaled down version of the hydraulic jump air entrainment documented in Chanson [65] and the references within.

The bubble distribution that exists in the base film in between disturbance waves is likely to be the result of break up and subsequent turbulent mixing that spreads apart bubble clusters resulting from the breakup of large bubbles. Evidence of these processes may be seen in the backlit images and cross cut images obtained using Planar Laser Induced Fluorescence (PLIF) as described in Chapter 3. Figure 2.9 compares cross-cut images of interfacial waves against backlit images of the bubbles that remain in the base film.

The cross cut images, shown on the left, each present an axial slice that is about 0.5 mm thick (into the page) and 5 mm long (in the flow direction) of a typical wave on the liquid film. These images clearly document the entrainment of large bubbles by waves and show how the nature and size of waves change as the air flow rate increases. At lower superficial gas velocities ( $U_{sg} = 28$  and  $37 \text{ m s}^{-1}$ ), waves are similar to roll waves and larger in size, and many large bubbles are entrained by them. The higher superficial gas velocities ( $U_{sg} = 47$  to

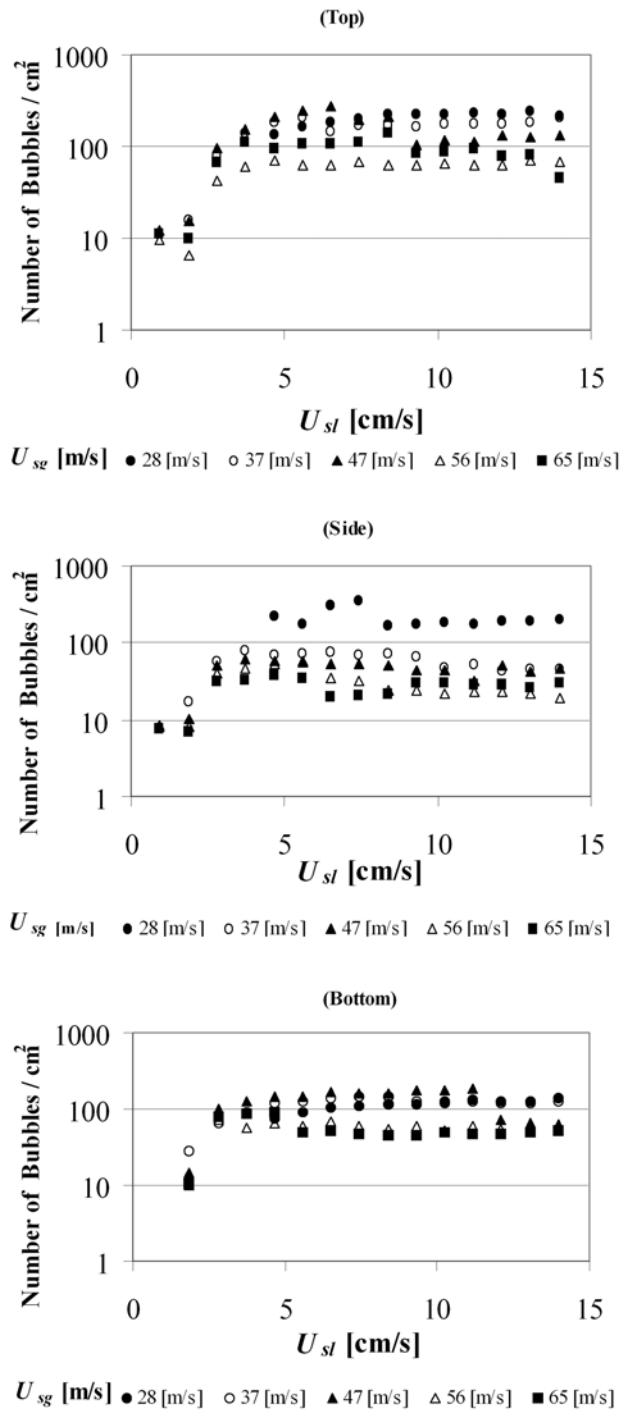


Figure 2.8: Bubble number concentration.

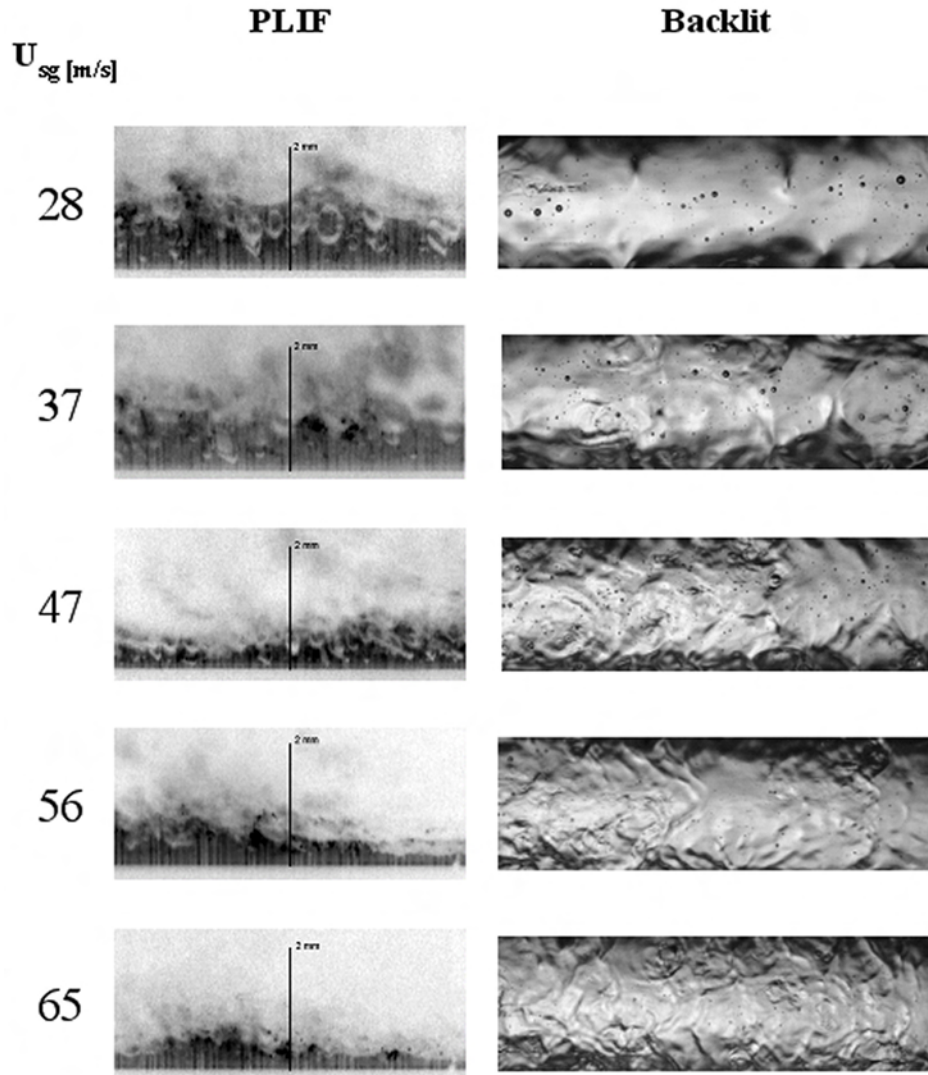


Figure 2.9: PLIF images of disturbance waves (left) and backlit images of base film (right) for increasing  $U_{sg}$ . Backlit images represent a 12.5 x 3.9 mm area. All images depict the bottom of the tube for  $U_{sl} = 9.3 \text{ cm s}^{-1}$ . The two parallel sets of data correspond to separate experimental runs. Flow from right to left.

$65 \text{ m s}^{-1}$ ) produce disturbance waves that, unlike the roll waves, appear to travel as separate entities on top of the base film; fewer and smaller bubbles are entrained by them. Changes in liquid flow rate do not produce significant changes in wave nature or size (the additional liquid is carried by additional waves, as frequency and wave velocity increase as documented by [6]). The backlit images in Figure 2.9, corresponding to the same flow conditions of each wave image on the left, show how the bubble size distribution changes within the base film between disturbance waves. In agreement with the results for the power law exponent and mean bubble diameter (Figures 2.6 and 2.7), the distribution shifts towards smaller sizes as air flow rate increases.

The most striking feature of the bubble number concentration results is that the most bubbles are entrained for the lowest gas superficial velocity. This may be connected, at least in a speculative manner due to the limited amount of cross-cut images presented here, to the nature of the disturbance waves shown in Figure 2.9. The total entrained gas volume is larger for the wave observed at the lowest gas superficial velocity; this may ultimately produce a higher bubble number concentration in the base film. Even if the wave frequency increases for the higher gas superficial velocities, this doesn't appear to compensate for the reduction in the volume of gas entrained by each individual disturbance wave. See Chapter 3 for further discussion on the mechanism of gas entrainment by waves.

Droplet impacts and bursting bubbles are known to generate small bubbles in a thin film [57]. Although the existence of these events is acknowledged, this type of entrainment was not clearly documented by the visualization techniques and the image processing used in the present study. It is possible that these mechanisms may contribute to the total entrainment, particularly at the higher air flow rates where a mist flow condition may exist in the gas core. These mechanisms could explain the increase in bubble number concentration at  $U_{sg} = 65 \text{ m s}^{-1}$ , while this quantity decreases as  $U_{sg}$  varies from  $28 \text{ m s}^{-1}$  to  $56 \text{ m s}^{-1}$  as shown in Figure 2.8. The contribution of droplet impacts to total bubble entrainment

appears to be a secondary effect, as this behavior would be expected to show a stronger dependence on liquid flow rate. In addition, if droplet impacts were a significant source of entrainment at the lower superficial gas velocities, higher concentrations would be expected towards the bottom of the tube since gravity is important when compared to inertia at the lower gas flow rates. This increased concentration at the bottom is not observed in the bubble number concentration data.

### 2.3.2 Bubble Breakup

Increasing the gas flow rate produces higher exponent values, as shown in Figure 2.6, which translates into distributions with a larger amount of small bubbles. From the data presented, it appears that elevated interfacial shear promotes the breakup of the larger bubbles in the distribution. On the other hand, the power-law exponent remains fairly constant as liquid flow rate changes.

Measurements of the mean base film thickness between disturbance waves are shown in Figure 2.10. The base film thickness remains nearly constant at the higher gas flow rates, suggesting that an increment in liquid flow rate will increase the disturbance wave frequency through the generation of more waves. This has been documented for these flows using a non-intrusive total internal reflection optical sensor [6, 7]. The relative independence of bubble entrainment with respect to liquid flow rate in the annular regime appears to be related to the fact that disturbance wave velocities are a strong function of air flow rate, but a much weaker function of liquid flow rate. The film thickness data also suggest that, once a bubble escapes the disturbance wave and remains in the base film, it will experience nearly constant shear forces regardless of the liquid flow rate over the range studied. As observed in the last panel of Figure 2.5, the largest bubbles in the base film can be even larger than the mean film thickness. These bubbles are unlikely to survive very long before they break up.

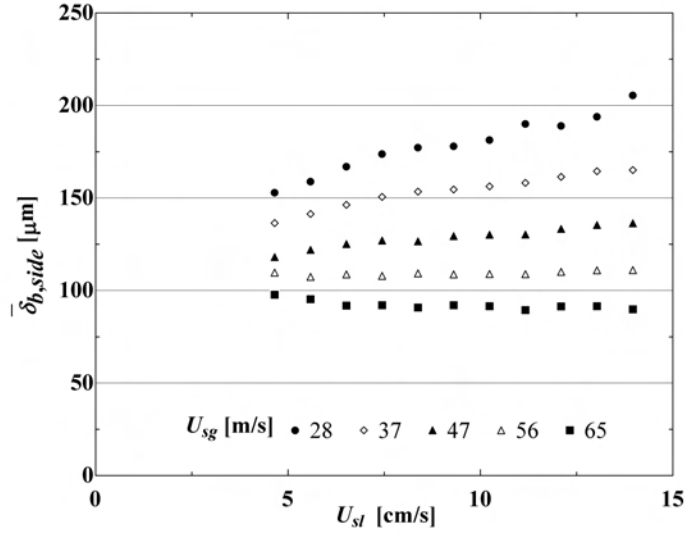


Figure 2.10: Base film thickness along the side of the tube measured by Schubring and Shedd [6] using optical method developed by Shedd and Newell [7].

The data suggest, then, that gas is entrained in a random manner by trapping and folding at the gas/liquid interface of a disturbance wave. These bubbles are then broken up under shear between the fast moving wave and the wall. We have found that the critical Weber number,

$$We_c = \frac{\rho_l U_{dw}^2 D_{max}}{\sigma}, \quad (2.2)$$

based on the mean disturbance wave velocity,  $U_{dw}$ , liquid density,  $\rho_l$ , surface tension,  $\sigma$ , and maximum bubble diameter,  $D_{max}$ , attains a value between 40 and 100 for the majority of data measured at  $U_{sg} = 37 \text{ m s}^{-1}$  and higher and superficial liquid velocities,  $U_{sl}$ , greater than  $0.05 \text{ m s}^{-1}$ . A notable exception occurs for the two lower gas flow rates along the bottom of the tube, where values of  $We_c$  between 100 and 140 are observed.  $We_c$  for the lower liquid flow rates is typically lower than 40. Figure 2.11 shows values of  $We_c$  calculated using values of  $U_{dw}$  from [6] and values of  $D_{max}$  from the present study. Weber numbers based on other characteristic velocities do not appear to correlate the data at all.

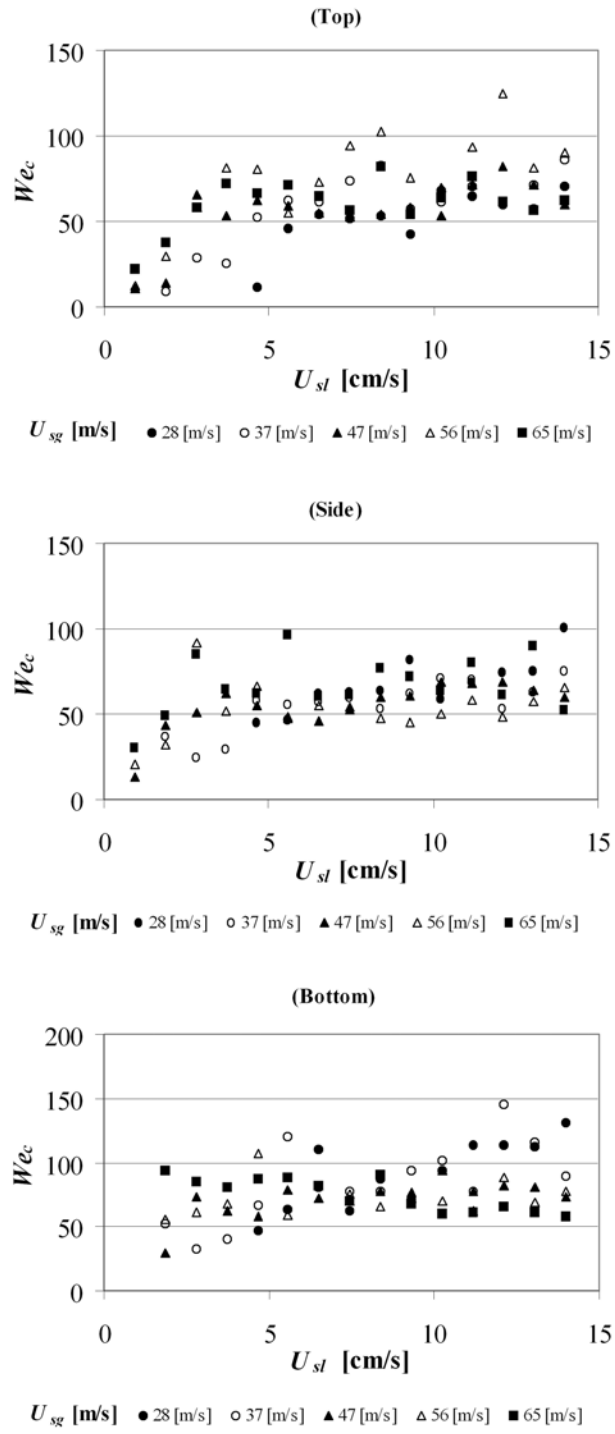


Figure 2.11: Critical Weber number.

### 2.3.3 Exponential Size Distribution

The exponential distribution of bubble sizes has been observed in other studies of bubble entrainment due to waves on large bodies of water. Deane and Stokes [66] found that bubbles entrained by breaking ocean waves followed exponential trends with exponents of  $10/3$  for bubbles with radii between 1 and 10 mm and  $3/2$  for bubbles between 0.1 and 1 mm. Although they did not present a large amount of data for bubbles smaller than this, it appears that the exponent would decrease again for bubbles with radii below 0.1 mm. Thus, the shape of the size distribution obtained in the present study is consistent with this previous work, although the change in exponent indicates that the shearing mechanisms in annular flow differ from those in breaking ocean waves. For the Deane and Stokes situation, the critical Weber number is 4.7 and the critical Reynolds number is 450 (both based on the turbulent velocity fluctuation component at the scale of the bubble). Those critical numbers essentially describe a breakup mechanism directly associated with turbulence at the scale of the bubbles; they are thus much smaller than critical numbers based on the disturbance wave velocity. In the present study, the breakup mechanism is probably different; it is more likely to be associated with the disturbance wave velocity and the velocity gradient that exists across the film thickness.

## Chapter 3

# Cross-cut Imaging of the Base Film and Interfacial Waves

Due to the reduction in machine time required for the digital processing of large batches of images, direct visualization of cross-cut images of the liquid film in annular flow is now a viable alternative to conductance probe film thickness measurements. Conductance probe measurements are very repeatable, provide high temporal resolution and are relatively simple to implement. However, they are intrusive in nature, they are considered inadequate for films that are thinner than  $50 \mu m$  [67] and are very likely to underestimate the film thickness when the void fraction in the liquid film is significant. The void fraction within the base film is not negligible and it is very high within interfacial waves as shown in Chapter 2.

The planar laser induced fluorescence (PLIF) technique used in the present study for capturing cross-cut images provides several improvements upon other visualization studies in the literature. Improvements include good contrast between the gas and liquid phases, a very narrow depth of focus and visualization of the liquid film down to a distance of about  $10 \mu m$  from the tube wall. An image processing algorithm was also implemented that yielded accurate measurements of the film thickness and its root-mean-square (RMS) value. These two quantities are essential for a complete understanding of the mechanics of horizontal annular flow. More specifically, interfacial friction (pressure drop) and liquid atomization (droplet entrainment into the gas core) are determined by the roughness of the interface. Circumferential wetting, mixing and transport phenomena in general are other examples of

flow features related to these liquid film measurements. For instance, the mean liquid film thickness is essential in calculating the local heat transfer coefficient in current models.

The experimental matrix of the present visualization study is extensive, covering ranges of superficial velocities comparable to detailed conductance probe measurements such as the ones by Paras and Karabelas [67]. Superficial velocities are the most frequent way of specifying two-phase flow conditions inside a pipe and they are defined as the volumetric flow rate of the specific phase divided by the flow cross sectional area of the pipe. Thus, the superficial gas velocity is given in terms of the volumetric gas flow,  $\dot{V}_g$ , and the tube cross-section area,  $A_{cs}$ , as

$$U_{sg} = \frac{\dot{V}_g}{A_{cs}} \quad , \quad (3.1)$$

and the superficial liquid velocity is given in terms of the volumetric liquid flow,  $\dot{V}_l$ , as

$$U_{sl} = \frac{\dot{V}_l}{A_{cs}} \quad . \quad (3.2)$$

The cross-cut visualization of waves for the current experimental matrix permitted a qualitative and quantitative characterization of the variation of their shape and size with changes in liquid and gas flow rates. Also, a folding action mechanism is proposed and illustrated in the present study as a connection between interfacial wave (IW) action and the bubble entrainment statistics observed in Chapter 2. Interfacial waves are highly turbulent masses of liquid that travel along the tube faster than the mean base film velocity. Experiments by Schubring and Shedd [6] studied their velocity and frequency and determined that, in general, this velocity is approximated by the friction velocity,  $u^*$ , over much of the wavy, wavy annular and annular regimes although the physical explanation for this match is still

unclear. The friction velocity is defined as

$$u^* = \sqrt{\frac{\tau_0}{\rho_l}} \quad , \quad (3.3)$$

where  $\tau_0$  is the wall shear stress and  $\rho_l$  is the liquid density. The cross-cut images of the liquid film presented in this chapter provide a characterization of the IW size, shape and the void fraction that exists within them. The IW and base film asymmetry inherent to horizontal annular flow is captured by taking images at the top, bottom and side locations along the circumference of the tube. The images also help in the interpretation and validation of total internal reflection film thickness measurements by Shedd and Newell [7].

### 3.1 Background

The bulk of the measurements for the present study were performed in the wavy-annular and fully annular regimes. The experiments' flow regimes, although achieved in an adiabatic situation, resemble particular stages of the flow boiling process described in Figure 1.2. Initial testing of the experimental method was performed in a low gas velocity stratified regime in which all the liquid travels along the bottom of the tube.

Many studies [68–73] have performed conductance probe measurements on pipes of varying diameters for a limited number of flow conditions and varying pipe diameters. Other, more comprehensive conductance probe studies are available in the open literature. Paras and Karabelas [67] performed conductance probe measurements on an experimental matrix of 17 flow conditions, recording time series data at six circumferential locations. The range of superficial velocities covered by Paras and Karabelas ( $U_{sg} = 31$  to  $66 \text{ m s}^{-1}$  and  $U_{sl} = 1.9$  to  $20 \text{ cm s}^{-1}$ ) closely matches the experimental matrix of the present work, although they used a 50.8 mm I.D. pipe. Some data from Jayanti *et al.* [74] for a 32 mm I.D. pipe at lower

$U_{sg}$  settings are also available. These two sets of data will be used for comparison against the quantitative PLIF results in §3.3.2.

Several research groups have developed visualization techniques that document the structure of the liquid film and the bubble entrainment mechanisms for two-phase flow inside tubes with varying degrees of success. Jacowitz and Brodkey [53] obtained images of backlit turpentine flowing in a glass tube and defined their cross-cut plane using the depth of field of a microscope objective. However, their images were blurred since they were limited by the shutter speed of the camera, and the finite depth of field of the microscope was not small compared with the circumferential scale of the visible features. Also, the fact that turpentine does not exactly match the index of refraction of glass limits the visibility near the wall, as discussed below. It should also be pointed out that using a very volatile test fluid like turpentine may significantly alter the void fraction that is observed in the experiment. Arnold and Hewitt [55] performed imaging of the film with the camera looking axially into the tube. Their images successfully depict the full circumference of the film, and the instantaneous thickness of the film. However, the entrainment mechanism is not very well documented without looking at the full length of the interfacial waves and the void fraction that exists inside the film is hardly discernible. The average void fraction inside a pipe can be imaged when no optical access is possible by using X-Ray tomography as reported by Modi *et al.* [75]. The technique, however, is not yet suitable for instantaneous visualization of the film profile. High frame-rate neutron radiography (NRG) images of two-phase flow inside a narrow rectangular channel have been obtained by Hibiki *et al.* [76]. The NRG technique is essentially a backlit imaging method and, while it is useful in visualizing the void fraction in a narrow channel, it is not suitable for obtaining cross-cut images for direct film thickness measurements inside a round tube.

Hewitt *et al.* [8] used fluorinated ethylene propylene (FEP) tubing and a water-filled box around their test section; this basic setup was reproduced for the present study. The

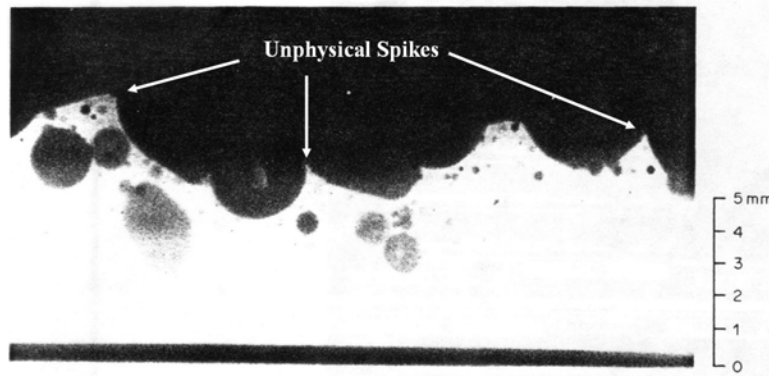


Figure 3.1: Sample image from Hewitt *et al.* [8]. Arrows and label are absent in the original paper.

resulting match in indices of refraction is excellent and allows the visualization of very thin films. A transmitted light illumination system based on high intensity flashlamps was used by Hewitt *et al.* together with high-frame rate ciné film. The short duration of each exposure successfully eliminated the motion blur. A vertical plane was isolated using narrow depth of focus optics, similar to Jacowitz and Brodkey. Nevertheless, the interface between the liquid film and the gas core seems unphysical in their images (see Figure 3.1). For example, sharp spikes appear as a result of overlapping shadows of interfacial features in the background of the imaged plane. The latter problem is inherent to the backlit illumination employed by Hewitt *et al.*

## 3.2 PLIF Experimental Setup

### 3.2.1 PLIF Flow Loop

The flow loop shown in Figure 3.2 was used for the measurements. The configuration is almost identical to the one described in §2.1.1 except for the visualization region. The flow was allowed  $265 L/D$  ( $L=4.0$  m) of straight, clear PVC tube length (15.1 mm I.D.) to develop before reaching the visualization region.

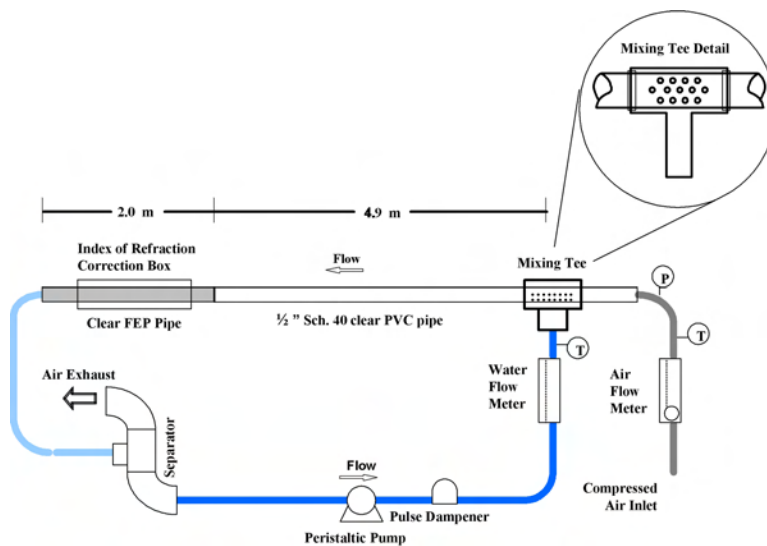


Figure 3.2: Flow loop schematic for PLIF measurements.

The pipe in the visualization region is made of fluorinated ethylene propylene (FEP) of nearly the same I.D. as the PVC, but with a thinner wall. Visualization took place one meter after the coupling of both pipes, to allow some distance for the flow to redevelop. The air/water flow exiting from the test section passed into a centrifugal gravity separator, and the water was recirculated from a holding tank using a variable speed peristaltic pump fitted with a pulse dampener. Air was sent into the laboratory fume exhaust system to avoid inhalation of the potentially hazardous Rhodamine B dye. The setup allowed measurable water flow rates ranging from 0.2 to 1.5  $\text{l min}^{-1}$  and air flow rates ranging from 200 to 700  $\text{l min}^{-1}$ . Variable-area flow meters were employed for measuring the water and air flow rates. These flow meters have manufacturer-specified accuracies of 0.045  $\text{l min}^{-1}$  and 28  $\text{l min}^{-1}$  for the liquid and air models, respectively. The air flow meter was verified to within 5 % of the indicated flow using an insertion thermal flow meter with a NIST-traceable calibration. Flow settings corresponded to graduations marked by the manufacturer on the meters to ensure accuracy and repeatability.

### 3.2.2 PLIF Image acquisition

A square cross section, clear acrylic box was fitted over the FEP tube at the viewing section, and the gap was filled with water as shown in 3.3. This setup minimizes distortions caused by the curvature of the tube wall. FEP has an index of refraction of 1.338<sup>1</sup>, which is very close to the index of refraction of water. The index of refraction of water is 1.333 for  $\lambda = 589$  nm at 293K according to [77]. An Abbe refractometer was used in the present study to confirm that the dye had little effect on the index of refraction,  $n$ . The index of refraction of water at the actual water temperature of 284K is only slightly different since  $\partial n/\partial T$  is very small ( $\partial n/\partial T \approx -0.92 \times 10^{-4} \text{ K}^{-1}$  according to [78]). Thus, the indices of refraction of the liquid film, the FEP pipe, and the gap between the acrylic box and the pipe are matched. This is more convenient than machining a test section from a solid FEP blank because this polymer has a lower optical transmittance than acrylic or water. The indices of refraction can also be matched by dissolving salt, iodine or other solutes in water<sup>2</sup> and accurate calculations for the index of refraction of aqueous electrolyte solutions can be performed following the procedure described by [79]. However, due to the continuous evaporation of liquid from the loop, maintaining a constant concentration of solute can be impractical. The reason for matching the indices of refraction using the rather turbid FEP, instead of using higher transmittance glass or PVC pipes, is related to avoiding near-wall distortion and dark band effects.

A dual-pulsed, frequency doubled, Nd:YAG laser was used to generate a pulsed laser light sheet (120 mJ, 5 ns FWHM,  $\lambda = 532$  nm). The laser was run at a lower energy ( $\approx 40$  mJ/pulse) setting for the measurements, since the intensity of the fluorescence at 120 mJ was excessive and caused blooming (image noise) in the CCD of the video camera. Focusable light sheet optics designed by Rodenstock generated a 500  $\mu\text{m}$  thick light sheet

---

<sup>1</sup>According to an FEP manufacturer's website: [www.texloc.com/closet/cl\\_fep\\_properties.htm](http://www.texloc.com/closet/cl_fep_properties.htm)

<sup>2</sup>From a personal communication with Dr. Steve Anderson from LaVision Inc.

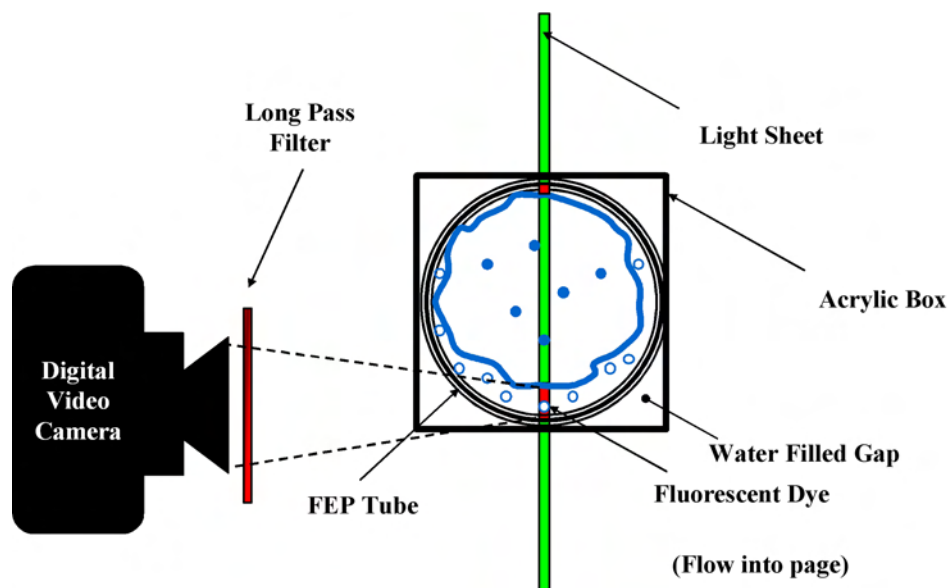


Figure 3.3: Setup for PLIF images.

that produced cross sections of the liquid film (see Figure 3.3) along a plane containing the axis of the tube. A small amount ( $\approx 70 \text{ mg l}^{-1}$ ) of fluorescent dye (Rhodamine B) was mixed with the water. The concentration of the dye is not critical to the method's performance although it should be kept as low as the available laser power allows it to avoid significant variations in the liquid's surface tension and viscosity.

A single pulse from the laser excited the dye molecules, which have an absorption peak at  $\lambda = 545 \text{ nm}$ . The dye molecules subsequently fluoresced with an emission peak at  $\lambda = 565 \text{ nm}$ . With adequate optical filtering (long pass or narrow band filters), only the light emitted from the liquid phase fluorescence reached the camera. This filtering eliminates any stray reflections from the excitation laser pulse. The freezing in time of instantaneous images of the flow was accomplished due to the short duration of the laser pulse (3–5 ns FWHM) and the very fast time response of the fluorescence of the dye (less than a nanosecond). A Canon XL1 digital video camera fitted with a Tamron 60 mm macro lens was used to obtain a resolution of about  $8.2 \text{ } \mu\text{m pixel}^{-1}$ . The original color images were cropped, converted to 8-bit grayscale, and the gray level histogram was stretched to enhance contrast. The relatively

low resolution ( $640 \times 480$  pixels) and low signal to noise ratio (SNR) of this camera are tolerated since it captures individual frames at video rate (30 Hz). This frame rate allowed large numbers of base film and interfacial wave frames to be captured for each flow setting in the large experimental matrix within a reasonable time. This large number of frames is necessary for the statistical significance of the subsequent digital processing of the film thickness data.

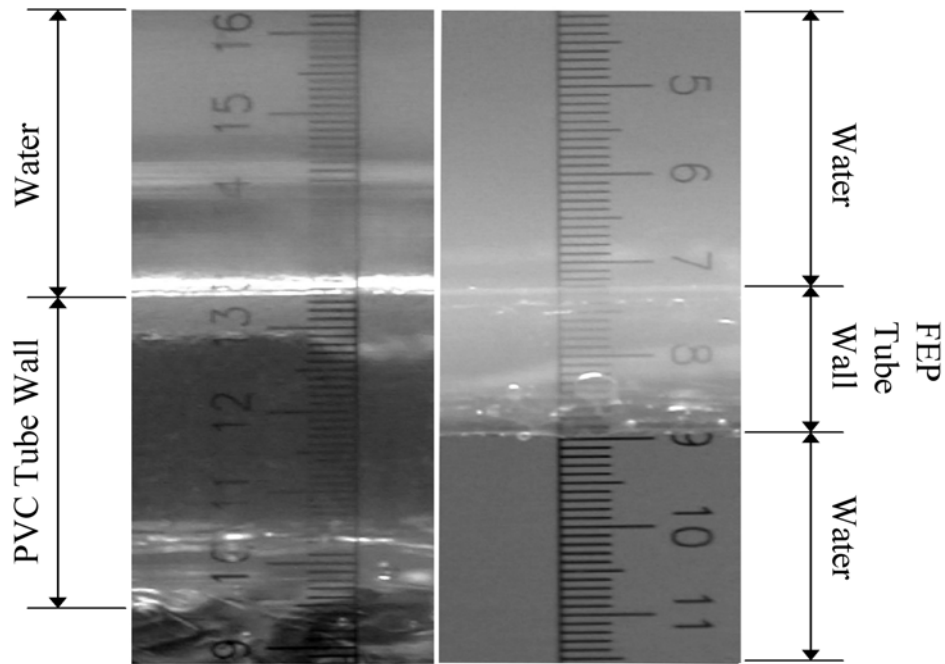


Figure 3.4: Reduction of near-wall dark band and distortion. Scale markings every 0.1 mm.

The near-wall resolution the PLIF technique is limited in the case of round tubes by the difference in index of refraction between the liquid (water) and the tube wall material. This difference results in reflection and refraction at the inner tube wall (generally with  $n_i < n_t$ ) causing vertical scale distortion and the dark band effect near the wall. For PVC the mismatch in index of refraction is significant since  $n_t = 1.53$  [80]. Due to this limitation, if PVC tubes are used, PLIF images are dark up to about 1 mm away from the tube wall and are significantly distorted slightly above 1 mm. This dark band hides most, if not all,

of the thickness of the liquid film for the annular regime of air/water flow. Using FEP instead of PVC improves the near wall quality of the images by reducing the dark band to about 0.01 mm. Figure 3.4 shows how the scale markings are blurred and distorted near the PVC/water interface while they remain visible and correctly scaled near the FEP/water interface.

### 3.3 PLIF Results

#### 3.3.1 Qualitative PLIF Results

Figure 3.5 shows a PLIF image of the thicker film produced by a stratified flow regime that illustrates some features of the technique in detail. The bubbles that are cut by the light sheet appear as dark spots. A shadow region above the dark spots is also visible. PLIF images require careful interpretation since dark spots may not correspond to the full diameter of the bubble and some bubbles may be hidden in the shadow region produced by other bubbles. Bubbles out of the focal plane and located between the light sheet and the camera appear as backlit contours instead of producing dark spots. The vertical fringes are produced by extrusion patterns in the tube material and they were convenient for focusing on the light sheet. The presence of out of plane features was reduced when taking images of annular flows. For the images taken in annular regimes, base films are much thinner (in the order 300  $\mu\text{m}$  or less) and interfacial waves are up to 2 mm thick. At the greater magnification needed for imaging annular flow, the depth of focus is narrower than in Figure 3.5 so that out of plane features are blurred or absent.

Figure 3.6 shows typical images of the base film and interfacial waves for wavy annular and fully annular flows inside a 15.1 mm I.D. tube. The scale included in both cases is useful in noticing the difference in thickness between the interfacial wave frames (2 mm scale) and

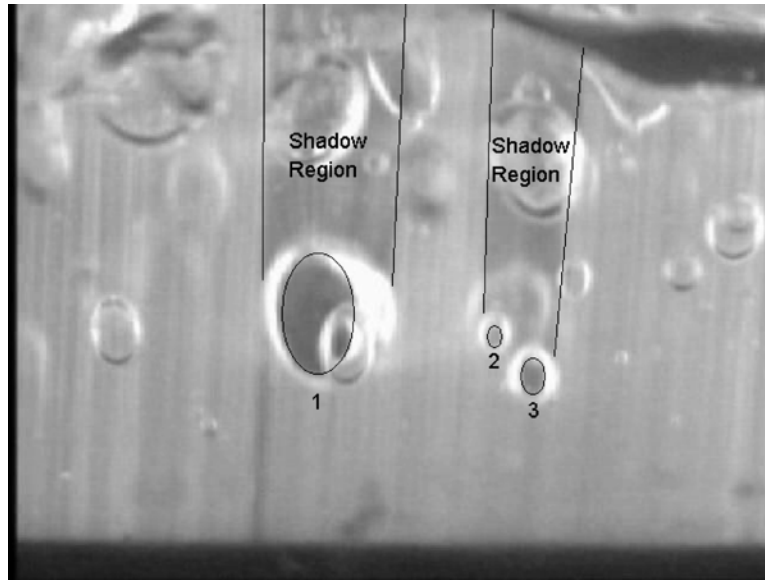


Figure 3.5: PLIF image of stratified flow. Three dark spots and the corresponding shadow regions have been traced for clarity. The positive of the original image is displayed here.

the base film frames (1 mm scale). Note how the structure of the interfacial waves differs for both flow regimes. Definite peaks or crests are observed for the wavy-annular case, while the wave profile is flatter and less structured for the fully annular case.

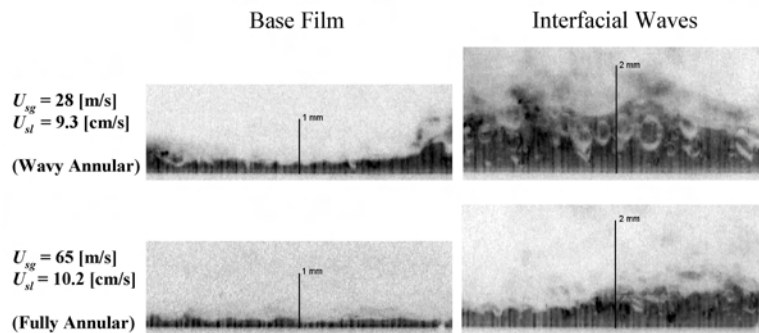


Figure 3.6: Typical cross-cut images obtained with the PLIF technique for the wavy-annular and fully annular flow regimes. The negatives of the original images are displayed here. Flow direction is from right to left.

A significant number of large bubbles is entrained by the interfacial waves in the wavy annular regime. The interfacial wave in the fully annular regime contains fewer and smaller bubbles. The larger bubbles within interfacial waves experience breakup due to shear, pro-

ducing the smaller bubbles present in the base film. The diameter of largest bubbles remaining within the base film rarely exceeds the base film thickness as documented in § 2.2.1.

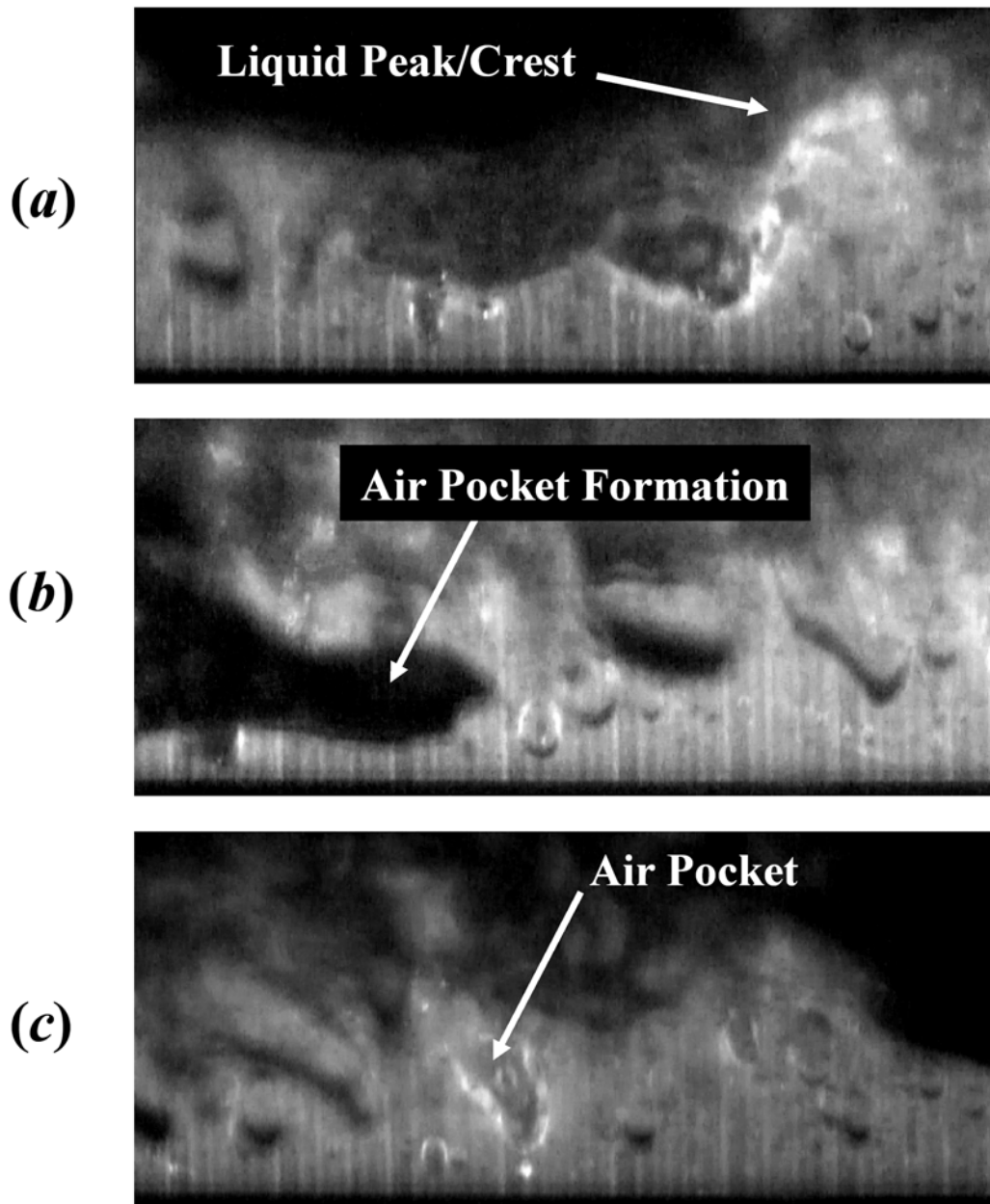


Figure 3.7: Three stages of the folding action mechanism. (a) formation of liquid peak/crest, (b) folding of peak around air pocket and (c) entrained air pocket. The positives of the original images are displayed here. Flow direction is from right to left.

Two mechanisms are plausible sources of bubble entrainment. The entrainment of air

by droplet impacts is a mechanism that has been observed by many researchers and is fully acknowledged by the author. However, §2.2.3 shows that the bubble number concentration ranges from 10 to 100 counts per  $\text{cm}^2$  of imaged area, while droplet impacts are observed to occur only once or twice per  $\text{cm}^2$  of imaged area over a wide range of flows. Thus, a second entrainment mechanism is contemplated by the present study, which is directly associated with interfacial waves. The proposed folding action mechanism, consisting in peaks or crests that entrap pockets of air when folding onto the bulk liquid, is illustrated by the interfacial wave images in Figure 3.7. The three stages do not correspond to an actual time sequence of events. The three frames in Figure 3.7 were hand selected from a single batch of images to illustrate the proposed mechanism. Obtaining an actual sequence of events requires proper synchronization of the laser pulses with the frame rate of a high speed camera.

The information provided by the cross-cut images is most valuable when displayed in a matrix of  $U_{sg}$  vs.  $U_{sl}$  settings spanning from the transition from stratified (or dryout) to wavy-annular flow, up to fully annular flow regimes. For each of the 68 flow settings, images from the top, side and bottom circumferential locations describe the asymmetric nature of horizontal annular flow. The arrangement of the top, side and bottom cross cut images in the charts, as well as the setup orientation for each location are explained in Figure 3.8. Separate charts were created for interfacial wave and base film information (see Figures 3.9 and 3.10). The interfacial wave chart also includes interfacial wave frequency information for most settings. It should be made clear that each image triad (top, side and bottom) was not captured at the same instant of time since that would require a much more complex setup. Every frame was selected from among many similar video frames as being representative of the mean interfacial wave or base film behavior for each flow setting. It should also be noted that FEP is a hydrophobic material, so it may allow a transition to a stratified/dryout condition more readily than other materials. Thus, the dryout boundary included in the charts should be interpreted as specific for the water/FEP combination.

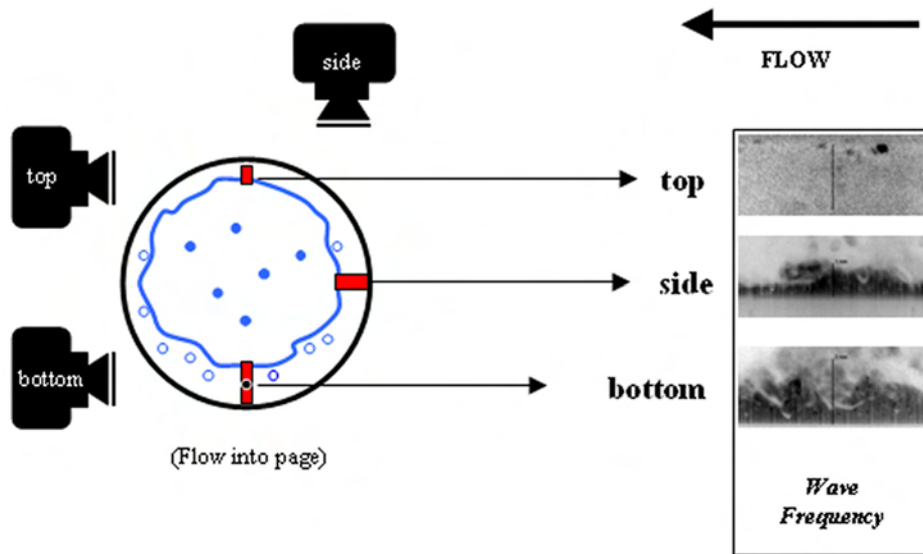


Figure 3.8: Schematic of setup orientation and image arrangements for top, side, and bottom PLIF cross-cuts shown in Figures 3.9 and 3.10.

### 3.3.2 Quantitative PLIF Results

Film thickness measurements were taken for 40 batches of 100 PLIF images each. A batch processing algorithm was implemented using LabVIEW<sup>TM3</sup> and IMAQ<sup>TM4</sup> software. The standard image processing operations used for the present study will only be mentioned or described briefly in the following discussion. Gonzalez and Woods [58] provide detailed information on each of them.

Initial preprocessing cropped the original video frame down to  $630 \times 274$  pixels and converted it to 8-bit grayscale. The histogram was then stretched to enhance contrast. Next, the negative of the grayscale image was produced so that the liquid appeared as dark, while the air and the pipe wall appeared clear. The enhanced contrast helped in the effective detection of the liquid (dark) portions of the image. Only the pixels with the darkest gray levels were selected by the threshold operation. The thresholding of the grayscale image

<sup>3</sup>LabVIEW<sup>TM</sup>, National Instruments<sup>TM</sup>, ©2000

<sup>4</sup>IMAQ<sup>TM</sup> Vision, National Instruments<sup>TM</sup>, ©1999,2000

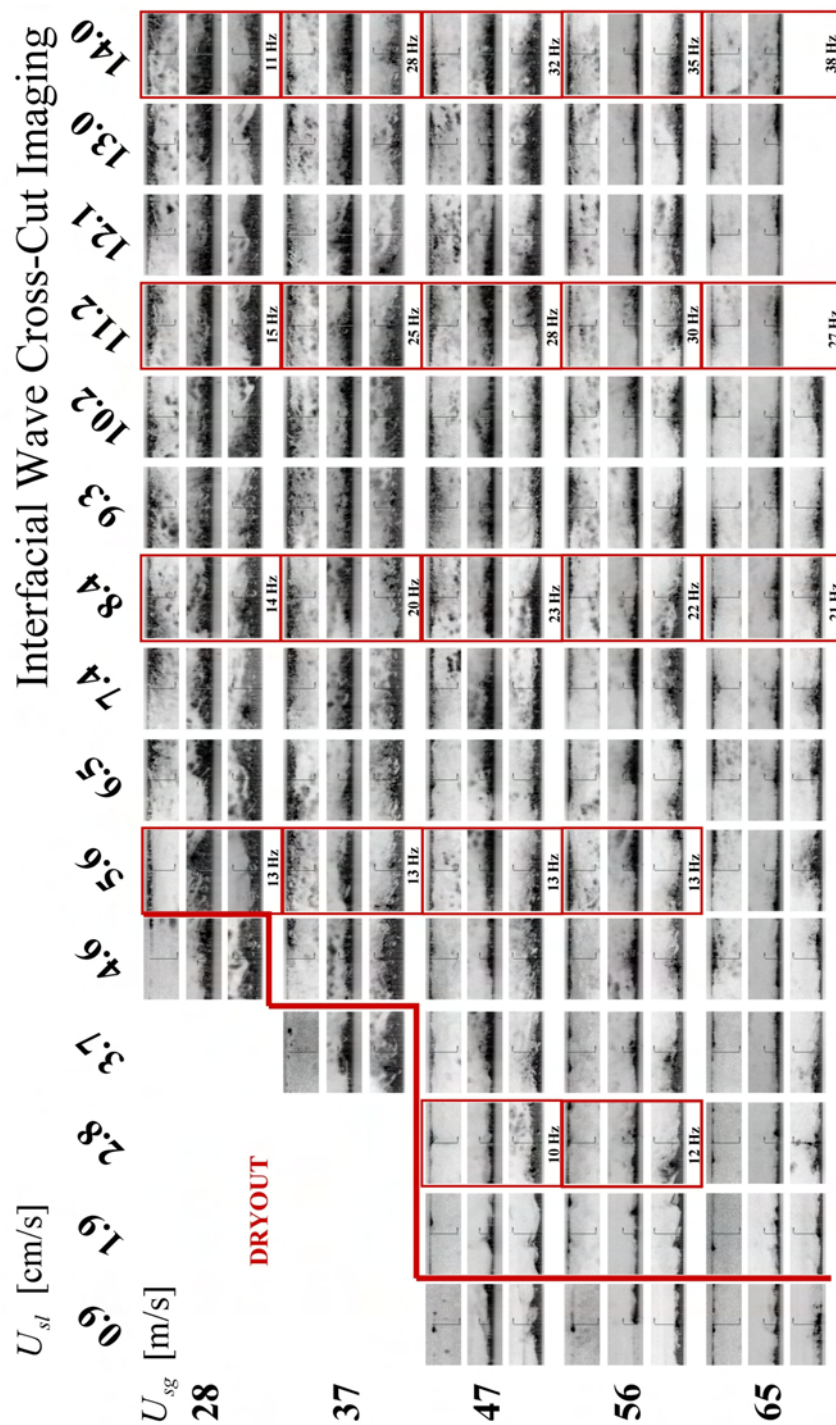


Figure 3.9: PLIF Imaging of Interfacial Waves. Flow from right to left. The scale marks on the bottom and top images represent 2 mm while the scale marks in the side images (center image of each set) represent 1 mm.

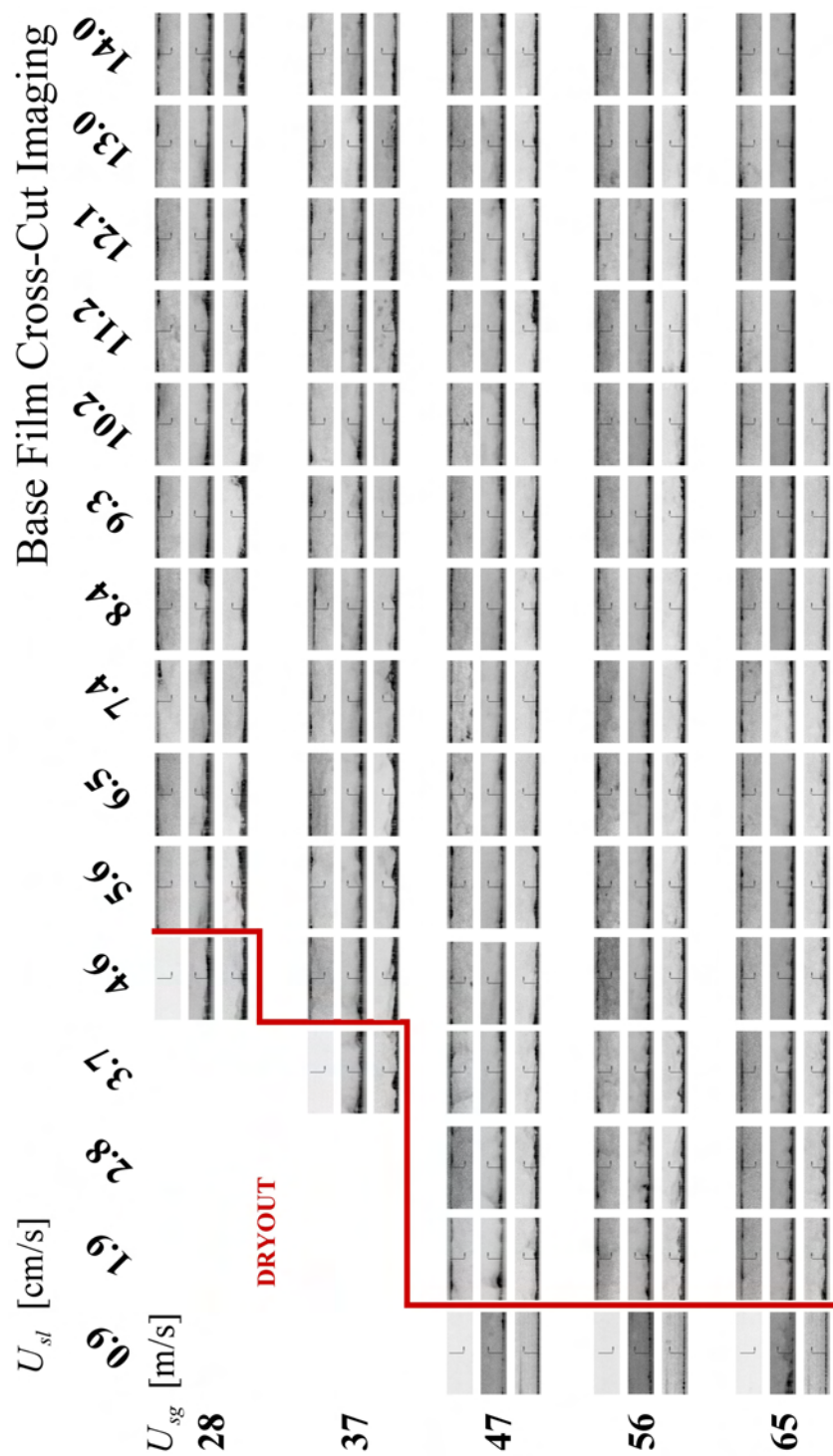


Figure 3.10: PLIF Imaging of the base film. Flow from right to left. The scale marks on all images represent 1 mm.

produced a binary image. Some bubbles near the air/water interface did not appear as fully closed contours. A proper open operation completed nearly closed bubble contours (holes) and a hole fill operation blended those voids into the surrounding liquid. The binary image also included some noise, entrained droplets and liquid filaments that were not part of the liquid film. These unwanted dark pixels were discarded by a particle removal operation. The resulting image was scanned along each vertical line of pixels in order to detect the location of the interface at every horizontal location. Film thickness was then determined as the perpendicular distance from every sample point at the interface to the manually determined baseline. From each video frame, 630 film thickness samples are obtained; a total of 63,000 per batch.

It was critical that the location of the pipe wall was detected very accurately since this line was used as a baseline for all the film thickness measurements. Not all batches can share a single baseline since small rotations of the camera around the lens axis with respect to the pipe were likely to occur. After comparing images of the flooded pipe fluorescence against images obtained under conventional illumination, it was determined that reflections of the fluorescent liquid at the tube wall hide the true location of the baseline. Thus, the processing for each batch required manual input of the true baseline intercepts. Since the camera and the laser were not synchronized, there was noticeable variation in brightness and contrast among the frames of a single batch despite the stretching of the histogram. Maximum reliability in locating the air/water interface also required setting the upper threshold limit for each frame by hand. The threshold values and the baseline intercepts were stored for accelerating the repeated processing of a given batch.

The magnification of the imaging system is not large enough for diffraction to dominate the uncertainty of the measurements. The manual determination of the threshold level and the manual baseline location were the largest sources of error in measuring the distances on each frame. The error in locating the baseline is estimated as  $\pm 24.6 \mu\text{m}$  ( $\pm 3$  pixels). Since

the baseline was constant for all frames in a given batch, the averaging of 100 frames does not affect this source of uncertainty. The manual threshold also introduced an uncertainty estimated as  $\pm 24.6 \mu\text{m}$  ( $\pm 3$  pixels) for each frame. Nevertheless, the uncertainty introduced by the threshold varies in a random manner from frame to frame so that the averaging over 100 frames effectively reduces this source of uncertainty by  $\frac{1}{\sqrt{100}}$ . The overall uncertainty for batch film thickness results is therefore estimated as  $\pm 27.1 \mu\text{m}$ .

Figure 3.11 shows three stages in the progress of the image processing for two sample frames. The sample frames were selected among images from the bottom of the tube since they have more interesting features than the images from the top and side circumferential locations. The frame processed in column (a) was obtained at  $U_{sg} = 56 \text{ m s}^{-1}$  and  $U_{sl} = 4.6 \text{ cm s}^{-1}$ . The frame processed in column (b) was obtained at  $U_{sg} = 28 \text{ m s}^{-1}$  and  $U_{sl} = 4.6 \text{ cm s}^{-1}$ . Stage (i) corresponds to the original grayscale image cropped down to  $630 \times 274$  pixels. Stage (ii) corresponds to the result of the manual image threshold. The liquid components of the frame are highlighted as white regions. Voids within the liquid film as well as entrained liquid filaments in the gas core are visible; ellipses were drawn around the liquid filaments on the figure for clarity. Notice that some of the liquid filaments were still included under the threshold highlight. Stage (iii) shows the results of the edge detection along the 630 columns of the frame. The vertical scanning of each column of pixels found both a top and a bottom edge. The thin lines indicated by vertical arrows indicate the vertical location of the highest and lowest points on the detected edges. The film thickness at the highest point was stored as the wave height for the current frame in case the frame is determined to be a wave frame according to the critical standard deviation multiplier criterion explained in the following paragraphs. The particle removal operation has discarded the liquid filaments and the hole filling and proper open operations filled the voids generated by bubbles before reaching stage (iii). These three operations made the detection of the true interface (top edge) possible. Note, however, that the bottom edge does not correspond

to the true location of the tube wall. Instead, the manually determined baseline (i.e., the horizontal line located just above the detected bottom edge) was used as a reference for all measurements in a given batch.

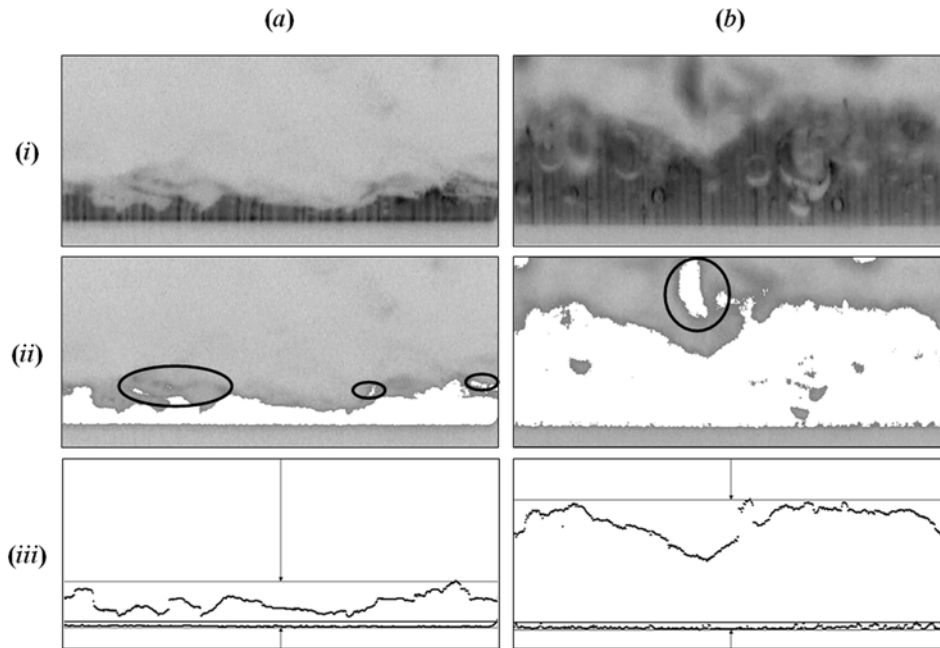


Figure 3.11: Samples of image processing for film thickness measurements. Liquid filaments marked with ellipses on stage (ii). Flow from right to left.

### Mean Film Thickness and RMS Value

The mean film thickness results are plotted in Figure 3.12. Data obtained at similar superficial velocities by [67] and [74] are included for comparison in the plots. For the side and bottom film thickness data obtained in the present study, there is a clear trend for decreasing film thickness as  $U_{sg}$  increases. A definite trend for film thickness variation with increasing  $U_{sl}$  is not observed along the top and the side of the pipe. Along the bottom of the pipe, film thickness increases for increasing  $U_{sl}$ . For the three circumferential locations, the film thickness appears to be independent of  $U_{sl}$  at high  $U_{sg}$  settings. For the data along the top

of the tube, the behavior is more erratic. Dryout conditions may exist along the top at the lower gas flow rates because of the hydrophobicity of the pipe wall. Also, the particle removal step for processing along the top of the pipe was implemented with a more relaxed condition in order to preserve the very thin and discontinuous profiles of the film. Consequently, for some data along the top of the pipe, portions of entrained liquid may have been erroneously detected as the actual film interface. Due to these image processing difficulties no data will be presented for the top of the pipe in the following subsection.

Comparison against the conductance probe film thickness measurements confirms the decreasing trend for film thickness with increasing  $U_{sg}$ . Increased circumferential asymmetry was expected for the larger pipe diameters in which the conductance probe experiments took place. Surprisingly, some of the 32 mm I.D. data (JHW) lie below the 15.1 mm I.D. data. The 50.8 mm I.D. data are thicker for the bottom of the pipe at the lower  $U_{sg}$  but no corresponding thinning of the film along the side and the top of of the pipe is observed relative to the 15.1 mm I.D. data. At the higher  $U_{sg}$  values, conductance probe data from the 32 mm I.D. pipe lie below the PLIF data.

The RMS values are plotted in Figure 3.13. The data along the top of the pipe were affected by entrainment that was not eliminated by the processing, causing the RMS values to be overestimated for that circumferential location. The RMS values for the PLIF data along the side of the tube are larger than the conductance data. This is not true for the bottom, where RMS values are lower for the PLIF data at low  $U_{sg}$  settings. This behavior is in agreement with the usual expectation for increased wave asymmetry inside the larger pipe diameter used for the conductance probe data. The variation of RMS with  $U_{sl}$  is higher for the conductance probe data but the liquid flow rate effect is reduced as  $U_{sg}$  increases. It should be recalled that the conductance probe measurements tend to underestimate wave height at low  $U_{sg}$  values, where the void fraction within waves is high.

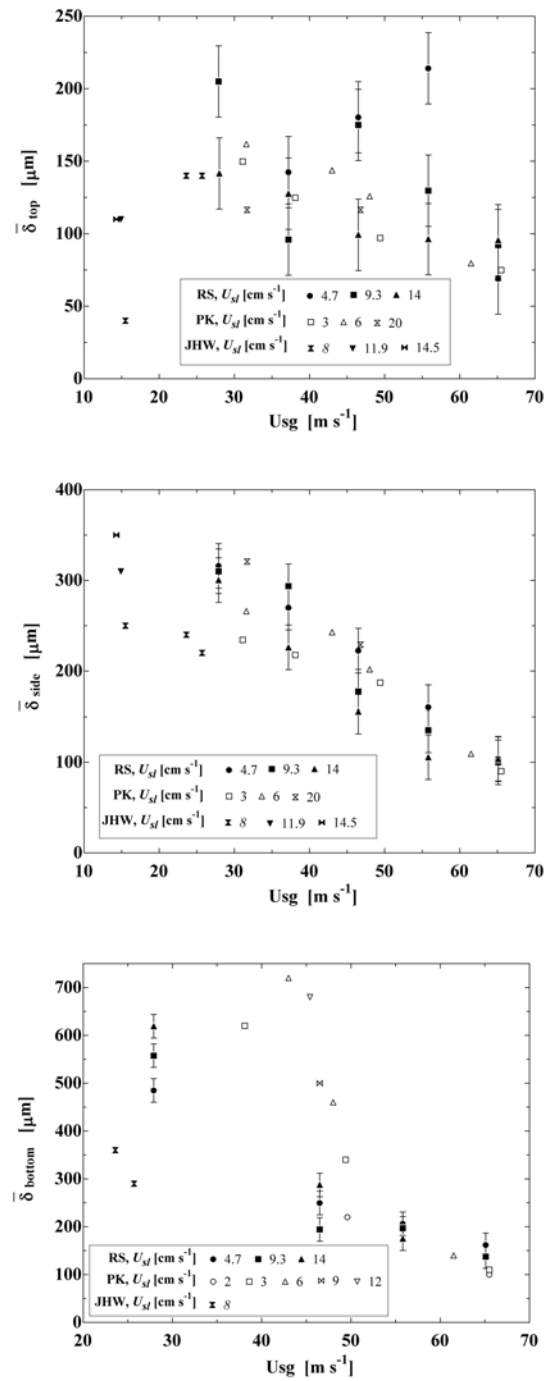


Figure 3.12: Mean film thickness along the top, side and bottom of the pipe. Data by [67] (*PK*) and [74] (*JHW*) are included for comparison against PLIF measurements performed for the current study (*RS*).

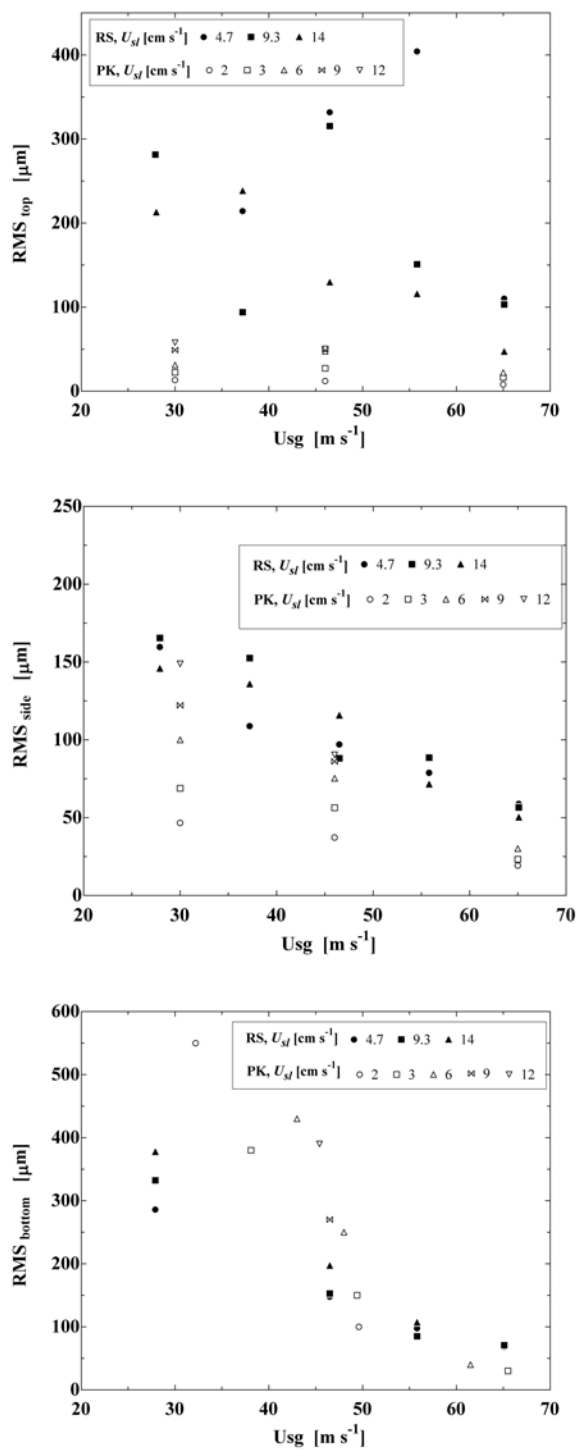


Figure 3.13: RMS values.

## Interfacial Wave Detection

It is physically more interesting to obtain the mean and RMS values of the base film thickness, the mean interfacial wave height,  $\overline{h_w}$ , and the interfacial wave intermittence,  $I$ . A criterion based on the mean and standard deviation ( $\sigma \approx RMS$ ) of the base film thickness was developed in the current study for the automatic detection of interfacial waves. Datapoints below the critical thickness defined by the criterion can be treated in two ways. Under the Non-Wave (NW) hypothesis, all points below the critical thickness were considered to belong to the base film. Under the Skip-Wave (SW) hypothesis, only points belonging to frames with no datapoints exceeding the critical thickness were considered as base film points. Under the latter hypothesis, some datapoints in the batch will necessarily remain unclassified. Under both hypotheses, any film thickness measurement will belong to an interfacial wave if it exceeds a critical thickness,  $h_c$  defined by

$$h_c = \overline{\delta_{NW}} + k_c \sigma_{NW} \quad , \quad (3.4)$$

where  $k_c$  is the critical standard deviation multiplier.

Based on the critical thickness criterion expressed by (3.4), an iterative scheme was implemented for determining the mean and standard deviation base film thickness and the wave height as well as the wave intermittence. Figure 3.14 is a flowchart representation of the iterative scheme. The overall mean film thickness,  $\overline{\delta_{Batch}}$ , and standard deviation,  $\sigma_{Batch}$ , of the entire batch were used as initial guesses. Based on these first guesses, separate arrays containing NW and SW base film data were created. The sorting of arrays is based on the comparison of each film thickness datapoint against  $h_c$ . Arrays contain datapoints for the entire batch, and data buffers were used to temporarily hold data from a single frame. At the end of each individual frame processing sequence, the information contained in frame buffers is appended to batch arrays. At the end of the iterative process, the film thickness

data for the entire batch is sorted into five arrays. A Batch array containing all datapoints, an NW array containing all the non-wave base film data points (NW array  $\subset$  Batch array) and an SW array containing all the skip-wave base film data points (SW array  $\subset$  NW array) were created for each batch of 100 frames. A wave data point array was also created but it does not appear on Figure 3.14 since no statistics are produced from it (wave array  $\subset$  Batch array). Finally, a wave height array containing all the peak thickness values for wave frames was also created (wave height array  $\subset$  wave array). The mean base film thickness under the NW hypothesis,  $\overline{\delta_{NW}}$ , and the corresponding base film standard deviation,  $\sigma_{NW}$ , were used as updates for the initial guesses. Iteration proceeded until no change was detected in the statistics of the NW base film array. An upper limit of 100 iterations was set since no convergence is reached for some of the lower standard deviation multiplier,  $k_c$ , values. Low  $k_c$  values may also lead to the spurious detection of interfacial waves in every frame, which leaves the SW array empty. An empty SW array can only be physically meaningful in annular-wavy regimes where the distinction between ripples and interfacial waves is not very clear. Spurious convergence is also possible for fully annular regimes or flow regimes without interfacial waves, because an infinite set of base film standard deviation guesses produce convergence for a single overall mean. Uniqueness in the solution of the iterative scheme is only granted when the presence of interfacial waves introduces an asymmetry in the number of data above and below the mean base film value. In this latter case, there is a single base film standard deviation value that produces convergence for a given mean base film thickness.

Distinguishing interfacial waves from lower amplitude ripples (i.e. specifying the value of  $k_c$ ) can be a subjective exercise if no further considerations on the nature of interfacial waves is taken into account. Wolf *et al.* [81] refined the classification of interfacial waves into disturbance waves and ephemeral waves, which can add further complexity to the criteria for detecting and measuring interfacial waves. True interfacial waves are turbulent structures

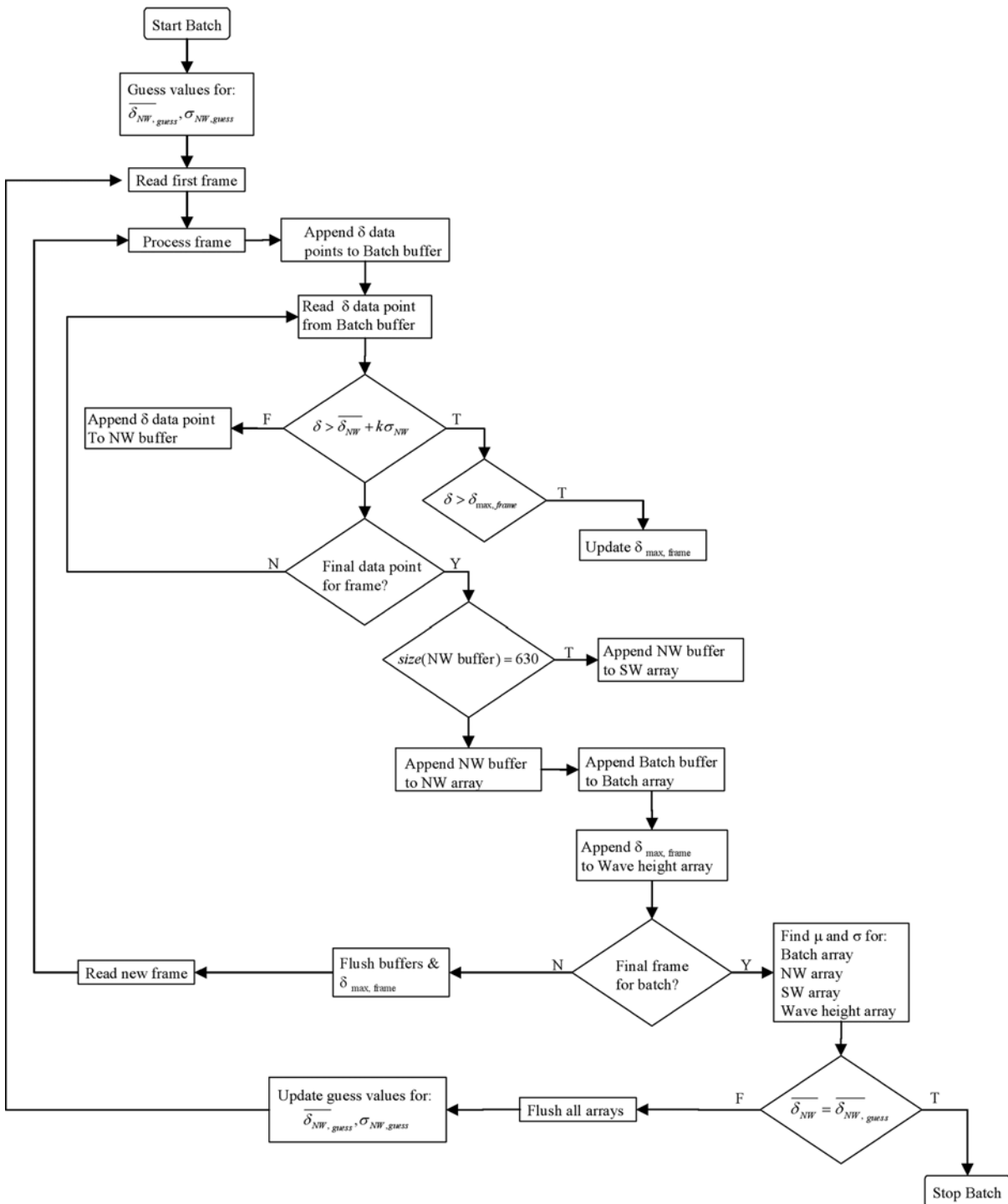


Figure 3.14: Flowchart representing the iterative scheme used in the quantitative processing of the PLIF images.

that travel at a higher velocity than the mean film thickness. The height of interfacial waves, as seen in the sample images, is usually several times greater than the base film thickness. Interfacial wave separation,  $l_s$ , and width,  $l_w$ , can be defined as in Figure 3.15. Intermittency can then be geometrically defined as

$$I = \frac{l_w}{l_s} . \quad (3.5)$$

Wave intermittency data by Paras & Karabelas along the bottom of the pipe varied within a narrow range (0.35–0.45). Intermittency results for the entire PLIF experimental matrix also varied within narrow ranges for any given  $k_c$  setting. Therefore, a match between the average intermittency measured using conductance probes and the average intermittency that results from varying the value of  $k_c$  can be used in narrowing the range for  $k_c$ . Figure 3.16 suggests that a value of  $k_c \approx 1.6$  would produce good agreement along the bottom of the pipe.

A second argument for finding an adequate  $k_c$  if the base film ripples are idealized as sine waves as in Figure 3.15. Then, the relation

$$h_c = \bar{\delta}_b + \sqrt{2}RMS_b \quad (3.6)$$

that defines  $h_c$  as the upper envelope of the base line ripples is exact. An analogy between (3.4) and (3.6) suggests  $k_c = \sqrt{2}$ .

The iterative scheme was run for  $k_c = \sqrt{2}, 1.5, 2, 2.5, 3$ . Figure 3.17 compares PLIF data for the base film thickness under both the SW and NW hypotheses and for the side and bottom of the tube against total internal reflection (TIR) film thickness measurements obtained by Schubring and Shedd [6] using the method developed by Shedd and Newell [7]. The relative deviation (% error) from the optical method shows a decreasing trend with decreasing  $k_c$ . The SW hypothesis fails at the lower  $k_c$  values since every frame contains

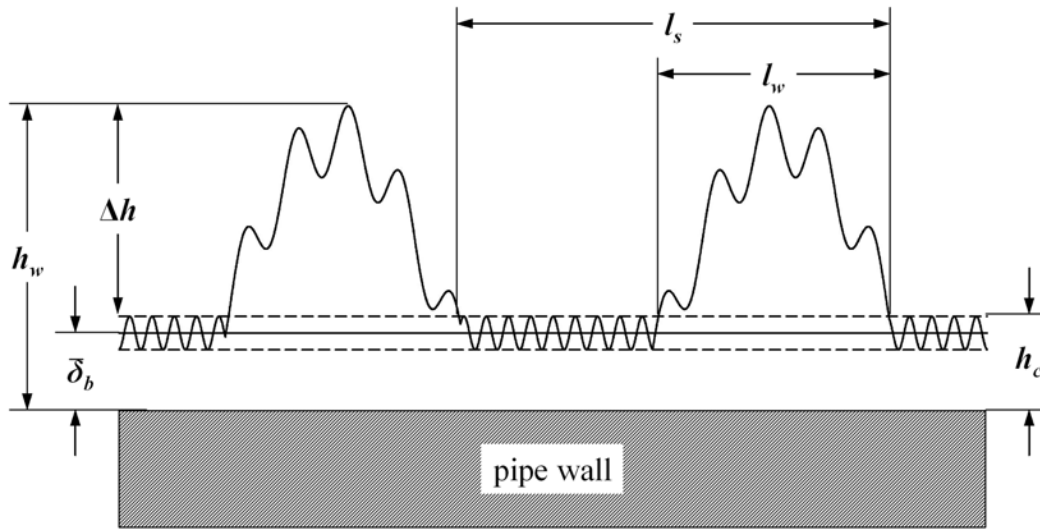


Figure 3.15: Idealized geometry for interfacial waves and the base liquid film.

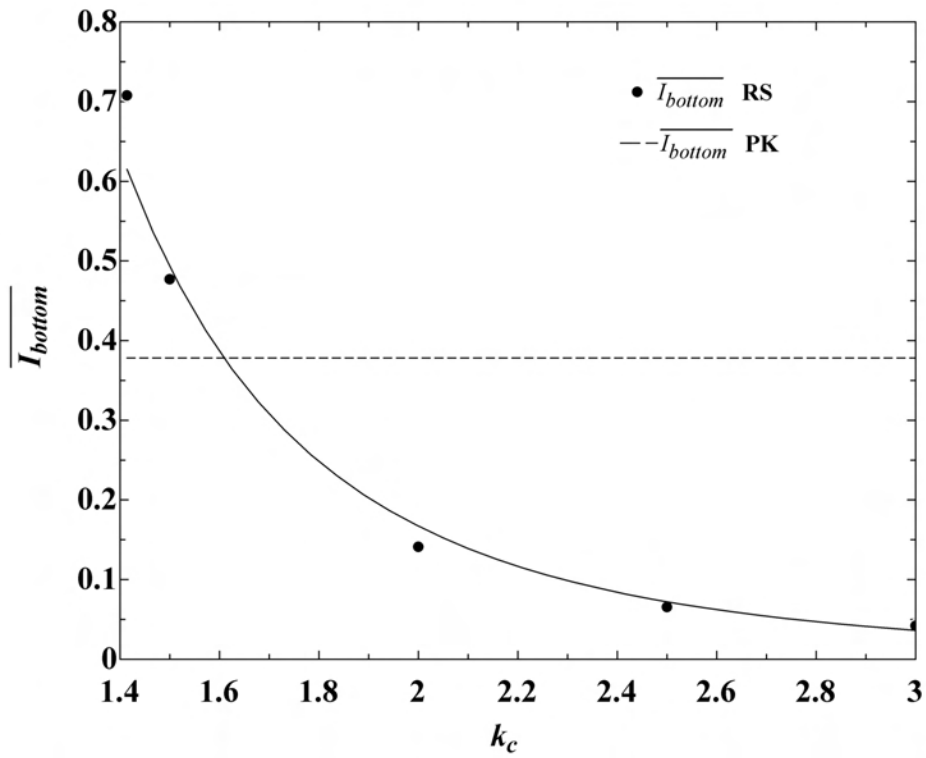


Figure 3.16: Average wave intermittence.

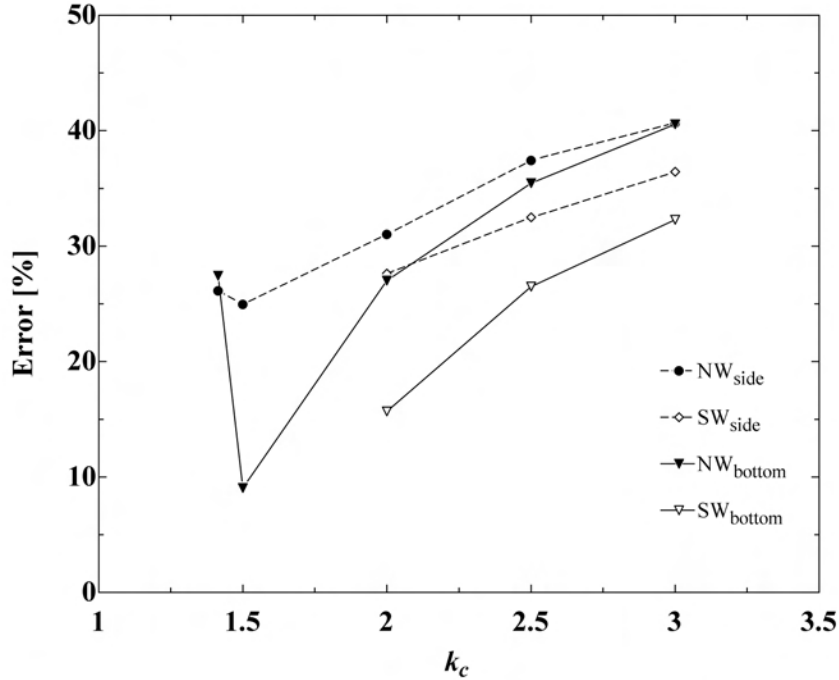


Figure 3.17: Comparison of base film thickness measured by the PLIF method for varying  $k_c$  values against film thickness measurements using the TIR method by Shedd and Newell [7].

an interfacial wave in those cases. However, the NW hypothesis data show that the TIR method effectively rejects waves according to  $k_c \approx 1.5$ .

Waves along the top of the tube are hardly distinguishable from ripples for most flow settings. The same is true for the side and bottom locations at the higher  $U_{sg}$  (fully annular) regimes. The base mean film thickness,  $\bar{\delta}_b$ , should be defined in these cases as the overall mean film thickness  $\bar{\delta}$ , so there is no need for a  $k_c$  value.

From the above considerations about  $k_c$ , it seems appropriate to present here interfacial wave and base film statistics based on  $k_c = 1.5$ . Mean base film thickness data based on the NW hypothesis,  $\overline{\delta_{NW}}$ , along the side and bottom of the pipe are presented in Figure 3.18. The general decreasing trend in base film thickness is observed for both the TIR and PLIF data sets. There is not a clear trend for the variation with  $U_{sl}$  since the uncertainty cause

the data to overlap. However, it is clear that the base film thickness becomes less dependent on  $U_{sl}$  as  $U_{sg}$  increases. The PLIF measurements of  $\overline{\delta_{NW}}$  along the side of the tube for high  $U_{sg}$  are lower than the ones obtained with the TIR method. This happens because interfacial waves are absent along the side of the pipe for high  $U_{sg}$  settings. When no waves are present, it is no longer meaningful to use the  $k_c$  criterion. Notice that for  $U_{sg} = 65 \text{ m s}^{-1}$  the TIR data along the side of the tube match the PLIF data reported in Figure 3.12. Thus, when no interfacial waves are present, the mean base film thickness detected by the TIR method is the overall mean film thickness,  $\overline{\delta}$ . Base film standard deviation data based on the NW hypothesis,  $\sigma_{NW}$ , along the side and bottom of the pipe are presented in Figure 3.19.

Mean wave height,  $\overline{h_w}$ , data based on the NW hypothesis along the side and bottom of the pipe are presented in Figure 3.20. A decreasing trend in  $\overline{h_w}$  for increasing  $U_{sg}$  is observed. Along the bottom of the pipe,  $\overline{h_w}$  increases for increasing  $U_{sl}$  at the two lower  $U_{sg}$  settings. The wave height data along the bottom of the pipe are compared against conductance probe measurements in Figure 3.21. The larger 50.8 mm I.D. pipe used for the PK data increases the asymmetry of the flow and consequently the observed wave heights along the bottom of the tube are larger than for the smaller diameter pipes. On the other hand, it is encouraging to see that the wave height data from the smaller 32 mm I.D. pipe used for the JHW study follows the trends of the PLIF measurements. Figure 3.22 shows that  $\overline{h_w}$  is linear with the overall RMS value. Therefore, the interfacial roughness is dominated by the interfacial waves when they are present. Note that for  $k_c = 1.5$ ,  $\overline{h_w}$  is lower than the conductance probe data (PK), due to the increased asymmetry of the flow inside the larger pipe. Table 3.3.2 summarizes some relevant average ratios between interfacial statistics measured using  $k_c = 1.5$ . The averaging is performed over all flow settings at each circumferential location. For most of the quantities listed on the table the standard deviations are small enough to suggest geometric similarity among flow settings. These statistics, when interpreted with the aid of the idealized geometry of Figure 3.15 (with  $\overline{\delta_b} = \overline{\delta_{NW}}$ ,  $h_c = \overline{\delta_b} + \sqrt{2}\sigma_{NW}$  and

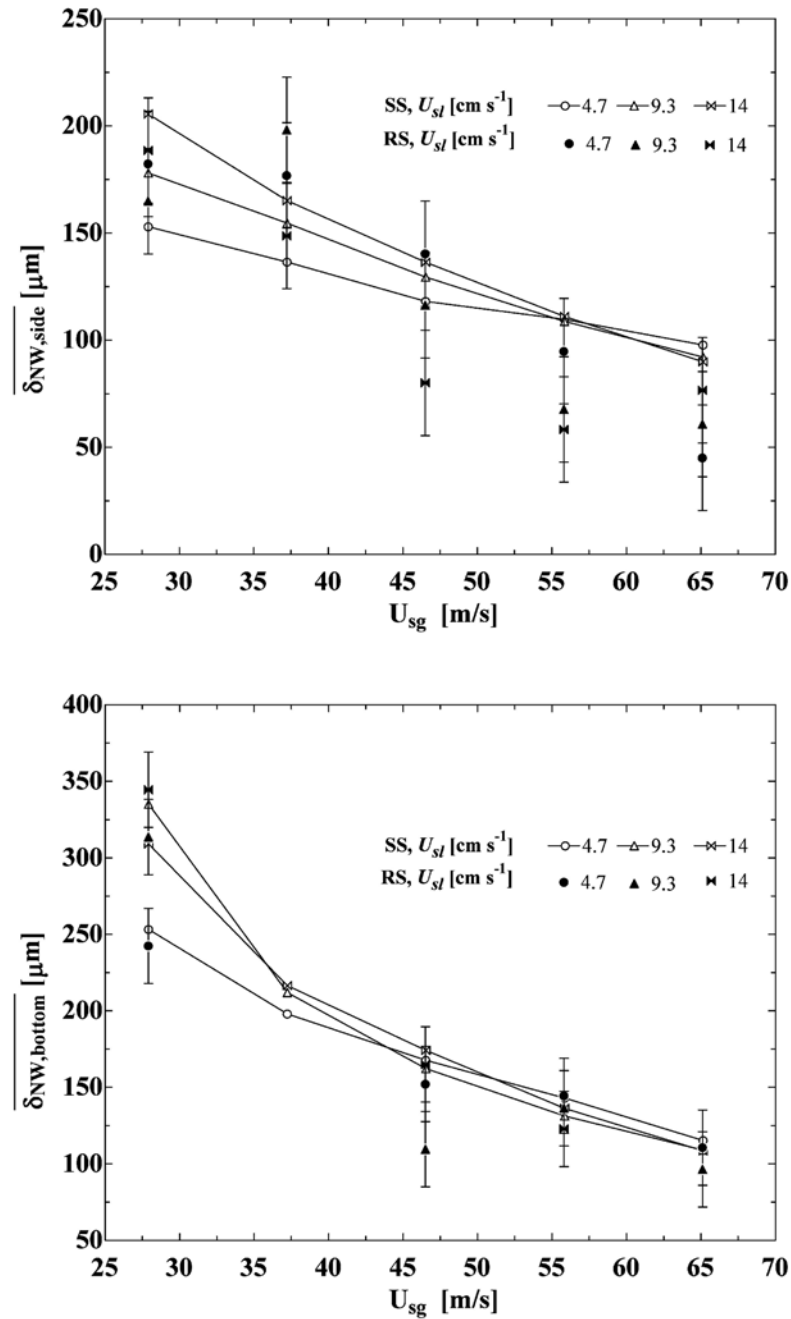


Figure 3.18: Mean base film thickness along the side and bottom of the pipe for  $k_c = 1.5$  (RS). TIR measurements from [6] are also displayed (SS).

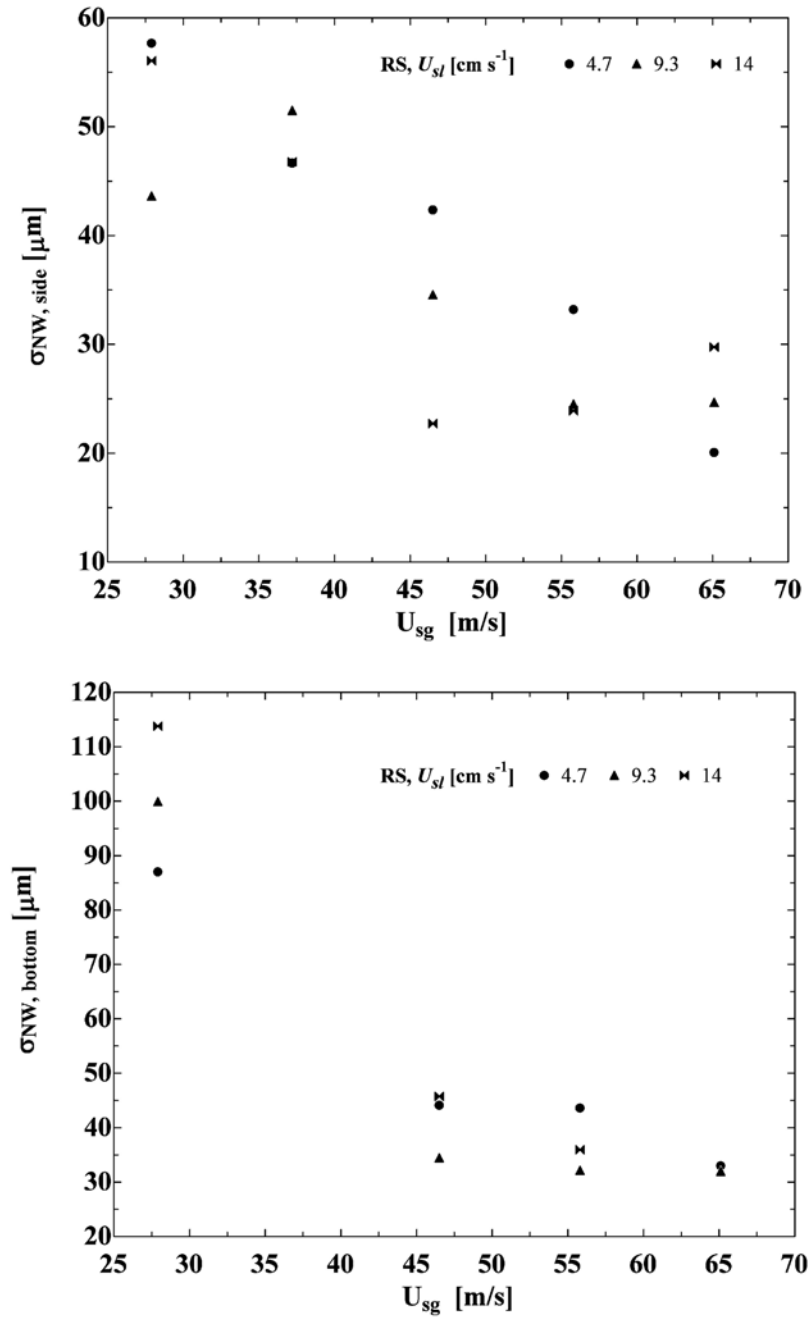


Figure 3.19: Base film standard deviation along the side and bottom of the pipe for  $k_c = 1.5$ .

quantity	$\frac{\overline{h_w}}{\delta}$	$\frac{\overline{\delta_{NW}}}{\delta}$	$\frac{\overline{h_w}}{(\sqrt{2}\sigma_{NW})}$	$\frac{\overline{h_w}}{\overline{\delta_{NW}}}$	$I$
side					
average	1.93	0.60	7.13	3.31	0.52
std. dev.	0.14	0.08	1.15	0.67	0.09
bottom					
average	1.86	0.62	7.02	3.01	0.48
std. dev.	0.09	0.08	0.56	0.30	0.07

Table 3.1: Length proportions for the idealized interface based on  $k_c = 1.5$ .

$I = l_w/l_s$ ) give a better understanding of the relative proportions of the interfacial features, regardless of the specific  $U_{sg}$  and  $U_{sl}$ . Interfacial geometric similarity among circumferential locations or pipe diameters could be further investigated in future studies.

### 3.4 Discussion

The application of the PLIF technique to film thickness measurements proved to be successful in several ways. These measurements provide a better qualitative understanding of the interfacial geometry as well as visual documentation of events like gas bubble entrainment and droplet entrainment. For instance, conductance and capacitance probe studies usually assimilate the slope of the time traces to the actual geometry of waves. This assumption is often a flawed interpretation of the instrument's readings since a wide variety of wave front shapes can produce identical probe readings. Direct observation of the film cross-cut images eliminates any geometrical ambiguity as long as the depth of field is made thin enough. Also, the existence of a high void fraction within the film does not affect PLIF film thickness measurements. It should be kept in mind that all the wave height and base film measurements depend on the choice of  $k_c$ . Three different arguments were presented for the choice of  $k_c = 1.5$ . The analytical argument based on the sinusoidal ripples on the base film is perhaps the strongest argument. The other argument depend on the interpretation

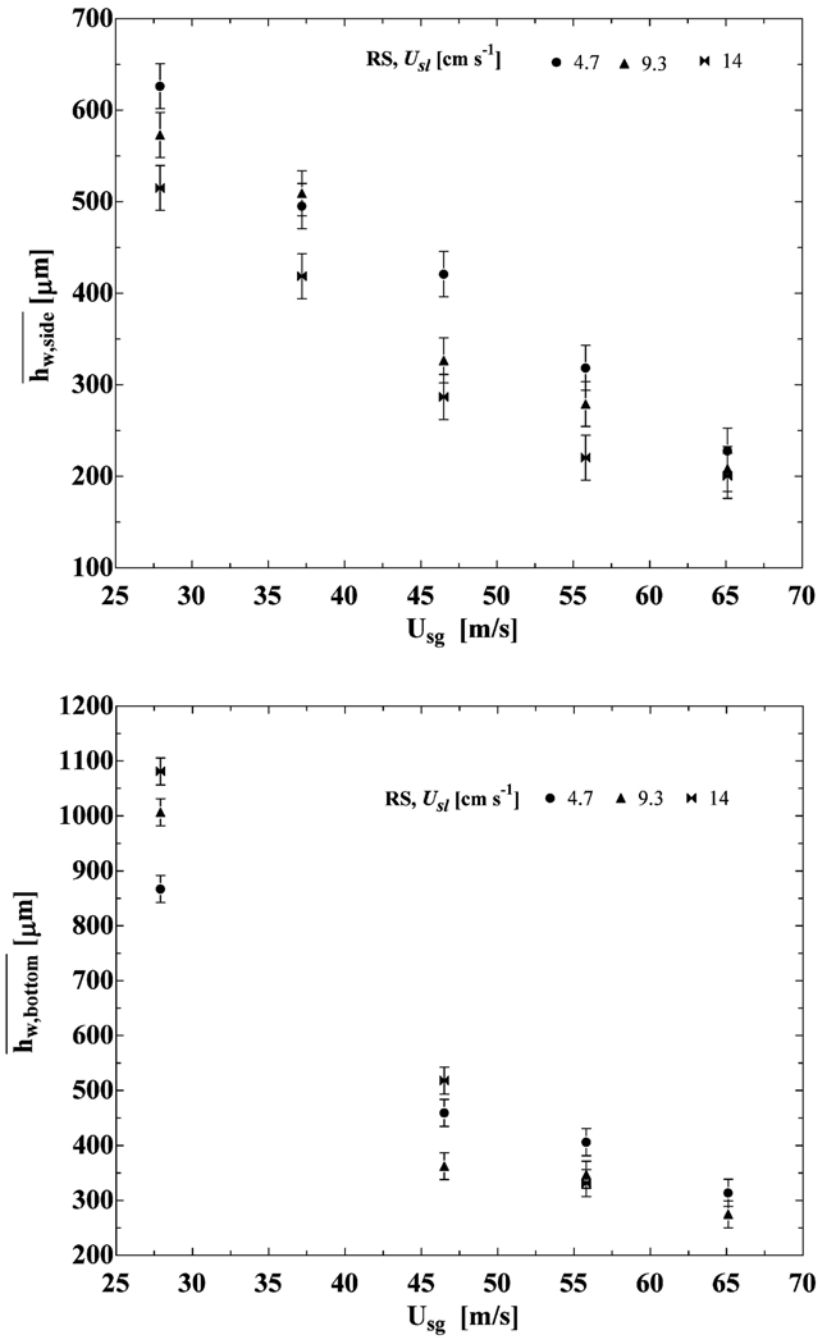


Figure 3.20: Mean wave height along the side and bottom of the pipe for  $k_c = 1.5$  (RS).

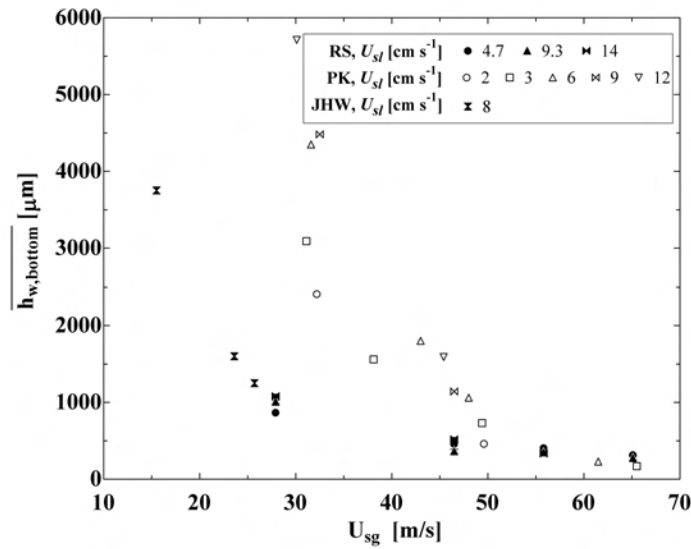


Figure 3.21: Comparison of mean wave height along the bottom of the pipe against conductance probe data. Data by [67] (*PK*) and [74] (*JHW*) are included for comparison against PLIF measurements performed for the current study (*RS*).

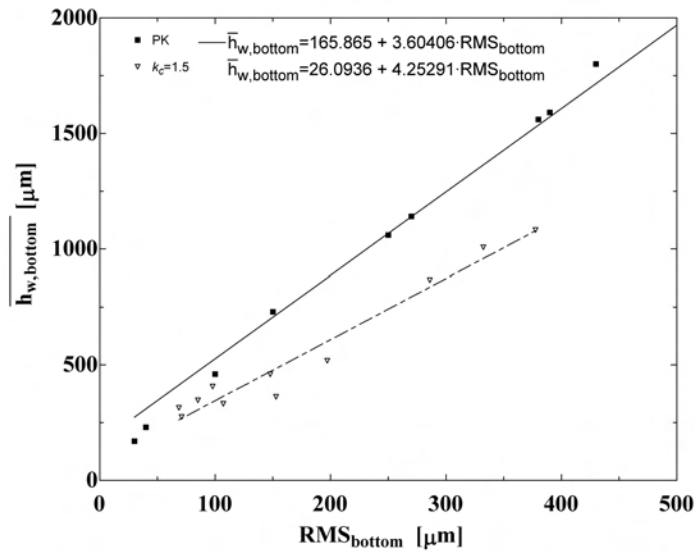


Figure 3.22: Mean wave height vs. RMS along the bottom of the pipe. Data by [67] (*PK*) are included for comparison against PLIF measurements performed for the current study (*RS*).

of the physical meaning of readings from alternative film thickness measurement techniques. Even if the choice of a specific value for  $k_c$  is avoided, the iterative scheme can be applied using different values to explore the physical meaning of the output of other film thickness measurement techniques. For example, the comparison of the PLIF mean base film thickness data against the TIR data suggest that the latter technique filters out interfacial wave data points according to  $k_c \approx 1.5$ .

The geometrical similarity suggested by the average proportions presented in Table 3.3.2 together with the measurements of wave height, mean base film thickness and base film standard deviation can be used for validating annular flow models that couple the gas/vapor core model and the liquid film model through the calculation of an interfacial shear. This interfacial shear is based the interfacial roughness. In the past, this interfacial roughness has been calculated based on correlations that relied on limited empirical measurements. This impact of the PLIF data upon annular flow modeling is discussed in Chapter 4.

The significant uncertainty in the quantitative results can be reduced if the resolution of the imaging setup is increased. A perfect match in indices of refraction or the use of a rectangular test section can further reduce the spatial uncertainty of near-wall measurements. Diffraction limited spatial resolution provides the ultimate boundary for the uncertainty of the measurements. Adequate seeding of the liquid can extend the applicability of the PLIF technique to perform cross-cut micro-PIV measurements. This possibility is further discussed in Chapter 6.

Unlike some of the conductance probe data cited in § 3.1, the PLIF data in this study are not suitable for spectral analysis because the slow frame rate of 30 Hz and the lack of synchronization do not allow for the capture of a continuous time series of data. Instead the slow, unsynchronized system effectively performs a random spatial sampling. The use of a synchronized high speed imaging system on an otherwise identical experimental setup would allow spectral analysis. The required high speed frame rate for an interfacial velocity

estimated at  $3 \text{ m s}^{-1}$  is approximately 580 Hz at the current frame size of  $630 \times 274$  pixels and spatial resolution of  $8.2 \text{ } \mu\text{m pixel}^{-1}$ . However, the light scattering measurements by Schubring and Shedd [6] perform spectral analysis for an identical flow loop and similar flow conditions to the ones established for the PLIF measurements.

# Chapter 4

## Interfacial Roughness and Pressure

### Drop Modeling

#### 4.1 Background

The goal of phenomenological (mechanistic) modeling is to replace strictly empirical correlations that have traditionally exhibited a limited ability to predict new situations. Current progress in phenomenological annular flow modeling relies on better measurements of void fraction, film thickness, liquid and gas entrainment fractions, as well as liquid and gas mean velocity profiles and turbulence. The enhanced characterization of the interface presented in Chapter 3 suggests some potential improvements in pressure drop modeling. Some models for annular flow pressure drop use an interfacial shear to couple the liquid film and gas core force balances. The Owen and Hewitt [52] model, for example, uses an interfacial friction factor based on Nikuradse's single-phase rough pipe flow equation. Thus, the liquid film/gas core interface is treated as a fully rough surface. The specification of this roughness was accomplished by them using a correlation of empirical data for the liquid behavior obtained with conductance probes. An implementation of the Owen-Hewitt model using pressure drop data as an input can be used instead to obtain interfacial roughness estimates derived from empirical correlations as an output (Run mode 1 in §4.2.4). PLIF interfacial roughness measurements can then be used for assessing the validity of interfacial roughness correlations used in pressure drop modeling. Conversely, a mismatch between the predicted and

the measured pressure drop with the PLIF data used as a roughness input may indicate a more fundamental flaw in the modeling of pressure drop as an effect of interfacial roughness alone (Run mode 2 in §4.2.4).

## 4.2 Implementation of the Owen-Hewitt Model

The Owen-Hewitt model is intended for application to vertical annular flow. Thus, the complexities of horizontal annular flow asymmetry are not included. Because of this limitation, comparisons should preferably be performed against horizontal measurements in the fully annular regime, where asymmetry is reduced and inertial forces dominate over gravity. Interfacial roughness comparisons in particular should account for the horizontal flow asymmetry by performing an adequate circumferential averaging of the roughness features. The equations from the Owen-Hewitt model are summarized below with the original nomenclature preserved where possible.

### 4.2.1 Liquid Film Model

The Owen-Hewitt model consists of two sub-models. The first one is a liquid film sub-model that is analogous to the triangular relationship as described by Hewitt and Hall-Taylor [82]. The triangular relationship specifies that for fixed fluid properties and pipe diameter, four other quantities remain as system unknowns. These unknowns are liquid film flow rate, liquid film thickness, total pressure gradient and interfacial shear stress. Since the interfacial shear stress can be calculated from a momentum balance for the gas core, three unknowns remain. In general, any specification of the relationship among these three unknowns constitutes a triangular relationship. The Owen-Hewitt liquid film sub-model requires the local axial pressure gradient,  $\frac{\partial P}{\partial z}$ , and the interfacial shear stress,  $\tau_i$ , as inputs. The Von Kármán universal velocity profile is assumed within the base film. This assumption allows for a

straightforward integration (not presented in the original Owen-Hewitt paper) of the non-dimensional liquid film mass flow rate,  $\dot{m}_{LF}^+$ , in terms of the non-dimensional (wall units) base film thickness,  $\delta^+$ , as

$$\begin{aligned} \dot{m}_{LF}^+ &= 0.5(\delta^+)^2 & \text{for } \delta^+ < 5 \\ \dot{m}_{LF}^+ &= -64 + 3\delta^+ + 2.5\delta^+ \ln \delta^+ & \text{for } 5 < \delta^+ < 30 \\ \dot{m}_{LF}^+ &= 12.5 - 8.05\delta^+ + 5\delta^+ \ln \delta^+ & \text{for } \delta^+ > 30 \text{ ,} \end{aligned} \quad (4.1)$$

where

$$\dot{m}_{LF}^+ = \frac{\dot{m}_{LF}}{\pi D \mu_l} \quad (4.2)$$

and

$$\delta^+ = \frac{u^* \rho_l \bar{\delta}_b}{\mu_l} \text{ .} \quad (4.3)$$

The friction velocity,  $u^*$ , is defined within the context of (4.3) in terms of the average liquid film shear stress,  $\tau_{avg}$ , as

$$u^* = \sqrt{\frac{\tau_{avg}}{\rho_l}} \text{ .} \quad (4.4)$$

The liquid film sub-model produces the interfacial velocity,  $u_i$ , as an output.

## 4.2.2 Core Model

The second sub-model represents the behavior of the gas core, and it calculates  $\tau_i$  from the gas flow rate and measurements of liquid entrainment fraction,  $X_{LE}$ . This quantity is defined as

$$X_{LE} = \frac{\dot{m}_{LE}}{\dot{m}_g + \dot{m}_{LE}} \text{ .} \quad (4.5)$$

where  $\dot{m}_{LE}$  and  $\dot{m}_g$  are the entrained liquid mass flow rate and the gas mass flow rate respectively. However, in the current implementation, the measurements of  $X_{LE}$  are replaced by mean base film thickness measurements. A liquid phase mass balance

$$\dot{m}_l = \dot{m}_{LE} + \dot{m}_{LF} \quad (4.6)$$

is used to calculate  $X_{LE}$  from the base film thickness measurements. The interfacial shear is coupled to the pressure gradient via

$$\tau_i = \frac{R_i}{2} \left\{ -\frac{\partial P}{\partial z} - [(\dot{m}_g + \dot{m}_{LE}) / (\pi R_i^2)] \frac{\partial \overline{u_H}}{\partial z} - \rho_H g \right\} , \quad (4.7)$$

where  $R_i$  is the radial distance from the center of the pipe to the base film/gas core interface and  $g$  is the gravitational acceleration, which should not be confused with the subscript nomenclature symbol used for referring to the gas phase. The core mean homogeneous velocity,  $\overline{u_H}$ , and density,  $\rho_H$ , used in (4.7) are defined as

$$\overline{u_H} = \frac{1}{\pi R_i^2} \left( \frac{\dot{m}_g}{\rho_g} + \frac{\dot{m}_{LE}}{\rho_l} \right) \quad (4.8)$$

and

$$\rho_H = \frac{\dot{m}_g + \dot{m}_{LE}}{\dot{m}_g/\rho_g + \dot{m}_{LE}/\rho_l} \quad (4.9)$$

respectively. The gravitational term in (4.7) should be dropped when applying the model to horizontal flow. It is also worth noting here that the term in  $\frac{\partial \overline{u_H}}{\partial z}$  represents the acceleration of the core due to the change in gas density along the axial direction.

The connection between  $\tau_i$  and the friction factor,  $f_i$ , is expressed as

$$f_i = \frac{\tau_i}{\frac{1}{2}\rho_H (\overline{u_H} - \overline{u}_i)^2} . \quad (4.10)$$

The classical Nikuradse equation for single phase pipe flow was modified by Owen and Hewitt by introducing a two-phase Von Kármán constant,  $\kappa_{tp}$ . Experimental data for the gas core velocity profile can be used to obtain empirical correlations for  $\kappa_{tp}$  by using the modified velocity-defect law

$$\frac{u_{max} - u}{u_i^*} = -\frac{1}{\kappa_{tp}} \ln \frac{y}{R_o} , \quad (4.11)$$

where  $u_{max}$  is the maximum axial core velocity,  $y$  is the radial distance from the wall and  $R_o$  is the inner radius of the pipe. The friction velocity,  $u_i^*$ , is defined as

$$u_i^* = \sqrt{\frac{\tau_i}{\rho_H}} . \quad (4.12)$$

The values of  $\kappa_{tp}$  found from experiments are lower than the single phase value of  $\kappa \approx 0.36$ .

The power-law velocity profile

$$\frac{u}{u_{max}} = \left(\frac{2y}{D}\right)^{1/n} , \quad (4.13)$$

which is reasonably accurate except when  $y \rightarrow 0$  or  $y \simeq \frac{D}{2}$  [83], has a smaller value of  $n$  for the two-phase situation. This smaller value of  $n$  results in a center-peaked velocity profile as has been measured in previous works [84–86] and consequently, from (4.11), the value of  $\kappa_{tp}$  is smaller than the single phase value of  $\kappa$ . Since the mixing length,  $l_m$ , is proportional to the Von Kármán constant, the effect of the interfacial features and the entrained liquid droplets is to lower the characteristic mixing length within the gas core. The value of  $n$  can be related to the the friction factor through the expression

$$f \approx \frac{1}{4n^2} \quad (4.14)$$

from Nunner's results [83]. For single phase flow inside smooth pipes,  $6 < n < 10$  for  $4 \times 10^3 < Re_D < 3 \times 10^6$ ; for rough pipes  $4 < n < 5$  [83]. The latter range can be used for

comparison against the results of the present study.

Owen and Hewitt provide a tentative correlation for  $\kappa_{tp}$  based on five data sets from other researchers. That tentative correlation was used for the current implementation.

The re-derivation of Nikuradse's equation by Owen [87] to include  $\kappa_{tp}$  yields the following equation for  $f_i$  in terms of the effective roughness height,  $e_E$ :

$$\sqrt{\frac{2}{f_i}} = \frac{1}{\kappa_{tp}} \ln \left( \frac{R_i}{e_E} \right) + A_r - \frac{1.5}{\kappa_{tp}} + \frac{1}{\kappa_{tp}} \left( \frac{2\bar{\delta}_b}{R_o} \ln \left( \frac{R_o}{\bar{\delta}_b} \right) - \frac{\bar{\delta}_b}{R_o} \right) . \quad (4.15)$$

The effective roughness height is the portion of the interfacial roughness height,  $e$ , that penetrates beyond the viscous sublayer of the core. The interfacial roughness height is specified in the original Owen-Hewitt model using an empirical correlation. The roughness prediction from that correlation or other correlations available in the literature can be compared against the PLIF roughness measurements when pressure drop is used as an input to the model. The traditional form of the single phase Nikuradse equation is

$$\sqrt{\frac{2}{f}} = \frac{1}{\kappa} \ln \left( \frac{R_o}{e} \right) + A_r - \frac{1.5}{\kappa} . \quad (4.16)$$

Comparison between (4.15) and (4.16) reveals that the last term on the right hand side is absent from the original single phase version of Nikuradse's equation and it compensates for the use of  $R_o$  instead of  $R_i$  in (4.11).  $A_r$ , which appears on both versions of the equation is a function of the roughness Reynolds number,  $Re^*$ .  $A_r$  characterizes the transition behavior from a smooth wall to a fully rough interface. The definition of  $Re^*$  for the two phase situation is

$$Re^* = \frac{e u_i^* \rho_H}{\mu_H} \quad (4.17)$$

where

$$\mu_H = \frac{\dot{m}_g + \dot{m}_{LE}}{\dot{m}_g/\mu_g + \dot{m}_{LE}/\mu_l} \quad (4.18)$$

is the definition of the homogeneous viscosity by McAdams *et al.* [88] although it could be substituted by alternative definitions available in the literature [89, 90].

### 4.2.3 Empirical Correlations

The original correlation plots from the Owen-Hewitt model are reproduced here for convenience. A quadratic fit for the  $\kappa_{tp}$  correlation in Figure 4.1 is given by

$$\kappa_{tp} = 0.0918 * Q_{GH}^2 + 0.1186 * Q_{GH} + 0.1391 \quad (4.19)$$

where

$$Q_{GH} = \frac{\rho_g U_{sg}^2}{\rho_H \bar{u}_H^2} . \quad (4.20)$$

Figure 4.2 reproduces the original plot by Nikuradse correlating  $A_r$  in terms of  $\log_{10} Re^*$ . The asterisk over  $A_r$  in this plot is a typographical error in the original document and should be ignored.

Figure 4.3 reproduces the original plots from [52] correlating the roughness height in term of the non-dimensional quantities  $e^*$ ,  $\delta^*$ ,  $We$  and  $Re_{LF}$  given by

$$e^* = \frac{2e}{D} , \quad (4.21)$$

$$\delta^* = \frac{2\bar{\delta}_b}{D} , \quad (4.22)$$

$$We = \frac{\rho_H \bar{u}_H^2 (D - 2\bar{\delta}_b)}{\sigma} \quad (4.23)$$

and

$$Re_{LF} = \frac{G_{LF} D}{\mu_l} \quad (4.24)$$

respectively. Part (a) of Figure 4.3 is used for  $\delta^* > 0.01$ . Part (b) is used for  $\delta^* < 0.008$ . An

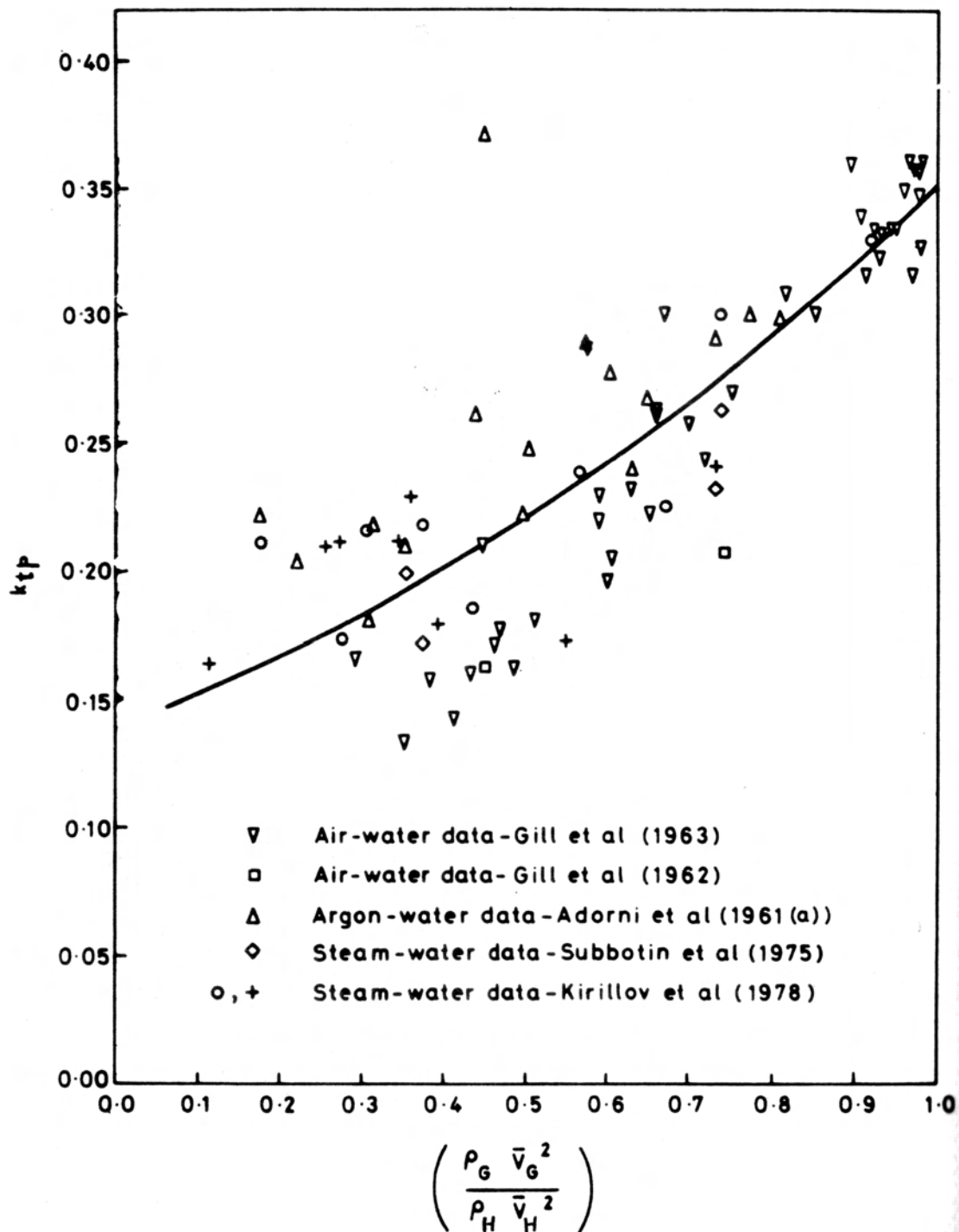


Figure 4.1: Correlation for  $\kappa_{tp}$ . Reproduced from [52].  $\bar{V}_G$  corresponds to  $U_{sg}$  and  $\bar{V}_H$  to  $\bar{u}_H$  in the nomenclature of the present work.

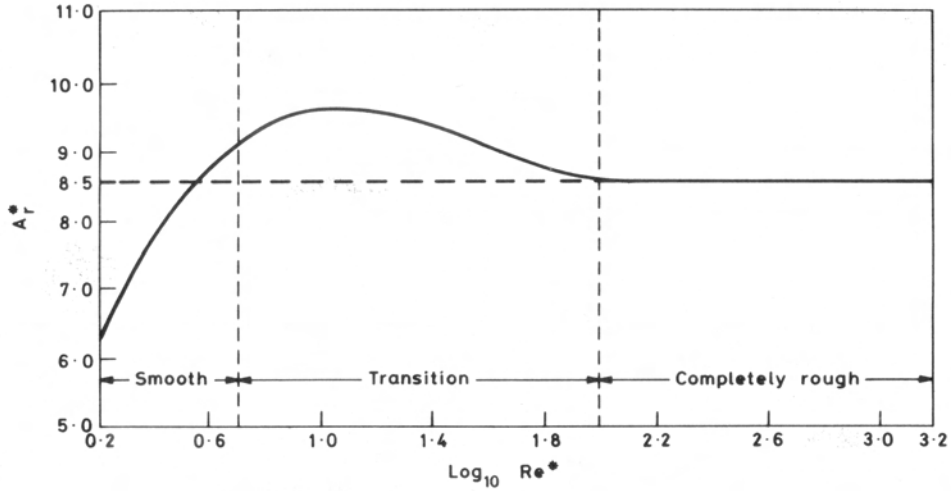


Figure 4.2:  $A_r$  function by Nikuradse. Reproduced from [52].

interpolation of the two correlations is used for the range  $0.008 < \delta^* < 0.01$ .

#### 4.2.4 Modifications to the Original Owen-Hewitt Model

Several modifications were made to the original Owen-Hewitt model described above during the present implementation. First, the base film thickness that is used as an input for both run modes needs to be circumferentially averaged to accommodate the use of horizontal flow measurements in a model that does not include asymmetry effects. Both TIR and PLIF data were used as sources for the base film thickness in the current implementation with little apparent difference between them in the final results. The TIR base film data from [6] were reliable along the top of the tube. Thus the circumferential averaging rule is

$$\overline{\delta_b} = \frac{\overline{\delta_{b,top}} + 2\overline{\delta_{b,side}} + \overline{\delta_{b,bottom}}}{4} . \quad (4.25)$$

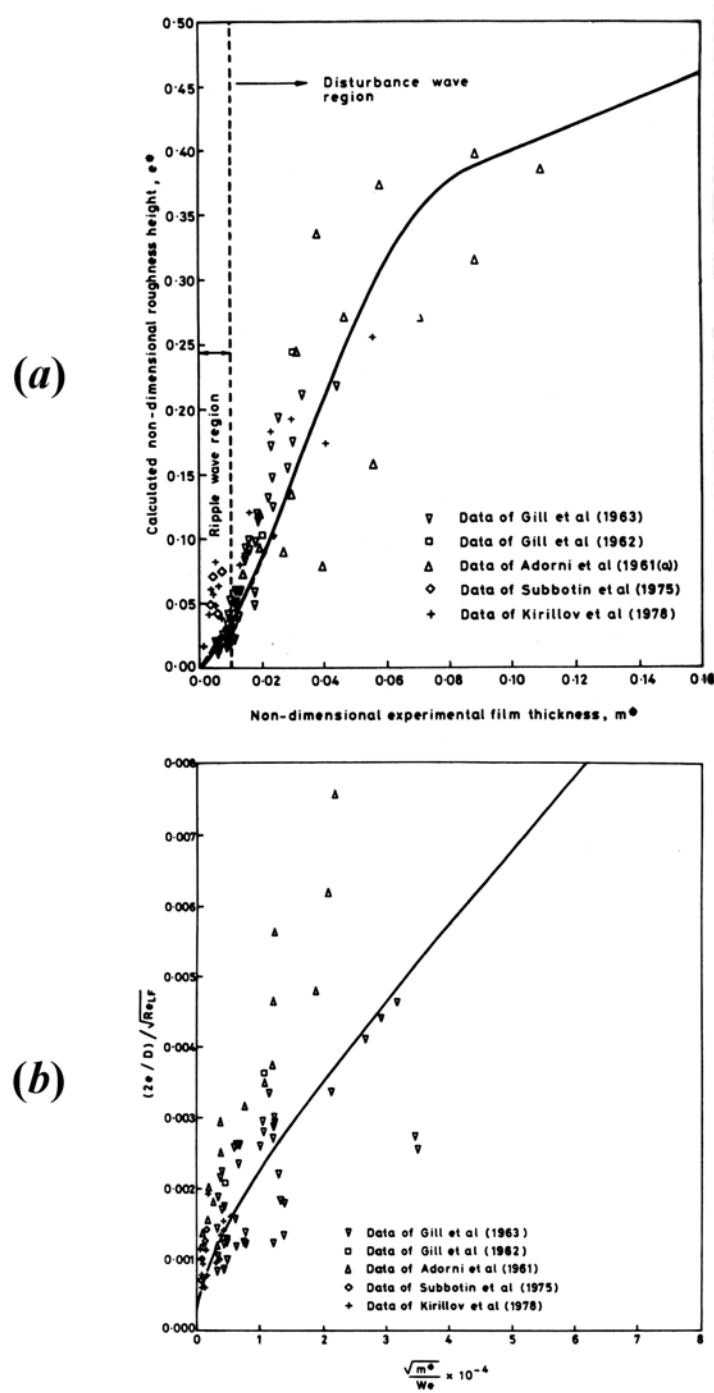


Figure 4.3: (a) low  $\delta^*$  and (b) high  $\delta^*$  roughness height correlations ( $\delta^*$  corresponds to  $m^*$  in the plot notation). Reproduced from [52].

Since the PLIF base film thickness data along the top of the pipe were unreliable (as explained in §3.3.2), the circumferential averaging rule is modified as

$$\overline{\delta_b} = \frac{2\overline{\delta_{b,side}} + \overline{\delta_{b,bottom}}}{3} \quad (4.26)$$

to include only the side and bottom data. Since the film thickness along the top is usually very small for the more asymmetric (low  $U_{sg}$ ) flows, there is very little difference between the two circumferential averaging rules. It should be remembered that the base film thickness measurements replace the liquid entrainment fraction measurements used for the original implementation.

In run mode 1 (RM1), the experimental pressure drop is used as an input and an interfacial roughness height prediction is obtained from the roughness correlations shown in Figure 4.3. The pressure gradient was provided for the current implementation by the measurements by Schubring and Shedd. The core acceleration term in (4.7) is obtained as an output for RM1. Since the roughness correlations couple film thickness and roughness height, any discrepancy between the measured pressure drop and the roughness originated pressure drop is accounted for by the core acceleration term.

Run mode 2 (RM2) uses the experimental roughness height data obtained from the PLIF technique as an input to obtain pressure gradient predictions as an output. The roughness height could be expressed in terms of either the mean wave height (Figure 3.20) or the overall RMS values (Figure 3.13). Both definitions of roughness height are essentially equivalent since the overall RMS value is dominated by the mean wave height as shown by Figure 3.22. However the definition of roughness height in terms of the overall RMS is more robust, since it also covers the flow settings and circumferential locations for which interfacial waves are absent. The definition of roughness height for a given batch,  $e_{Batch}$ , in terms of the RMS

value at any circumferential location is

$$e_{Batch} = 2\sqrt{2}RMS_{Batch} . \quad (4.27)$$

The PLIF RMS data along the top of the tube are more reliable than the PLIF base film thickness data, and they can be included in the circumferential averaging of roughness height.

The resulting circumferential averaging rule is

$$e = \frac{e_{top} + 2e_{side} + e_{bottom}}{4} . \quad (4.28)$$

The core acceleration term was set to zero for RM2 since the goal is to obtain a prediction of pressure drop exclusively attributable to interfacial roughness.

### 4.3 Results

The results for the analysis performed in this chapter are best summarized by plotting several non-dimensional quantities. The plots present data for both the TIR (hollow symbols) and PLIF (filled symbols) base film thickness input. RM1 produces the core acceleration term as an output. Also interesting is the ratio of this term to the experimental pressure gradient input,  $\frac{\partial P}{\partial z}$ , as plotted in Figure 4.4 because it represents the relative importance of components of the measured pressure gradient that are not attributable to interfacial roughness. The ratio of the roughness height predicted by the correlations in Figure 4.3 to the measured PLIF roughness height can be obtained from either run mode. Figure 4.5 shows that roughness ratio for varying  $U_{sg}$  with  $U_{sl}$  as a parameter. A more direct comparison of the roughness height correlation against PLIF roughness data using the same parameters as part (a) of Figure 4.3 is shown in Figure 4.6. Finally, RM2 allows a comparison of the experimental pressure gradient against the predicted interfacial roughness pressure gradient.

Figure 4.7 plots the ratio of both pressure gradients for varying  $U_{sg}$  with  $U_{sl}$  as a parameter. Figure 4.8 shows the variation of  $f_i$  with  $U_{sg}$  with  $U_{sl}$  as a parameter obtained by running the model in RM2. Closely related to  $f_i$  is the power-law coefficient plotted in Figure 4.9.

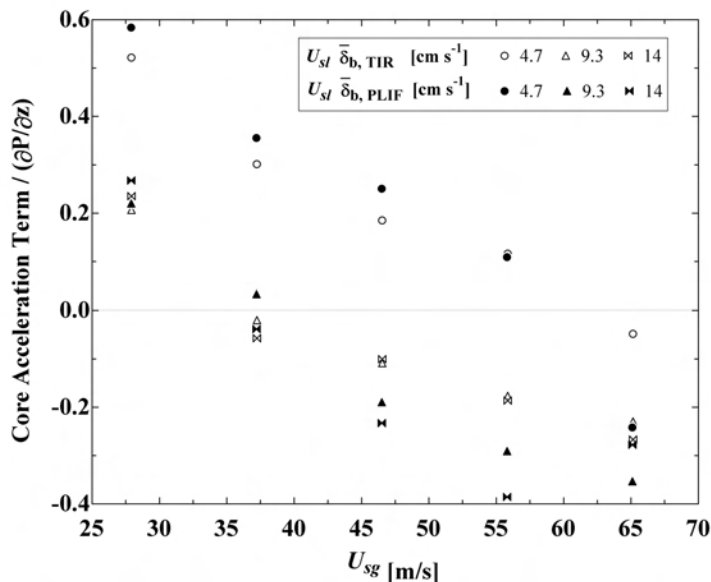


Figure 4.4: Ratio of the core acceleration term to the experimental  $\frac{\partial P}{\partial z}$  value.

Dimensional values of input and output variables for each run mode are shown in Table 4.3 to give an idea of the real magnitudes of the quantities involved in the calculations for a single  $U_{sg}$  and  $U_{sl}$  combination. It should be noted that the flow settings for the sample runs shown in this table are atypical in the sense that the pressure gradient is overpredicted for RM2. This overprediction happens only for the flows at  $U_{sl} = 4.7 \text{ cm s}^{-1}$ . Also notice that  $n$  is within the expected range for rough tubes, indicating a center-peaked profile, and that  $\kappa_{tp}$  is lower than the single phase value of  $\kappa$ , as expected. The liquid entrainment fraction,  $X_{LE}$ , is rather high, since it is forced to include liquid that actually travels as disturbance waves.

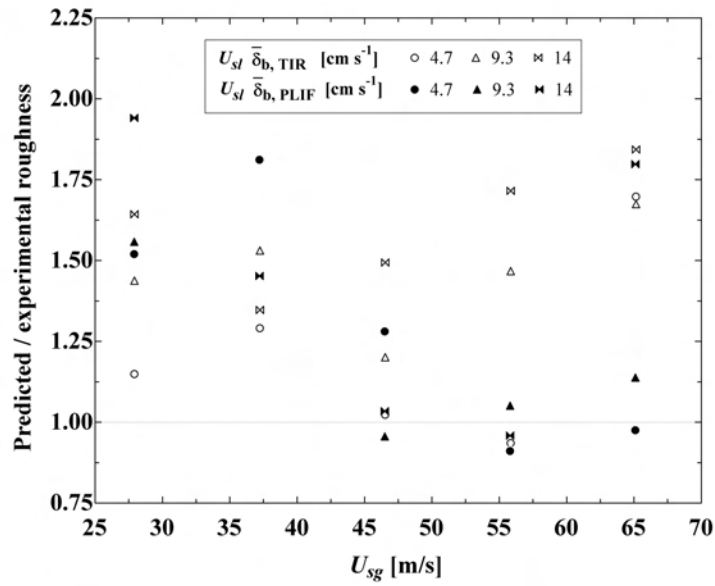


Figure 4.5: Ratio of the predicted roughness height to the experimental PLIF roughness height.

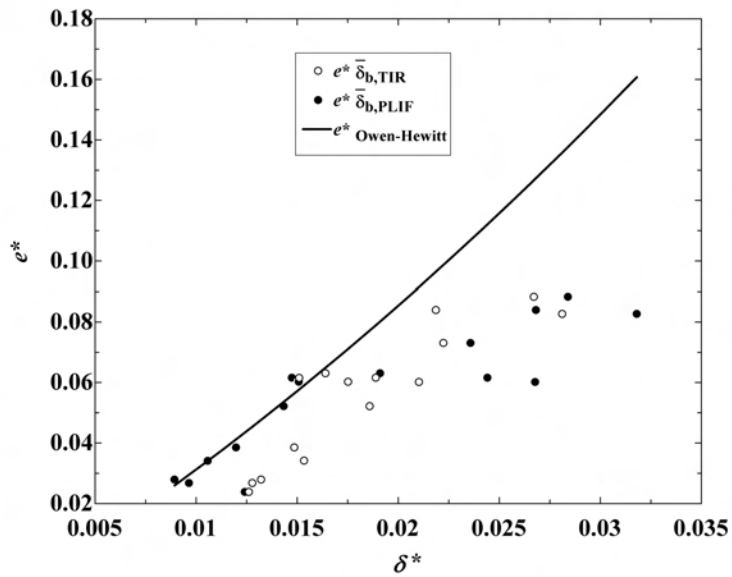


Figure 4.6: Comparison between the non-dimensional roughness height correlation from Figure 4.3 and experimental PLIF data.

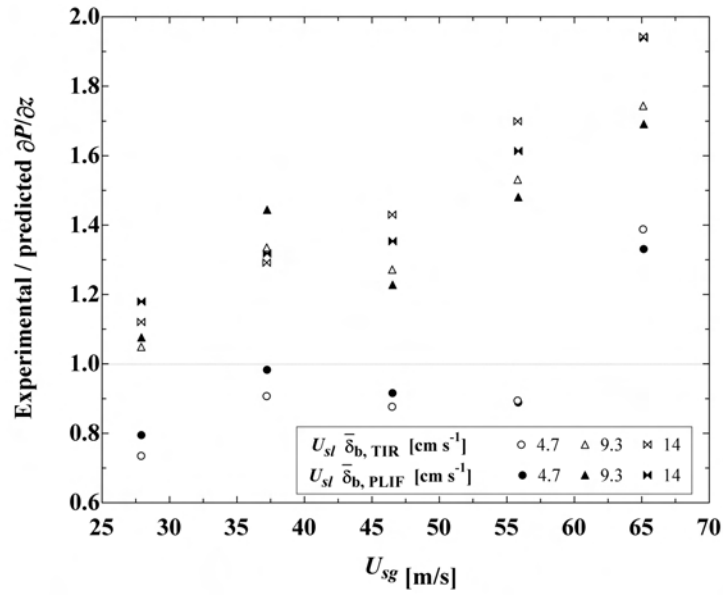


Figure 4.7: Ratio of experimental pressure gradient to predicted interfacial roughness pressure gradient from RM2.

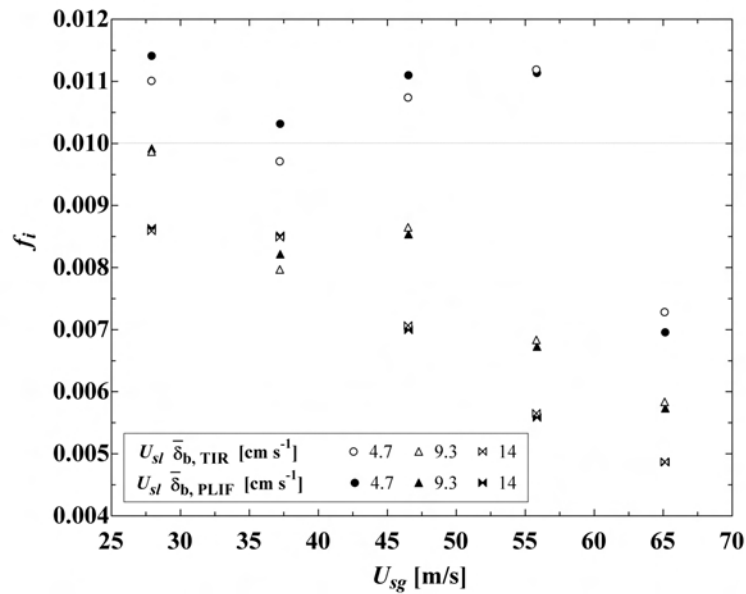


Figure 4.8: Interfacial friction factor from RM2.

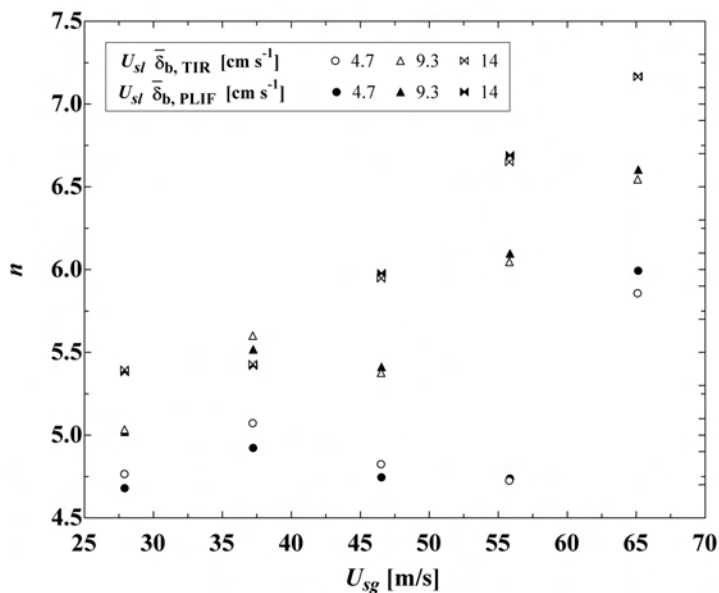


Figure 4.9: Power-law coefficient from RM2.

## 4.4 Discussion

The original Owen-Hewitt paper does not specifically indicate the use of the base film thickness in its equations. However, it does identify the disturbance waves as separate entities. Furthermore, the universal velocity profile assumption is only reasonable when applied to the base film. Since the liquid mass flow rate is only divided between liquid film flow,  $\dot{m}_{LF}$ , and entrained liquid flow  $\dot{m}_{LE}$ , the disturbance waves are tacitly classified as entrained liquid. This classification is not entirely correct because the disturbance waves do not travel at the core velocity. It is also inconsistent with the liquid entrainment measurements that remove the liquid film through a porous pipe section because these included the liquid travelling in disturbance waves as part of  $\dot{m}_{LF}$ . A more rigorous modeling of the liquid flow should treat the disturbance wave flow separately (perhaps considering a disturbance wave liquid flow rate  $\dot{m}_{DW}$ ). Similarly, the significant void fraction that exists within the liquid (Chapter 2) warrants the future inclusion of an entrained gas fraction in the model.

variable	RM1		RM2		units
	value	I/O	value	I/O	
CAT	-861.7	O	0	I	Pa m <sup>-1</sup>
$\delta_b$	123.8	I	144.2	I	$\mu\text{m}$
$D$	15.1	I	15.1	I	mm
$\frac{\partial P}{\partial z}_{\text{experimental}}$	-4648	I	–	–	Pa m <sup>-1</sup>
$\frac{\partial P}{\partial z}_{\text{predicted}}$	–	–	-5072	O	Pa m <sup>-1</sup>
$e_{OH}$	487.6	O	610.2	O	$\mu\text{m}$
$e_{PLIF}$	–	–	476.5	I	$\mu\text{m}$
$f_i$	0.0113	O	0.0111	O	–
$\kappa_{tp}$	0.28	O	0.28	O	–
$n$	4.70	O	4.75	O	–
$P_{abs}$	106.8	I	106.8	I	kPa
$T_g$	293	I	293	I	K
$T_l$	284	I	284	I	K
$U_{sg}$	46.5	I	46.5	I	m s <sup>-1</sup>
$U_{sl}$	4.7	I	4.7	I	cm s <sup>-1</sup>
$X_{LE}$	0.24	O	0.17	O	–

Table 4.1: Input and output variables for both run modes of the Owen-Hewitt model. I/O denotes the input or output status of each variable depending on the run mode (RM1 or RM2). CAT is the core acceleration term value. The sample RM2 run used PLIF base film thickness input while the sample RM1 run used TIR base film thickness input.

The value of the core acceleration term obtained from RM1 (see Figure 4.4) is not negligible in the current implementation since it acts as residual term to compensate for the mismatch between the experimental pressure gradient input and the pressure gradient originated by the interfacial roughness alone. For this reason it is very likely that the value of the core acceleration term in RM1 does not represent the real (often negligible) magnitude of the core acceleration effect.

The *underprediction* of pressure drop from interfacial roughness effects alone suggests that other sources of pressure drop remain unaccounted for in the present model. Disturbance wave formation and acceleration, liquid filament breakup (droplet formation) and droplet acceleration are other momentum transfer mechanisms that could make up for the difference between the experimental pressure gradient and the pressure gradient predicted

from interfacial roughness alone. Figure 4.7 shows that up to 50 percent of the experimental pressure drop could be attributed to these alternative mechanisms of momentum transfer at the highest  $U_{sg}$  setting. There is also a trend for a more severe underprediction as  $U_{sg}$  and  $U_{sl}$  increase, which coincides with an expected increase in droplet entrainment.

On the other hand, at the lowest  $U_{sl}$  setting the pressure drop is *overpredicted* by up to 20 percent at the lowest  $U_{sg}$  setting. In these situations, the real reduction in  $\kappa_{tp}$  could be more severe than predicted by Figure 4.1, creating a lower  $f_i$  than predicted. In addition, it is likely that the alternative momentum transfer mechanisms are less significant for the low  $U_{sl}$  flows, except at the highest  $U_{sg}$  setting where underprediction takes place.

The roughness height correlation in Figure 4.3 could be re-mapped as a correlation for the interfacial friction factor in terms of the mean base film thickness. Several correlations for  $f_i$  in terms of  $\bar{\delta}_b$  are available in the literature [91–93]. Fore *et al.* [94] recently reviewed the development of those correlations and proposed an improved correlation given by

$$f_i = 0.005 \left\{ 1 + 300 \left[ \left( 1 + \frac{17500}{Re_g} \right) \frac{\bar{\delta}_b}{D} - 0.0015 \right] \right\} , \quad (4.29)$$

which incorporates the effect of the transitional roughness behavior ( $Re_g$  dependence) and the effect of the base film thickness. However, it is perhaps more physically meaningful to try to express this correlation in terms of the interfacial roughness instead of the base film thickness, while preserving the Reynolds number dependence. It could also be more meaningful to use the roughness Reynolds number,  $Re^*$ , as defined by (4.17), instead of using  $Re_g$ . In the same paper, Fore *et al.* also perform a more detailed momentum balance that includes a core acceleration term as well as a term that accounts for momentum changes due to the entrainment and deposition of droplets. Additional terms that include the effects of filament breakup and wave formation/acceleration are also conceivable for future modeling efforts.

# Chapter 5

## CFD Simulation of the Sliding Bubble Mechanism

### 5.1 Motivation

Using the knowledge about bubble entrainment acquired in Chapter 2 together with information about saturated flow boiling nucleation site density [63, 64] and some assumptions regarding nucleation site suppression, nucleation site frequency and bubble lifetime, a macroscopic analysis of the viability of the sliding bubble heat transfer mechanism can be performed. However, two fundamental questions remain regarding the microscopic behavior associated with a single bubble entrained in the liquid film or sliding in close proximity to the pipe wall: the localized turbulent enhancement of the heat transfer coefficient for each bubble and the area of pipe affected by the presence of each bubble.

A simple CFD simulation was implemented using FLUENT<sup>TM</sup>5.5<sup>1</sup> to explore, if only in a preliminary way, these microscopic issues. Although experimental verification is still necessary, the numerical simulations can give an idea of the spatial and temporal resolutions required in the experiment to resolve the features of the flow (i.e., the length of the wake, the size of turbulent eddies and the magnitude of the highest velocity gradients in the flow).

---

<sup>1</sup>FLUENT<sup>TM</sup> 5.5, Fluent Inc.<sup>TM</sup>, ©2003

## 5.2 Simulation Setup

### 5.2.1 Simulation Geometry and Mesh

A Couette-like flow with a translating top boundary was used to model the liquid film geometry both in 2D and 3D. In the 2D case, the obstacle (i.e., the bubble) was represented by a round cylinder, while in the 3D case it was represented by a sphere. The obstacle diameter was set at  $15\ \mu\text{m}$ , or approximately 2.9 wall units for the boundary conditions specified in §5.2.2.

The GAMBIT<sup>TM</sup> <sup>2</sup> software was used to generate the mesh. The axial length of the domain, the  $x$  dimension, was 5 mm, and the film thickness, the  $y$  dimension, was  $97.7\ \mu\text{m}$ . The latter dimension is equivalent to 18.9 wall units. For the 3D case, a symmetry plane at  $z = 0$  (bisecting the spherical obstacle) was used, and the domain spanned  $200\ \mu\text{m}$  in the  $z$  direction. Figure 5.1 shows some details of the mesh with the obstacle located at  $y = 24.43\ \mu\text{m}$ . Note the progressive refinement of the mesh in the proximity of the obstacle. A minimum of 50 cells were used across the film thickness at any given  $x$  location, even in the regions several millimeters before and after the obstacle. In general, the goal is to properly resolve the laminar sublayer to profit from the enhanced wall treatment feature of FLUENT<sup>TM</sup> (details of this feature can be found in §9.7.3 of the FLUENT<sup>TM</sup> 5.5 manual). Wall-adjacent cells should be located at  $y^+ \approx 1$  for the enhanced wall treatment implementation. Also, at least 10 cells have to be located within the viscosity-affected near-wall region,  $Re_y < 200$ , to resolve the mean velocity and turbulent quantities. The wall distance-based turbulent Reynolds number,  $Re_y$ , is defined as

$$Re_y = \frac{\rho_l y \sqrt{k}}{\mu_l} , \quad (5.1)$$

---

<sup>2</sup>GAMBIT<sup>TM</sup>, Fluent Inc. <sup>TM</sup>, ©1988–2004

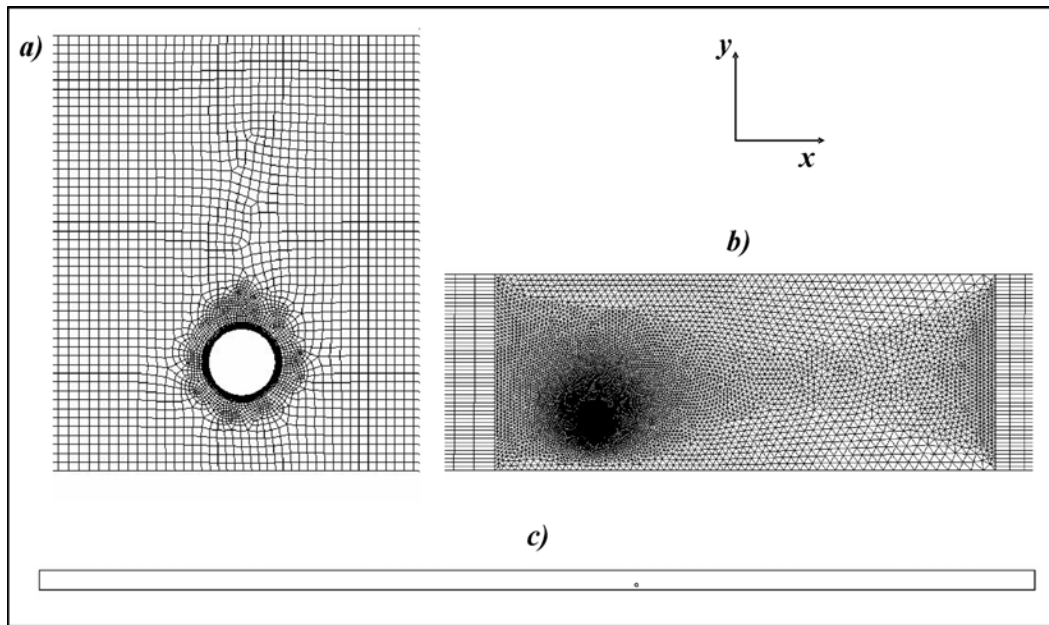


Figure 5.1: Mesh details. *a)* 2D quadrilateral element mesh around circular boundary. *b)* 3D tetrahedral element mesh near spherical boundary, and connection with outer hexahedral mesh. *c)* Aspect ratio of the flow field, and axial location of the cylindrical/spherical obstacle.

where  $k$  is the local turbulent kinetic energy.

The flow profile was allowed some distance to develop before the obstacle. Preliminary runs, without introducing an obstacle in the flow, showed that a developed velocity profile was obtained before reaching  $x = 3$  mm. The obstacle was placed three millimeters from the flow inlet, and two additional millimeters were allowed behind the obstacle to capture the wake effects. Thus, the developed velocity profile at the flow outlet ( $x = 5$  mm) should recover the shape that the velocity profile has before the obstacle (i.e., at  $x = 2.5$  mm). Three  $y$  positions for the obstacle were studied (middle,  $y = 48.85 \mu\text{m}$ ; quarter,  $y = 24.43 \mu\text{m}$  and low,  $y = 9.5 \mu\text{m}$  ).

### 5.2.2 Boundary Conditions

The specification of the inlet, and top (interfacial) boundary conditions was accomplished by using the output from the implementation of the Owen-Hewitt model presented in §4.2. The Owen-Hewitt model assumes that the liquid film behaves like a turbulent boundary layer with a profile that follows the Von Kármán universal velocity profile. In particular, the interfacial velocity,  $u_i = 2.8 \text{ m s}^{-1}$ , was used for specifying the translation speed of the top moving wall and the liquid film mass flux,  $G_{LF} = 1808 \text{ kg m}^{-2} \text{ s}^{-1}$ , to specify the inlet of the flow field. Inlet turbulence was specified by its intensity (5%) and the length scale (the length scale is estimated as  $\bar{\delta}_b/2 \approx 50 \text{ } \mu\text{m}$ , assuming the largest turbulent structures are on the order of magnitude of the film thickness). The aforementioned values corresponded to a fully annular flow regime.

The outlet is a pressure outlet set at the operating gauge pressure and the same turbulence specification as the inlet. The obstacle is a translating cylindrical wall in the 2D case and a translating hemispherical surface in the 3D case. Since the kinematics of the obstacle are specified *a priori*, the model has only one-way kinematic coupling (i.e., the fluid is affected by the movement of the obstacle, but the opposite is not true). The translation speed of the obstacle is given by the  $x$  velocity observed in the developed velocity profile at the  $y$  location of the center of the obstacle. Thus, a positive slip exists at the bottom of the obstacle and a negative slip exists at the top of the obstacle. Unfortunately, version 5.5 of the FLUENT™ software only allowed specifying either translation or rotation of the obstacle, while the most likely physical situation is that both movements take place.

### 5.2.3 Turbulence Models

Due to the very small thickness of the liquid layer being modeled ( $y^+ = 18.91$  at the film/core interface), the full domain is well below the lower bound of the log-layer ( $y^+ \approx 30$ ) and a

significant portion of it is covered by the viscous sublayer ( $y^+ < 5$ ). In these regions, the standard assumptions underlying the  $k - \epsilon$  and Reynolds stress turbulence models are no longer valid. Thus, in everyday macroscopic/industrial, high  $Re$  simulations, these near wall regions are treated using wall functions that bridge the viscosity-affected region between the wall and the outer, fully-turbulent, region. This treatment is called the wall function approach.

The present simulation benefits from a more detailed treatment called the near-wall model approach. Under the near-wall model approach, the flow is resolved all the way down to the wall. The most detailed implementation of the near-wall model approach in the FLUENT™ software is called the two-layer model. The two-layer model uses the one-equation model of Wolfstein [95], which retains the momentum and turbulent kinetic energy equations while solving the dissipation algebraically for cells in the viscosity affected region ( $Re_y < 200$ ). A check of the wall distance based turbulent Reynolds number within the domain showed that, for the present simulation, all the cells lie within the viscosity affected region. If there were any cells in the domain above  $Re_y = 200$ , they would have been solved by the standard  $k - \epsilon$  or Reynolds stress turbulence models, which are valid in the fully turbulent region. Using the Reynolds stress model preserves the possibility of representing non-isotropic turbulence wherever it is necessary by solving an additional equation for each Reynolds stress component throughout the domain. In order to take advantage of the detailed implementation of the near-wall model approach described above, the meshing guidelines mentioned in §5.2.1 have to be followed.

#### 5.2.4 Solver

Even though the mesh was very similar in principle for all  $y$  locations of the obstacle, the segregated and the coupled explicit solvers were alternately used. This method was utilized

as a result of some cases failing to converge using the segregated solver, while others resulted in reversed flow at the outlet using the coupled solver. Second order upwind discretization was used for solving the mean flow and the turbulent kinetic energy equations.

## 5.3 Simulation Results

### 5.3.1 X-Velocity Profiles

Figure 5.2 shows how the developed mean flow velocity profile away from the obstacle looks very similar for the output of either turbulence model and the 2-D geometry. The numerical model profiles closely match the analytical Von Kármán velocity profile.

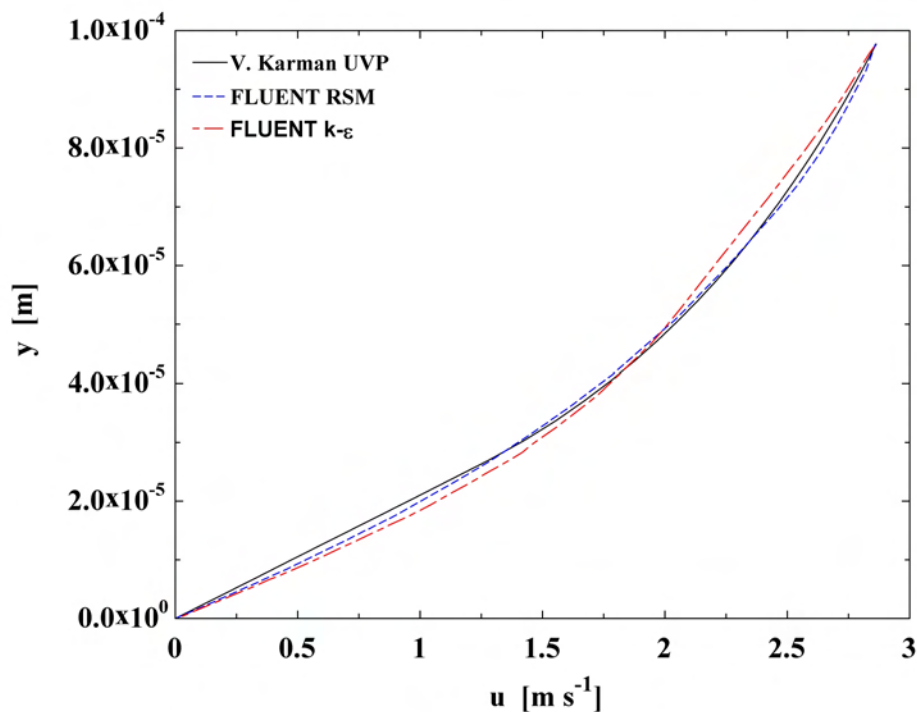


Figure 5.2: Universal velocity profile. FLUENT<sup>TM</sup> output was obtained from the 2D geometry.

It could be surprising to see a difference in the results between the  $k-\epsilon$  and RSM solutions

since both should default to the one equation Wolfstein model for the near-wall solution. The difference is caused by the action of the blending function used by FLUENT<sup>TM</sup> to match the near-wall solution with the fully turbulent solution. Also, the RSM solution is also solving for each Reynolds stress component throughout the domain. Figure 5.3 shows a comparison of the  $x$ -velocity profiles at varying  $x$  locations for the two turbulence models applied to 2D and 3D geometries. At  $x = 0$  mm, the undeveloped profile is S-shaped. At  $x = 2.9$  mm, the profile approaches the developed Von Kármán solution for all but the  $k - \epsilon$  3D case. For this latter case, the profile remains slightly S-shaped. The  $x = 3$  mm location corresponds to the obstacle position. A discontinuity in the velocity profile at about  $0.5 \text{ m s}^{-1}$  indicates the presence of the obstacle, which translates at about that velocity. Note that the profiles recover their pre-obstacle shape at  $x = 4$  mm except for the RSM 3D case.

### 5.3.2 Turbulent Viscosity Ratio

The turbulent viscosity ratio gives the relative magnitude of the eddy momentum transport to the molecular momentum transport. This quantity provides a good idea of the potential for turbulent heat transfer enhancement due to the presence of the obstacle. Since the entire flow domain is within the viscosity dominated region, this ratio is always less than one for the current simulation. However, any positive value indicates a turbulent enhancement of transport beyond the value expected from molecular viscosity alone. Results are presented in Figures 5.4 and 5.5 for the  $k - \epsilon$  and the RSM fully turbulent models respectively. The contours are cropped to show only the region affected by the presence of the obstacle. The Wolfstein one equation model is being blended by FLUENT<sup>TM</sup> with either fully turbulent model to avoid discontinuities in the dissipation. This blending, together with the non-isotropic nature of the RSM equations, generate the differences observed between the two sets of results. Unfortunately, convergence was not achieved for the 3D geometries with the

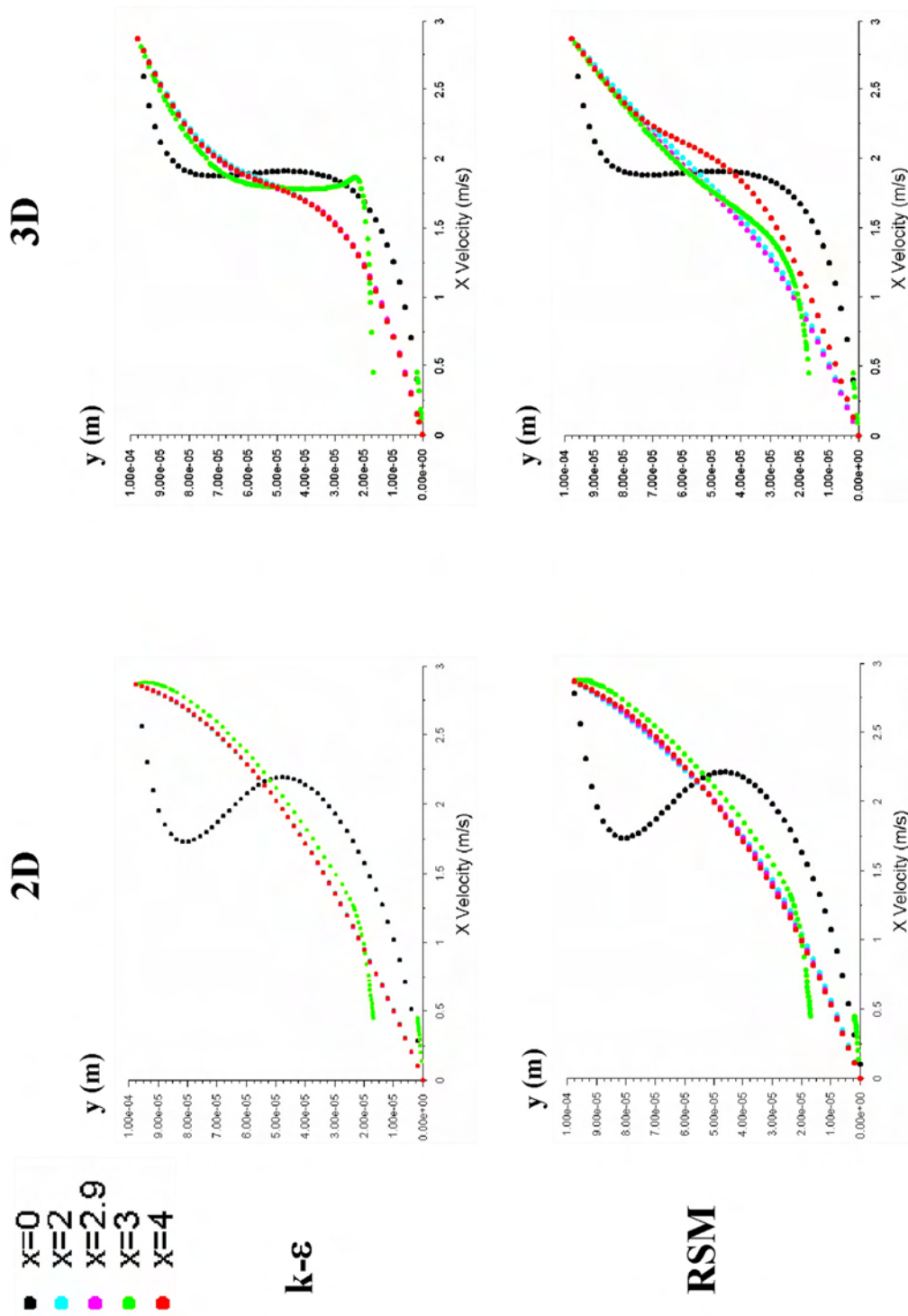


Figure 5.3: Comparison of the x-velocity profiles. Obstacle located at  $y = 9.5 \mu\text{m}$ .

particle at  $y = 24.43 \mu\text{m}$  regardless of the solver used.

## 5.4 Discussion

### 5.4.1 Discussion of Simulation Results

The velocity profiles for both 3D cases in Figure 5.3 show how the RSM model is less dissipative than the  $k - \epsilon$  model; the developed profile is not reached by  $x=3$  mm for either model, but this is especially true for the  $k - \epsilon$  model. Also, at  $x = 4$  mm, the initial profile is not fully recovered for the 3D RSM case. As a result, the RSM model may consequently predict larger wakes behind the obstacle.

The  $k - \epsilon$  and Reynolds Stress models produced similar film velocity profiles away from the obstacle. However, when observing the turbulent viscosity ratio results, the two models calculate noticeably different results. The reason for this can be seen in Figure 5.6. This figure shows a vertical and horizontal plane with contours of the turbulence viscosity ratio. Note the smoothing effect (i.e., turbulence damping) that the bubble has on the surrounding liquid, represented by the dark teardrop profile around the bubble. The flattened profile of the teardrop when it is sliding near the wall, and the general anisotropy of the flow due to the proximity of the wall, suggest that the 3D RSM results should be preferred.

The effect of the bubble on the liquid film can also be understood by analogy to the energy cascade idea for isotropic homogeneous turbulence as shown in Figure 5.7. Although the flow near the wall is far from being isotropic and homogeneous, the mechanism for turbulence damping can be interpreted based on the same ideas. The larger eddies are broken up as they pass over the bubble, whose surface tension maintains the shape of a rigid sphere. This, in turn, decreases the size of the inertial subrange within the film. The inertial subrange will then grow as the liquid flows further past the bubble and the bubble's lowered-

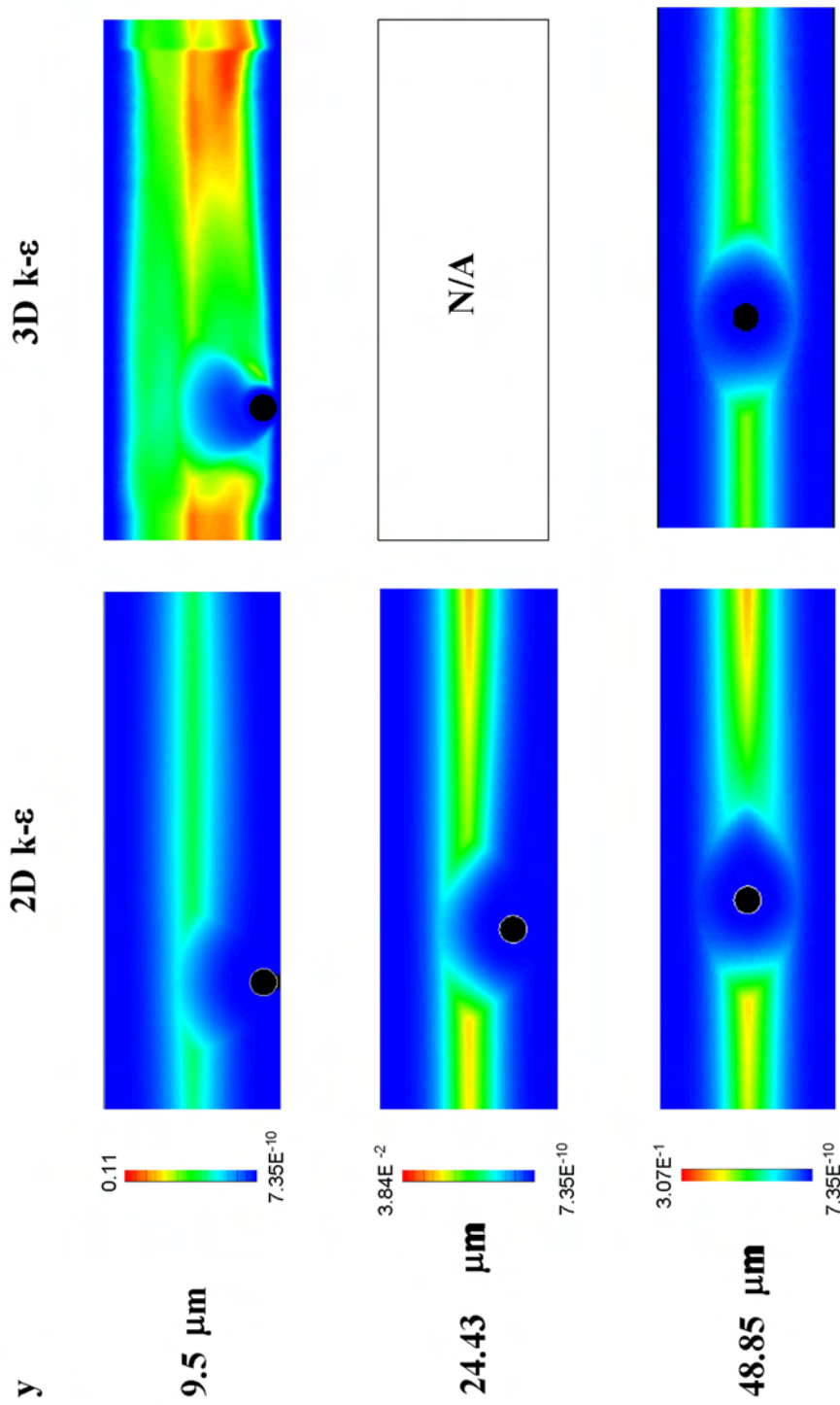


Figure 5.4:  $k - \epsilon$  turbulent viscosity ratio.

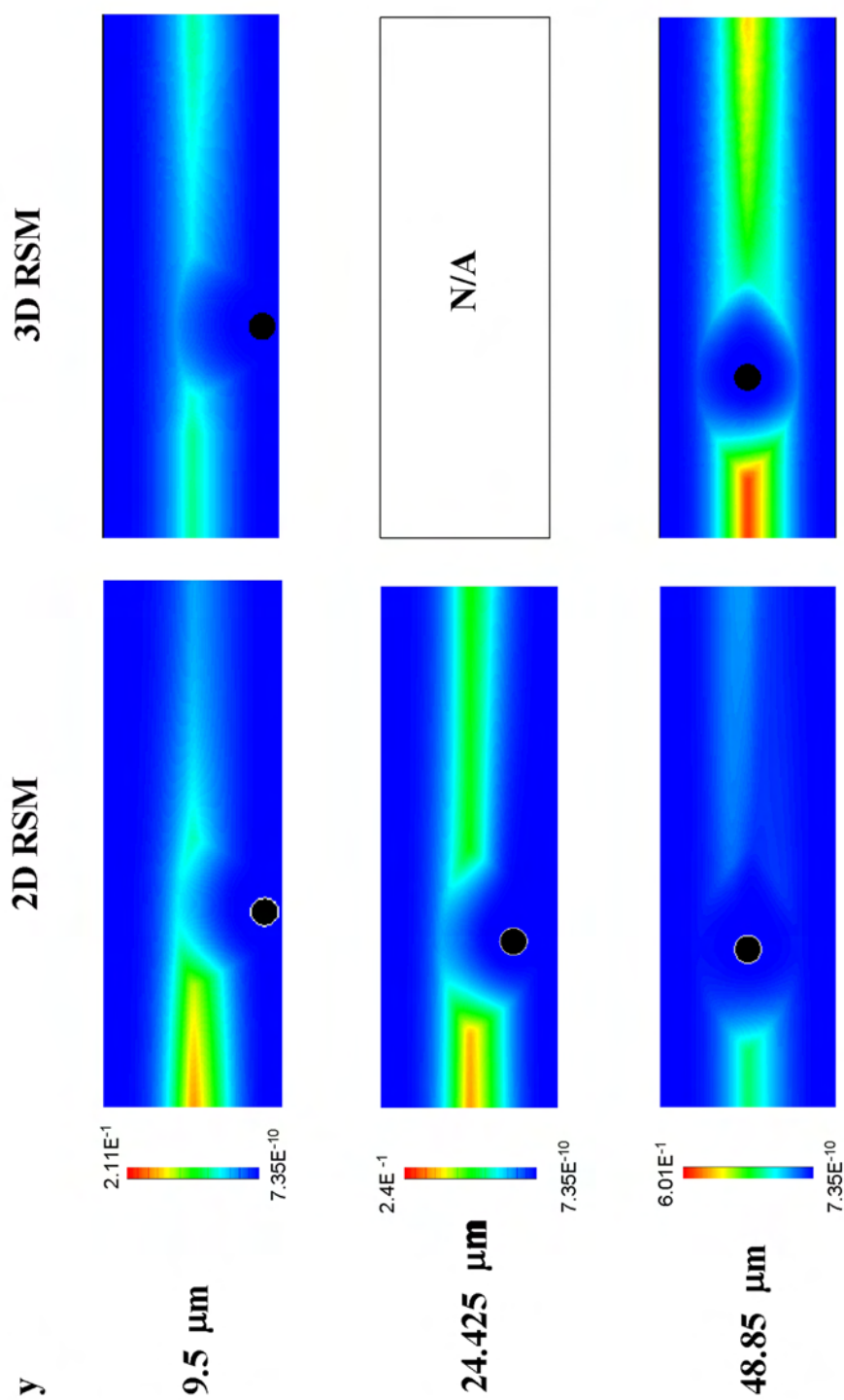


Figure 5.5: RSM turbulent viscosity ratio.

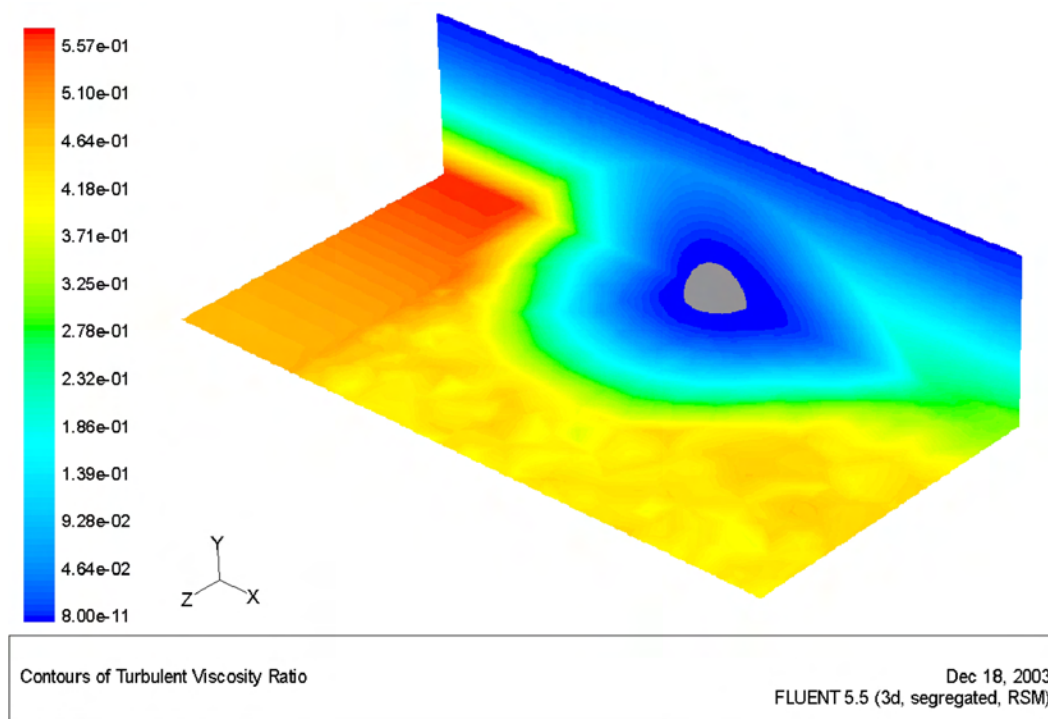


Figure 5.6: Turbulent viscosity ratio along the vertical and horizontal planes for the bubble in the middle of the channel (3D, RSM).

turbulence wake eventually disappears. Since the low frequency turbulence is assumed to be non-isotropic, it becomes less likely that the high frequency turbulence immediately after the bubble remains isotropic.

Two fundamental microscopic questions were posed as a motivation for the CFD simulation at the beginning of this chapter. The first question, whether a localized turbulent enhancement of the heat transfer coefficient exists or not, is answered negatively. Bubbles that are  $15 \mu\text{m}$  in diameter actually *suppressed* turbulence in the surrounding flow. Gore and Crowe [96] plotted experimental data of the modulation of turbulence against the ratio of the particle diameter to the size of the energy containing eddies for a variety of flow geometries. They found that when this ratio is above 0.1, particles enhance turbulence. On the other hand, particles for which the ratio is below 0.1 suppress turbulence. More recently, Hetsroni *et al.* [97] performed a direct numerical simulation (DNS) of the heat transfer and thermal

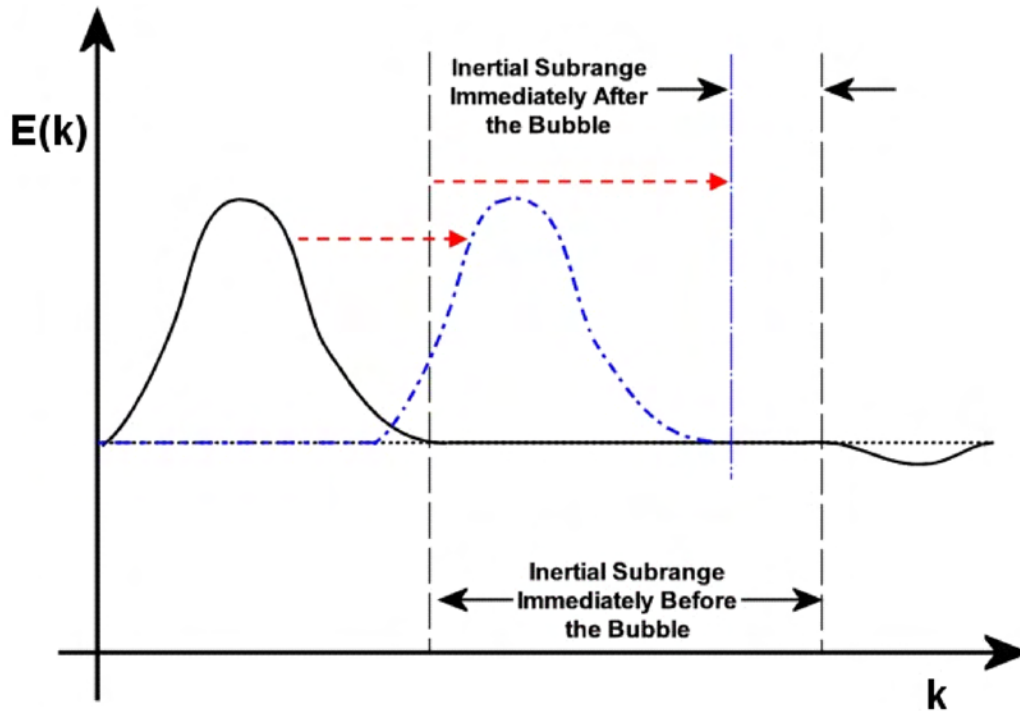


Figure 5.7: Effect of bubble on the energy cascade.

pattern around a sphere in a water turbulent boundary layer ( $Pr = 5.4$ ). For spheres ranging from 17 to 34 wall units in diameter, they found a localized enhancement of the heat transfer coefficient of up to 2.8 times the mean value away from the obstacle. For the present simulation, assuming that the size of energy containing eddies is on the order of magnitude of the film thickness, the ratio of the particle diameter to the size of the energy containing eddies is 0.154. It is likely that larger obstacle sizes might have predicted an enhancement and that smaller obstacles might have also predicted suppression.

It may also be hypothesized that the mechanism for heat transfer enhancement is not related exclusively to the enhancement of turbulent mixing. Instead, the displacement of the flow above the front stagnation point by the bubble may briefly put it in contact with the colder region that exists in the proximity of the vapor/liquid interface. Also, the displacement of the flow below the stagnation point may bring cold liquid into closer contact with the wall.

However, the validity of this “scraping” mechanism can not be assessed using the results of the present simulation.

The second question, regarding the area of pipe affected by the presence of each bubble, remains unsolved since the simulation did not show any enhancement. There is no particular reason for predicting that the suppression wake has the same dimensions as the enhancement wake. However, the width and length of the suppression wake from Figures 5.6 and 5.5 are used as a first estimate for the calculation in §5.4.2. These dimensions can also be used for estimating the size of the region of interest (ROI) for visualization experiments.

#### 5.4.2 Expected Localized Heat Transfer Enhancement per Entrained Bubble

A significant fraction of the measured annular flow boiling heat transfer coefficient has to be associated to the effect of entrained bubbles in order to accept this mechanism as important (or even dominant). This fraction can be used to determine the localized enhancement of the heat transfer coefficient that is expected from each bubble. The localized enhancement can be expressed as the ratio  $\frac{\bar{h}_b}{\bar{h}}$  where  $\bar{h}_b$  is the mean heat transfer coefficient over the area of influence of a single bubble and  $\bar{h}$  is the overall mean heat transfer coefficient.

The results of §2.2.3 showed that the entrained bubble number concentration that exists within the base film is comparable to the saturated flow boiling nucleation site density (10–100 sites per  $\text{cm}^2$ ). Both entrained bubbles and bubbles originated at nucleation sites are likely to participate in the sliding bubble mechanism introduced in §1.6. To obtain a total bubble number concentration estimate, the nucleated bubble number concentration,  $n_{nbf}$ , should be added to the entrained bubble number concentration,  $n_{ent}$ , measured in §2.2.3. In the annular flow situation, the active nucleation site density is likely to be suppressed below the saturated flow boiling value of 10–100 sites per  $\text{cm}^2$ . A suppression factor,  $F_{sup}$ , can be

introduced to represent this effect with  $F_{sup} = 1$  representing no suppression and  $F_{sup} = 0$  representing complete suppression so that

$$n_{sup} = F_{sup}n_{sat} \quad , \quad (5.2)$$

where  $n_{sat}$  is the nucleation site density for saturated flow boiling and  $n_{sup}$  is the unsuppressed nucleation site density. Also, at any given instant, more than one bubble that originated at the same nucleation site exists within the liquid film. This fact can be represented by a downstream nucleation site effect represented by an integer multiplier,  $F_{dn}$ , that gives the nucleated bubble number concentration for annular flow boiling as

$$n_{nbf} = F_{dn}n_{sup} \quad . \quad (5.3)$$

The  $F_{dn}$  multiplier is determined by the nucleated bubble lifetime within the film and the nucleation site frequency, and it condenses the relevant information from those two quantities into a single parameter. The total bubble number concentration for annular flow boiling  $n_{tot}$  is then simply given by

$$n_{tot} = n_{ent} + n_{nbf} \quad . \quad (5.4)$$

With  $n_{tot}$  available, an area (within the reference area of  $1 \text{ cm}^2$ ) affected by bubble wakes can be calculated as

$$A_w = n_{tot}F_{ww}F_{wl}D_b^2 \quad , \quad (5.5)$$

where the shape of the wake of each bubble is approximated with a rectangular area,  $F_{ww}F_{wl}D_b^2$ .  $F_{ww}$  and  $F_{wl}$  are multipliers of the bubble diameter that determine the approximate wake width and length respectively. From the results in Figures 5.6 and 5.5, these multipliers are set as  $F_{ww} = 3$  and  $F_{wl} = 5$ . The mean heat transfer coefficient is then given

by

$$\bar{h} = \frac{\bar{h}_b A_w + h_{lam} A_{lam}}{A_{ref}} \quad , \quad (5.6)$$

where  $h_{lam}$  is the heat transfer coefficient for the area that remains unaffected by bubble wakes,  $A_{lam}$ . The reference area,  $A_{ref}$  of 1 cm<sup>2</sup> is the result of the sum

$$A_{ref} = A_{lam} + A_w \quad . \quad (5.7)$$

Finally, the ratio,  $Q_h$ , of the heat transferred through  $A_w$  to the total heat transfer is calculated as

$$Q_h = \frac{\bar{h}_b A_w}{\bar{h} A_{ref}} \quad . \quad (5.8)$$

The following calculations for finding  $\frac{\bar{h}_b}{\bar{h}}$  will be performed assuming  $n_{ent} = 50$  bubbles per cm<sup>2</sup> and  $n_{sat} = 50$  sites per cm<sup>2</sup>. A mean bubble diameter of 20  $\mu$ m is also assumed. Because most flow boiling heat transfer models have accuracies of approximately  $\pm 20$  percent at best, it is reasonable to use the criterion,  $Q_h = 0.2$ , to calculate the required value of  $\frac{\bar{h}_b}{\bar{h}}$  for the sliding bubble mechanism to be significant (i.e., the unaccounted for physics may be due to the bubbles). Figure 5.8 is a plot of  $\frac{\bar{h}_b}{\bar{h}}$  against  $F_{dn}$  with  $F_{sup}$  as a parameter. The highest required enhancement is  $\frac{\bar{h}_b}{\bar{h}} = 33.33$  for the worst case scenario of 90 percent nucleation suppression ( $F_{sup} = 0.1$ ) and  $F_{dn} = 10$ . However, the results by Hetsroni *et al.* [97] suggest that the actual enhancement is in the range  $1 < \frac{\bar{h}_b}{\bar{h}} < 3$ . The high sensitivity of the required  $1 < \frac{\bar{h}_b}{\bar{h}} < 3$  with respect to ( $F_{sup}$  and  $F_{dn}$  (see 5.8), shows that an accurate value is desirable for a broader range of bubble sizes and flow settings. More detailed experimental studies or simulations of the turbulence and the thermal pattern in the vicinity of entrained and sliding bubbles are warranted. Chapter 6 describes a viable implementation of cross-cut micro-PIV measurements that could be of great utility in solving these microscopic, mechanistic questions and in validating future simulations.

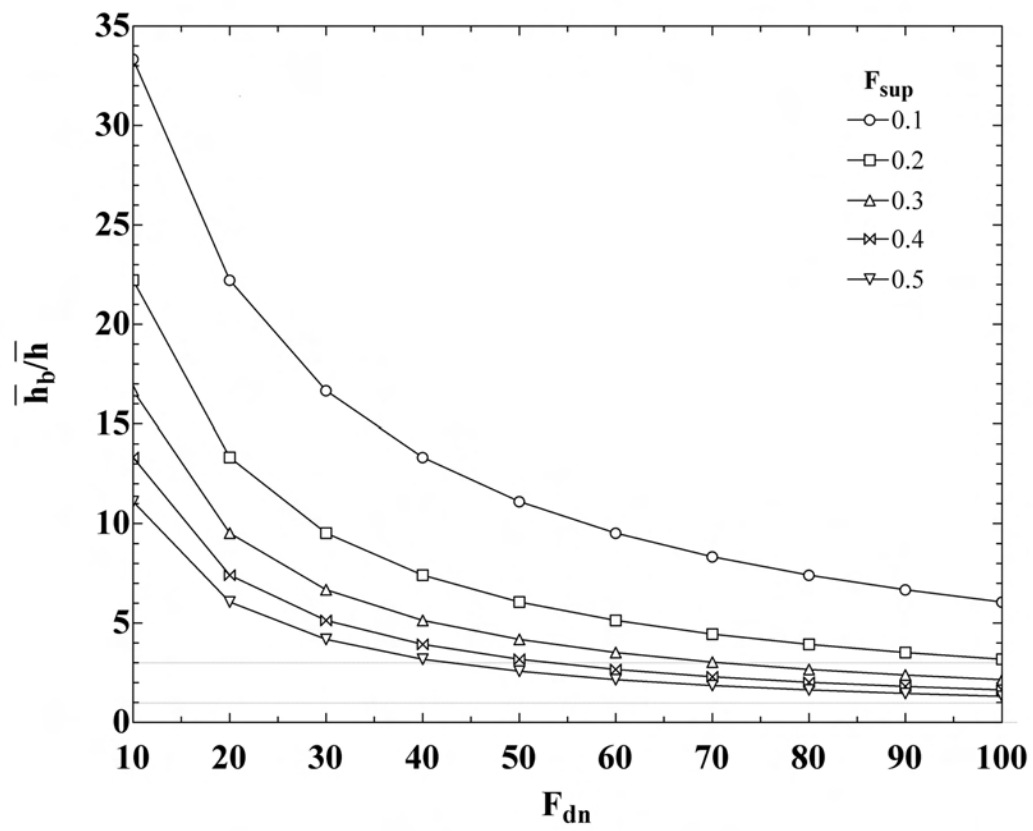


Figure 5.8: Required localized turbulent heat transfer enhancement based on  $Q_h = 0.2$ .

# Chapter 6

## Setup and Considerations for Cross-cut micro-PIV Measurements

The distance from the wall, slip velocity and wake turbulence of entrained bubbles are required for a detailed characterization of the enhancement of convection heat transfer that they may produce. Cross-cut Particle Image Velocimetry (PIV) can be used for documenting this dynamic behavior of entrained bubbles for horizontal annular flow. Departure and lift-off behavior was documented by Thorncroft [5] for subcooled boiling in vertical upflow and downflow, but the annular flow situation is of greater practical interest for heat transfer since it occurs in a wide variety of industrial equipment and exists over a wide range of qualities and mass fluxes.

This chapter discusses some of the special imaging considerations that need to be taken into account due to the very high spatial resolution required for measuring velocities within the liquid film of annular two-phase flow and the limitations on near-wall optical access described in §3.2.2. Although some sample images are shown to demonstrate the viability of the image acquisition technique, no velocity vectors were measured.

### 6.1 Test Section and Imaging System Setup

Even the small mismatch in index of refraction between water and the FEP material of the round pipe used for the PLIF measurements produced a 10  $\mu\text{m}$  dark band at the wall.

This source of uncertainty was acceptable for measuring the film thickness, but it is highly inconvenient for measuring the wall shear stress and the turbulence modulation due to small bubbles sliding along the wall. The solution to this problem is to study the flow inside a square channel while being aware of the differences in the liquid film thickness distribution (e.g., thinning of the liquid film at the corners) as measured by Shedd [98].

The flow loop used for obtaining the samples presented in §6.3 is similar to the one shown in Figure 2.1 except that the pipe length before the test section is replaced by a 3/4 in. acrylic square channel with a wall thickness of 1.6 mm. The corners of the extruded acrylic channel have finite radius that hampers the cross-cut imaging of the film just as the round pipe did. A special test section was designed so that the side walls are perpendicular to the top and bottom walls while not creating a radius at the corner. Two precision ground polycarbonate blanks were used as the top and bottom walls of the test section. The surfaces of the blanks had a thickness tolerance of  $\pm 0.127$  mm. This is important to ensure the perpendicularity of all faces and the parallelism of the side walls. The top and bottom polycarbonate walls of the test section and the surfaces parallel to them on the polycarbonate walls were polished with an abrasive compound to achieve maximum clarity and to minimize wall roughness. The side walls were 3.3 mm thick float glass windows with an anti-reflective coating and 96 percent light transmission in the visible spectrum. These side windows are clamped against square 1/8 in. seals that sit on grooves that were machined on the polycarbonate blocks. This arrangement allows full optical access within the base film along the bottom or the top of the channel without any distortion or dark-band effects due to refraction or reflection.

Figure 6.1 is an axial view of the test section components. The windows, polycarbonate blocks, seals and clamps extend 304.8 mm along the axial direction. The square acrylic channel that connects to the inlet and outlet of the test section (marked with a diagonal hatch on the drawing) is clamped in position by the polycarbonate blocks. The acrylic channel penetrates 6.35 mm into the test section at each end. Figure 6.2 shows a side view

of the test section with the acrylic channel partially inserted at both ends. The gray PVC parts are the clamps that hold the glass windows onto the seals. Each clamp is held in place by 12 screws to distribute the load on the seal evenly. There is a 25.4 mm separation between the screws. This separation is enough for performing measurements without any adverse effect from the shadows produced by the screws. Although the original design shown in Figure 6.1 specified a height of 25.4 mm for the polycarbonate blocks, due to the high clarity of the polycarbonate resin, the blocks were not machined down to this height to preserve the original tolerance of the precision blank. Note that the top and bottom walls of the test section protrude slightly beyond the edges of the gray PVC clamps. This permits an unobstructed view of the edges of the polycarbonate blocks through the glass windows.

Figure 6.3 is a schematic of the imaging setup used for obtaining the cross-cut images in §6.3. The imaging setup was very similar to the one described in §3.2.2 for the acquisition of the PLIF images. The only changes in the flow loop were the test section (as described above) and the development conduit, which was a square acrylic channel. The same Nd:YAG laser was used, but a beam expander was used instead of laser sheet optics to facilitate the alignment and focusing of the system. The detector was a Roper Scientific 1300YHS-DIF camera with a  $1300 \times 1030$  pixel CCD detector. The camera was coupled via an extension tube to a  $10\times$  (NA=0.28), infinity corrected, plano-apochromat Mitutoyo microscope objective or a  $5\times$  (NA=0.14) objective of the same type. The extension tube housed a red filter that removed all stray reflections from the laser beam while transmitting the fluorescence from the dye. The camera was attached to a three-axis translation stage and a tilt goniometer for accurate focusing and alignment.

A Princeton Instruments 5 MHz MicroMax controller drives the camera and interfaces with a computer. The resolution of the imaging system was  $0.67 \mu\text{m pixel}^{-1}$  for the  $10\times$  objective and  $1.34 \mu\text{m pixel}^{-1}$  for the  $5\times$  . The laser and the camera were synchronized by a Berkeley Nucleonics Corp. Model 555-8 pulse generator. The internal exposure control mode

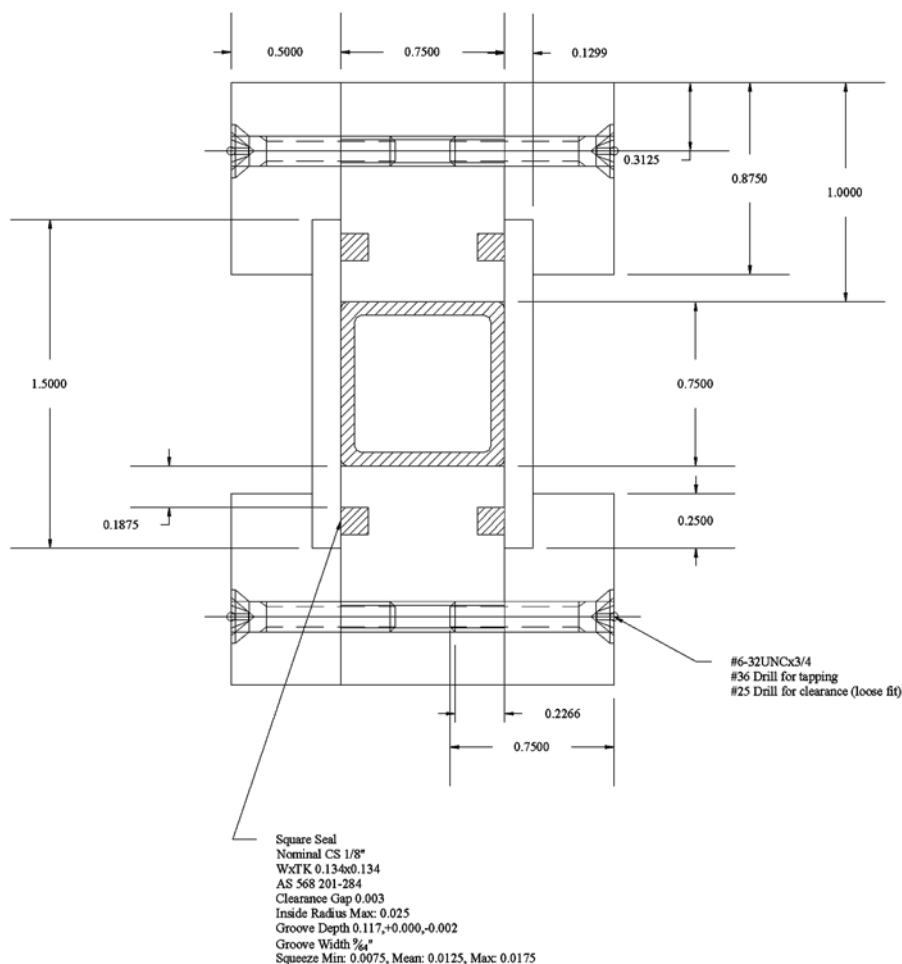


Figure 6.1: Dimensions of the square channel test section (dimensions in inches). Axial view.

was used for the timing of the camera shutter. In this mode, a single trigger signal from the pulse generator started the collection of two separate frames with identical exposure time, and readout takes place only after both frames are captured. The exposure time was specified by the software that runs the controller from the computer. There is a 200 ns hardware delay in between the two exposures. There is also a 200 ns hardware delay between the trigger signal for the camera and the first exposure.

The laser power can be modulated by adjusting the delay between the flashlamp trigger signal and the Q-switch for each laser. This trim adjustment was necessary to perfectly

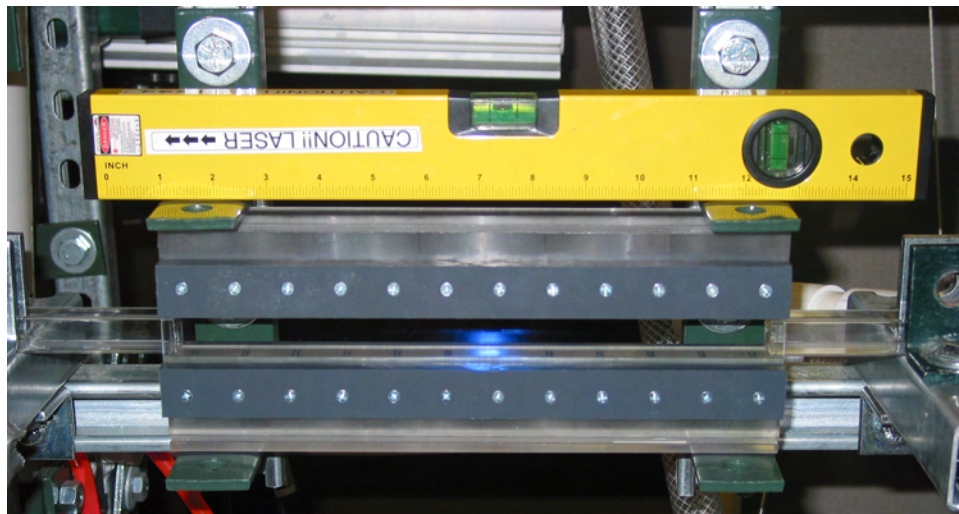


Figure 6.2: Square channel test section. Side View.

Channel	Name	Width ( $\mu\text{s}$ )	Delay ( $\mu\text{s}$ )
1	camera	100	170
2	flashlamp 1	100	0
3	flashlamp 2	100	75
4	Q-Switch 1	100	185
5	Q-Switch 2	100	265

Table 6.1: Pulse width and delay for IEC mode.

balance the brightness of both frames. The timing sequence for the capture of a pair of frames started with the trigger signal from the pulse generator to the flashlamp of the first laser. Then, the trigger for the camera and the second flashlamp signal followed. The Q-switches were fired next to match the exposure window for each frame. The exposure time was set at  $100 \mu\text{s}$  (this is the amount of time the camera shutter remains open). Table 6.1 summarizes the pulse width and delay produced by the pulse generator for each channel. The actual exposure time  $t_{exp}$  is given not by the time the camera shutter is open, but instead, by the fluorescence decay time ( $t_{exp} \approx 10 \text{ ns}$ ).

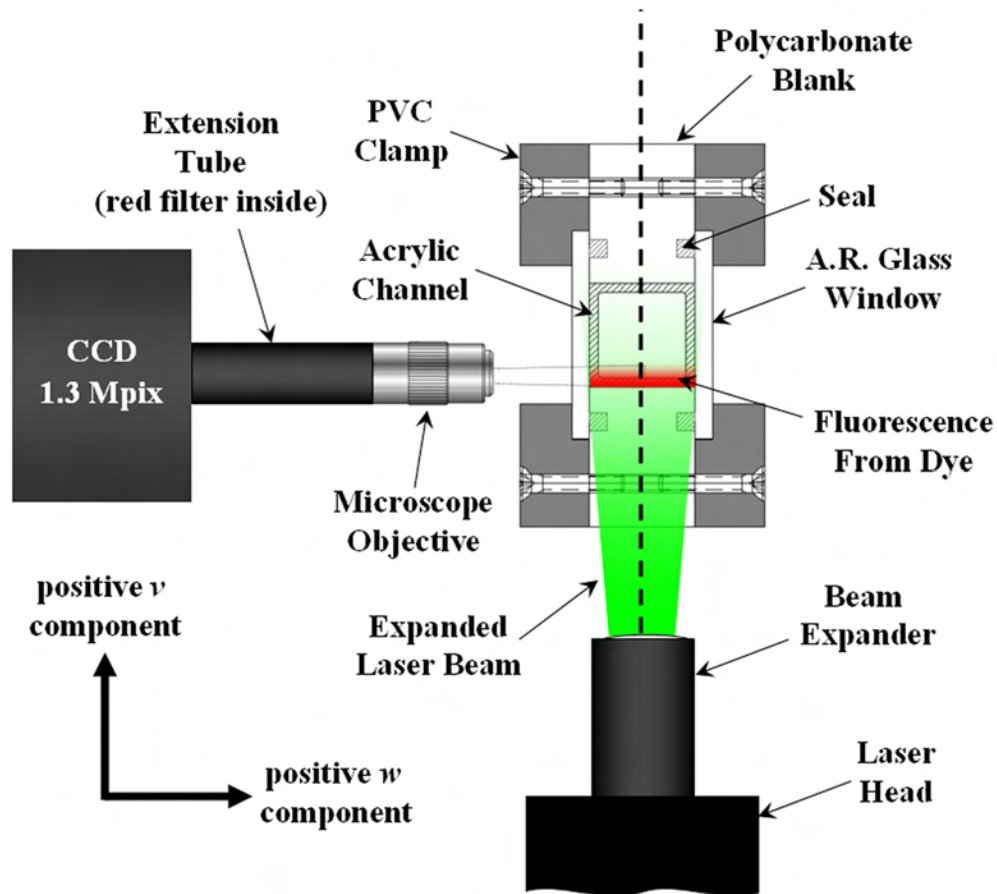


Figure 6.3: Schematic of setup for cross-cut images inside square channel. The vertical dotted line indicates the location of the cross-cut plane.

## 6.2 Flow Seeding, Depth of Field and Spatial Resolution

Wereley *et al.* [99] describe a technique for implementing particle image velocimetry (PIV) at a micron scale spatial resolution. A summary of the contents of their study follows, as well as some calculations for the case of the annular flow situation at hand.

### 6.2.1 Diffraction Limited Resolution

The diffraction image of a point focused through a circular aperture is given by the Airy function [100] as

$$A(r) = \left( \frac{J_0(r)}{r} \right)^2, \quad (6.1)$$

where  $J_0(r)$  is the zero-order Bessel function of the first kind, and  $r$  is the radius. The diameter of the diffraction-limited point spread Airy function,  $D_{sp}$ , is given by Wereley *et al.* as

$$D_{sp} = 2.44M \frac{\lambda}{2NA}, \quad (6.2)$$

where  $M$  and  $NA$  are the total magnification and numerical aperture of the microscope optics and  $\lambda$  is the light wavelength.

The point spread function is convolved with the geometric image to form the actual image that the camera detects. Both functions can be approximated by Gaussian functions, and the resulting convolution produces a Gaussian function from which the effective particle image diameter  $D_E$  is defined as

$$D_E = \sqrt{M^2 D_p^2 + D_{sp}^2}, \quad (6.3)$$

where  $D_p$  is the geometric diameter of the particle. The effective image diameter on the detector can be projected back on to the flow from knowledge of the magnification. Also according to Prasad *et al.* [101], the spatial uncertainty is an order of magnitude smaller than the resolution of the microscope if the particle is resolved by three to four pixels across the diameter. Consequently, the diffraction-originated uncertainty for locating a particle on the image plane (i.e., the  $xy$  plane) is given by

$$\delta_x = \frac{D_E}{10M}. \quad (6.4)$$

### 6.2.2 Depth of Field

The thickness of the measurement domain (out of plane resolution) is not determined for micro-PIV by the thickness of a laser sheet like in normal PIV measurements. Instead, it is determined by the depth of field of the microscope optics. Some of the particles will produce out of focus images so, ultimately, the definition of the depth of field has an arbitrary component. Wereley *et al.* used an expression to estimate (conservatively) the depth of *focus* in their calculations. However, the depth of focus refers to the image plane not to the object plane. An estimate for the depth of *field*<sup>1</sup>,  $\delta_z$ , for microscope optics is given by

$$\delta_z = \frac{n\lambda}{NA^2} + \frac{ne}{NA(M)} \quad , \quad (6.5)$$

where  $n$  is the index of refraction of the fluid in which the objective is immersed and  $e$  is the smallest distance resolved by a detector that is placed on the image plane of the microscope objective. For the calculations below,  $e$  was estimated as three times the size of a pixel.

### 6.2.3 Super-resolution Using The Sub-correlation PTV Method

The super-resolution PIV analysis method is motivated by the desire to have PIV measurements with an in-plane spatial resolution on the order of the Kolmogorov length scale,  $\eta$ , which yield measurements of vorticity and viscous dissipation of the turbulent kinetic energy. The method uses the vector determined for a given interrogation spot as a guess vector for performing particle tracking velocimetry (PTV) measurements for each individual particle image pair within the interrogation spot. Many of the available commercial PIV analysis software packages implement some form of the super-resolution algorithm<sup>2</sup>. Keane *et al.* [102] provide experimental design rules for the specification of key PIV measurement parameters

<sup>1</sup>Microscopy Primer from the Nikon online microscopy primer by Molecular Expressions<sup>TM</sup>. [www.microscopyu.com/tutorials/java/depthoffield/index.html](http://www.microscopyu.com/tutorials/java/depthoffield/index.html)

<sup>2</sup>From a personal communication with Dr. Steve Anderson from LaVision Inc.

such as the time between exposures,  $\Delta t$ , the particle seeding density,  $C$ , and the interrogation spot size,  $D_I$ , that guarantee the acquisition of images suitable for super-resolution processing. The relation between  $D_I$  and  $\Delta t$  comes from limiting the loss of particle image pairs due to out-of-plane and in-plane motion. This relation is expressed by the following three equations [103–105] as

$$\Delta t = \frac{D_I}{4\sqrt{u^2 + v^2}} \quad , \quad (6.6)$$

$$\Delta t = \frac{\delta_z}{4w} \quad , \quad (6.7)$$

or

$$\Delta t = \frac{D_E}{\left(\frac{\partial u}{\partial y}\right) D_I M} \quad . \quad (6.8)$$

A required previous step for the third calculation is obtaining an *a priori* estimate of  $\frac{\partial u}{\partial y}$  within the interrogation spot. The three expressions determine the maximum value  $\Delta t$  can have according to a particular way of losing particle image pairs from the interrogation spot. The minimum of the three values of  $\Delta t$  should be used for the time interval between exposures.

The image density,  $N_I$ , gives the number of particles per interrogation spot and it is defined as

$$N_I = CD_I^2\delta_z \quad , \quad (6.9)$$

where  $C$  is the particle seeding density (number of particles per unit volume). The optimal image density for super-resolution is 12 particles per interrogation spot [102]. The use of the sub-correlation PTV method improves linear resolution by a factor of  $\sqrt{N_I}$  approximately.

### 6.2.4 Brownian Motion Error

A potential source of error is that due to Brownian motion of the tracers for micron-scale PIV measurements. Assuming that Stokes' drag dampens the Brownian motion, the diffusion,  $D_{pf}$ , is given by the Einstein-Stokes equation for a sufficiently long time  $t$  as

$$D_{pf} = \frac{\kappa_B T_l}{3\pi\mu_l D_p} , \quad (6.10)$$

where  $T_l$  and  $\mu_l$  are the temperature and dynamic viscosity of the liquid respectively,  $D_p$  is the tracer particle diameter and  $\kappa_B$  is Boltzmann's constant. The root-mean-square displacement is given by Uhlenbeck and Ornstein [106] as

$$\langle s^2 \rangle = 2D_{pf}\Delta t , \quad (6.11)$$

where  $\Delta t$  is the time delay between exposures. The tracers will travel a distance

$$\Delta x = u\Delta t , \quad (6.12)$$

where  $u$  is an estimate for the flow velocity. Thus, the relative error produced by Brownian motion is defined as

$$\varepsilon_B = \frac{\langle s^2 \rangle^{\frac{1}{2}}}{\Delta x} = \frac{1}{u} \sqrt{\frac{2D_{pf}}{\Delta t}} . \quad (6.13)$$

If each particle contributes equally to the average velocity vector, and the Brownian error is a statistically independent value for each particle, ensemble averaging over  $N$  particles ( $N_r$  realizations, with  $N_p$  tracer particles per realization yield  $N = N_r N_p$  total averaged particles) reduces the error to  $\frac{\varepsilon_B}{\sqrt{N}}$ .

### 6.2.5 Seeding

The flow is ideally seeded by tracers of neutral buoyancy and a diameter that the imaging system can resolve with 3 to 4 pixels for a given region of interest of the measurement plane. With the imaging system proposed in §6.1, but using a  $20\times$  (NA=0.42) microscope objective, an area of 0.435 mm by 0.345 mm can be imaged at enough resolution to have 5 pixels across the diameter of the image of a 300 nm particle. Polystyrene microspheres, with a density of  $1.05 \text{ g cm}^{-3}$  and a refractive index of 1.59 at 589 nm are commercially available as water suspensions with a narrow size distribution ( $< 5\% \text{ CV}$ )<sup>3</sup>.

Previous micro-PIV studies have normally employed particles of similar size and material with the addition of a fluorescent dye [107]. However, these measurements have been performed by imaging into very shallow flow fields in which the probability for particle overlap is minimal. This is the case for the radial-view micro-PIV measurements performed by Kopplin [108] for horizontal annular flow. For the case of cross-cut images, like the ones proposed in this chapter, the overlap between particles is not minimal. In fact, during preliminary tests of the imaging system, fluorescence from out of focus particles was blurred into a continuous, bright background. This bright background made the fluorescence from the focused particles indistinguishable from the surrounding fluid.

Consequently, it was decided to invert the contrast of the images by adding fluorescent dye to the liquid. Rhodamine B was used as a dye, in identical concentration as employed for the PLIF measurements in Chapter 3. Opaque particles should be used for this alternative imaging technique, although the sample images presented in §6.3 were obtained using hollow glass microballoons that were 8–12  $\mu\text{m}$  in diameter. The dark images produced by the hollow glass microballoons do not correspond to their real diameter since the scattering occurs at the internal air/glass interface. Opaque particles should produce shadow images that are closer

---

<sup>3</sup>Coefficient of Variation (CV): standard deviation as a percent of the mean.

to the real diameter of the tracer except for the diffraction-originated resolution limitations described above.

### 6.2.6 Calculations for the Micro-PIV Imaging System

Based on the radial view measurements performed by Kopplin [59], estimates for the axial, radial and circumferential velocities can be made ( $u$ ,  $v$  and  $w$  respectively). The  $u$  and  $v$  components determine the in-plane motion while the  $w$  component determines the out-of-plane motion. These velocity components, together with the characteristics of the seeding and the optical system, can be used for specifying  $\Delta t$  and  $C$  for the desired interrogation spot size. The interrogation spot size should be determined from the estimates for sliding bubble diameter, film thickness and the Kolmogorov scale.

Table 6.2.6 shows the most important variables in the specification of the cross-cut micro-PIV imaging system. Note how the high velocities make the Brownian error negligible for this application.

## 6.3 Sample Images

This section shows the viability of the imaging method for obtaining good contrast between the seeding and the fluorescing liquid. The particle concentration is low in these images. This sparse seeding is more suitable for PTV analysis. However, the particle concentration could be increased according to the calculations performed in §6.2.6 in order to obtain images suitable for cross-correlation analysis. The size of the dark particle images actually corresponds to the size of the inner core of the microballoons. The images produced by the microballoons are essentially indistinguishable from the images bubbles of a similar diameter.

Figure 6.4 shows large entrained bubbles together with the particle images. The depth of field at  $5\times$  magnification ( $\approx 58 \mu\text{m}$ ), is 5 to 10 times the size of the microballoons. This fact

variable	value	units
$C$	$2.144 \times 10^{10}$	$\frac{\text{particles}}{\text{cm}^{-3}}$
$D_E$	33.36	$\mu\text{m}$
$D_I$	10	$\mu\text{m}$
$D_p$	300	nm
$D_{pf}$	$4.23 \times 10^{-14}$	$\text{m}^2 \text{s}^{-1}$
$D_{sp}$	32.84	$\mu\text{m}$
$e$	20.1	$\mu\text{m}$
$\varepsilon_B$	$1.506 \times 10^{-4}$	$\mu\text{m}$
$\delta_x$	166.8	nm
$\delta_z$	5.60	$\mu\text{m}$
$\Delta t$	1.658	$\mu\text{s}$
$\Delta x$	2.49	$\mu\text{m}$
$\lambda$	565	nm
$M$	20	–
$\mu_l$	0.00127	$\text{kg m}^{-1} \text{s}^{-1}$
$n$	1	–
$N_I$	12	$\frac{\text{particles}}{\text{int. spot}}$
$NA$	0.42	–
resolution	0.335	$\mu\text{m pixel}^{-1}$
$s$	0.37	nm
$t_{exp}$	10	ns
$T_l$	284	K
$u$	1.5	$\text{m s}^{-1}$
$\frac{\partial u}{\partial y}$	46156	$\text{s}^{-1}$
$v$	0.15	$\text{m s}^{-1}$
$w$	0.075	$\text{m s}^{-1}$

Table 6.2: Results of calculation for micro-PIV imaging system.

makes in-focus particle overlap a likely occurrence. The increase in bubble concentration that is necessary for cross-correlation analysis increases the chances for particle overlap. Therefore, it is desirable to use a higher magnification for micro-PIV to reduce the depth of field and to increase the resolution. Note that some bubbles and particle images are out of focus. These blurred images can be excluded from the measurements using digital an image processing script like the one implemented by Kopplin [108].

Figures 6.5 through 6.7 show samples of image pairs captured using IEC mode as de-

scribed in §6.1. Figure 6.6 is an excellent example of a sliding bubble with great likelihood of producing a turbulent enhancement of heat transfer. The vertical white lines were used as references for tracking the motion of individual particles and bubbles. Very small horizontal lines on the bottom frames of each figure show the measured displacements. With the time delay between the Q-switch signals for the lasers and the measured displacements, the in-plane velocity components can be calculated. For the particle and the bubble in Figure 6.5, the  $u$  components of their velocities were  $0.21 \text{ m s}^{-1}$  and  $0.23 \text{ m s}^{-1}$  respectively. For the large bubble in Figure 6.6, the  $u$  component was  $0.52 \text{ m s}^{-1}$ . A particle near the equator of the large bubble, which is expected to have little slip with respect to the bubble, was travelling at  $u = 0.50 \text{ m s}^{-1}$ . Another particle on the same figure, located well below the equator of the large bubble, was travelling at  $u = 0.12 \text{ m s}^{-1}$  indicating significant slip at the bottom of the bubble. The particles tracked in Figure 6.5 were travelling at  $u = 0.08 \text{ m s}^{-1}$  and  $u = 0.15 \text{ m s}^{-1}$  for the lower and higher particle respectively.

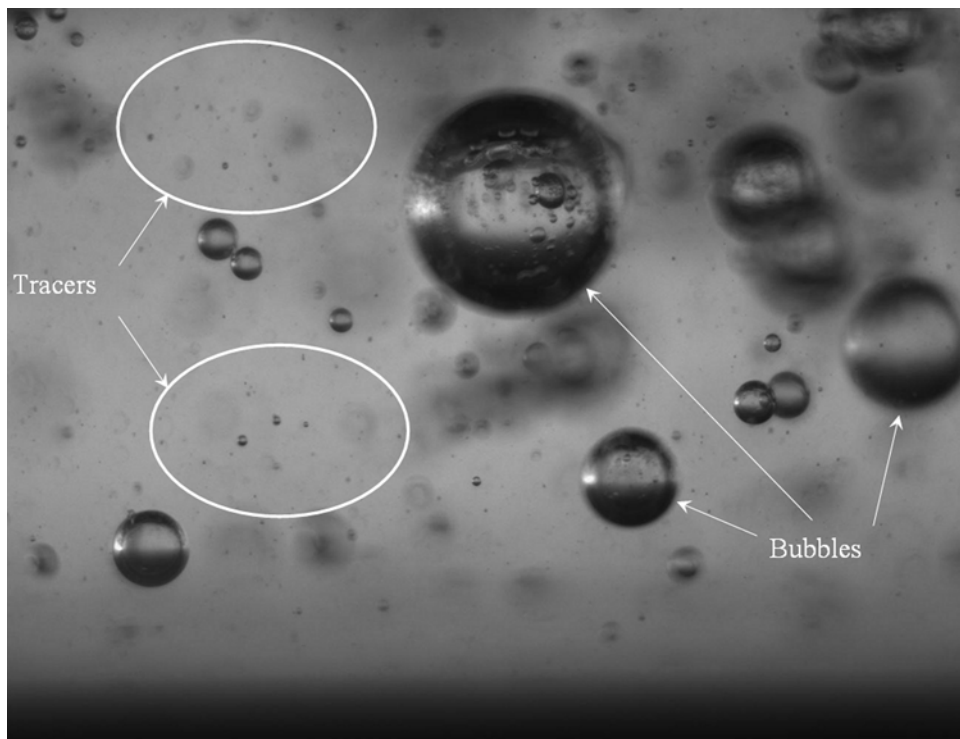


Figure 6.4: Entrained bubbles and hollow glass microballoons. Captured at  $5\times$  magnification for a stratified flow. Flow from left to right.

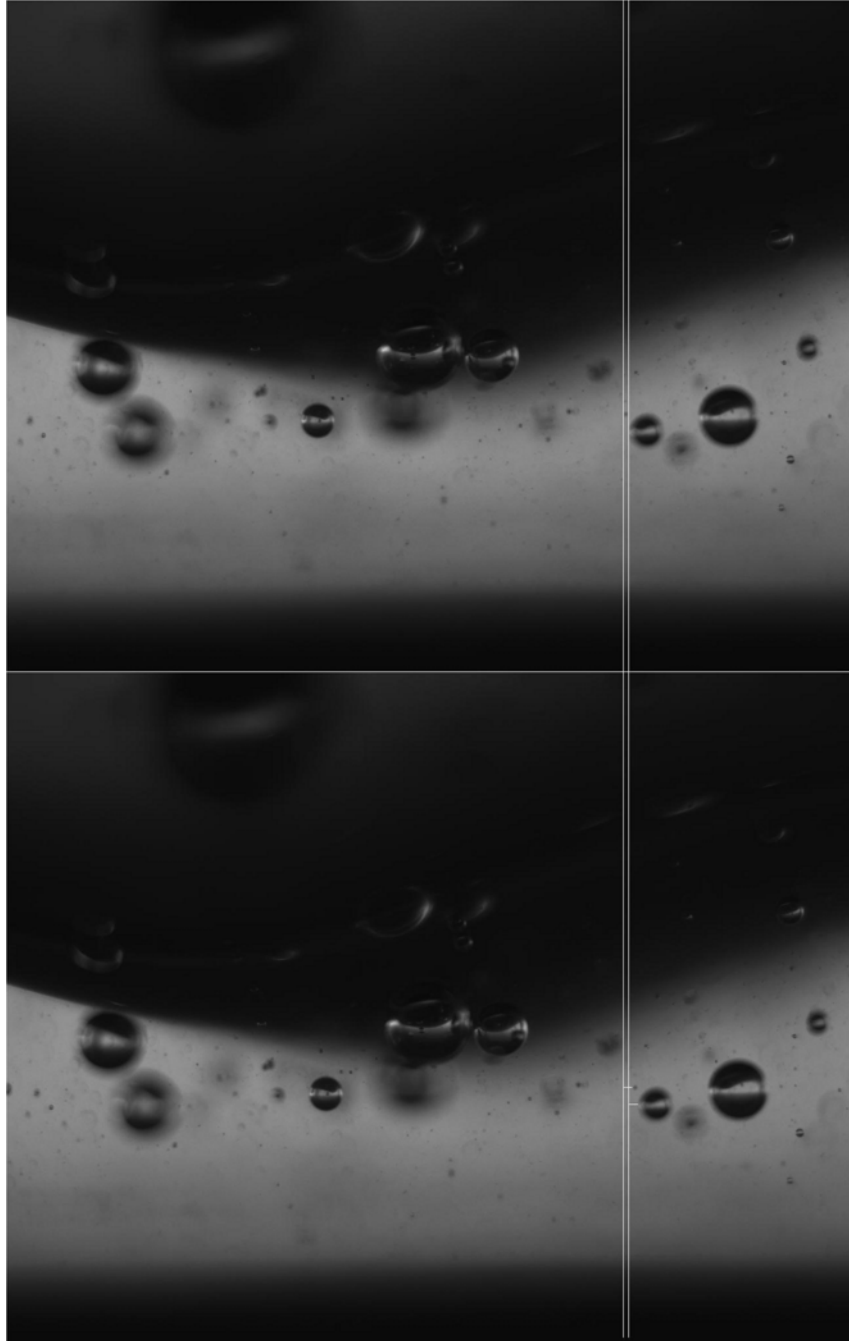


Figure 6.5: First sample pair of IEC images. Captured at  $5\times$  magnification for a stratified flow. The frame represents an area of  $1.742 \times 1.380$  mm. The white vertical lines were used for assistance in tracking individual tracers. Flow from left to right.

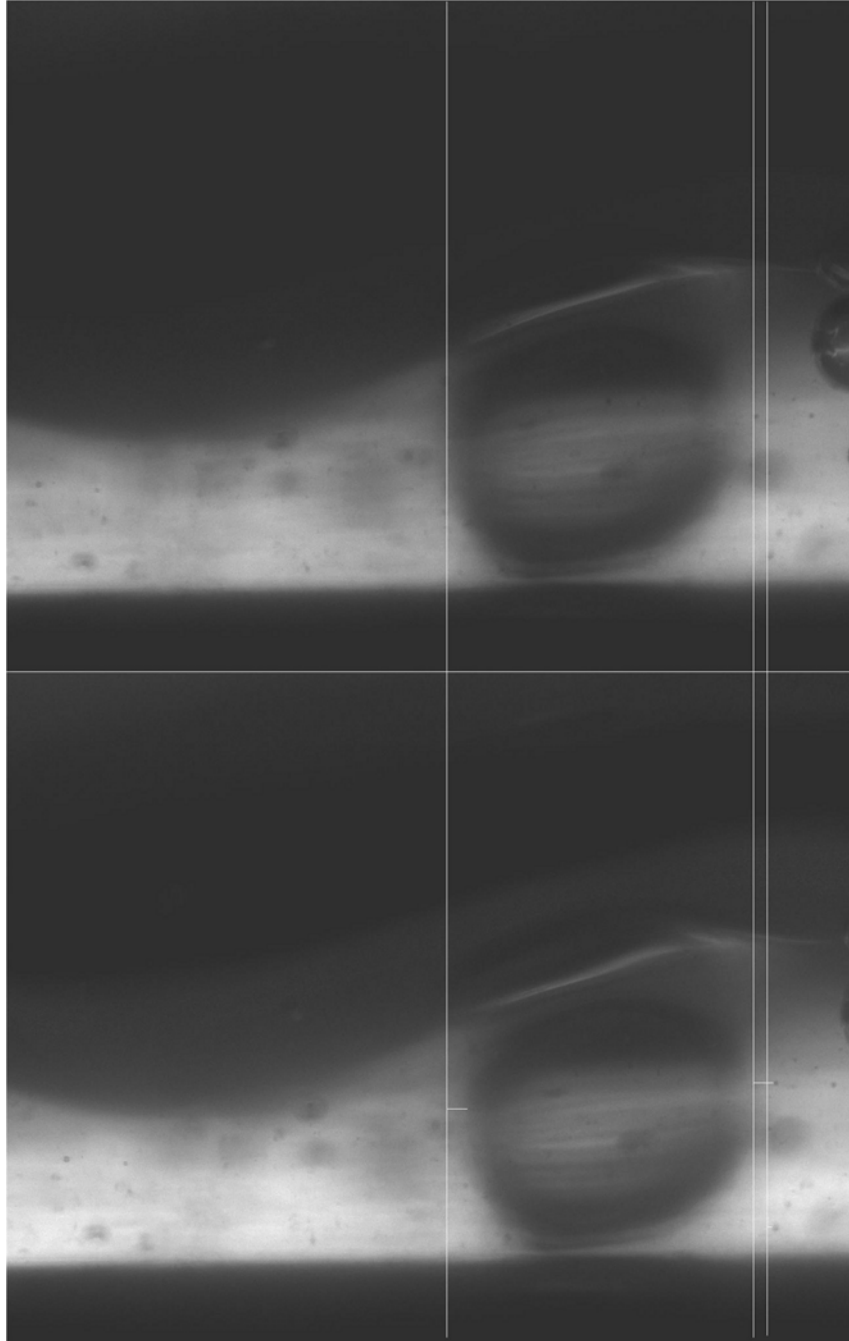


Figure 6.6: Second sample pair of IEC images. Captured at  $5\times$  magnification for a stratified flow. The frame represents an area of  $1.742 \times 1.380$  mm. The white vertical lines were used for assistance in tracking individual tracers. Flow from left to right.

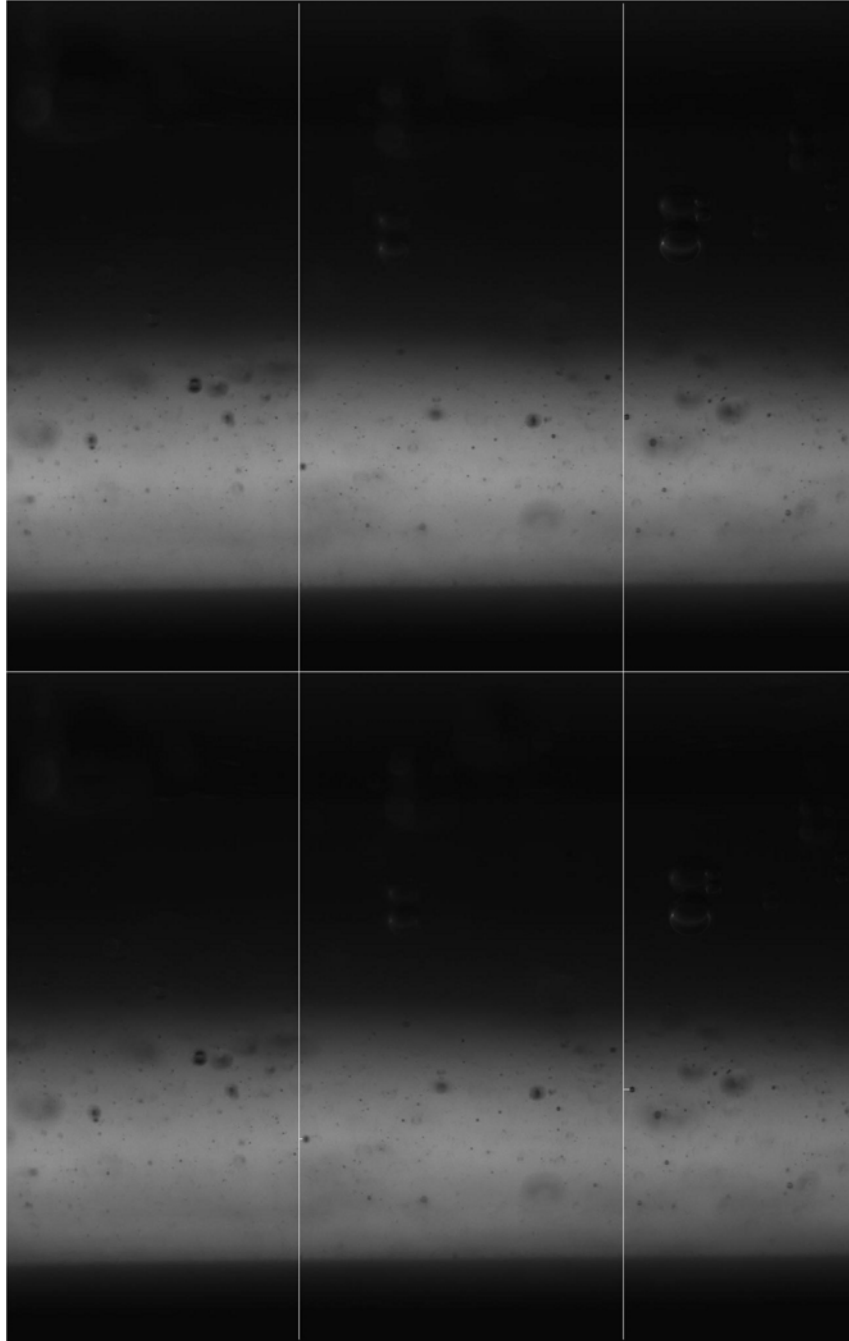


Figure 6.7: Second sample pair of IEC images. Captured at  $5\times$  magnification for a stratified flow. The frame represents an area of  $1.742 \times 1.380$  mm. The white vertical lines were used for assistance in tracking individual tracers. Flow from left to right.

# Chapter 7

## Conclusions

### 7.1 Conclusions from Chapter 2

- A clear association has been established between disturbance wave action and bubble entrainment in the liquid film of horizontal annular flow. Bubble breakup is also linked to the flow mechanics as indicated by the behavior of the power-law exponent.
- Bubble statistics show strong dependence on air flow rate, but only a weak influence of liquid flow rate over the flow conditions studied. This behavior may be explained by the fact that air flow rate determines the velocity, size and nature of waves (i.e., disturbance or roll waves).
- Liquid flow determines disturbance wave frequency but does not affect the bubble distribution.
- The consistent values of the critical Weber number based on mean disturbance wave velocity confirm the association between wave action and bubble breakup for flow settings where dryout was not imminent.
- The entrained bubble number concentration is comparable to the wall nucleation site density during saturated flow boiling. Thus, any potential heat transfer mechanism associated to entrained bubbles should be comparable to the effect of bubbles originated at wall nucleation sites.

## 7.2 Conclusions from Chapter 3

- The PLIF technique provides an enhanced qualitative understanding of the interfacial geometry.
- A better interpretation of conductance probe, capacitance probe and TIR film thickness measurements follows from the statistics produced by the iterative scheme.
- The interfacial wave height and film thickness are strongly dependent on the gas flow rate and weakly dependent on the liquid flow rate.
- The wave folding action bubble entrainment mechanism is very likely to be dominant except at the highest  $U_{sg}$  settings for which the droplet impingement mechanism may become increasingly important.
- Interfacial roughness (RMS) is dominated by interfacial waves whenever they are present.
- Wave detection using the iterative scheme based on  $h_c$  is successful in sorting out film thickness data once an appropriate value of  $k_c$  is determined.
- Care should be taken not to misinterpret the results of the iteration scheme when applied on a waveless interface. Initial guess values that might lead to spurious convergence must be avoided.
- Geometric similarity is suggested by the small standard deviation for the average geometrical proportions among the features of the interface. Further investigation is warranted to extend the generality of the similarity among a wider range of circumferential locations and pipe diameters.

### 7.3 Conclusions from Chapter 4

- For most flows in the current experimental matrix, the pressure gradient originated from interfacial roughness effects is insufficient to account for the measured total pressure gradient. On the other hand, overprediction of the pressure gradient only occurred for the lowest  $U_{sl}$  setting.
- The values of the core acceleration term are expected to be negligible. However the magnitude of this term in one of the run modes of the current implementation suggests the consideration of alternative mechanisms for momentum transfer.
- Disturbance wave formation and acceleration, liquid filament breakup and droplet acceleration are alternative mechanisms of momentum transfer that could be incorporated into the model.
- A more rigorous treatment of the liquid and gas mass balances should include a disturbance wave liquid flow rate as well as an entrained gas fraction.
- The reduction in the value of the two-phase Von Kármán constant could be more severe than predicted by Figure 4.1 for low  $U_{sl}$  flows. This is suggested by the overprediction of the pressure gradient for these flows.
- It is likely that the alternative momentum transfer mechanisms are less significant for the low  $U_{sl}$  flows, except at the highest  $U_{sg}$  setting where underprediction takes place.
- The current form of the Fore *et al.* correlation for the interfacial friction factor could benefit from a more physically meaningful formulation in terms of the roughness Reynolds number and the interfacial roughness.

## 7.4 Conclusions from Chapter 5

- The flattened profile of the teardrop bubble wake when it is sliding near the wall, and the general anisotropy of the flow due to the proximity of the wall, suggest that the 3D RSM results should be preferred.
- The Reynolds stress model may predict larger wakes behind the bubble in the CFD simulation.
- Suppression of turbulence in the surrounding flow was predicted by the CFD simulation of a 15  $\mu\text{m}$  bubble. No turbulent enhancement of heat transfer is expected from this situation. However, the literature indicates that turbulence may be enhanced for larger bubbles.
- The mean heat transfer coefficient in the area influenced by the bubble wake would need to be up to 33 times higher than the overall mean heat transfer coefficient to make the mechanism significant depending on the degree of nucleation suppression, bubble lifetime and nucleation site frequency.
- Further experimental evidence and simulations are required to evaluate whether the localized enhancement of heat transfer is high enough to include the sliding bubble mechanism in future phenomenological models of annular flow boiling heat transfer.
- Two-way coupled, high Reynolds number DNS simulations for bubbles of larger diameters and cross-cut micro-PIV measurements are required to describe the sliding bubble mechanism in more detail.

## 7.5 Conclusions from Chapter 6

- The sample images shown in §6.3 demonstrate the viability of the cross-cut imaging method on a square test section. The full implementation of the method according to the calculations performed in §6.2.6 can become a valuable tool in the study of the sliding bubble mechanism in particular, and the mechanics of annular flow in general.
- Due to the relatively high axial velocities, the Brownian error is negligible for the application of cross-cut micro-PIV to an annular flow regime.
- The high concentration of tracers required for super-resolution PIV analysis may significantly change the properties of the liquid film. For example, suppression of turbulence and foaming are likely to occur. Some sacrifice in spatial resolution may be necessary in order to preserve the non-intrusive nature of the micro-PIV technique.

# Appendix A

## EES Implementation of Flow Boiling

### Correlations

procedure shah( $Fr_L$ ,  $Bo_{Shah}$ ,  $Co$ ,  $h_{DB}$ ,  $ORIENTATION\$$  :  $h_{Shah}$ )

  If ( $ORIENTATION\$ = \text{'Vertical'}$ ) OR ( $Fr_L > 0.04$ ) then

$$N := Co \tag{A.1}$$

  else

$$N := 0.38 \cdot Fr_L^{-0.3} \cdot Co \tag{A.2}$$

  endif

$$h_c := h_{DB} \cdot \frac{1.8}{N^{0.8}} \tag{A.3}$$

  If ( $N > 1.0$ ) then

    If ( $Bo_{Shah} > 0.0003$ ) then

$$h_{NcB} := h_{DB} \cdot 230 \cdot Bo_{Shah}^{0.5} \tag{A.4}$$

    else

$$h_{NcB} := h_{DB} \cdot \left(1 + 46 \cdot Bo_{Shah}^{0.5}\right) \tag{A.5}$$

  endif

else

  If ( $Bo_{Shah} > 0.0011$ ) then

$$F := 14.7 \quad (A.6)$$

  else

$$F := 15.43 \quad (A.7)$$

  endif

  If ( $N < 0.1$ ) then

$$h_{NcB} := h_{DB} \cdot F \cdot Bo_{Shah}^{0.5} \cdot \exp(2.47 \cdot N^{-0.15}) \quad (A.8)$$

  else

$$h_{NcB} := h_{DB} \cdot F \cdot Bo_{Shah}^{0.5} \cdot \exp(2.74 \cdot N^{-0.10}) \quad (A.9)$$

  endif

endif

$$h_{Shah} := \max(h_{NcB}, h_c) \quad (A.10)$$

end *shah*

procedure E2S2( $Fr_l$ ,  $ORIENTATION\$$  :  $E_2$ ,  $S_2$ )

  If ( $ORIENTATION\$ = 'Vertical'$ ) OR ( $Fr_l > 0.05$ ) then

$$E_2 := 1 \quad (A.11)$$

$$S_2 := 1 \quad (A.12)$$

else

$$E_2 = Fr_l^{0.1-2 \cdot Fr_l} \quad (\text{A.13})$$

$$S_2 = Fr_l^{0.5} \quad (\text{A.14})$$

endif

end *E2S2*

procedure kand(*BoKand*, *Co*, *Fr<sub>l</sub>*, *x*, *Re<sub>lo</sub>*, *Fr<sub>L</sub>*, *k<sub>L</sub>*, *D*, *h<sub>DB</sub>*, *h<sub>DB,lo</sub>*,  
*ORIENTATION*\$, *MATERIAL*\$, *FLUID*\$ : *h<sub>Kandlikar</sub>*, *h<sub>NBD</sub>*, *h<sub>CBD</sub>*)

If (*MATERIAL*\$ = 'Copper' ) then

$$F_{Fl} = \text{Lookup}(\text{'Copper'}, 1, \text{FLUID}\$) \quad (\text{A.15})$$

else

$$F_{Fl} = 1 \quad (\text{A.16})$$

endif

$$f = (1.58 \cdot \ln(Re_{lo}) - 3.28)^{-2} \quad (\text{A.17})$$

If (*ORIENTATION*\$ = 'Vertical' )OR(*Fr<sub>L</sub>* > 0.04) then

$$f_2 := 1 \quad (\text{A.18})$$

else

$$f_2 := (25 \cdot Fr_l)^{0.3} \quad (\text{A.19})$$

endif

If  $(Pr_L \geq 0.5) \text{AND} (Pr_L \leq 2000)$  then

If  $(Re_{lo} < 10000) \text{AND} (Re_{lo} \geq 2300)$  then

$$h_l := \frac{(Re_{lo} - 1000) \cdot Pr_L \cdot (f/2) \cdot (k_L/D)}{1 + 12.7 \cdot (Pr_L^{2/3} - 1) \cdot (f/2)^{0.5}} \quad \text{Gnielinski (1976)} \quad (\text{A.20})$$

endif

If  $(Re_{lo} \geq 10000) \text{AND} (Re_{lo} \leq 5000000)$  then

$$h_l := \frac{Re_{lo} \cdot Pr_L \cdot (f/2) \cdot (k_L/D)}{1.07 + 12.7 \cdot (Pr_L^{2/3} - 1) \cdot (f/2)^{0.5}} \quad \text{Petukhov and Popov (1963)} \quad (\text{A.21})$$

endif

If  $(Re_{lo} < 2300) \text{OR} (Re_{lo} > 5000000)$  then

$$h_l := h_{DB,lo} \quad (\text{A.22})$$

endif

else

$$h_l := h_{DB,lo} \quad (\text{A.23})$$

endif

$$h_{NBD} := 0.6683 \cdot Co^{-0.2} \cdot (1 - x)^{0.8} \cdot f_2 \cdot h_l + 1058.0 \cdot Bo_{Kand}^{0.7} \cdot (1 - x)^{0.8} \cdot F_{Fl} \cdot h_l \quad (\text{A.24})$$

$$h_{CBD} := 1.136 \cdot Co^{-0.9} \cdot (1 - x)^{0.8} \cdot f_2 \cdot h_l + 667.2 \cdot Bo_{Kand}^{0.7} \cdot (1 - x)^{0.8} \cdot F_{Fl} \cdot h_l \quad (\text{A.25})$$

$$h_{Kandlikar} := \max(h_{NBD}, h_{CBD}) \quad (\text{A.26})$$

end *kand*

procedure thome( $x, h_{Cooper,Thome}, G, \mu_L, \mu_V, \rho_V, \rho_L, \sigma, Pr_L, Pr_V, k_L, k_V, D, \theta_{dry}, \theta_{strat}, REGIME\$ : h_{thome}, h_{wet}, h_{vapor}, \delta$ )

$$\alpha_R = (x/\rho_V) \cdot ((1 + 0.12 \cdot (1 - x)) \cdot \left( (x/\rho_V) + \frac{1 - x}{\rho_L} \right) + \quad (A.27)$$

$$\left( 1.18 \cdot (1 - x) \cdot (g\# \cdot \sigma \cdot (\rho_L - \rho_V))^{0.25} / (G \cdot \rho_L^{0.5}) \right)^{-1}$$

Rouhani-Axelsson (1970) as appears on Zurcher et.al.

$$C = 0.0133 \quad (A.28)$$

$$m = 0.69 \quad (A.29)$$

If ( $REGIME\$ = \text{'Stratified Wavy'}$ ) OR ( $REGIME\$ = \text{'Stratified'}$ ) then

  If ( $REGIME\$ = \text{'Stratified Wavy'}$ ) then

$$\theta_{dry,thome} = \theta_{dry} \quad (A.30)$$

  else

$$\theta_{dry,thome} = \theta_{strat} \quad (A.31)$$

endif

else    If ( $REGIME\$ = \text{'Annular'}$ ) OR ( $REGIME\$ = \text{'Intermittent'}$ ) then

$$\theta_{dry,thome} = 0 \quad (A.32)$$

else

$$\theta_{dry,thome} = 2 \cdot \pi \quad \text{For Mist Flow, Added by D. J. Rodríguez} \quad (A.33)$$

endif  
endif

$$\delta = \frac{\pi \cdot D \cdot (1 - \alpha_R)}{2 \cdot (2 \cdot \pi - \theta_{dry})} \quad (\text{A.34})$$

$$Re_L = \frac{4 \cdot G \cdot (1 - x) \cdot \delta}{(1 - \alpha_R) \cdot \mu_L} \quad (\text{A.35})$$

$$Re_V = \frac{G \cdot x \cdot D}{\alpha_R \cdot \mu_v} \quad (\text{A.36})$$

$$h_{cb} := C \cdot Re_L^m \cdot Pr_L^{0.4} \cdot \left( \frac{k_L}{\delta} \right) \quad \text{KTF (1998)} \quad (\text{A.37})$$

Dittus-Boelter (1930) for vapor heat transfer

$$h_{vapor} := 0.023 \cdot Re_V^{0.8} \cdot Pr_V^{0.4} \cdot (k_V/D) \quad (\text{A.38})$$

$$h_{nb} := h_{Cooper,Thome} \quad (\text{A.39})$$

$$h_{wet} := (h_{nb}^3 + h_{cb}^3)^{1/3} \quad (\text{A.40})$$

$$h_{thome} := \frac{\theta_{dry,thome} \cdot h_{vapor} + (2 \cdot \pi - \theta_{dry,thome}) \cdot h_{wet}}{2 \cdot \pi} \quad (\text{A.41})$$

end *thome*

procedure flowregime( $G, x, G_{strat}, G_{wavy}, G_{MF}, x_{AI} : REGIME\$$ )

  If ( $G < G_{strat}$ ) then

$$REGIME\$ := \text{'Stratified'} \quad (\text{A.42})$$

  else

If ( $G < G_{wavy}$ ) then

$$REGIME\$ := \text{'Stratified Wavy'} \quad (A.43)$$

else

If ( $G < G_{MF}$ ) then

If ( $x < x_{AI}$ ) then

$$REGIME\$ := \text{'Intermittent'} \quad (A.44)$$

else

$$REGIME\$ := \text{'Annular'} \quad (A.45)$$

endif

else

$$REGIME\$ := \text{'Mist Flow'} \quad (A.46)$$

endif

endif

endif

end *flowregime*

module *stratified*( $\nu, x, G, \rho_L, \rho_V, \mu_L, \mu_V, D, A : G_{strat}, \theta_{strat}, \theta_{wet}, \alpha_{TD}, A_V$ )

$$S_L = D \cdot \theta_{wet}/2 \quad (A.47)$$

$$S_V = D \cdot (\pi - \theta_{wet}/2) \quad (A.48)$$

$$Perimeter = S_L + S_V \quad (A.49)$$

$$S_i = D \cdot \sin(\theta_{wet}/2) \quad (\text{A.50})$$

$$A_L = \frac{D^2}{8} \cdot (\theta_{wet} - \sin(\theta_{wet})) \quad (\text{A.51})$$

$$A_L = (1 - \alpha_{TD}) \cdot A \quad (\text{A.52})$$

$$A_V = A - A_L \quad (\text{A.53})$$

$$\bar{h}_L = 0.5 \cdot (1 - \cos(\theta_{wet}/2)) \quad (\text{A.54})$$

$$X_{tt} = (\mu_L/\mu_V)^{0.125} \cdot \left(\frac{1-x}{x}\right)^{0.875} \cdot (\rho_V/\rho_L)^{0.5} \quad (\text{A.55})$$

Taitel-Dukler (1976)

$$X_{tt}^2 \cdot \left(\frac{S_L^{1.2}}{(1 - \alpha_{TD})^3}\right) - \left((S_V + S_i)^{0.2} / \alpha_{TD}^2 \cdot ((S_V + S_i) / \alpha_{TD} + S_i / (1 - \alpha_{TD}))\right) = 0 \quad (\text{A.56})$$

$$G_{strat} = \left(800 \cdot \frac{\alpha_{TD}^2 \cdot (1 - \alpha_{TD})}{(x^2 \cdot (1 - x))} \cdot \rho_V \cdot g\# \cdot (\rho_L - \rho_V) \cdot \mu_L \cdot \cos(\nu)\right)^{1/3} \quad (\text{A.57})$$

$$\theta_{strat} = (2 \cdot \pi - \theta_{wet}) \quad (\text{A.58})$$

end stratified

*SUBPROGRAM*gwt(*G1*, *G2*,  $\bar{h}_L$ , *Re<sub>D</sub>*,  $\nu$ ,  $\lambda$ , *B<sub>r</sub>*,  $\rho_V$ ,  $\rho_L$ , *D*, *FrWe*, *x*,  $\theta_{wet}$ ,  $\sigma : G_{wavy}$ )

Zurcher 2002

$$G_{wavy} = \left(\frac{g\# \cdot D \cdot \rho_L \cdot \rho_V \cdot \alpha_R^3 \cdot \pi}{2 \cdot x^2 \cdot \sqrt{(2 \cdot (1 - \cos(\theta_{wet}))}}\right) \quad (\text{A.59})$$

$$\cdot \left(1 + \pi^2 / (25 \cdot \bar{h}_L^2) \cdot (1 - x)^{G1} \cdot (FrWe)^{G2} + (\bar{h}_L \cdot \lambda \cdot G_{wavy}^2 \cdot x^2) / (B_r \cdot \rho_V \cdot \alpha_R^{5/2})\right)^{0.5}$$

Rouhani- Axelsson (1970) as appears on Zurcher et.al.

$$\alpha_R = (x/\rho_V) \cdot ((1 + 0.12 \cdot (1 - x)) \cdot \left((x/\rho_V) + \frac{1-x}{\rho_L}\right) + \quad (\text{A.60})$$

$$\left(1.18 \cdot (1 - x) \cdot (g\# \cdot \sigma \cdot (\rho_L - \rho_V))^{0.25} / (G_{wavy} \cdot \rho_L^{0.5})\right)^{-1}$$

end *gwt*

procedure *wavy*( $\nu$ ,  $\sigma$ ,  $\rho_V$ ,  $\rho_L$ ,  $D$ ,  $A$ ,  $FrWe$ ,  $q_{crit}$ ,  $\bar{q}$ ,  $G$ ,  $\mu_L$ ,  $\mu_V$ ,  $x$ ,  $G_{MF}$ ,  $G_{strat}$ ,  $\theta_{wet}$   
:  $LIQUID_{FLOW\$}$ ,  $G_{wavy}$ )

$$\bar{h}_L = 0.5 \cdot (1 - \cos(\theta_{wet}/2)) \quad (A.61)$$

$$Re_D = G \cdot (1 - x) \cdot D / \mu_L \quad (A.62)$$

$$\lambda = (1.8 \cdot \ln(Re_D) - 1.64)^{-2} \quad \text{Friction Factor} \quad (A.63)$$

$$B_r := 3.0 \quad (A.64)$$

$$q_{star} := \bar{q} / q_{crit} \quad (A.65)$$

If ( $q_{star} \geq 0.0374$ ) then

$$G1 := -24.12 \cdot q_{star} \quad (A.66)$$

$$G2 := 4.825 \cdot q_{star} + 1 \quad (A.67)$$

else

$$G1 := 0 \quad (A.68)$$

$$G2 := 1 \quad (A.69)$$

endif

If ( $(Re_D > 650) \text{ or } (x < 0.9)$ ) then

$$LIQUID_{FLOW\$} := \text{'Turbulent'} \quad (A.70)$$

call  $gwt(G1, G2, \bar{h}_L, Re_D, \nu, \lambda, B_r, \rho_V, \rho_L, D, FrWe, x, \theta_{wet}, \sigma : G_{wavy})$

else

$$LIQUID_{FLOW\$} := \text{'Laminar'}$$
 (A.71)

$$G_{wavy} := \frac{650 \cdot \mu_L}{(1-x) \cdot D}$$
 (A.72)

endif

end *wavy*

procedure *wavymin*( $\sigma, \rho_V, \rho_L, D, FrWe, q_{crit}, \bar{q}, G, \mu_L, \mu_V, x, \theta_{wet}, Re_D :$   
 $G1, G2, \bar{h}_L, \lambda, B_r$ )

$$\bar{h}_L = 0.5 \cdot (1 - \cos(\theta_{wet}/2))$$
 (A.73)

$$\lambda = (1.8 \cdot \ln(Re_D) - 1.64)^{-2} \quad \text{Friction Factor}$$
 (A.74)

$$B_r := 3.0$$
 (A.75)

$$q_{star} := \bar{q}/q_{crit}$$
 (A.76)

If ( $q_{star} \geq 0.0374$ ) then

$$G1 := -24.12 \cdot q_{star}$$
 (A.77)

$$G2 := 4.825 \cdot q_{star} + 1$$
 (A.78)

else

$$G1 := 0$$
 (A.79)

$$G2 := 1$$
 (A.80)

endif  
end *wavym*

*SUBPROGRAM**xwavym*(*D*, *A*,  $\rho_L$ ,  $\rho_V$ , *FrWe*,  $\sigma$ , *G*,  $\mu_L$ ,  $\mu_V$ ,  $\nu$ , *qcrit*,  $\bar{q} : x_{wavy,min}$ )

$$\delta_x = 0.000001 \quad (\text{A.81})$$

determines *xwavy,min*

call *stratified*( $\nu$ , *xplus*, *G*,  $\rho_L$ ,  $\rho_V$ ,  $\mu_L$ ,  $\mu_V$ , *D*, *A* :

*G*<sub>*strat,plus*</sub>,  $\theta_{strat,plus}$ ,  $\theta_{wet,plus}$ ,  $\alpha_{TD,plus}$ , *A*<sub>*V,plus*</sub>)

call *stratified*( $\nu$ , *xminus*, *G*,  $\rho_L$ ,  $\rho_V$ ,  $\mu_L$ ,  $\mu_V$ , *D*, *A* :

*G*<sub>*strat,minus*</sub>,  $\theta_{strat,minus}$ ,  $\theta_{wet,minus}$ ,  $\alpha_{TD,minus}$ , *A*<sub>*V,minus*</sub>)

$$x_{plus} = (x_{wavy,min} + \delta_x) \quad (\text{A.82})$$

$$x_{minus} = (x_{wavy,min} - \delta_x) \quad (\text{A.83})$$

$$Re_{D,plus} \cdot \mu_L = G \cdot (1 - x_{plus}) \cdot D \quad (\text{A.84})$$

$$Re_{D,minus} \cdot \mu_L = G \cdot (1 - x_{minus}) \cdot D \quad (\text{A.85})$$

call *wavym*( $\sigma$ ,  $\rho_V$ ,  $\rho_L$ , *D*, *FrWe*, *qcrit*,  $\bar{q}$ , *G*,  $\mu_L$ ,  $\mu_V$ , *xplus*,  $\theta_{wet,plus}$ , *Re*<sub>*D,plus*</sub> :

*G*<sub>*1,plus*</sub>, *G*<sub>*2,plus*</sub>,  $\bar{h}_{L,plus}$ ,  $\lambda_{plus}$ , *B*<sub>*r,plus*</sub>)

call *wavym*( $\sigma$ ,  $\rho_V$ ,  $\rho_L$ , *D*, *FrWe*, *qcrit*,  $\bar{q}$ , *G*,  $\mu_L$ ,  $\mu_V$ , *xminus*,  $\theta_{wet,minus}$ , *Re*<sub>*D,minus*</sub> :

*G*<sub>*1,minus*</sub>, *G*<sub>*2,minus*</sub>,  $\bar{h}_{L,minus}$ ,  $\lambda_{minus}$ , *B*<sub>*r,minus*</sub>)

call *gwt*(*G*<sub>*1,plus*</sub>, *G*<sub>*2,plus*</sub>,  $\bar{h}_{L,plus}$ , *Re*<sub>*D,plus*</sub>,  $\nu$ ,  $\lambda_{plus}$ , *B*<sub>*r,plus*</sub>,  $\rho_V$ ,  $\rho_L$ , *D*, *FrWe*,

*xplus*,  $\theta_{wet,plus}$ ,  $\sigma : G_{wavy,plus}$ )

call *gwt*(*G*<sub>*1,minus*</sub>, *G*<sub>*2,minus*</sub>,  $\bar{h}_{L,minus}$ , *Re*<sub>*D,minus*</sub>,  $\nu$ ,  $\lambda_{minus}$ , *B*<sub>*r,minus*</sub>,  $\rho_V$ ,  $\rho_L$ , *D*, *FrWe*,

*xminus*,  $\theta_{wet,minus}$ ,  $\sigma : G_{wavy,minus}$ )

$$dG_{wavy} \cdot (2 \cdot \delta_x) = (G_{wavy,plus} - G_{wavy,minus}) \quad (\text{A.86})$$

$$dG_{wavy} = 0 \quad (\text{A.87})$$

end *xwavymin*

module *xmfmin*( $D, \rho_L, \rho_V, FrWe, \sigma, G, \mu_L, \mu_V : x_{MF,min}$ )

$$\delta_x = 0.000001 \quad (\text{A.88})$$

determines  $x_{MF,min}$

Zurcher(2002)

$$\alpha_{R,plus} = \left( \frac{x_{MF,min} + \delta_x}{\rho_V} \right) \cdot ((1 + 0.12 \cdot (1 - (x_{MF,min} + \delta_x))) \cdot (\text{A.89})$$

$$\begin{aligned} & (((x_{MF,min} + \delta_x) / \rho_V) + (1 - (x_{MF,min} + \delta_x)) / \rho_L) \\ & + (1.18 \cdot (1 - (x_{MF,min} + \delta_x)) \cdot (g\# \cdot \sigma \cdot (\rho_L - \rho_V))^{0.25} / (G_{MF,plus} \cdot \rho_L^{0.5}))^{-1} \end{aligned}$$

Zurcher(2002)

$$\alpha_{R,minus} = \left( \frac{x_{MF,min} - \delta_x}{\rho_V} \right) \cdot ((1 + 0.12 \cdot (1 - (x_{MF,min} - \delta_x))) \cdot (\text{A.90})$$

$$\begin{aligned} & (((x_{MF,min} - \delta_x) / \rho_V) + (1 - (x_{MF,min} - \delta_x)) / \rho_L) \\ & + (1.18 \cdot (1 - (x_{MF,min} - \delta_x)) \cdot (g\# \cdot \sigma \cdot (\rho_L - \rho_V))^{0.25} / (G_{MF,minus} \cdot \rho_L^{0.5}))^{-1} \end{aligned}$$

$$G_{MF,plus} \cdot (x_{MF,min} + \delta_x) = (\alpha_{R,plus}) \cdot \left( 1.138 + 2 \cdot \log \left( \frac{8}{3 \cdot (1 - \alpha_{R,plus})} \right) \right) \cdot (\text{A.91})$$

$$(480 \cdot g\# \cdot D \cdot \rho_L \cdot \rho_V \cdot FrWe)^{0.5}$$

$$G_{MF,minus} \cdot (x_{MF,min} - \delta_x) = (\alpha_{R,minus}) \cdot \left( 1.138 + 2 \cdot \log \left( \frac{8}{3 \cdot (1 - \alpha_{R,minus})} \right) \right). \quad (\text{A.92})$$

$$(480 \cdot g\# \cdot D \cdot \rho_L \cdot \rho_V \cdot FrWe)^{0.5}$$

$$dG_{MF} = \frac{G_{MF,plus} - G_{MF,minus}}{2 \cdot \delta_x} \quad (\text{A.93})$$

$$dG_{MF} = 0 \quad (\text{A.94})$$

end *xmfmin*

procedure mf(*x*, *x*<sub>MF,min</sub>,  $\rho_V$ ,  $\rho_L$ , *FrWe*,  $\sigma$ , *G*, *D*,  $\mu_L$ ,  $\mu_V$  : *G*<sub>MF</sub>)

Rouhani-Axelsson (1970) as appears on Zurcher et.al.

$$\alpha_{R,min} = (x_{MF,min}/\rho_V) \cdot ((1 + 0.12 \cdot (1 - x_{MF,min}))). \quad (\text{A.95})$$

$$\left( (x_{MF,min}/\rho_V) + \frac{1-x_{MF,min}}{\rho_L} \right) + \left( 1.18 \cdot (1 - x_{MF,min}) \cdot (g\# \cdot \sigma \cdot (\rho_L - \rho_V))^{0.25} / (G \cdot \rho_L^{0.5}) \right)^{-1}$$

Rouhani-Axelsson (1970) as appears on Zurcher et.al.

$$\alpha_R = (x/\rho_V) \cdot ((1 + 0.12 \cdot (1 - x))). \quad (\text{A.96})$$

$$\left( (x/\rho_V) + \frac{1-x}{\rho_L} \right) + \left( 1.18 \cdot (1 - x) \cdot (g\# \cdot \sigma \cdot (\rho_L - \rho_V))^{0.25} / (G \cdot \rho_L^{0.5}) \right)^{-1}$$

If  $(x < x_{MF,min})$  then

$$G_{MF} := (\alpha_R/x) \cdot \left( 1.138 + 2 \cdot \log \left( \frac{8}{3 \cdot (1 - \alpha_R)} \right) \right). \quad (\text{A.97})$$

$$(480 \cdot g\# \cdot D \cdot \rho_L \cdot \rho_V \cdot FrWe)^{0.5}$$

else

$$G_{MF} := (\alpha_{R,min}/x_{MF,min}) \cdot \left( 1.138 + 2 \cdot \log \left( \frac{8}{3 \cdot (1 - \alpha_{R,min})} \right) \right). \quad (\text{A.98})$$

$$(480 \cdot g\# \cdot D \cdot \rho_L \cdot \rho_V \cdot FrWe)^{0.5}$$

endif

end *mf*

module *xmax*( $\nu, G, \rho_L, \rho_V, \mu_L, \mu_V, D, A, \sigma, FrWe, q_{crit}, \bar{q}, x_{MF,min} :$

$\theta_{max}, \theta_{strat,max}, x_{max}$ ) Calls of procedures for finding  $x_{max}$  and  $\theta_{max}$

call *stratified*( $\nu, x_{max}, G, \rho_L, \rho_V, \mu_L, \mu_V, D, A :$

$G_{strat,max}, \theta_{strat,max}, \theta_{wet,max}, \alpha_{TD,max}, A_{V,max}$ )

call *wavy*( $\nu, \sigma, \rho_V, \rho_L, D, A, FrWe, q_{crit}, \bar{q}, G, \mu_L, \mu_V, x_{max}, G_{MF,max}, G_{strat,max},$

$\theta_{wet,max} : LIQUIDFLOW,max\$, G_{wavy,max}$ )

call *mf*( $x_{max}, x_{MF,min}, \rho_V, \rho_L, FrWE, \sigma, G, D, \mu_L, \mu_V : G_{MF,max}$ )

$$G_{wavy,max} = G_{MF,max} \quad \text{determine } x_{max} \quad (\text{A.99})$$

determine  $\theta_{max}$ , (dry angle for  $x_{max}$ )

$$\theta_{max} \cdot (G_{wavy,max} - G_{strat,max}) = \theta_{strat,max} \cdot (G_{wavy,max} - G) \quad (\text{A.100})$$

end *xmax*

procedure *thetadry*(*x*, *xmax*,  $\theta_{max}$ ,  $\theta_{strat}$ ,  $\theta_{strat,max}$ ,  $G_{strat}$ ,  $G_{wavy}$ ,  $G$ ,  $\theta_{dry,star}$  :  
 $\theta_{dry}$ ,  $\theta_{wet,wavy}$ )

If ( $x < x_{max}$ ) then

$$\theta_{dry} = \theta_{dry,star} \quad (\text{A.101})$$

else

$$\theta_{dry} = (2 \cdot \pi - \theta_{max}) \cdot \frac{x - x_{max}}{1.0 - x_{max}} + \theta_{max} \quad (\text{A.102})$$

endif

$$\theta_{wet,wavy} = 2 \cdot \pi - \theta_{dry} \quad (\text{A.103})$$

end *thetadry*

Fluid Properties

$$C_{pL} = c_p(\text{FLUID}\$, T = T_{mix}, x = 0) \quad \text{Specific heat of liquid} \quad (\text{A.104})$$

$$k_L = \lambda(\text{FLUID}\$, T = T_{mix}, x = 0) \quad \text{conductivity of liquid} \quad (\text{A.105})$$

$$k_V = \lambda(\text{FLUID}\$, T = T_{mix}, x = 1) \quad \text{conductivity of vapor} \quad (\text{A.106})$$

$$\rho_L = \rho(\text{FLUID}\$, T = T_{mix}, x = 0) \quad \text{density of liquid} \quad (\text{A.107})$$

$$\rho_V = \rho(\text{FLUID}\$, T = T_{mix}, x = 1) \quad \text{density of Vapor} \quad (\text{A.108})$$

$$\mu_L = \mu(\text{FLUID}\$, T = T_{mix}, x = 0) \quad \text{viscosity of liquid} \quad (\text{A.109})$$

$$\mu_V = \mu(\text{FLUID}\$, T = T_{mix}, x = 1) \quad \text{viscosity of Vapor} \quad (\text{A.110})$$

$$\sigma = \gamma(\text{FLUID}\$, T = T_{mix}) \quad (\text{A.111})$$

$$Pr_L = P_r(\text{FLUID}\$, T = T_{mix}, x = 0) \quad \text{Prandtl number of liquid} \quad (\text{A.112})$$

$$Pr_V = P_r(\text{FLUID}\$, T = T_{mix}, x = 1) \quad \text{Prandtl number of vapor} \quad (\text{A.113})$$

$$h_V = h(\text{FLUID}\$, T = T_{mix}, x = 1) \quad \text{enthalpy of vapor} \quad (\text{A.114})$$

$$h_L = h(\text{FLUID}\$, T = T_{mix}, x = 0) \quad \text{enthalpy of liquid} \quad (\text{A.115})$$

$$T_{mix} = T(\text{FLUID}\$, P = P_{mix}, x = 0.5) \quad \text{sat. pressure at bulk temperature} \quad (\text{A.116})$$

$$h_{lv} = h_V - h_L \quad \text{enthalpy of vaporization} \quad (\text{A.117})$$

$$P_{crit} = P_{crit}(\text{FLUID}\$) \quad (\text{A.118})$$

$$T_{crit} = T_{crit}(\text{FLUID}\$) \quad (\text{A.119})$$

$$M = MW(\text{FLUID}\$) \quad (\text{A.120})$$

### Dimensionless Quantities

$$Re_D = G \cdot (1 - x) \cdot D / \mu_L \quad (\text{A.121})$$

$$Re_L = Re_D \quad (\text{A.122})$$

$$Re_{lo} = G \cdot D / \mu_L \quad (\text{A.123})$$

$$X_{tt} = (\mu_L / \mu_V)^{0.125} \cdot \left( \frac{1 - x}{x} \right)^{0.875} \cdot (\rho_V / \rho_L)^{0.5} \quad (\text{A.124})$$

$$Fr_l = \frac{G^2}{\rho_L^2 \cdot g_{\#} \cdot D} \quad (\text{A.125})$$

$$Bo_{Shah} = \bar{q}_{Shah} \cdot \frac{\left| 0.001 \frac{kW}{W} \right|}{G \cdot h_{lv}} \quad (\text{A.126})$$

$$Bo_{GW} = \bar{q}_{GW} \cdot \frac{\left| 0.001 \frac{kW}{W} \right|}{G \cdot h_{lv}} \quad (A.127)$$

$$Bo_{Kand} = \bar{q}_{Kandlikar} \cdot \frac{\left| 0.001 \frac{kW}{W} \right|}{G \cdot h_{lv}} \quad (A.128)$$

$$Co = \left( \frac{1-x}{x} \right)^{0.8} \cdot (\rho_v/\rho_l)^{0.5} \quad (A.129)$$

$$FrWe = \frac{\sigma}{g\# \cdot D^2 \cdot \rho_L} \quad (A.130)$$

$$P_{reduced} = P_{mix}/P_{crit} \quad (A.131)$$

Inclination angle

$$\nu = 0.7853 \quad (A.132)$$

Critical Heat Flux

$$q_{crit} = 0.131 \cdot \rho_V^{0.5} \cdot h_{lv} \cdot \left| 1000 \frac{J}{kJ} \right| \cdot (g\# \cdot (\rho_L - \rho_V) \cdot \sigma)^{0.25} \quad \text{Kutateladze} \quad (A.133)$$

Dittus-Boelter single phase convection (1930) for Chen,Shah,GW and LW

$$C = 20 \quad (A.134)$$

$$\phi_{Ltt} = \left( 1 + C/X_{tt} + \frac{1}{X_{tt}^2} \right)^{0.5} \quad (A.135)$$

$$F = \left( \phi_{Ltt}^2 \right)^{0.444} \quad \text{from heat-momentum transfer analogy} \quad (A.136)$$

$$h_{DB} = 0.023 \cdot Re_L^{0.8} \cdot Pr_L^{0.4} \cdot (k_L/D) \quad (A.137)$$

$$h_{DB,lo} = 0.023 \cdot Re_{lo}^{0.8} \cdot Pr_L^{0.4} \cdot (k_L/D) \quad (A.138)$$

$$h_{mac} = h_{DB} \cdot F \quad (A.139)$$

Forster-Zuber pool boiling (1955) for Chen (1966)

$$Re_{tp} = Re_L \cdot F^{1.25} \quad (\text{A.140})$$

$$S_{Chen} = \frac{1}{1 + 2.56 \times 10^{-6} \cdot Re_{tp}^{1.17}} \quad (\text{A.141})$$

from Collier's (1981) fit to Chen's original curve

$$\Delta P = P_{w,Chen} - P_{mix} \quad (\text{A.142})$$

$$h_{FZ} = 0.00122 \cdot \left( \frac{k_l^{0.79} \cdot C_{pL}^{0.45} \cdot \rho_L^{0.49}}{\left( \sigma \cdot \left| 0.001 \frac{kN}{N} \right| \right)^{0.5} \cdot \mu_L^{0.29} \cdot h_{lv}^{0.24} \cdot \rho_v^{0.24}} \right) \cdot \Delta T_{Chen}^{0.24} \cdot \Delta P^{0.75} \quad (\text{A.143})$$

$$h_{mic} = h_{FZ} \cdot S_{Chen} \quad (\text{A.144})$$

Chen (1966)

$$h_{Chen} = h_{mic} + h_{mac} \quad (\text{A.145})$$

$$\Delta T_{Chen} = T_{W,Chen} - T_{mix} \quad (\text{A.146})$$

$$P_{w,Chen} = P(\text{FLUID}, T = T_{W,Chen}, x = 0.5) \quad (\text{A.147})$$

sat. pressure at wall temperature

$$\bar{q}_{Chen} = h_{Chen} \cdot \Delta T_{Chen} \quad (\text{A.148})$$

Shah (1976,1982)

$$\Delta T_{Shah} = T_{W,Shah} - T_{mix} \quad (\text{A.149})$$

$$\bar{q}_{Shah} = h_{Shah} \cdot \Delta T_{Shah} \quad (\text{A.150})$$

call shah( $Fr_l$ ,  $Bo_{Shah}$ ,  $Co$ ,  $h_{DB}$ ,  $ORIENTATION\$$  :  $h_{Shah}$ )

Gungor-Winterton (1986)

$$E_{GW} = 1 + 24000 \cdot Bo_{GW}^{1.16} + 1.37 \cdot (1/X_{tt})^{0.86} \quad (A.151)$$

$$S_{GW} = \frac{1}{1 + 1.15 \times 10^{-6} \cdot E_{GW}^2 \cdot Re_L^{1.17}} \quad (A.152)$$

$$\text{call E2S2}(Fr_l, ORIENTATION\$ : E_2, S_2) \quad (A.153)$$

Cooper pool boiling (1984a)

$$h_{Cooper,GW} = 55 \cdot P_{reduced}^{0.12} \cdot (-\log(P_{reduced}))^{-0.55} \cdot M^{-0.5} \cdot \bar{q}_{GW}^{0.67} \quad (A.154)$$

$$h_{GungorWinterton} = E_2 \cdot E_{GW} \cdot h_{DB} + S_2 \cdot S_{GW} \cdot h_{Cooper,GW} \quad (A.155)$$

$$\Delta T_{GW} = T_{W,GW} - T_{mix} \quad (A.156)$$

$$\bar{q}_{GW} = h_{GungorWinterton} \cdot \Delta T_{GW} \quad (A.157)$$

Liu-Winterton (1991)

$$E_{LW} = (1 + x \cdot Pr_L \cdot (\rho_l/\rho_v - 1))^{0.35} \quad (A.158)$$

$$S_{LW} = \frac{1}{1 + 0.055 \cdot E_{LW}^{0.1} \cdot Re_L^{0.16}} \quad (A.159)$$

Cooper pool boiling (1984a)

$$h_{Cooper,LW} = 55 \cdot P_{reduced}^{0.12} \cdot (-\log(P_{reduced}))^{-0.55} \cdot M^{-0.5} \cdot \bar{q}_{LW}^{0.67} \quad (A.160)$$

$$h_{LiuWinterton} = \left( (E_2 \cdot E_{LW} \cdot h_{DB,lo})^2 + (S_2 \cdot S_{LW} \cdot h_{Cooper,LW})^2 \right)^{0.5} \quad (A.161)$$

$$\Delta T_{LW} = T_{W,LW} - T_{mix} \quad (\text{A.162})$$

$$\bar{q}_{LW} = h_{LiuWinterton} \cdot \Delta T_{LW} \quad (\text{A.163})$$

Kandlikar (1990) with modifications as shown in Handbook of Phase Change

call `kand(BoKand, Co, Frl, x, Relo, PrL, kL, D, hDB, hDB,lo, ORIENTATION$, MATERIAL$, FLUID$ : hKandlikar, hNBD, hCBD)`

$$\Delta T_{Kand} = T_{W,Kand} - T_{mix} \quad (\text{A.164})$$

$$\bar{q}_{Kandlikar} = h_{Kandlikar} \cdot \Delta T_{Kand} \quad (\text{A.165})$$

Kattan-Thome-Favrat (1998) using ZFT(2002) flow pattern map

Cooper pool boiling (1984a)

$$h_{Cooper,Thome} = 55 \cdot P_{reduced}^{0.12} \cdot (-\log(P_{reduced}))^{-0.55} \cdot M^{-0.5} \cdot \bar{q}_{Thome}^{0.67} \quad (\text{A.166})$$

call `thome(x, hCooper,Thome, G, μL, μV, ρV, ρL, σ, PrL, PrV, kL, kV, D, θdry, θstrat, REGIME$ : hthome, hwet, hvapor, δ)`

$$\Delta T_{Thome} = T_{W,Thome} - T_{mix} \quad (\text{A.167})$$

$$\bar{q}_{Thome} = h_{Thome} \cdot \Delta T_{Thome} \quad (\text{A.168})$$

Condensation: - Shah

$$Nu_{Shah} = 0.023 \cdot Re_L^{0.8} \cdot Pr_L^{0.4} \cdot \left( (1-x)^{0.8} + \frac{3.8 \cdot x^{0.76} \cdot (1-x)^{0.04}}{(P_{mix}/P_{crit})^{0.38}} \right) \quad (\text{A.169})$$

$$Nu_{Shah} = h_{cshah} \cdot D/k_L \quad (\text{A.170})$$

Condensation: Dobson

$$Nus = 0.023 \cdot Re_L^{0.8} \cdot Pr_l^{0.4} \cdot \left( 1 + \left( \frac{2.22}{X_{tt}^{0.89}} \right) \right) \quad (\text{A.171})$$

$$Nus = htc_{dobson} \cdot D/k_L \quad (\text{A.172})$$

Fix Heat Flux

$$\bar{q}_{Chen} = \bar{q} \quad (\text{A.173})$$

$$\bar{q}_{Shah} = \bar{q} \quad (\text{A.174})$$

$$\bar{q}_{GW} = \bar{q} \quad (\text{A.175})$$

$$\bar{q}_{LW} = \bar{q} \quad (\text{A.176})$$

$$\bar{q}_{Kandlikar} = \bar{q} \quad (\text{A.177})$$

$$\bar{q}_{Thome} = \bar{q} \quad (\text{A.178})$$

ZFT(2002) flow pattern map

$$A = \pi \cdot \frac{D^2}{4} \quad (\text{A.179})$$

Stratified

call *stratified*( $\nu$ ,  $x$ ,  $G$ ,  $\rho_L$ ,  $\rho_V$ ,  $\mu_L$ ,  $\mu_V$ ,  $D$ ,  $A$  :  $G_{strat}$ ,  $\theta_{strat}$ ,  $\theta_{wet}$ ,  $\alpha_{TD}$ ,  $A_V$ )

Annular/intermittent

$$(\mu_L/\mu_V)^{0.125} \cdot \left( \frac{1 - x_{AI}}{x_{AI}} \right)^{0.875} \cdot (\rho_V/\rho_L)^{0.5} = 0.34 \quad (\text{A.180})$$

Wavy

call wavy( $\nu, \sigma, \rho_V, \rho_L, D, A, FrWe, q_{crit}, \bar{q}, G, \mu_L, \mu_V, x, G_{MF}, G_{strat}, \theta_{wet} :$   
 $LIQUID_{FLOW\$}, G_{wavy}$ )

Mist

call  $xmfmin(D, \rho_L, \rho_V, FrWe, \sigma, G, \mu_L, \mu_V : x_{MF,min})$   
 call  $mf(x, x_{MF,min}, \rho_V, \rho_L, FrWe, \sigma, G, D, \mu_L, \mu_V : G_{MF})$

Dry angle

call  $xmax(\nu, G, \rho_L, \rho_V, \mu_L, \mu_V, D, A, \sigma, FrWe, q_{crit}, \bar{q}, x_{MF,min} :$   
 $\theta_{max}, \theta_{strat,max}, x_{max})$

$$\theta_{dry,star} \cdot (G_{wavy} - G_{strat}) = \theta_{strat} \cdot (G_{wavy} - G) \quad (A.181)$$

call  $thetadry(x, x_{max}, \theta_{max}, \theta_{strat}, \theta_{strat,max}, G_{strat}, G_{wavy}, G, \theta_{dry,star} : \theta_{dry}, \theta_{wet,wavy})$

Regime

call  $flowregime(G, x, G_{strat}, G_{wavy}, G_{MF}, x_{AI} : REGIME\$)$

## Appendix B

# EES Implementation of the Owen-Hewitt Model

```
function MoodyChart(Re, RR)
```

```
  If (Re < 2100) then
```

$$f = 64/Re \quad (\text{B.1})$$

```
  else
```

```
    call Colebrook(Re, RR, f)
```

```
  endif
```

$$\text{MoodyChart} = f \quad (\text{B.2})$$

```
end MoodyChart
```

```
function  $u_p(y_{plus})$ 
```

```
  If ( $y_{plus} < 5$ ) then
```

$$u_p := y_{plus} \quad (\text{B.3})$$

else

  If ( $y_{plus} > 30$ ) then

$$u_p := 5.5 + 2.5 \cdot \ln(y_{plus}) \quad (\text{B.4})$$

  else

$$u_p := -3.05 + 5 \cdot \ln(y_{plus}) \quad (\text{B.5})$$

  endif

endif

end  $u_p$

function  $W_{LF,plus}(m_{plus})$

  If ( $m_{plus} < 5$ ) then

$$W_{LF,plus} := 0.5 \cdot m_{plus}^2 \quad (\text{B.6})$$

  else

    If ( $m_{plus} > 30$ ) then

$$W_{LF,plus} := -64 + 3 \cdot m_{plus} + 2.5 \cdot m_{plus} \cdot \ln(m_{plus}) \quad (\text{B.7})$$

    else

$$W_{LF,plus} := 12.5 - 8.05 \cdot m_{plus} + 5 \cdot m_{plus} \cdot \ln(m_{plus}) \quad (\text{B.8})$$

    endif

  endif

end  $W_{LF,plus}$

function roughness( $m_{star,value}$ ,  $Re_{LF}$ ,  $We$ ,  $R_o$ )

If ( $m_{star,value} > 0.01$ ) then

use fig. 10

$$roughness = \text{Interpolate}(\text{'Fig 10'}, \text{'e\_star'}, \text{'m\_star'}, \quad (\text{B.9})$$

$m_{star} = m_{star,value}$ )

else

If ( $m_{star,value} < 0.008$ ) then

use fig. 11

$$x_{11,value} = \frac{m_{star,value}^{0.5}}{We} \quad (\text{B.10})$$

$$roughness = Re_{LF}^{0.5} \cdot \text{Interpolate}(\text{'Fig 11'}, \text{'y11'}, \text{'x11'}, \quad (\text{B.11})$$

$x_{11} = x_{11,value}$ )

else

weighted average of both

$$x_{11,value} = \frac{m_{star,value}^{0.5}}{We} \quad (\text{B.12})$$

$$roughness_{10} = \text{Interpolate}(\text{'Fig 10'}, \text{'e\_star'}, \text{'m\_star'}, \quad (\text{B.13})$$

$m_{star} = m_{star,value}$ )

$$roughness_{11} = Re_{LF}^{0.5} \cdot \text{Interpolate}(\text{'Fig 11'}, \text{'y11'}, \text{'x11'}, \quad (\text{B.14})$$

$x11 = x_{11,value}$  )

$$roughness = \left( \frac{0.01 - m_{star,value}}{0.002} \right) \cdot roughness11+ \quad (B.15)$$

$((0.002 - (0.01 - m_{star,value})) / (0.002)) \cdot roughness10$

endif

endif

end *roughnes*

#### LOOKUP OF SCHUBRING'S 15 mm ID DATA

$$FT_{top} = \text{Interpolate2d}('top15', Usg, Usl, FT_{top}, Usg = \dot{V}_g, Usl = \dot{V}_{l,ccm}). \quad (B.16)$$

$\left| 1 \times 10^{-6} \frac{m}{micron} \right|$

$$FT_{side} = \text{Interpolate2d}('side15', Usg, Usl, FT_{side}, Usg = \dot{V}_g, Usl = \dot{V}_{l,ccm}). \quad (B.17)$$

$\left| 1 \times 10^{-6} \frac{m}{micron} \right|$

$$FT_{bottom} = \text{Interpolate2d}('bottom15', Usg, Usl, FT_{bottom}, Usg = \dot{V}_g, \quad (B.18)$$

$Usl = \dot{V}_{l,ccm}) \cdot \left| 1 \times 10^{-6} \frac{m}{micron} \right|$

$$p_{zgradient,sch} = -\text{Interpolate2d}('pressuredrop15', Usg, Usl, dpdz, Usg = \dot{V}_g, \quad (B.19)$$

$Usl = \dot{V}_{l,ccm})$

$$P_G = \text{Interpolate2d}(\text{'Pabsolute15'}, U_{sg}, U_{sl}, P_{abs}, U_{sg} = \dot{V}_g, U_{sl} = \dot{V}_{l,ccm}) \quad (\text{B.20})$$

$$R_o = 0.00755 \text{ [m]} \quad (\text{B.21})$$

## LIQUID PROPERTIES

$$T_l = 284 \quad (\text{B.22})$$

$$\rho_L = \rho(\text{Water}, T = T_l, P = P_L) \text{ [kg/m}^3\text{]} \text{ [kg/m}^3\text{]} \quad (\text{B.23})$$

$$\mu_L = \mu(\text{Water}, T = T_l, P = P_L) \text{ [kg/m}\cdot\text{s]} \quad (\text{B.24})$$

$$\sigma = \gamma(\text{Water}, T = T_l) \quad (\text{B.25})$$

value for water and steam

## GAS PROPERTIES

$$T_g = 293 \quad (\text{B.26})$$

$$\rho_G = \rho(\text{Air}_{ha}, T = T_g, P = P_G) \text{ [kg/m}^3\text{]} \quad (\text{B.27})$$

$$\mu_G = \mu(\text{Air}_{ha}, T = T_g, P = P_G) \text{ [kg/m}\cdot\text{s]} \quad (\text{B.28})$$

## MEASUREMENTS

$$\delta = m \cdot \left| 1000000 \frac{\text{micron}}{m} \right| \quad (\text{B.29})$$

$$m_{side} = \text{Interpolate2d}(\text{'FT Side CCA14'}, U_{sg}, U_{sl}, FTNWsigma, \quad (\text{B.30})$$

$$U_{sg} = U_{sg}, U_{sl} = U_{sl}) \cdot \left| 1 \times 10^{-6} \frac{m}{\text{micron}} \right|$$

$$m_{bottom} = \text{Interpolate2d}(\text{'FT Bottom CCA14'}, U_{sg}, U_{sl}, FTNWsigma, \quad (\text{B.31})$$

$$U_{sg} = U_{sg}, \quad U_{sl} = U_{sl}) \cdot \left| 1 \times 10^{-6} \frac{m}{micron} \right|$$

$$m_{top} = \text{Interpolate2d}(\text{'FT Top CCA14'}, U_{sg}, U_{sl}, FTNWsigma, \quad (\text{B.32})$$

$$U_{sg} = U_{sg}, \quad U_{sl} = U_{sl}) \cdot \left| 1 \times 10^{-6} \frac{m}{micron} \right|$$

$$m = \frac{2 \cdot m_{side} + m_{bottom}}{3} \quad (\text{B.33})$$

$$A_{cs} = \pi \cdot R_o^2 \quad (\text{B.34})$$

$$P_L = P_G \quad (\text{B.35})$$

$$U_{sl} = \left( \dot{V}_l / A_{cs} \right) \cdot \left| 100 \frac{cm/s}{m/s} \right| \quad (\text{B.36})$$

$$U_{sg} = \dot{V}_g \cdot \frac{\left| 1.66667 \times 10^{-5} \frac{m^3/s}{L/min} \right|}{A_{cs}} \quad (\text{B.37})$$

## FILM MODEL

$$u_{plus,i} = u_p(y_{plus,i}) \quad (\text{B.38})$$

$$u_{plus,i} = V_i / u_{star} \quad (\text{B.39})$$

$$u_{star} = \sqrt{(\tau_{avg} / \rho_L)} \quad [\text{m/s}] \quad (\text{B.40})$$

friction velocity

$$y_{plus,i} = u_{star} \cdot \rho_L \cdot y_i / \mu_L \quad (\text{B.41})$$

Definition of non-dimensional distance parameter

$$m_{plus} = m \cdot \rho_l \cdot u_{star} / \mu_l \quad (\text{B.42})$$

$$W_{LF} = W_{LF,plus}(m_{plus}) \cdot \pi \cdot (2 \cdot R_o) \cdot \mu_l \quad (\text{B.43})$$

$$G_{LF} = \frac{W_{LF}}{(\pi \cdot (R_o^2 - R_i^2)) \text{ [kg/m}^2 \cdot \text{s]}} \quad (\text{B.44})$$

liquid film mass flux

$$y_i = m \text{ [m]} \quad (\text{B.45})$$

$$R_i = R_o - y_i \quad (\text{B.46})$$

$$W_L = \dot{V}_L \cdot \rho_l \text{ [kg/s]} \quad (\text{B.47})$$

$$\dot{V}_{l,ccm} = \dot{V}_l \cdot \left| 6 \times 10^7 \frac{\text{cm}^3/\text{min}}{\text{m}^3/\text{s}} \right| \text{ [cm}^3/\text{min]} \quad (\text{B.48})$$

$$\tau_o = \tau_i \cdot (R_i/R_o) - 0.50 \cdot (+p_{zgradient}) \cdot \frac{R_o^2 - R_i^2}{R_o} \quad (\text{B.49})$$

axial gravity neglected

$$\tau_{avg} = \frac{\tau_i + \tau_o}{2} \quad (\text{B.50})$$

CORE MODEL

$$\tau_i = (R_i/2) \cdot (- (p_{zgradient}) - acc_{gas}) \text{ [N/m}^2\text{]} \quad (\text{B.51})$$

axial gravity neglected

term due to gas acceleration linked to change in gas density

$$acc_{gas} = \left( \frac{W_G + W_{LE}}{\pi \cdot R_i^2} \right) \cdot \bar{V}_{H,zgradient} \quad (\text{B.52})$$

$$acc_{gas} = 0 \quad (\text{B.53})$$

$$\tau_i = f_i \cdot \left( (1/2) \cdot \rho_H \cdot (\bar{V}_H - V_i)^2 \right) \quad (\text{B.54})$$

$$\bar{V}_H = \left( \frac{1}{\pi \cdot R_i^2} \right) \cdot (W_G/\rho_G + W_{LE}/\rho_L) \text{ [m/s]} \quad (\text{B.55})$$

$$W_{LE} + W_{LF} = W_L \text{ [kg/s]} \quad (\text{B.56})$$

Entrained liquid mass flow rate

$$W_G = \dot{V}_g \cdot \left| 1.66667 \times 10^{-5} \frac{m^3/s}{L/min} \right| \cdot \rho_g \text{ [kg/s]} \quad (\text{B.57})$$

$$G_G = \frac{W_G}{(\pi \cdot R_o^2) \text{ [kg/m}^2 \cdot \text{s]}} \quad (\text{B.58})$$

Gas mass flux

$$G_L = \frac{W_L}{(\pi \cdot R_o^2) \text{ [kg/m}^2 \cdot \text{s]}} \quad (\text{B.59})$$

Liquid mass flux

$$\bar{V}_G = G_G / \rho_G \quad (\text{B.60})$$

mean superficial gas velocity

$$Re_G = \frac{\rho_G \cdot \bar{V}_G \cdot (2 \cdot R_o)}{\mu_G} \quad (\text{B.61})$$

$$V_{i,star} = \sqrt{(\tau_i / \rho_H)} \text{ [m/s]} \quad (\text{B.62})$$

$$Q_{GH} = \frac{\rho_G \cdot \bar{V}_G^2}{\rho_H \cdot \bar{V}_H^2} \quad (\text{B.63})$$

$$X_{G,CORE} = \frac{W_G}{W_G + W_{LE}} \quad (\text{B.64})$$

Mass fraction of liquid in the core

$$X_{LE,CORE} = \frac{W_{LE}}{W_G + W_{LE}} \quad (\text{B.65})$$

correlation for  $k_{tp}$  obtained from figure 9

$$k_{tp} = 0.0918 \cdot Q_{GH}^2 + 0.1186 \cdot Q_{GH} + 0.1391 \quad (\text{B.66})$$

$$A_r = \text{Interpolate}(\text{'Fig 6'}, \text{'Ar'}, \text{'lRe'}, \text{lRe} = \log(Re_{star})) \quad (\text{B.67})$$

Nikuradse friction factor for two-phase flow.  $k_{tp}$  is the two phase von Karman constant.

$$\sqrt{(2/f_i)} = (1/k_{tp}) \cdot \ln(R_i/e_E) + (A_r - 1.5/k_{tp}) + (1/k_{tp}) \cdot \quad (\text{B.68})$$

$$\left(\frac{2 \cdot m}{R_o} \cdot \ln(R_o/m) - m/R_o\right)$$

$$Re_{star} = e \cdot V_{i,star} \cdot \rho_H / \mu_H \quad (\text{B.69})$$

$$\rho_H = \frac{W_G + W_{LE}}{(W_G/\rho_G + W_{LE}/\rho_L) \text{ [kg/m}^3\text{]}} \quad (\text{B.70})$$

$$\mu_H = \frac{W_G + W_{LE}}{(W_G/\mu_G + W_{LE}/\mu_L) \text{ [kg/m}\cdot\text{s]}} \quad (\text{B.71})$$

McAdams et al. (1942)

Interfacial Roughness

$$y_b = \left(\frac{5 \cdot (2 \cdot R_o)}{Re_G}\right) \cdot \sqrt{(2/f_G)} \quad (\text{B.72})$$

$$f_G = \text{MoodyChart}(Re_G, RR) \quad (\text{B.73})$$

$$RR = \frac{e_E}{2 \cdot R_o} \quad (\text{B.74})$$

$$e_E = e - y_b \quad (\text{B.75})$$

$$m_{star} = \frac{2 \cdot m}{2 \cdot R_o} \quad (\text{B.76})$$

$$e_{star} = \frac{2 \cdot e}{2 \cdot R_o} \quad (\text{B.77})$$

$$e_{star,11} = \frac{e_{star}}{Re_{LF}^{0.5}} \quad (\text{B.78})$$

$$m_{star,11} = 10000 \cdot \frac{m_{star}^{0.5}}{We} \quad (\text{B.79})$$

$$Re_{LF} = \frac{G_{LF} \cdot (2 \cdot R_o)}{\mu_L} \quad (\text{B.80})$$

$$We = \frac{\rho_H \cdot \bar{V}_H^2 \cdot (2 \cdot R_o - 2 \cdot m)}{\sigma} \quad (\text{B.81})$$

$$e_{star,owen} = \text{roughness}(m_{star}, Re_{LF}, We, R_o) \quad (\text{B.82})$$

$$e_{star,owen} = \frac{2 \cdot e_{owen,m}}{2 \cdot R_o} \quad (\text{B.83})$$

$$e_{owen} = e_{owen,m} \cdot \left| 1000000 \frac{\text{micron}}{m} \right| \quad (\text{B.84})$$

$$e_{\sigma,PLIF,top} = 2 \cdot (2^{0.5}) \cdot \text{Interpolate2d}(\text{'FT Top CCA14'}, U_{sg}, U_{sl}, \sigma, \quad (\text{B.85})$$

$$U_{sg} = U_{sg}, \quad U_{sl} = U_{sl})$$

$$e_{\sigma,PLIF,side} = 2 \cdot (2^{0.5}) \cdot \text{Interpolate2d}(\text{'FT Side CCA14'}, U_{sg}, U_{sl}, \sigma, \quad (\text{B.86})$$

$$U_{sg} = U_{sg}, \quad U_{sl} = U_{sl})$$

$$e_{\sigma,PLIF,bottom} = 2 \cdot (2^{0.5}) \cdot \text{Interpolate2d}(\text{'FT Bottom CCA14'}, U_{sg}, U_{sl}, \sigma, \quad (\text{B.87})$$

$$U_{sg} = U_{sg}, \quad U_{sl} = U_{sl})$$

$$e_{\sigma,PLIF} = \frac{2 \cdot e_{\sigma,PLIF,side} + e_{\sigma,PLIF,bottom} + e_{\sigma,PLIF,top}}{4} \quad (\text{B.88})$$

$$h_{w,side} = \text{Interpolate2d}(\text{'FT Side CCA14'}, U_{sg}, U_{sl}, WH_{1.5sigma}, \quad (\text{B.89})$$

$$U_{sg} = U_{sg}, \quad U_{sl} = U_{sl})$$

$$h_{w,bottom} = \text{Interpolate2d}(\text{'FT Bottom CCA14' , } U_{sg}, U_{sl}, WH_{1.5sigma}, \quad (\text{B.90})$$

$$U_{sg} = U_{sg}, \quad U_{sl} = U_{sl})$$

$$h_{wave,PLIF} = \frac{2 \cdot h_{w,side} + h_{w,bottom}}{3} \quad (\text{B.91})$$

$$e_{wave,PLIF} = h_{wave,PLIF} - \delta \quad (\text{B.92})$$

$$e = e_{\sigma,PLIF} \cdot \left| 1 \times 10^{-6} \frac{m}{micron} \right| \quad (\text{B.93})$$

Ratios

$$gradratio = p_{zgradient,sch} / p_{zgradient} \quad (\text{B.94})$$

expression for approximating power-law velocity profile coefficient in Fore's paper

$$f_i = \frac{1}{4 \cdot n_{Nunner,1}^2} \quad (\text{B.95})$$

## Appendix C

### PLIF Images of Interfacial Waves

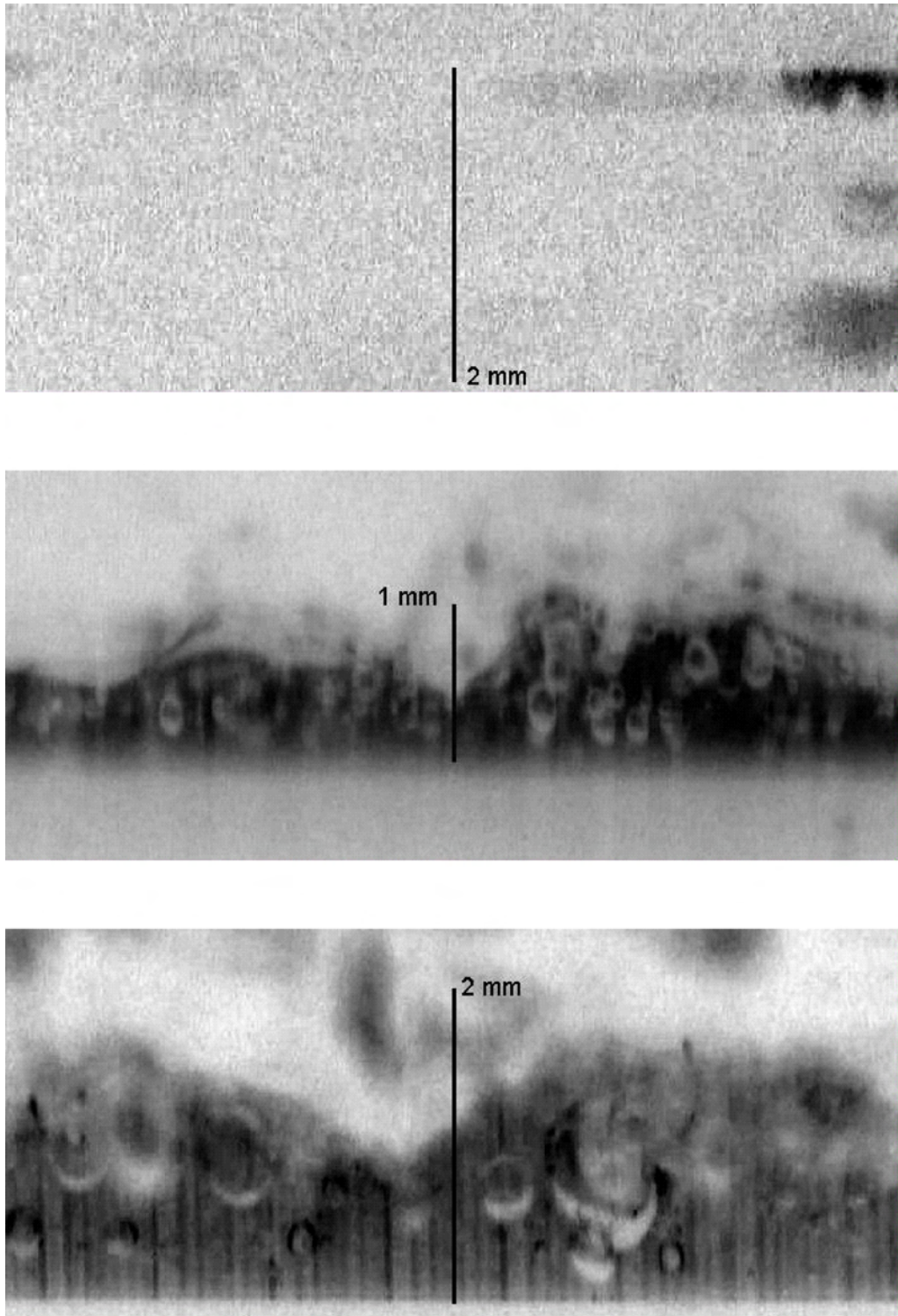


Figure C.1: PLIF Images of interfacial waves along the top, side and bottom of the pipe.  $U_{sg} = 28 \text{ m s}^{-1}$  and  $U_{sl} = 4.6 \text{ cm s}^{-1}$ . Flow from right to left.

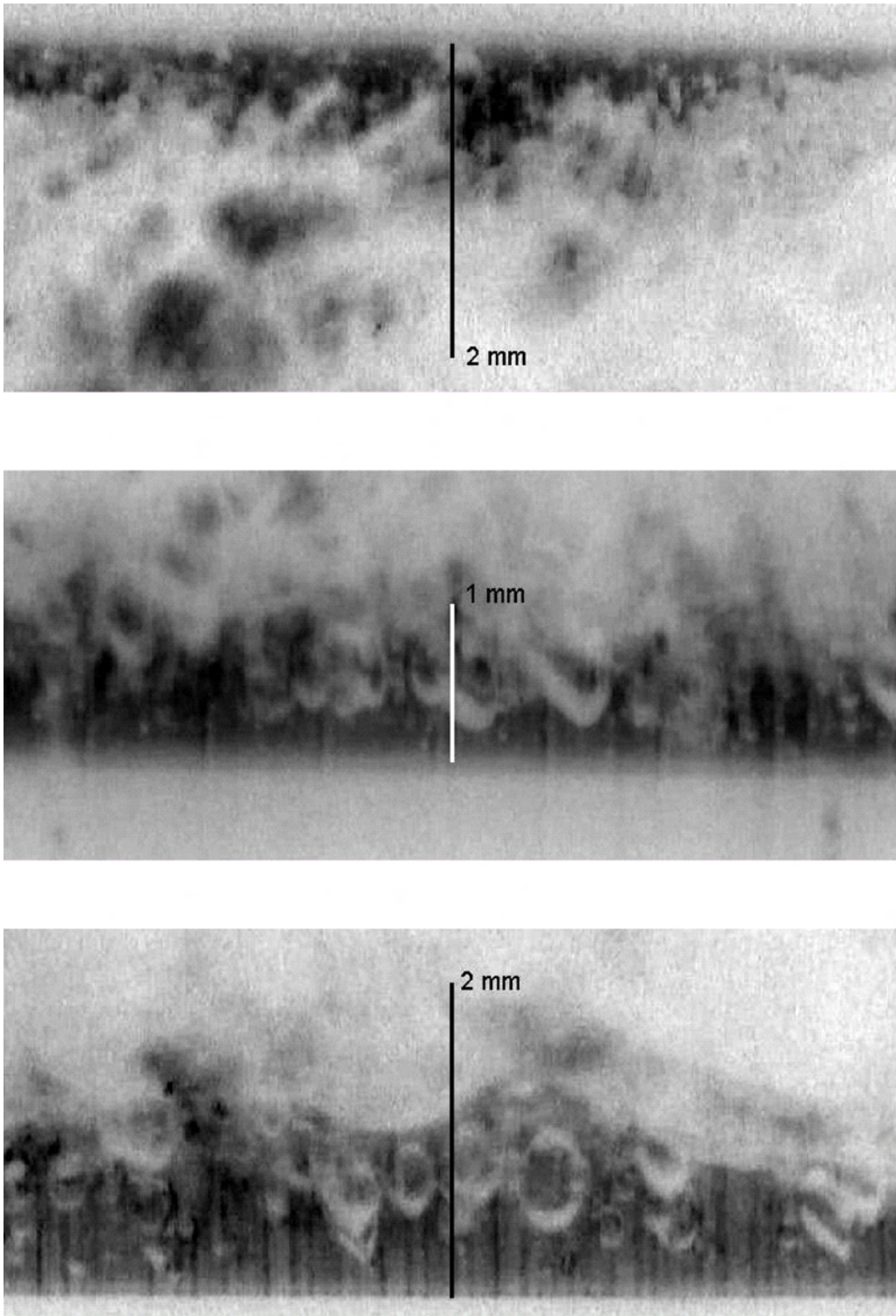


Figure C.2: PLIF Images of interfacial waves along the top, side and bottom of the pipe.  $U_{sg} = 28 \text{ m s}^{-1}$  and  $U_{sl} = 9.3 \text{ cm s}^{-1}$ . Flow from right to left.

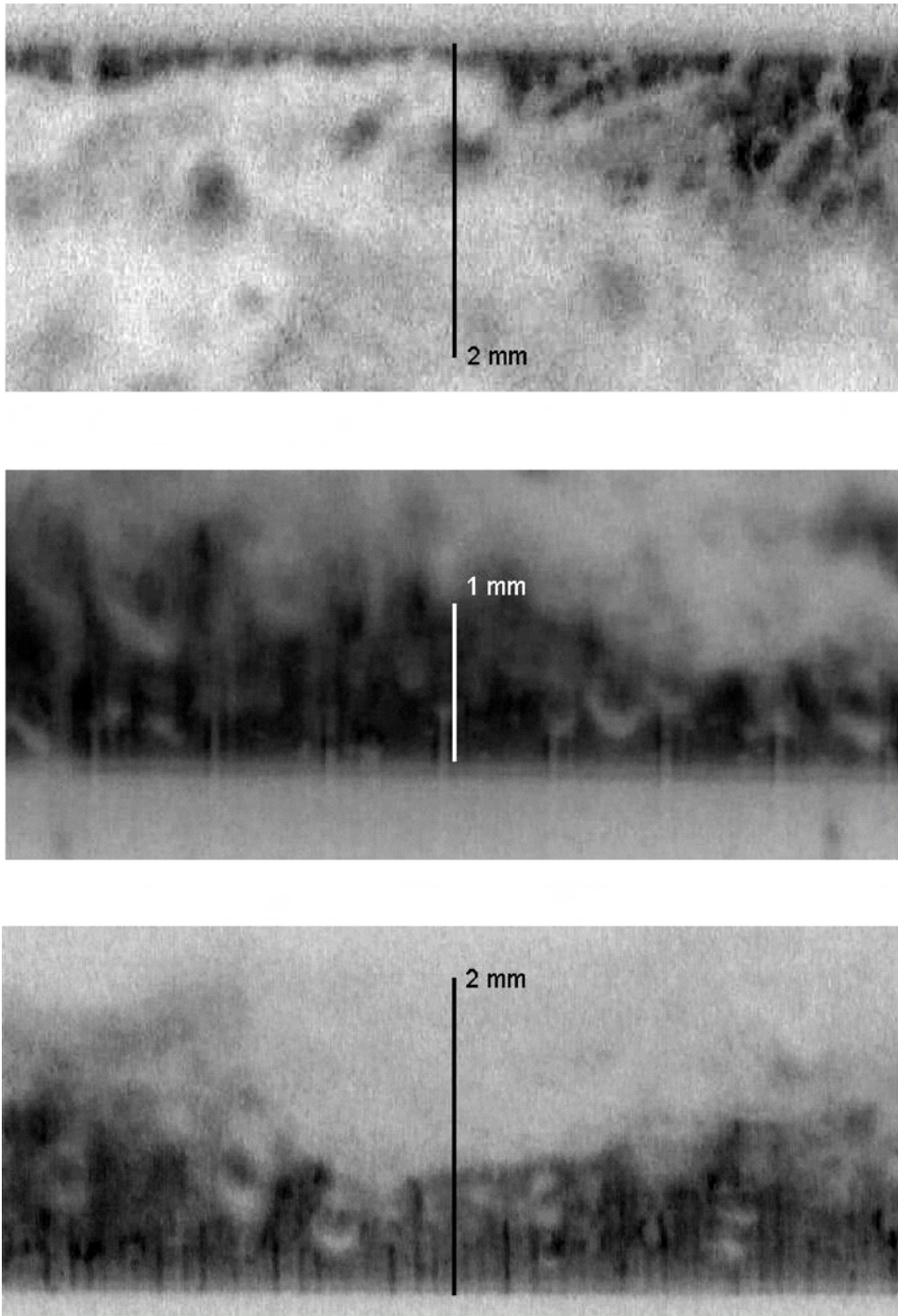


Figure C.3: PLIF Images of interfacial waves along the top, side and bottom of the pipe.  $U_{sg} = 28 \text{ m s}^{-1}$  and  $U_{sl} = 14.0 \text{ cm s}^{-1}$ . Flow from right to left.

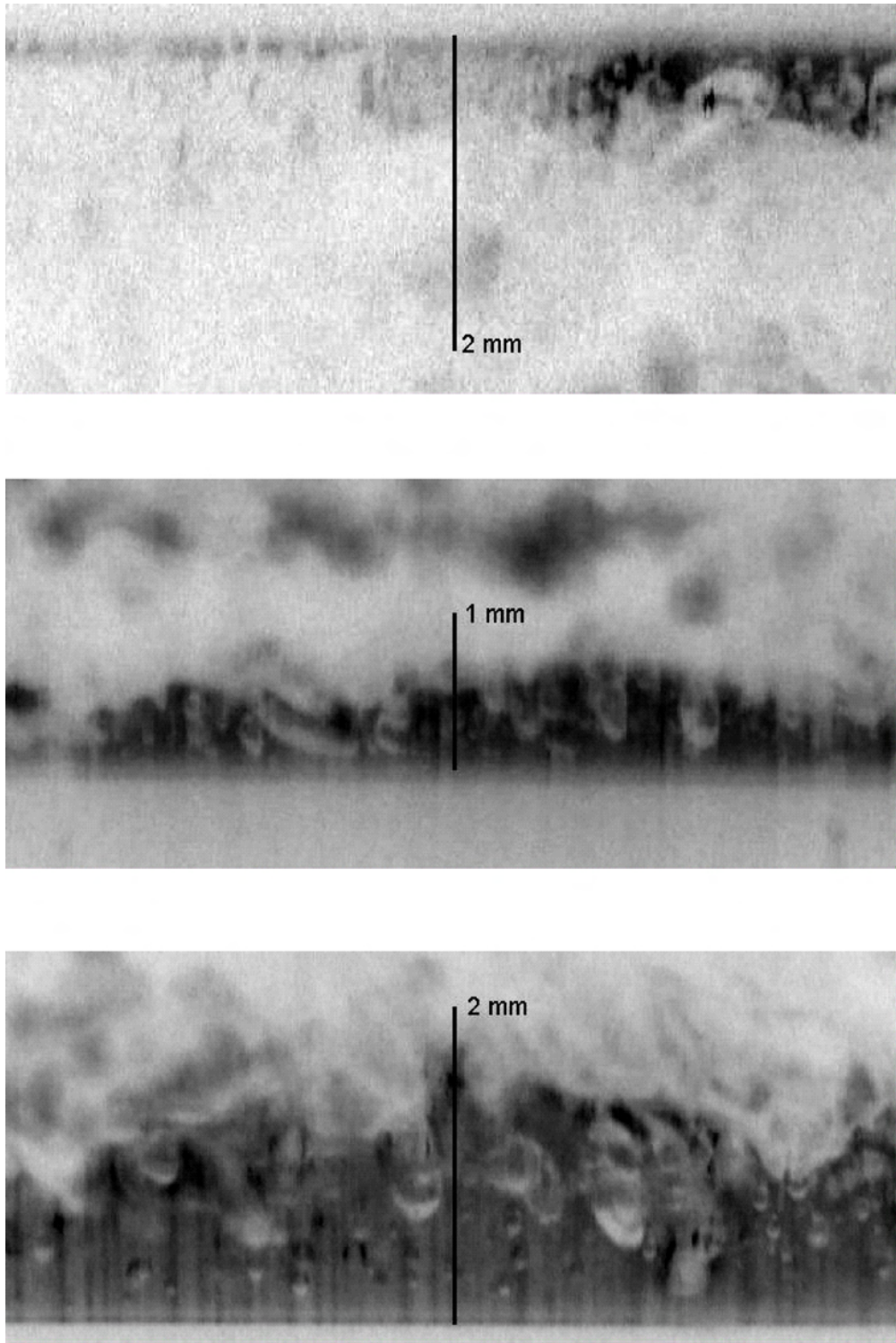


Figure C.4: PLIF Images of interfacial waves along the top, side and bottom of the pipe.  $U_{sg} = 37 \text{ m s}^{-1}$  and  $U_{sl} = 4.6 \text{ cm s}^{-1}$ . Flow from right to left.

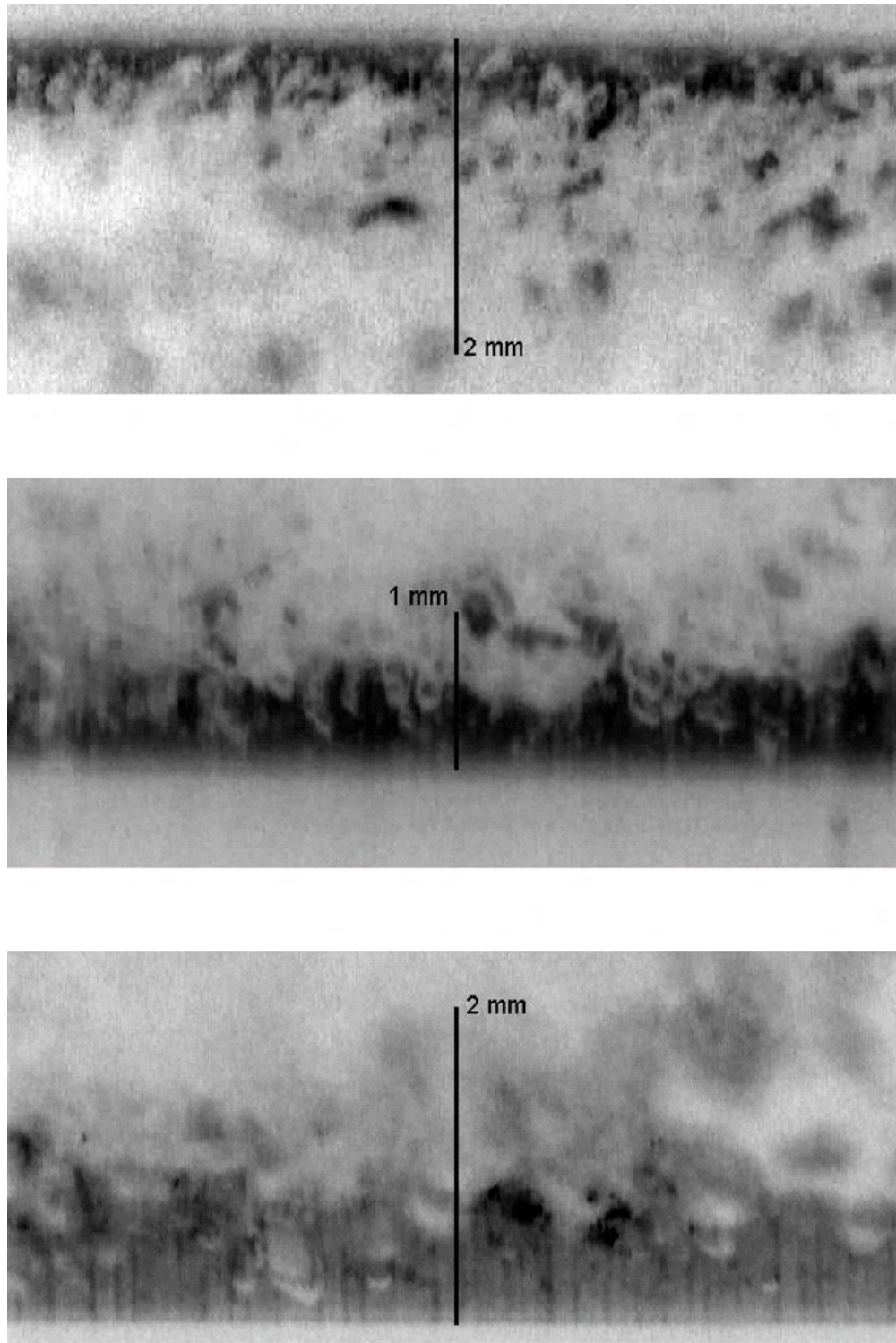


Figure C.5: PLIF Images of interfacial waves along the top, side and bottom of the pipe.  $U_{sg} = 37 \text{ m s}^{-1}$  and  $U_{sl} = 9.3 \text{ cm s}^{-1}$ . Flow from right to left.

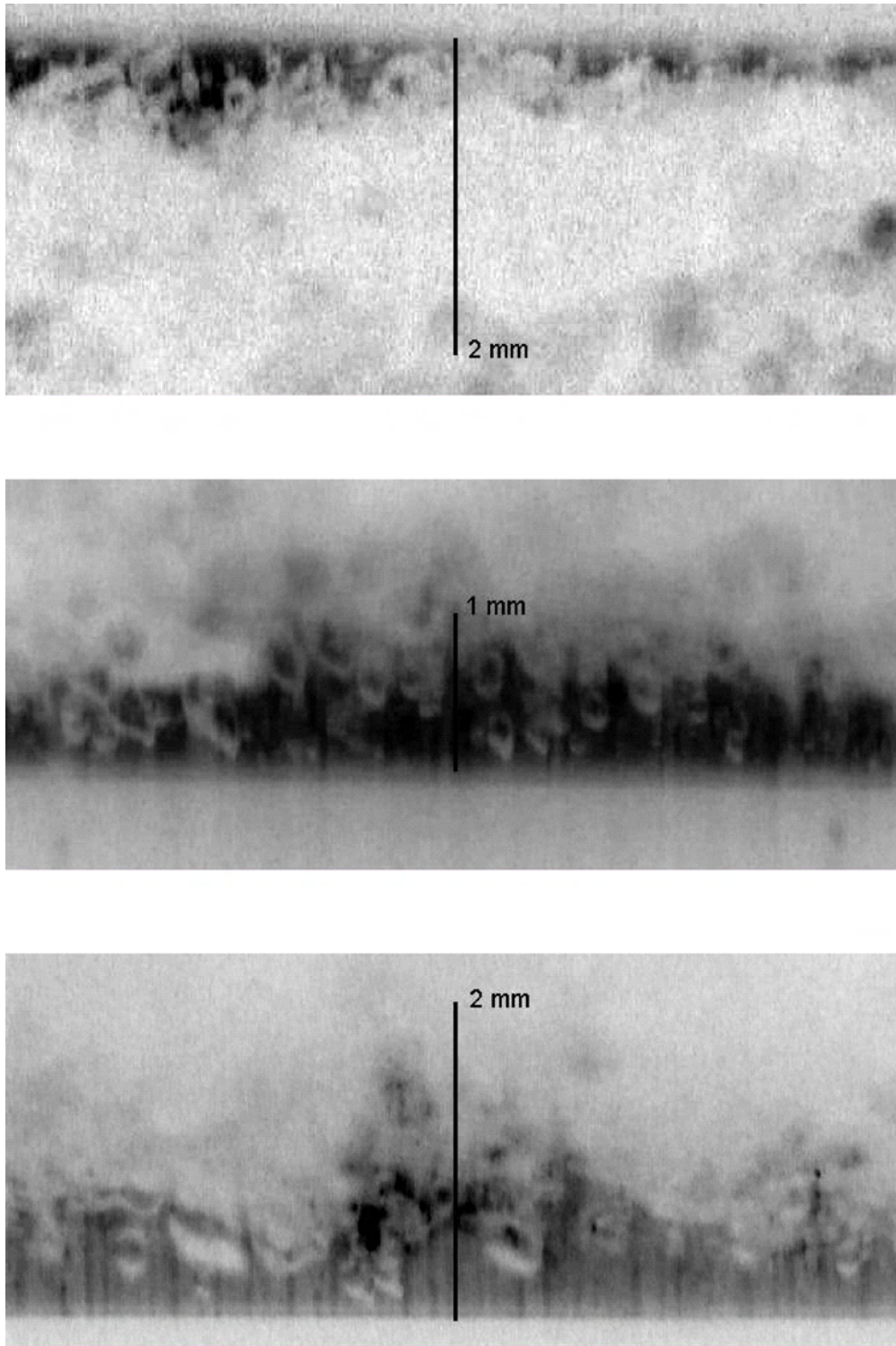


Figure C.6: PLIF Images of interfacial waves along the top, side and bottom of the pipe.  $U_{sg} = 37 \text{ m s}^{-1}$  and  $U_{sl} = 14.0 \text{ cm s}^{-1}$ . Flow from right to left.

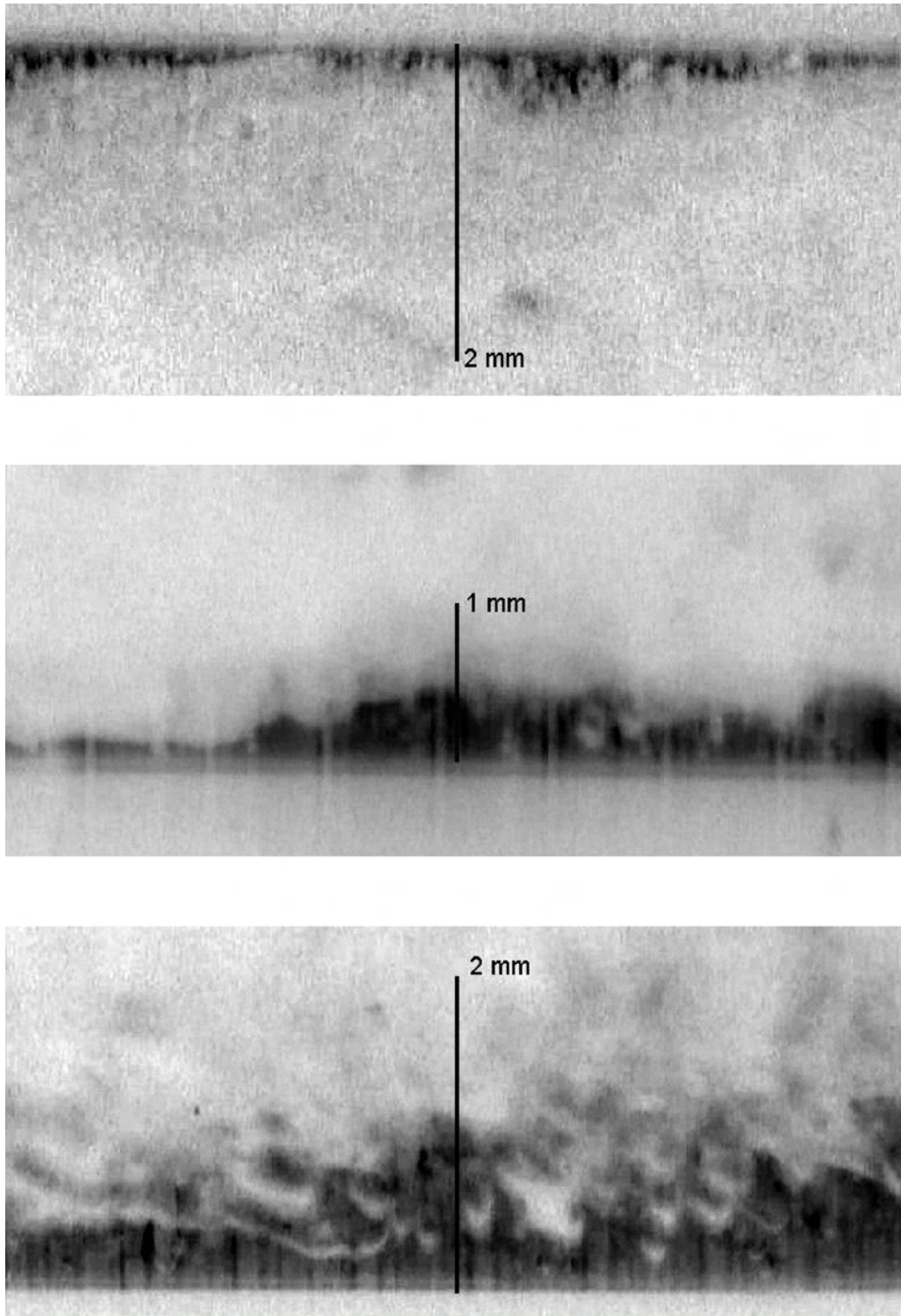


Figure C.7: PLIF Images of interfacial waves along the top, side and bottom of the pipe.  $U_{sg} = 47 \text{ m s}^{-1}$  and  $U_{sl} = 4.6 \text{ cm s}^{-1}$ . Flow from right to left.

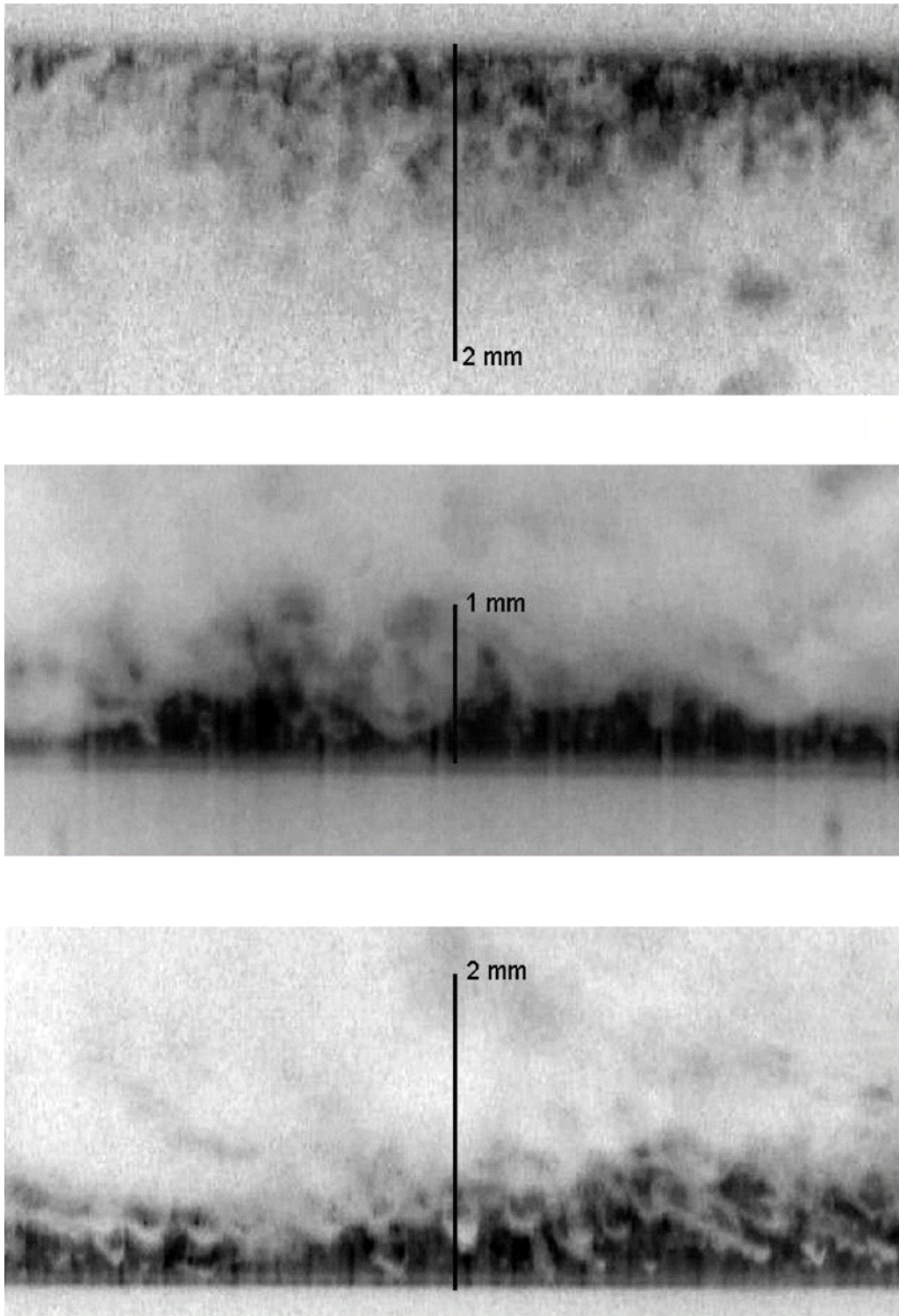


Figure C.8: PLIF Images of interfacial waves along the top, side and bottom of the pipe.  $U_{sg} = 47 \text{ m s}^{-1}$  and  $U_{sl} = 9.3 \text{ cm s}^{-1}$ . Flow from right to left.

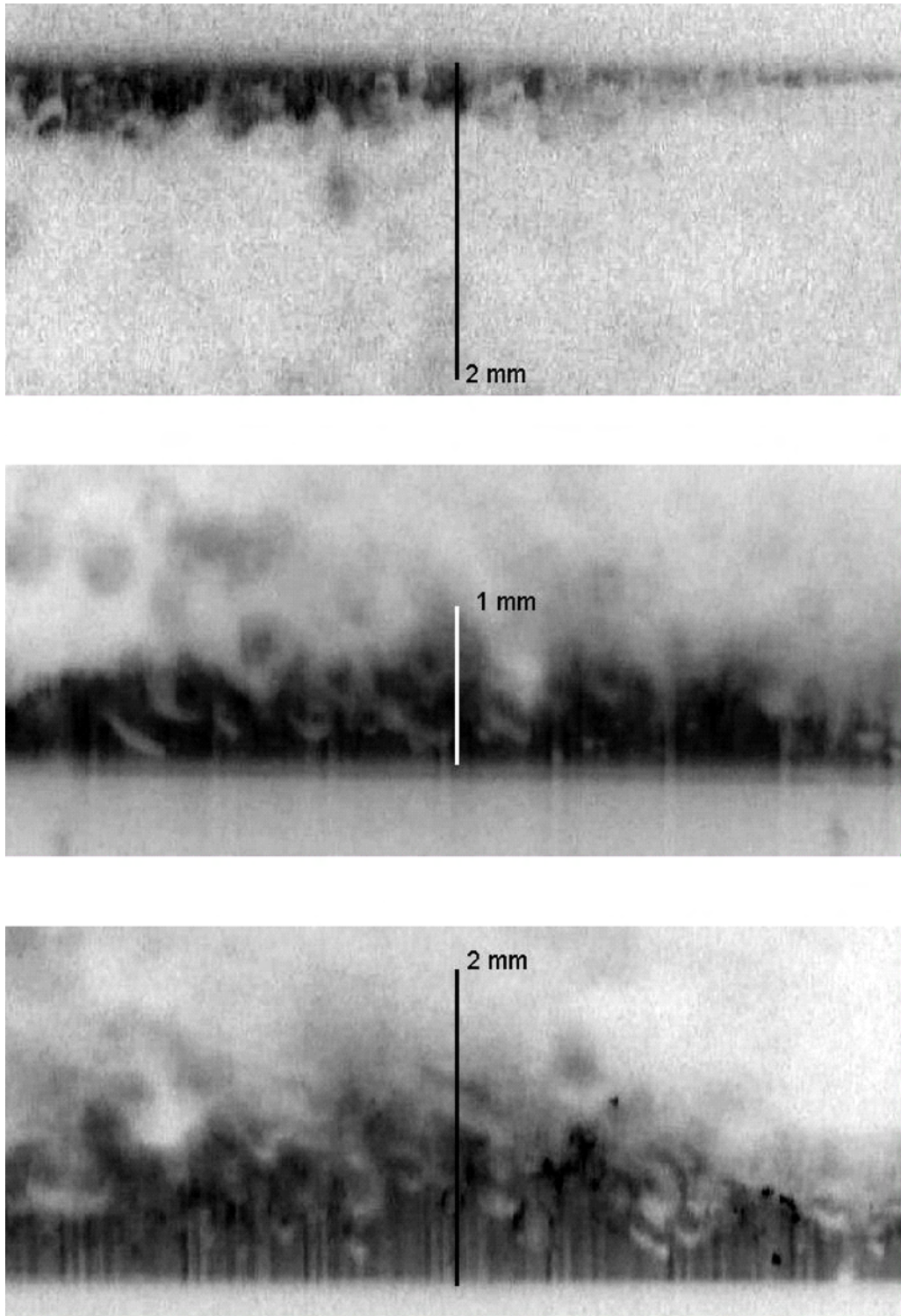


Figure C.9: PLIF Images of interfacial waves along the top, side and bottom of the pipe.  $U_{sg} = 47 \text{ m s}^{-1}$  and  $U_{sl} = 14.0 \text{ cm s}^{-1}$ . Flow from right to left.

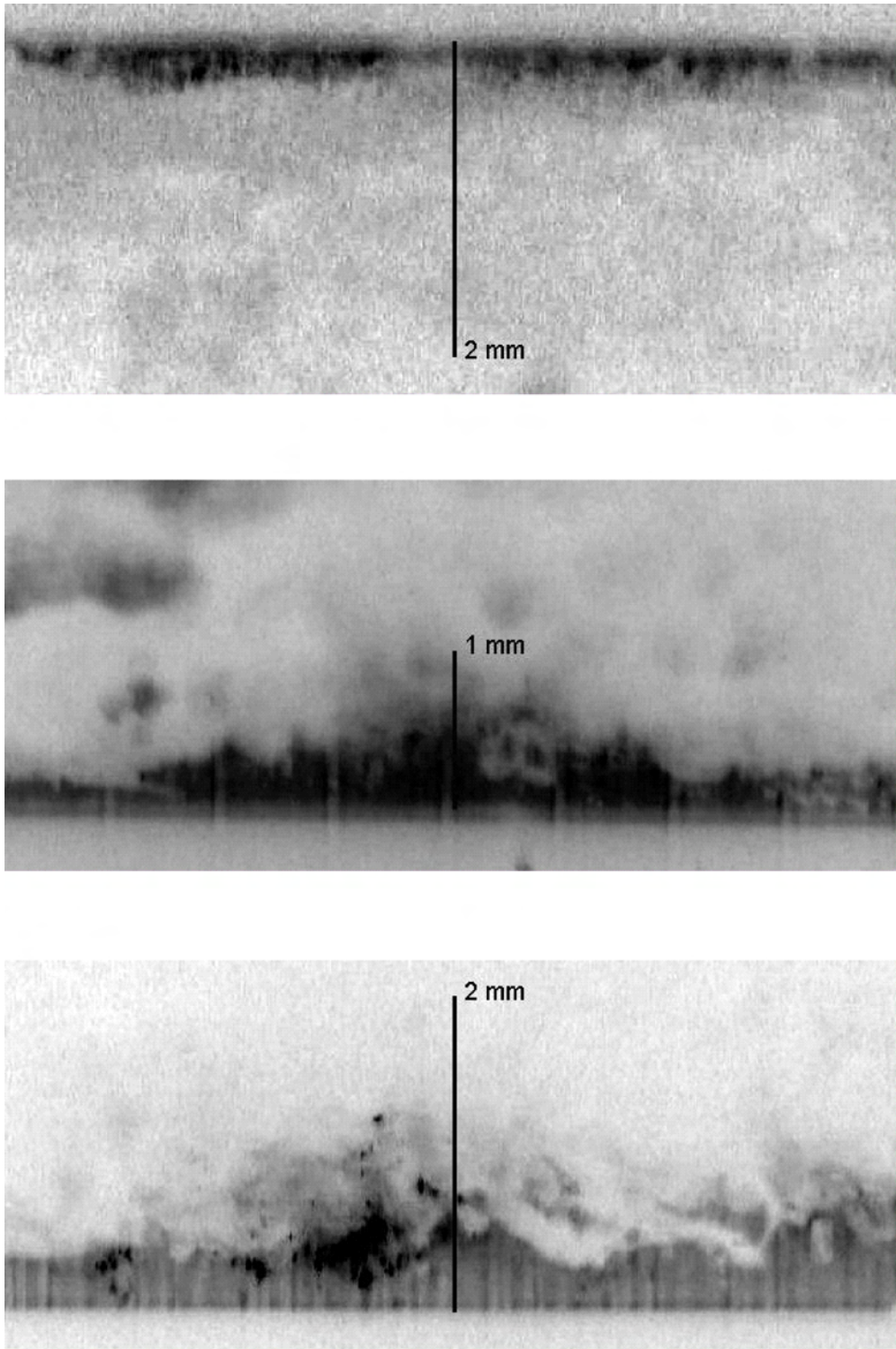


Figure C.10: PLIF Images of interfacial waves along the top, side and bottom of the pipe.  $U_{sg} = 56 \text{ m s}^{-1}$  and  $U_{sl} = 4.6 \text{ cm s}^{-1}$ . Flow from right to left.

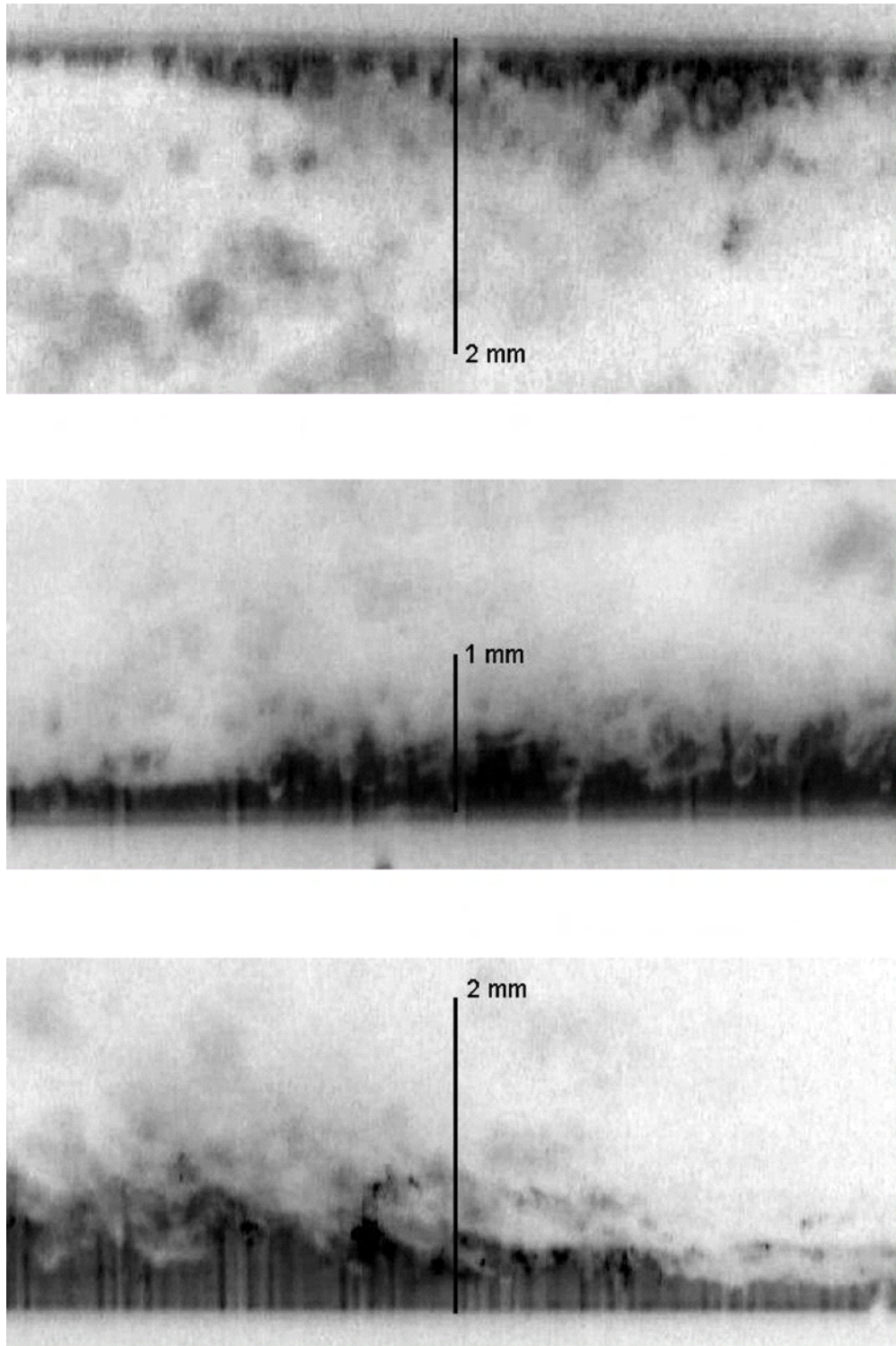


Figure C.11: PLIF Images of interfacial waves along the top, side and bottom of the pipe.  $U_{sg} = 56 \text{ m s}^{-1}$  and  $U_{sl} = 9.3 \text{ cm s}^{-1}$ . Flow from right to left.

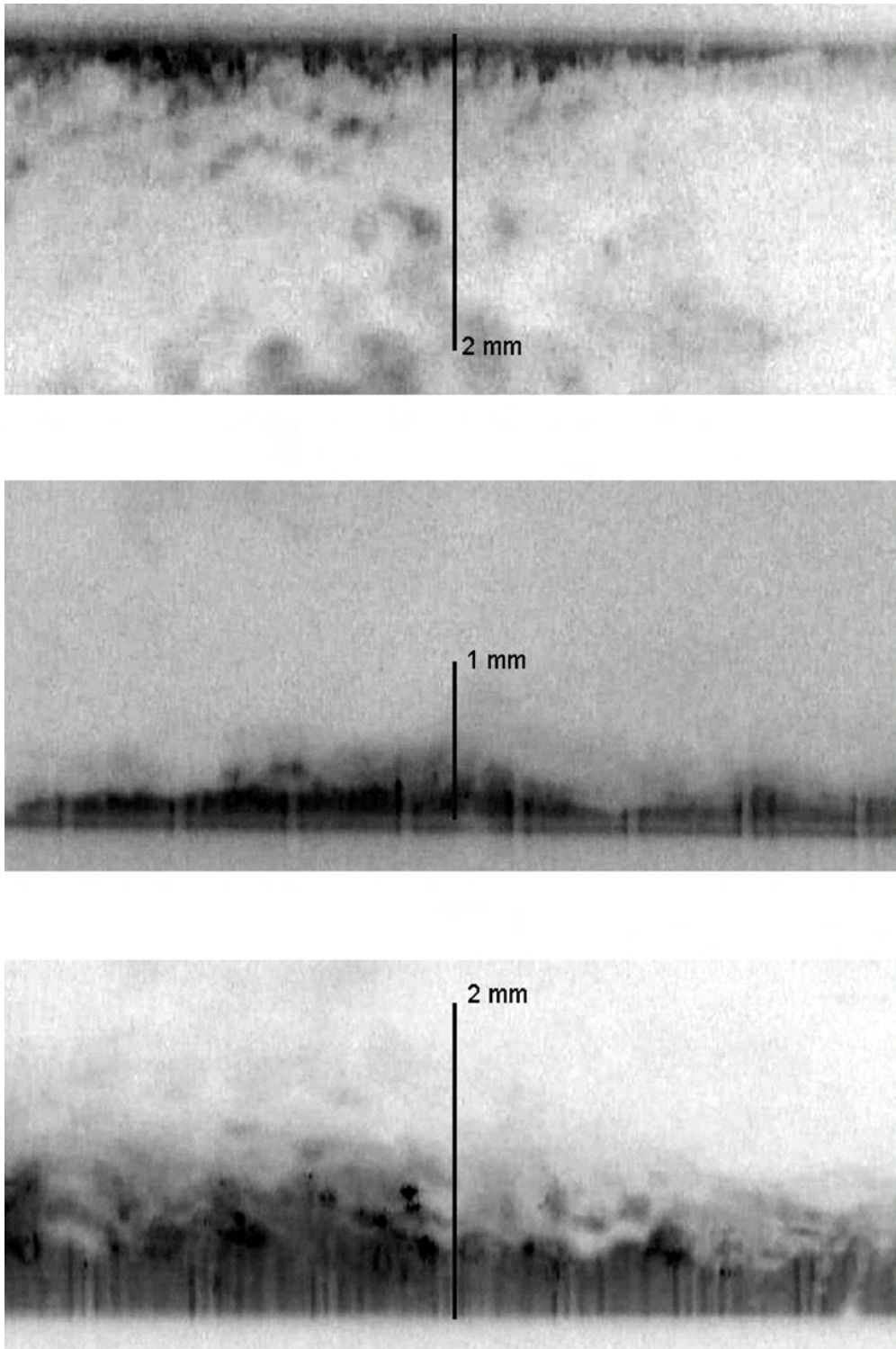


Figure C.12: PLIF Images of interfacial waves along the top, side and bottom of the pipe.  $U_{sg} = 56 \text{ m s}^{-1}$  and  $U_{sl} = 14.0 \text{ cm s}^{-1}$ . Flow from right to left.

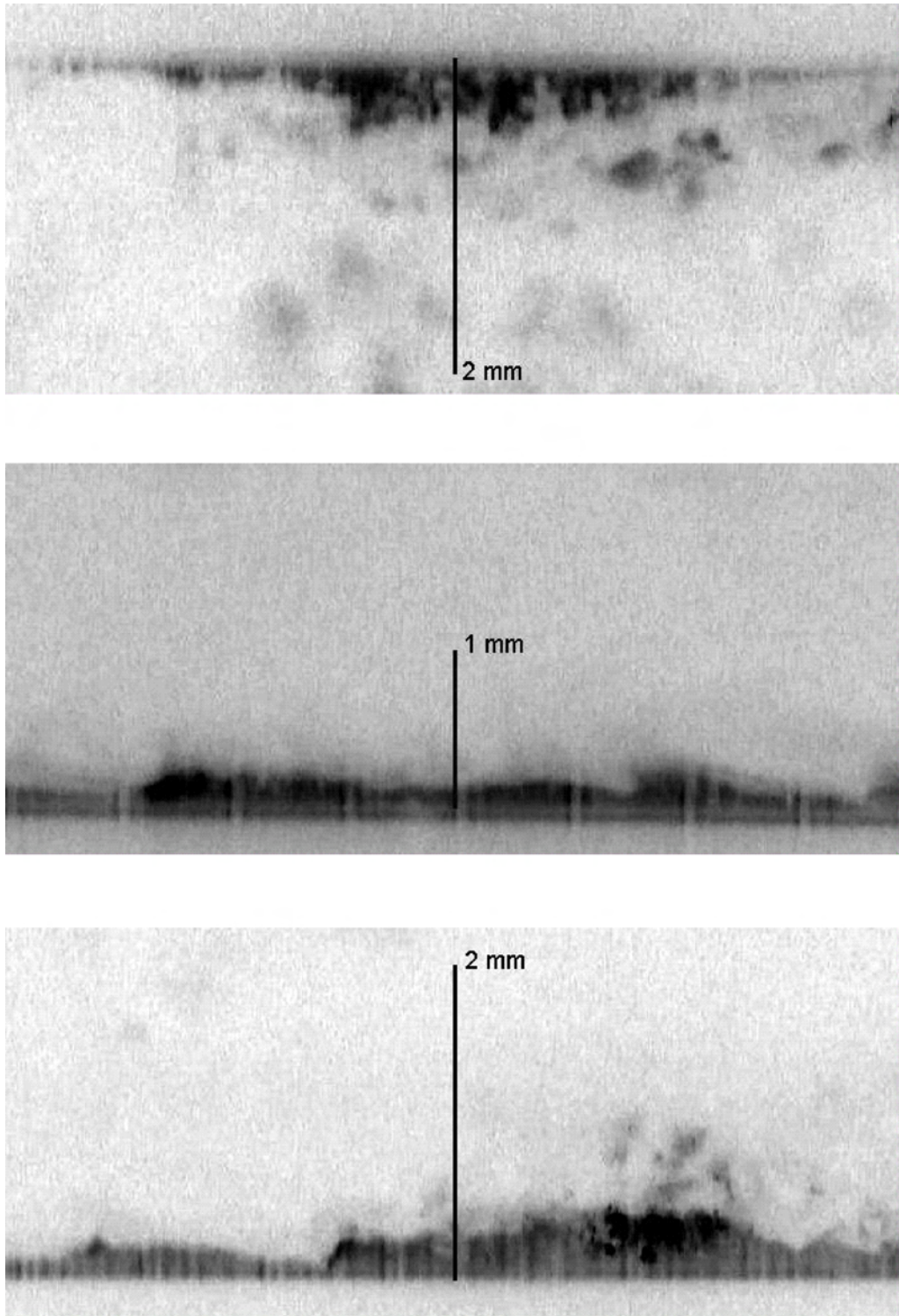


Figure C.13: PLIF Images of interfacial waves along the top, side and bottom of the pipe.  $U_{sg} = 65 \text{ m s}^{-1}$  and  $U_{sl} = 4.6 \text{ cm s}^{-1}$ . Flow from right to left.

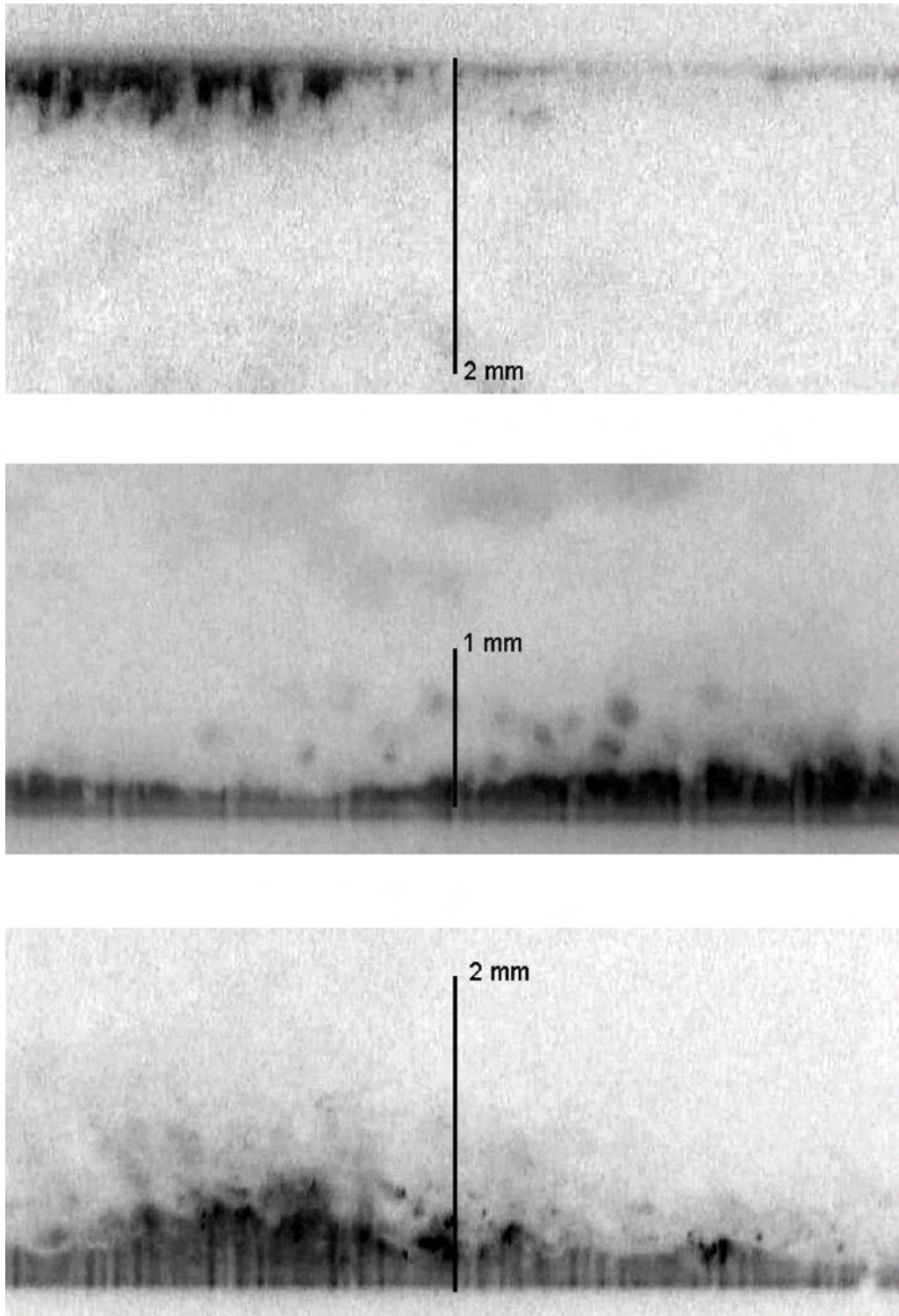


Figure C.14: PLIF Images of interfacial waves along the top, side and bottom of the pipe.  $U_{sg} = 65 \text{ m s}^{-1}$  and  $U_{sl} = 9.3 \text{ cm s}^{-1}$ . Flow from right to left.

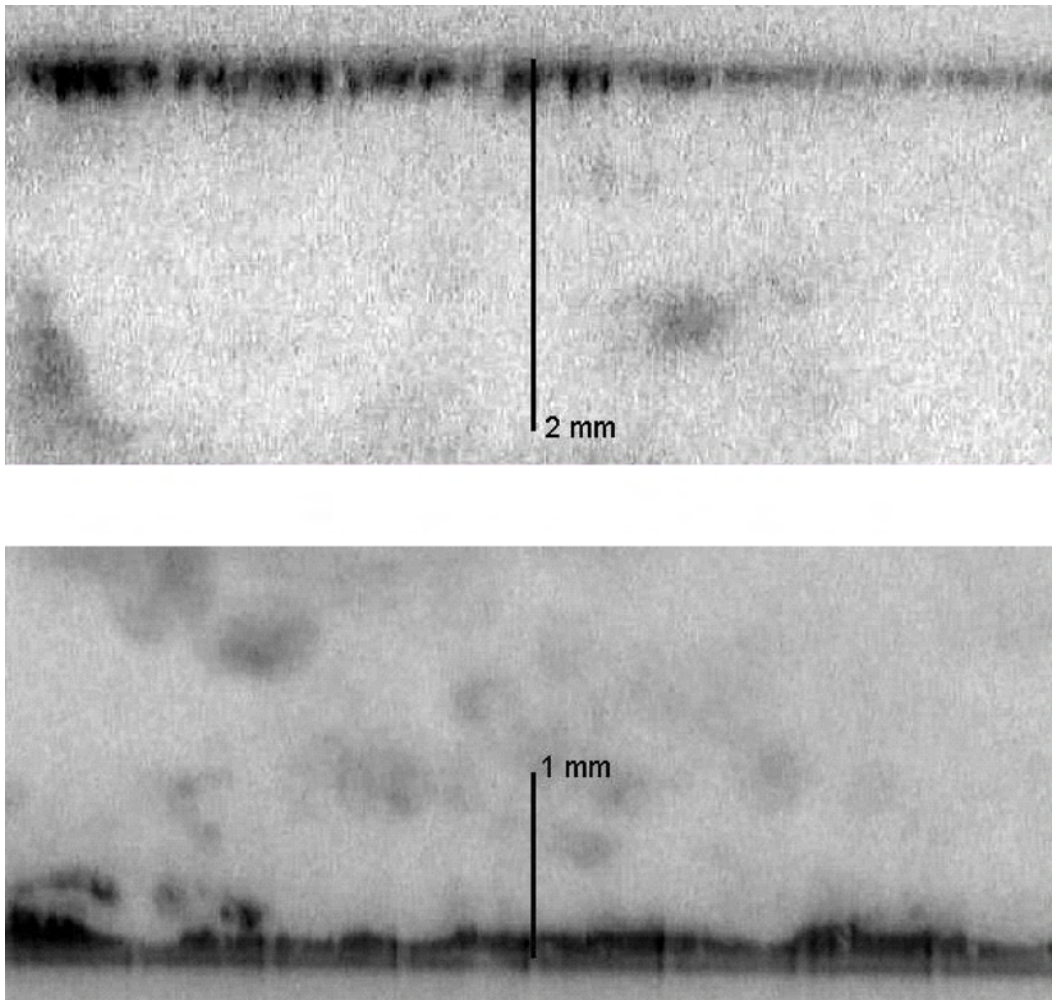


Figure C.15: PLIF Images of interfacial waves along the top and side of the pipe.  $U_{sg} = 65 \text{ m s}^{-1}$  and  $U_{sl} = 14.0 \text{ cm s}^{-1}$ . Flow from right to left.

# Bibliography

- [1] N. Kattan, J. R. Thome, and D. Favrat. Flow boiling in horizontal tubes: Part 2—New heat transfer data for five refrigerants. *Journal of Heat Transfer-Transactions of the ASME*, 120(1):148–55, February 1998.
- [2] O. Zürcher, D. Favrat, and J. R. Thome. Evaporation of refrigerants in a horizontal tube: an improved flow pattern dependent heat transfer model compared to ammonia data. *International Journal of Heat and Mass Transfer*, 45:303–317, 2002.
- [3] G. Sun and G. F. Hewitt. Evaporation and condensation of steam-water in a vertical tube. *Nuclear Engineering and Design*, 207:137–145, 2001.
- [4] B. B. Bayazit, D. K. Hollingsworth, and L. C. Witte. Heat transfer enhancement caused by sliding bubbles. *Journal of Heat Transfer*, 125(3):503–509, June 2003.
- [5] G. E. Thorncroft. *Heat transfer and vapor bubble dynamics in forced convection boiling*. PhD thesis, University of Florida, Gainesville, FL, 1997.
- [6] D. Schubring and T. A. Shedd. Detailed characterization of liquid film behavior in horizontal two-phase wavy and annular air/water flow. In *2004 ASME Heat Transfer/Fluids Engineering Summer Conference*, Charlotte, NC, July 2004.
- [7] T. A. Shedd and T. A. Newell. Automated optical film thickness measurement method. *Rev. Sci. Instruments*, 69(12):4205–4213, 1998.
- [8] G. F. Hewitt, S. Jayanti, and C. B. Hope. Structure of thin liquid films in gas–liquid horizontal flow. *International Journal of Multiphase Flow*, 16(6):951–957, 1990.

- [9] N. Kattan, J. R. Thome, and D. Favrat. Flow boiling in horizontal tubes: Part 3—Development of a new heat transfer model based on flow pattern. *Journal of Heat Transfer-Transactions of the ASME*, 120(1):156–65, February 1998.
- [10] S. G. Kandlikar. A general correlation for saturated two-phase flow boiling heat transfer inside horizontal and vertical tubes. *Journal of Heat Transfer*, 112:219–228, 1990.
- [11] D. Steiner and J. Taborek. Flow boiling heat transfer in vertical tubes correlated by an asymptotic model. *Heat Transfer Eng.*, 13(2):43–69, 1992.
- [12] W. M. Rohsenow. In *Heat Transfer, a Symposium*. University of Michigan, Ann Arbor, 1952.
- [13] C. E. Dengler and J. N. Addoms. Heat transfer mechanism for vaporization of water in a vertical tube. *Chem. Eng. Prog. Symp. Series*, 52(18):95–103, 1956.
- [14] J. C. Chen. Correlation for boiling heat transfer to saturated fluids in convective flow. *IEEC Process Design and Development*, 5(3):322–329, 1966.
- [15] J. G. Collier and J. R. Thome. *Convective Boiling and Condensation*. Oxford University Press, Oxford, third edition, 1994.
- [16] R. L. Webb and N. S. Gupte. A critical review of correlations for convective vaporization in tubes and tube banks. *Heat Transfer Engineering*, 13(3):58–81, 1992.
- [17] J. Darabi, M. Salehi, M. H. Saseedi, and M. M. Ohadi. Review of available correlations for prediction of flow boiling heat transfer in smooth and augmented tubes. *ASHRAE Transactions*, 105(1):965–975, 1995.
- [18] J. R. Thome. Flow boiling in horizontal tubes: a critical assessment of current methodologies. In G. P. Celata and R. K. Shah, editors, *Two-Phase Flow Modelling and Ex-*

- perimentation 1995*, volume 1, pages 41–52, Rome, Italy, October 1995. Edizioni ETS, Pisa.
- [19] S. G. Kandlikar, M. Shoji, and V. K. Dhir, editors. *Handbook of Phase Change: Boiling and Condensation*. Taylor and Francis, Philadelphia, 2003.
- [20] K. E. Gungor and R. H. S. Winterton. A general correlation for flow boiling in tubes and annuli. *International Journal of Heat and Mass Transfer*, 29(3):351–358, 1986.
- [21] S. S. Kurtz, Jr., S. Amon, and A. Sankin. Boiling heat transfer. *Int. J. Heat Mass Transfer*, 4:31–45, 1961.
- [22] S. W. Churchill. *The interpretation and use of rate data*. Hemisphere, New York, 1974.
- [23] J. M. Chawla. Wärmeübergang und druckabfall in waagrecht en rohren bei der strömung von verdampfenden kältemitteln. *Kältetechnik-Klimatisierung*, 19(8):246–252, 1967.
- [24] M. M. Shah. Chart correlation for saturated boiling heat transfer: Equations and further study. *ASHRAE Transactions*, 88(1):185–196, 1982.
- [25] H. K. Forster and N. Zuber. Dynamics of vapor bubbles and boiling heat transfer. *AIChE J.*, 1(4):531–535, 1955.
- [26] M. G. Cooper. Saturation nucleate pool boiling: A simple correlation. In *I. Chem. E. Symposium Series*, volume 2, pages 785–793, 1st U.K. National Conference on Heat Transfer, 1984.
- [27] F. W. Dittus and L. M. K. Boelter. Heat transfer in automobile radiators of the tubular type. In *Publ. Eng., University of California, Berkeley*, volume 2, page 443, 1930.

- [28] V. Gnielinski. New equations for heat and mass transfer in turbulent pipe and channel flow. *Int. Chem. Eng.*, 16:359–368, 1976.
- [29] B. S. Petukhov and V. N. Popov. Theoretical calculation of heat exchange in turbulent flow in tubes of an incompressible fluid with variable physical properties. *High Temp.*, 1(1):69–83, 1963.
- [30] D. Gorenflo. *VDI Wärmeatlas*, chapter Behältersieden, sect. Ha. VDI Verlag, 1988.
- [31] N. Kattan, J. R. Thome, and D. Favrat. Flow boiling in horizontal and vertical tubes: the effect of the orientation on heat transfer. In *International Flow Boiling Conference*, Paper IV-1, Banff, Canada, 1995.
- [32] D. C. Groeneveld and G. G. J. Delorme. Prediction of the thermal non-equilibrium in the post-dryout regime. *Nucl. Eng. Des.*, 36:17–26, 1976.
- [33] J. C. Chen, F.T. Ozkanyank, and K. Sundaram. A phenomenological correlation for post cht heat transfer. *Nuc. Eng. Des.*, 51:143–155, 1979.
- [34] N. Kattan, J. R. Thome, and D. Favrat. Flow boiling in horizontal tubes: Part 1—Development of a diabatic two-phase flow pattern map. *Journal of Heat Transfer-Transactions of the ASME*, 120(1):140–7, February 1998.
- [35] O. Zürcher, D. Favrat, and J. R. Thome. Development of a diabatic two-phase flow pattern map for horizontal flow boiling. *International Journal of Heat and Mass Transfer*, 45:291–301, 2002.
- [36] S. Z. Rouhani and E. Axelsson. Calculation of void volume fraction in the subcooled and quality boiling regions. *International Journal of Heat and Mass Transfer*, 13:383–393, 1970.

- [37] S. A. Klein. Engineering equation solver. *F-Chart software*, ©1992–2004.
- [38] Z. Liu and R. H. S. Winterton. A general correlation for saturated and subcooled flow boiling in tubes and annuli, based on a nucleate pool boiling equation. *International Journal of Heat and Mass Transfer*, 34(11):2759–2766, 1991.
- [39] Y. Aounallah and D.B.R. Kenning. Nucleate boiling and the Chen correlation for flow boiling heat transfer. *Exp. Heat Transfer.*, 1(2):87–92, 1987.
- [40] K. Stephan and M. Adbelsalam. Heat transfer correlations for natural convection boiling. *Int. J. Heat Mass Transfer*, 23:73–80, 1980.
- [41] Z. Liu and R. H. S. Winterton. Wet wall flow boiling correlation with explicit nuclear term. In *5th Int. Symp. Multiphase Transport and Particulate Phenomena*, Miami, Florida, 1988.
- [42] K. E. Gungor and R. H. S. Winterton. Simplified general correlation for saturated flow boiling and comparison of correlations with data. *Chemical Engineering Research and Design*, 65:148–156, 1987.
- [43] V. V. Klimenko. A general correlation for two-phase forced flow heat transfer. *Int. J. Heat Mass Transfer*, 31:541 – 552, 1988.
- [44] R. Mesler. An alternative to the dengler and addoms convection concept of forced convection boiling heat transfer. *AIChE Journal*, 23(4):448–453, 1977.
- [45] R. Mesler and G. Mailen. Nucleate boiling in thin liquid films. *AIChE Journal*, 23(6):954–957, 1977.
- [46] F. C. Gunther. Photographic study of surface-boiling heat transfer to water with forced convection. *Transactions ASME*, 73:115–124, 1951.

- [47] S. D. Houston and K. Cornwell. Heat transfer to sliding bubbles on a tube under evaporating and non-evaporating conditions. *International Journal of Heat and Mass Transfer*, 39(1):211–214, 1996.
- [48] A. J. Addlesee and K. Cornwell. Liquid film thickness above a bubble rising under an inclined plate. *Transactions of the Institution of Chemical Engineers*, 75(A):663–667, 1997.
- [49] D. B. R. Kenning, O. E. Bustnes, and Y. Yan. Heat transfer to a sliding bubble. *Multiphase Science and Technology*, 14(1):75–94, 2002.
- [50] D. Qiu and V. K. Dhir. Experimental study of flow pattern and heat transfer associated with a bubble sliding on downward facing inclined surfaces. *Experimental Thermal and Fluid Science*, 26:605–616, 2002.
- [51] A. J. Addlesee and P. A. Kew. Development of the liquid film above a sliding bubble. *Transactions of the Institution of Chemical Engineers*, 80(A):272–277, April 2002.
- [52] D. G. Owen and G. F. Hewitt. An improved annular two-phase flow model. In *3rd International Conference on Multi-Phase Flow*, pages 73–84, The Hague, Netherlands, May 1987.
- [53] L. A. Jacowitz and R. S. Brodkey. An analysis of geometry and pressure drop for the horizontal, annular, two-phase flow of water and air in the entrance region of a pipe. *Chemical Engineering Science*, 19:261–274, 1964.
- [54] K. D. Cooper, G. F. Hewitt, and B. Pinchin. Photography of two-phase gas/liquid flow. *The Journal of Photographic Science*, 12:269–278, 1964.
- [55] C. R. Arnold and G. F. Hewitt. Further developments in the photography of two-phase gas-liquid flow. *The Journal of Photographic Science*, 15:97–114, 1967.

- [56] G. E. Thorncroft and J. F. Klausner. A capacitance sensor for two-phase liquid film thickness measurements in a square duct. *Transactions of the ASME: Journal of Fluids Engineering*, 119(1):164–169, March 1997.
- [57] R. Mesler. A mechanism supported by extensive experimental evidence to explain high heat fluxes observed during nucleate boiling. *AIChE Journal*, 22(2):246–252, 1976.
- [58] R. C. Gonzalez and R. E. Woods. *Digital Image Processing*. Addison-Wesley, Reading, MA, third edition, 1992.
- [59] C. R. Kopplin. Local liquid velocities in horizontal, annular air/water flow. In *Proceedings of 2003 ASME International Mechanical Engineering Congress & Exposition*, pages Paper IMECE2003–43595, Washington D.C., 2003.
- [60] K. S. Kim and S. S. Kim. Drop sizing and depth-of-field correction in TV imaging. *Atomization and Sprays*, 4:65–78, 1994.
- [61] S. Y. Lee, B. S. Park, and I. G. Kim. Gray level factors used in image processing of two-dimensional drop images. *Atomization and Sprays*, 1:389–400, 1991.
- [62] K. U. Koh, J. Y. Kim, and S. Y. Lee. Determination of in-focus criteria an depth of field in image processing of spray particles.
- [63] V. K. Dhir. Nucleation site density. Contribution to the task group on Microphysics in Multiphase Flow at the DOE Workshop on Multiphase Flow, Urbana, IL, May 2002.
- [64] L. Z. Zeng and J. F. Klausner. Nucleation site density in forced convection boiling. *Journal of Heat Transfer*, 115:215–221, 1993.
- [65] H. Chanson. *Air Bubble Entrainment in Free-surface Turbulent Shear Flows, first ed.*, chapter seven. Acedemic Press, London, UK, 1996.

- [66] G.B. Deane and Stokes M.D. Scale dependence of bubble creation mechanisms in breaking waves. *Nature*, 418(22):839–844, 2002.
- [67] S. V. Paras and A. J. Karabelas. Properties of the liquid layer in horizontal annular flow. *International Journal of Multiphase Flow*, 17(4):439–454, 1991.
- [68] D. Butterworth and D. J. Pulling. RS95: Film flow and film thickness measurements for horizontal, annular, air-water flow. Technical Report AERE-R7576, U. K. Atomic Energy Research Establishment, Harwell, November 1973.
- [69] S. A. Fisher and D. L. Pearce. A theoretical model for describing horizontal annular flows. In F. Durst, G. V. Tsiklauri, and N. H. Afgan, editors, *Two-Phase Momentum, Heat and Mass Transfer*, volume 1, pages 327–337. Hemisphere Publishing Corporation, 1979.
- [70] J. E. Laurinat. *Studies on the Effects of Pipe Size on Horizontal Annular Two-Phase Flows*. PhD thesis, University of Illinois at Urbana-Champaign, Urbana, IL, July 1982.
- [71] K. Sekoguchi, A. Ousaka, T. Fukano, and T. Morimoto. Air-water annular two-phase flow in a horizontal tube. *Bulletin of the JSME*, 25(208):1559–1566, October 1982.
- [72] T. Fukano, A. Ousaka, T. Morimoto, and K. Sekoguchi. Air-water annular two-phase flow in a horizontal tube.2nd report. *Bulletin of JSME*, 26:1387–1395, 1983.
- [73] T. F. Lin, O. C. Jones, R. T. Lahey, R. C. Block, and M. Murase. Film thickness measurements and modelling in horizontal annular flows. *PCH: PhysicoChemical Hydrodynamics*, 6(1/2):197–206, 1985.
- [74] S. Jayanti, G. F. Hewitt, and S. P. White. Time-dependent behavior of the liquid film in horizontal annular flow. *International Journal of Multiphase Flow*, 16(6):1097–1116, 1990.

- [75] V. Modi, C. Gnafakis, and C.C. Gryte. Experiments with computed x-ray tomography to observe horizontal two-phase pipe flow. *Chem Eng. Comm.*, 116, 1992.
- [76] T. Hibiki, K. Mishima, Yoneda K, S. Fujine, A. Tsuruno, and M. Matsubayashi. Visualization of fluid phenomena using a high frame-rate neutron radiography with a steady thermal neutron beam. *Nucl. Methods and Instruments in Physics Research*, 1994.
- [77] D. R. Lide, editor. *CRC Handbook of Chemistry and Physics*. CRC Press, 1998.
- [78] J. Stone. Measurements of the absorption of light in low-loss liquids. *J. Opt. Soc. Am.*, 62:327–333, 1972.
- [79] J. V. Leyendekkers and R. J. Hunter. Refractive index of aqueous electrolyte solutions. extrapolations to other temperatures, pressures and wavelengths and to multicomponent systems. *Journal of Chemical and Engineering Data*, 22(4):427–431, 1977.
- [80] L. I. Nass, editor. *Encyclopedia of PVC*, volume 2. Marcel Dekker, Inc., New York, 1977.
- [81] A. Wolf, S. Jayanti, and G. F. Hewitt. On the nature of ephemeral waves in vertical annular flow. *International Journal of Multiphase Flow*, 22(2):325–333, 1996.
- [82] G. F. Hewitt and N. S. Hall-Taylor. *Annular Two-Phase Flow*. Pergamon Press, Oxford, England, 1970.
- [83] J. O. Hinze. *Turbulence*. McGraw-Hill, Inc., New York, second edition, 1975.
- [84] L. E. Gill, G. F. Hewitt, and P. M. C. Lacey. Sampling probe studies of the gas core in annular two-phase flow – II: Studies of the effect of phase flow rates on phase and velocity distribution. *Chemical Engineering Science*, 19:665–682, 1964.

- [85] S. S. Jayawardena. *Turbulent flow in the core region of vertical annular gas-liquid flow*. PhD thesis, University of Houston, Houston, TX, 1993.
- [86] B. J. Azzopardi and J. C. F. Teixeira. Detailed measurements of vertical annular two-phase flow. Part II: Gas core turbulence. *Journal of Fluids Engineering*, 116:796–800, 1994.
- [87] D. G. Owen. *An Experimental and Theoretical Analysis of Equilibrium Annular Flows*. PhD thesis, University of Birmingham, Birmingham, UK, 1986.
- [88] W. H. McAdams, W. K. Woods, and R. L. Bryan. Vaporization inside horizontal tubes –II– benzene-oil mixtures. *Trans. ASME*, 64:193, 1942.
- [89] A. Cicchitti, C. Lombardi, M. Silvestri, G. Soldaini, and R. Zavattarelli. Two-phase cooling experiments—pressure drop, heat transfer and burnout measurements. *Energia Nucleare*, 7(6):407–425, 1960.
- [90] A. E. Dukler, M. Wicks, and R. G. Cleveland. Pressure drop and hold-up in two-phase flow Part A—A comparison of existing correlations and Part B—An approach through similarity analysis. *AIChE Journal*, 10(1):38–51, 1964.
- [91] G. B. Wallis. *One-dimensional Two-phase Flow*. McGraw-Hill, Inc., New York, 1969.
- [92] W. H. Henstock and T. J. Hanratty. The interfacial drag and the height of the wall layer in annular flows. *AIChE Journal*, 22(6):990–1000, 1976.
- [93] J. C. Asali, T. J. Hanratty, and P. Andreussi. Interfacial drag and film height for vertical annular flow. *AIChE Journal*, 31(6):895–902, 1985.
- [94] L. B. Fore, S. G. Beus, and R. C. Bauer. Interfacial friction in gas-liquid annular flow: analogies to full transition and roughness. *International Journal of Multiphase Flow*, 26:1755–1769, November 2000.

- [95] M. Wolfstein. The velocity and temperature distribution of one-dimensional flow with turbulence augmentation and pressure gradient. *Int. J. Heat Mass Transfer*, 12:301–318, 1969.
- [96] R. A. Gore, , and C. T. Crowe. Effect of particle size on modulating turbulent intensity. *International Journal of Multiphase Flow*, 15(2):279–285, 1989.
- [97] G. Hetsroni, C. F. Li, A. Mosyak, and I. Tiselj. Heat transfer and thermal pattern around a sphere in a turbulent boundary layer. *Internation Journal of Multiphase Flow*, 14(7):1127–1150, 2001.
- [98] T. A. Shedd. *Characteristics of the Liquid Film in Horizontal Two-Phase Annular Flow*. PhD thesis, University of Illinois at Urbana-Champaign, Urbana, IL, 2001.
- [99] S. T. Wereley, J. G. Santiago, R. Chiu, C. D. Meinhart, and R. J. Adrian. Micro-resolution particle image velocimetry.
- [100] M. Born and E. Wolf. *Principles of Optics*. Cambridge University Press, Cambridge, 1999.
- [101] A. K. Prasad, R. J. Adrian, C. C. Landreth, and P. W. Offutt. Effect of resolution on the speed and accuracy of particle image velocimetry interrogation.
- [102] R. D. Keane, R. J. Adrian, and Y. Zhang. Super-resolution particle imaging velocimetry. *Meas. Sci. Technol.*, 6:754–768, 1995.
- [103] R. D. Keane and R. J. Adrian. Optimization of particle image velocimeters. Part i: Double pulsed systems. *Measurement Science and Technology*, 1:1202–1215, 1990.
- [104] R. D. Keane and R. J. Adrian. Optimization of particle image velocimeters. Part ii: Multiple pulsed systems. *Measurement Science and Technology*, 2:963–974, 1991.

- [105] R. D. Keane and R. J. Adrian. Theory of cross-correlation analysis of piv images. *Applied Scientific Research*, 49:191–215, 1992.
- [106] G. E. Uhlenbeck and L. S. Ornstein. On the theory of Brownian motion. *Physical Review*, 36, 1930.
- [107] C. D. Meinhart, S. T. Wereley, and J. G. Santiago. PIV measurements of a microchannel flow.
- [108] C. R. Kopplin. Local liquid velocity measurements in horizontal, annular two-phase flow. Master's thesis, University of Wisconsin-Madison, Madsion, WI, 2004.

# Vita

Daniel José Rodríguez C. was born in Bogotá, Colombia on May 23, 1976 to Leonel Rodríguez and Patricia Campo. He attended Colegio San Carlos and graduated from high school in 1994. Five years later, he received his B.S. in mechanical engineering from Universidad de los Andes in Bogotá, Colombia. Also at Universidad de los Andes, he completed his M.Sc. in mechanical engineering under the supervision of Dr. Alvaro E. Pinilla in 2001. He was married to Paola Jiménez in 2003. He completed his Ph.D. research in 2004 under the advice of Dr. Timothy A. Shedd at the University of Wisconsin-Madison.